De la résonance stochastique à la physique de l'information

David Rousseau

Université d'Angers
Laboratoire d'ingénierie des systèmes automatisés
LISA

Habilitation à diriger des recherches
Spécialité traitement du signal et des images

De la résonance stochastique à la physique de l'information

David ROUSSEAU

Soutenue publiquement le 5 juillet 2010 devant le jury

Rapporteur : François GOUDAIL, professeur CNU-63, institut d'optique, Paris-Tech
Rapporteur : Christophe COLLET, professeur CNU-61, université de Strasbourg
Rapporteur : Christophe GODIN, directeur de recherche, INRIA, Montpellier
Examinateur : Nigel STOCKS, professeur, university of Warwick (England)
Président du jury : Régis BARILLÉ, professeur CNU-30, université d'Angers
Garant : François CHAPEAU-BLONDEAU, professeur CNU-63, université d'Angers
Invité : Xavier MEYNIAL, entreprise Active-Audio

Résumé

Ce document d'HDR a pour but de démontrer ma capacité à diriger des recherches et à encadrer de jeunes chercheurs. On y trouve une synthèse de mes travaux situés à l'interface de la physique et des sciences de l'information :

✓les effets de résonance stochastique où le bruit joue un rôle utile dans le traitement non linéaire de l'information. Un point de vue original est en particulier développé en direction d'effets de bruit utile utilisant les nonlinéarités naturelles des capteurs de signaux ou d'images donnant lieu à des réalisations expérimentales sur des systèmes optiques;
✓l'analyse de signaux et d'images à travers les échelles par des outils d'analyse fractale et multifractale;
✓le projet de recherche que je développe actuellement en direction du traitement du signal et de l'imagerie appliqués aux sciences du vivant (biomédicale et végétale).

Ce faisant, le document présente la démarche suivie à travers ces thématiques de recherche tour à tour guidées par le développement de paradigmes informationnels, le déploiement d'outils transversaux issus de la théorie de l'information, le lien avec mes activités d'enseignement également situées à l'interface de la physique et des sciences de l'information ou encore les richesses, contraintes et opportunités liées à mon environnement actuel de recherche.

Mots clés: traitement non linéaire du signal, bruits, résonance stochastique, capteurs, systèmes optiques, théorie de l'information appliquée aux signaux et aux images, analyses en échelle, anémométrie laser Doppler appliquée au biomédical, imagerie biovégétale.

Remerciements

Le travail de recherche synthétisé dans ce mémoire a été réalisé entre 2005 et 2010 au Laboratoire d'Ingénierie des Systèmes Automatisés (LISA) de l'Université d'Angers. Je remercie l'ensemble des membres du laboratoire et en premier lieu Mr Jean-Louis BOIMOND, directeur du LISA, qui, par leur engagement en recherche, font du LISA un lieu enrichissant de stimulation intellectuelle. Je suis très sensible à l'honneur que me font messieurs les membres du Jury en acceptant de lire et de juger ce travail : Mr François GOUDAIL, professeur à l'institut d'optique, Paris-Tech, Mr Christophe COLLET, professeur à l'université de Strasbourg, Mr Christophe GODIN, directeur de recherche à l'INRIA, Montpellier pour s'être chargés de rapporter ce mémoire. Mr Nigel STOCKS, professeur à l'université de Warwick (Angleterre) et Mr Régis BARILLÉ, professeur à l'université d'Angers pour l'intérêt qu'ils manifestent en examinant la synthèse de mes travaux.

L'étape de l'HDR représente une sorte de passage à l'âge adulte dans l'activité de recherche. Je remercie Mr Philippe RÉFRÉGIER, professeur à l'institut Fresnel, Marseille et Pierre-Olivier AMBLARD, directeur de recherche au CNRS à Grenoble, qui, par les conseils et critiques qu'ils m'ont adressés au hasard de nos rencontres depuis 2005, ont joué (en tant que membres de mon jury de thèse) un véritable rôle de parrains. Je rends hommage, à travers ce mémoire, à mes pères de recherche que sont Xavier MEYNIAL avec qui j'ai effectué une année de recherche appliquée en électro-acoustique en 2000 et François CHAPEAU-BLONDEAU qui a été mon directeur de thèse entre 2001 et 2004 et avec lequel j'ai le plaisir de continuer depuis 2005 à collaborer au quotidien en recherche.

Ce mémoire est dédié à mon épouse Emmanuelle.

Table des matières

Chapitre 1

Introduction

Ce mémoire présente les travaux de recherche que j'ai effectués depuis ma thèse et a pour vocation de prouver aux membres de jury ma capacité à diriger des recherches. Dans ce court chapitre d'introduction, je commence par décrire le choix qui a motivé mon parcours en recherche, j'indique ensuite l'organisation générale de ce document d'habilitation à diriger des recherches (HDR) et les perspectives qu'il dégage, j'adresse pour finir quelques remerciements.

1.1 Motivation

Au moment où s'inscrivent ces lignes, j'aurai passé 10 années à l'université d'Angers. Recruté en tant que professeur agrégé de physique en septembre 2000 pour m'occuper de la formation des maîtres (CAPES externe et agrégation interne) à la faculté des sciences de l'université d'Angers, je n'avais a priori pas pour mission de m'impliquer en recherche. J'ai initialement choisi de m'investir dans une activité de recherche pour progresser en enseignement. Cet intérêt pour la recherche est me semble-t-il une originalité en ce sens qu'il est revendiqué et assumé. La dynamique enseignement-recherche que je développe depuis 10 ans s'exprime principalement par réflexivité [110]. Comment transmettre aux futurs enseignants une discipline vivante et la nécessité de la rendre vivante ? Comment transmettre surtout la nécessité pour le professeur de s'inscrire dans une analyse réflexive de sa pratique ? Ce sont là des questions fondamentales qui m'importent [86, 133] en tant que formateur pour les futurs enseignants de sciences physiques. Pour contribuer à y répondre, je pense qu'il faut payer de sa personne et rendre la discipline vivante en participant soi-même à l'évolution des disciplines. Quand bien même la contribution à faire "reculer les frontières de la connaissance" serait modeste, c'est la démarche qui prime. L'activité de recherche donne accès à la science en train de se construire et sensibilise ainsi, par la pratique, à l'histoire et la philosophie des sciences. Cette sensibilisation est utile au formateur de futurs enseignants que je suis puisque, l'histoire et la philosophie des sciences constituent des éléments de base de didactique des sciences physiques. L'activité de recherche ainsi conçue constitue également un puissant moteur d'autoformation utile pour l'enseignement. À l'occasion de la rédaction de ce document d'HDR, je m'aperçois avec un certain étonnement que ce que je présente ici tant en physique qu'en sciences de l'information n'était pas familier à l'agrégé de physique que j'étais il y a dix ans.

1.2 Organisation du document

L'esprit de chacune des parties de la suite de ce document est le suivant :

• Le chapitre 2, sous la forme d'un CV, constitue un bilan d'activité permettant d'apprécier la largeur du domaine scientifique et technologique que j'aborde en enseignement et en recherche. On trouve également dans ce chapitre 2 des éléments clés pour une HDR, comme un résumé de mon activité de recherche, le détail des encadrements de jeunes chercheurs auquel j'ai participé et la liste complète de mes publications depuis mon recrutement en tant que maître de conférences.

• Les chapitres 3 et 4 invitent à une appréciation dans l'épaisseur de mes travaux de recherche, de la démarche qui les guide et de la façon dont ils sont reliés à l'encadrement doctoral de jeunes chercheurs. Le chapitre 3 sur la résonance stochastique constitue une synthèse assez dense de ma contribution sur le sujet dans le prolongement de mon travail de thèse. Le chapitre 4, sur un mode plus pédagogique, présente le cadre élargi de *physique de l'information* dans lequel je situe l'évolution de mon activité de recherche avec des résultats récents sur l'analyse en échelle et des applications en sciences du vivant. Les introductions des chapitres 3 et 4 identiquement intitulées *contexte, objectifs et méthodes* se veulent des éléments d'appréciation de mes aptitudes en terme de stratégie de recherche.

• La section bibliographique est utilisée dans un double but. On y trouve, en complémentarité avec la liste de publications du chapitre 2, mes travaux auxquels le corps du document renvoie dans la continuité du discours. Ce référencement inclut les études [132, 31, 130, 131, 123, 124, 126, 120, 55, 33, 121, 118, 120] qui avaient donné lieu à publication dans le cadre de mon travail de thèse. La section bibliographique est par ailleurs constituée d'ouvrages et d'articles que je juge utiles pour situer la résonance stochastique et plus largement la physique de l'information.

• L'annexe propose un recueil de 14 manuscrits que j'ai sélectionné pour illustrer la diversité des domaines auxquels je m'intéresse. Pour autant, chaque manuscrit est cité plusieurs fois dans le corps du document. Ceci démontre, à mon sens, la cohérence de mes explorations. Pour motiver et éclairer leur lecture, les manuscrits de l'annexe sont systématiquement mentionnés comme tel dans le document en étant indiqués en gras et soulignés. Les titres des manuscrits présents dans l'annexe sont également indiqués en gras dans la section bibliographique.

1.3 Perspectives

La présentation de ce mémoire ne se veut ni une finalité ni un achèvement, c'est pourquoi il n'y a pas de chapitre de conclusion dans ce document. Des éléments de perspectives sont égrainés tout au long des chapitres 3 et 4, ils dessinent les contours du projet de recherche que je présenterai de façon rassemblée et détaillée lors de la soutenance orale de ce diplôme d'HDR.

1.4 Crédits

La rédaction de cette HDR me donne l'occasion de saluer les individus dont la rencontre à constitué un tournant dans mon parcours en recherche.

En arrivant à Angers en 2000 mon "bagage" en recherche (stage de DEA et année de recherche

appliquée voir CV) était plutôt celui d'un expérimentateur. Ma condition de PRAG de l'époque ne me permettant pas de m'impliquer dans des programmes expérimentaux connus pour leur caractère chronophage, j'ai choisi d'accepter la proposition de thèse en traitement du signal que me faisait mon collègue François CHAPEAU-BLONDEAU. C'est un choix que je n'ai jamais eu à regretter. Je lui suis redevable d'enrichissements techniques et culturels de mes capacités en science et en particulier de progrès en expression scientifique à l'oral et à l'écrit.

Une fois en position d'avoir une activité équilibrée en enseignement et en recherche (i.e. en 2005 après mon recrutement en tant que maître de conférences), j'ai eu à cœur de mettre à nouveau à l'œuvre mon goût pour l'expérimentation en initiant en 2007 une collaboration avec Denis GINDRE (maître de conférences en section 30 du CNU à l'Université d'Angers). Cette rencontre et ce virage ont été important puisqu'ils m'ont fait progresser en optique et élargir mon champ d'investigation en direction de l'imagerie et du traitement des images, ce qui me permet de revendiquer aujourd'hui un positionnement en sciences de l'information.

Parmi les actes fondateurs de la physique, il y a le geste de GALILÉE qui tourne, pour la première fois, sa lunette terrestre en direction de la lune. Aller y voir avant toute chose. Malheureusement ou heureusement, la physique, parfois présentée comme la mère de toutes les sciences, a atteint une certaine maturité. Même si on continue de repousser les frontières de la connaissances en direction des infinis (petit, grand et complexe), les phénomènes naturels du quotidien perceptibles à l'échelle humaine semblent suffisamment bien interprétables dans les cadres théoriques conceptuels de la physique. Il reste cependant de nombreuse voies d'évolution pour la physique en tant que méthode notamment en se mettant au service des autres sciences et en particulier des sciences du vivant. Depuis 2008, j'oriente une partie de mes travaux en direction d'applications des sciences de l'information pour les sciences du vivant. C'est grâce à la rencontre d'Anne HUMEAU (professeure au LISA) fortement implantée au CHU d'Angers et de Carolyne DURR (ingénieure de recherche à l'INRA) avec laquelle je coordonne un projet d'imagerie pour le végétal. Il y a une part de nécessité à se positionner sur ces sujets car les sciences du vivant attirent actuellement les financements. Il s'agit pour moi surtout du plaisir philosophique du physicien à marcher dans les pas des aînés en allant y voir avant toute chose.

Angers le 6 mars 2010 [1],
David ROUSSEAU.

[1] Version du manuscrit adressée le 23 mars 2010 aux rapporteurs corrigée de quelques fautes de frappes.

Chapitre 2

CURRICULUM VITAE

2.1 État civil

- *Nom* David ROUSSEAU
- *Naissance* 25 février 1973 au Mans
- *Nationalité* Française
- *Situation de famille* Marié, 2 enfants
- *Enseignement* Département de physique, Faculté des Sciences, Univ. Angers, 2 Bd Lavoisier, 49000 Angers
- *Recherche* Laboratoire d'Ingénierie des Systèmes Automatisés (LISA), Univ. Angers, 62 Av. Notre Dame du Lac, 49000 Angers
- *Téléphone* 02.41.22.65.11
- *Page web* http://www.istia.univ-angers.fr/LISA/ROUSSEAU/
- *Courriel* david.rousseau@univ-angers.fr

2.2 Titres universitaires

✓ **Doctorat** de l'Université d'Angers, préparé en 3 ans (2001-2004) au Laboratoire d'Ingénierie des Systèmes Automatisés (LISA) soutenu le 15 octobre 2004 suivi en 2005 de la qualification aux fonctions de maître de conférences par les sections 61, 63 et 28 du CNU.

- *Spécialité* Traitement du signal et des images
- *Intitulé* Contribution à l'étude du traitement de l'information dans les processus physiques non linéaires : résonance stochastique et rôle bénéfique du bruit
- *Directeur* François CHAPEAU-BLONDEAU
- *Jury* Philippe REFREGIER, Jean-Marie BILBAULT, Pierre-Olivier AMBLARD, Marc BRUNEL
- *Mention* Très honorable avec félicitations du jury

✓ **Diplôme d'Etudes Approfondies** en acoustique, traitement du signal et informatique appliqués à la musique (ATIAM), obtenu en 1998 avec mention Assez-Bien à l'Institut de Recherche et de Coordination Acoustique et Musique (IRCAM), Paris.

✓ **Agrégation de physique** option physique obtenue en 1997 après préparation à l'Université

de Rennes 1.

✓ **Licence et Maîtrise de physique** obtenues en 1995 et 1996 avec mention Bien à l'Université du Maine.

2.3 Activités professionnelles

✓**Enseignant dans le secondaire** [1997 – 1998] en sciences physique en tant que stagiaire agrégé à l'IUFM de Rennes. L'année de validation pratique de l'agrégation consiste en une alternance de formations pédagogiques et de stages en responsabilités dans des classes de niveaux allant du collège aux classes préparatoires aux grandes écoles. La titularisation est rendue effective après inspection par un inspecteur pédagogique régional.

✓**Préparateur agrégé** [1998 – 1999] à l'Université de Rennes 1 dans le cadre du service national : encadrement des travaux pratiques des préparations aux concours de l'agrégation de physique et du CAPES de sciences physiques et de physique appliquée.

✓**Ingénieur** [1999 – 2000] dans le cadre d'un contrat avec la société Klaxon, au Laboratoire d'Acoustique de l'Université du Maine (LAUM). Durant la même période, j'ai assuré un cours d'acoustique en tant qu'enseignant vacataire à l'IUT mesures physiques de l'Université de Caen.

✓**Professeur agrégé** [2000 – 2005] au département de physique de l'Université d'Angers.

✓**Enseignant-chercheur** depuis sept. 2005. J'assume les fonctions de maître de conférences en section 63 du CNU à l'Université d'Angers.

2.4 Activités pédagogiques

2.4.1 Enseignements

J'effectue mes enseignements (détails donnés sur la Fig. 2.1) au sein du département de physique de la faculté des sciences de l'Université d'Angers dans des formations ayant trait aux domaines :

✓ des sciences de l'information (Master 2 Photonique Signal Imagerie (PSI), Master 2 Systèmes Dynamiques et Signaux (SDS), en deuxième année de l'école d'ingenieurs de l'Université d'Angers ISTIA); C'est dans le cadre de ces formations proches de mes thématiques de recherche que je propose des sujets de stage de Master 2.

✓ de la physique. Je me consacre plus spécifiquement à l'enseignement de la physique pour la formation des maîtres. Depuis 2000, la majeure partie de mon service est consacrée à la préparation au CAPES de Sciences Physiques de l'Université d'Angers. J'enseigne dans ce cadre tous les domaines de physique générale de base avec un intérêt particulier pour ceux interconnectés aux sciences de l'information comme la thermodynamique, l'acoustique, la physique des ondes, l'électrocinétique.

DOMAINE	FILIÈRE	MATIÈRE	TYPE	VOL.
Formation des maîtres				
2002 – 2010	Agrégation	Thermodynamique	Cours+TP	20h
2000 – 2010	CAPES	Physique générale	TP	180h
2000 – 2005	CAPES	Acoustique	Cours+TD	10h
2000 – 2010	CAPES	Métrologie	Cours+TD	6h
2009 – 2010	CAPES	Électronique	Cours+TD	16h
Formation initiale				
2000 – 2002	L1	Physique générale	TP	100h
2000 – 2003	L2	Thermodynamique	Cours+TD	25h
2000 – 2002	L3	Ondes et vibrations	TD	21h
Sciences de l'information				
2000 – 2010	Master 2 PSI	Théorie de l'information	Cours+TD+TP	25h
2000 – 2003	Master 2 PSI	Traitement du signal et des images	TP	12h
2000 – 2003	Master 2 PSI	Physique de l'imagerie	Cours+TD+TP	25h
2004 – 2005	Master 2 SDS	Bases de Traitement du signal	Cours	6h
2008 – 2010	Master 2 SDS	Traitement numérique des images	Cours+TD+TP	20h
2008 – 2010	L2	Capteurs	Cours+TD+TP	24h

Figure 2.1 : Détail de mes enseignements depuis 2000 à l'Université d'Angers.

2.4.2 Responsabilités

Au-delà de mon service statutaire d'enseignement, je m'implique pleinement depuis mon recrutement comme professeur agrégé puis comme maître de conférences à l'Université d'Angers dans diverses entreprises collectives avec notamment un investissement particulier dans les **responsabilités logistiques** de travaux pratiques.

✓ Depuis 2000, j'assume la responsabilité de la préparation au CAPES de sciences physique pour la partie physique. J'assure la totalité de la préparation à l'épreuve orale du montage (2 heures de préparation pour présenter pendant 30 minutes des expériences autour d'un thème tiré parmi une liste de 30 intitulés couvrant l'ensemble des bases de la physique). En plus du travail pédagogique (encadrement des travaux pratiques, correction des présentations de montages), j'ai la responsabilité de l'organisation du planning des salles de travaux pratiques, la gestion et la commande du matériel, la fabrication de maquettes "maison". Enfin, je me suis investi dans la mise en ligne de ressources pédagogiques numériques pour préparer les étudiants aux techniques expérimentales en amont des séances de travaux pratiques[1]. Ces ressources pédagogiques numériques sont librement disponibles sur http://ead.univ-angers.fr/ capespc/ et rencontrent un certain succès puisque l'on compte plus de 15000 connections par an à travers le monde entier.

✓Je me suis chargé de la rédaction et du suivi, d'une demande de subvention auprès des collectivités territoriales à hauteur de 115k euros pour équiper des salles de travaux pratiques des départements de physique et de chimie. Cette demande, que j'ai initiée avec un collègue chimiste en 2005-2006 a été acceptée en 2006-2007. J'ai ensuite assuré pour la physique les commandes de matériel, leur réception, leur mise en œuvre et de l'agencement dans les salles de travaux pratiques en 2007-2008.

[1] J'ai monté ce projet en collaboration avec un collègue de l'Université d'Angers PRAG de Chimie. Nous avons bénéficié d'un financement de l'Université Virtuelle des Pays de la Loire (UVPL) et de l'assistance technique du Service des Technologies de l'Information et de la Communication (STIC) de l'Université d'Angers.

2.5 Activités de recherche

2.5.1 Bilan succint

La liste bibliographique de mes publications depuis mon recrutement comme maître de conférences en septembre 2005 est donnée dans la section 5 du dossier. J'indique ensuite comment j'ai progressivement élargi ma thématique de recherche en passant de l'étude de la résonance stochastique à des études sur la physique de l'information.

Type de publications depuis 2005	Nombre
Articles de revues avec comité de lecture	33
Conférences internationales avec comité de lecture	12
Conférences nationales avec comité de lecture	7

2.5.1.1 De la résonance stochastique ...

Mon travail de recherche a d'abord consisté à poursuivre et étendre l'investigation des effets de résonance stochastique dans les processus physiques non linéaires qui était le thème de ma thèse de doctorat.

Les processus physiques non linéaires ont des dynamiques plus riches que celles des processus linéaires ; ils manifestent des comportements qui peuvent présenter un intérêt particulier pour les sciences de l'information. J'étudie l'un de ces comportements intrinsèquement non linéaire : la possibilité d'améliorer, dans certains systèmes non linéaires, la transmission ou le traitement d'une information utile au moyen d'une augmentation du bruit dans le système. L'ensemble des situations qui peuvent donner lieu à un effet bénéfique du bruit est un secteur en constante évolution. L'ensemble des manifestations de ce phénomène est rassemblé, au profit d'une présentation unifiée, sous le terme de résonance stochastique. Cet effet paradoxal a originellement été introduit en 1981 dans le contexte de la physique non linéaire. Progressivement, la résonance stochastique a été observée et analysée dans une variété grandissante de processus, incluant des circuits électroniques, des dispositifs optiques, des systèmes neuronaux. Le laboratoire LISA de l'Université d'Angers a été l'un des laboratoires pionnier en France sur l'étude de la résonance stochastique. C'est le fait du professeur François CHAPEAU-BLONDEAU qui a initié le sujet au Laboratoire LISA en 1996. Il a été mon directeur de thèse. Nous poursuivons la collaboration sur ce sujet depuis 2005.

Les **résultats publiés** dans le cadre de mon travail sur la résonance stochastique peuvent s'organiser autour de 2 axes :

✓ **Des analyses fondamentales** :

en considérant les questions liées aux gains en rapport signal sur bruit dans les processus non linéaires [A3, A5, A6, A7], en montrant la possibilité de traitements optimaux améliorés par le bruit [A4, A15, B12,A26], en étudiant les propriétés de systèmes dynamiques bistables [A1] ou de réseaux parallèles de systèmes non linéaires en présence de bruit [A21, B2];

✓ **Des applications pratiques** :

en considérant en particulier des applications de la résonance stochastique dans des domaines liés aux compétences de la section CNU 63 comme les capteurs [A1, A8, A10, A11, A12, A19], les pro-

cessus neuronaux vus comme des systèmes électriques spécifiques de traitement de l'information [A13] et plus récemment en élargissant aux systèmes d'imagerie [A9, B4, A14, B3, B8, A20, A23, A24, B16]. Cette extension de la résonance stochastique aux images est un aspect particulièrement original de mon travail puisque les effets de bruits utiles avaient, jusqu'alors, essentiellement été étudiés sur des processus non linéaires dédiés aux signaux monodimmensionnels.

2.5.1.2 ... à la physique de l'information

Mes travaux sur la résonance stochastique m'ont amené à travailler sur des systèmes physiques et des tâches de traitement de l'information variés. J'ai ainsi développé des compétences larges en physique non linéaire et en théorie de l'information appliquée aux signaux et **aux images**. Ceci m'a permis de m'interesser à des questions autres que celles liées aux effets de bruits utiles mais ayant comme point commun d'être situées à l'interface entre la physique et les sciences de l'information. Dans ce contexte élargi de physique de l'information, je développe actuellement mes travaux selon 2 modalités :

• **Analyse en échelle et image**: les images de scènes naturelles sont des structures informationnelles complexes. Leur compréhension et leur modélisation sont essentielles pour de nombreuses tâches de traitement d'image ou de vision et de nouveaux progrès sont a priori intéressants dans cette direction. Parmi les propriétés spécifiques qui caractérisent les images naturelles, il y a les propriétés fractales. Des invariances d'échelles synonymes de fractalité ont principalement été observées dans l'organisation spatiale des images naturelles. De telles propriétés fractales dans le domaine spatial sont utiles pour construire des modèles plus réalistes des images naturelles tel que le perçoit le système visuel. Les études [A27, A30, B14] montrent un nouvel aspect des propriétés fractales des images naturelles. Au delà de l'organisation spatiale, nous avons considéré l'organisation colorimétrique. Nous avons montré au moyen de différents estimateurs que la distribution des pixels tend à se faire de façon auto-similaire dans l'espace colorimétrique. Sur le même thème de l'analyse en échelle, j'ai récemment initié des travaux sur la question de l'échelle optimale d'observation d'objets dans des images bruités [B18].

✓ **Application des sciences de l'information aux sciences du vivant**: j'explore également des approches applicatives en considérant les sciences du vivant. Dans le domaine du biomédical je m'intéresse à la fluxmétrie laser Doppler (LDF). Habituellement, seule la valeur moyenne du signal LDF est utilisée pour observer la circulation sanguine. Avec une équipe pluridisciplinaire de traiteurs de signaux et de praticiens du centre hospitalier universitaire d'Angers rassemblée autour d'Anne HUMEAU (professeure au Laboratoire LISA), nous cherchons à analyser les fluctuations autour de ces valeurs moyennes pour tenter de déterminer si elles peuvent être porteuses d'informations utiles pour la compréhension des phénomènes physiologiques. Dans ce cadre, nous avons utilisé des outils nouveaux pour l'analyse des signaux comme la transformée de Hilbert-Huang [A28], des mesures issues de la théorie statistique de l'information comme l'information de Fisher [A22, A25] ou encore l'analyse en échelle au moyen d'analyses multifractales [A16, A17, A28, A29, B5, B6, B7, B11, B13, B17] pour évaluer la complexité des signaux de LDF. Dans le cadre du projet PHENOTIC (voir section 2.5.3), je considère le domaine du biovégétal et les nouvelles applications des sciences de l'information pour le phénotypage. Je m'intéresse à trois supports d'étude à différentes échelles de taille et étapes de développement des plantes : la croissance d'une plantule depuis la semence jusqu'à la reprise de la photosynthèse; l'architecture du rosier; le développement de pathogènes dans différents tissus [B19].

2.5.2 Encadrement

Thèses

Thèse soutenue : Solenna BLANCHARD (durée 3 ans : septembre 2006 - Novembre 2008)
Titre de la thèse : Effet de bruit utile dans les processus non linéaires : Contribution sur de nouveaux mécanismes en traitement du signal et en imagerie.
Constitution du Jury : R. LE BOUQUIN-JEANNES (rapporteur, section CNU 61), J.-M. BILBAULT (rapporteur, section CNU 63), F. GOUDAIL (président du jury, section CNU 63), S. ZOZOR (examinateur, CNRS), D. GINDRE (examinateur, section CNU 30)
Encadrement : **50% D. ROUSSEAU**–F. CHAPEAU-BLONDEAU, professeur section CNU 63.
Financement : Allocation de recherche du ministère et monitorat.
Publications pendant la thèse sur la durée 2006-2008 : 6 articles dans des revues avec comité de lecture [A10, A13, A14, A20, A21, A24] et 3 congrès avec actes et comités de lecture [B3, B8, B9].
Situation actuelle de la diplômée : Solenna BLANCHARD a obtenu la qualification aux fonctions de maître de conférences par les sections CNU 61 et 63. Elle effectue actuellement un post-doctorat au Laboratoire Traitement du Signal et de l'Image (LTSI) UMR Inserm 642 de l'Université de Rennes 2.

Thèse en cours : Julien CHAUVEAU (début de la thèse en septembre 2007)
Titre provisoire de la thèse : Méthodes fractales en analyse et synthèse d'images. Application à l'imagerie couleur.
Encadrement : **50% D. ROUSSEAU**–F. CHAPEAU-BLONDEAU
Financement: Bourse des collectivités locales (Communauté d'Agglomération de Cholet).
Situation actuelle du doctorant : il est inscrit en troisième année, 2 articles [A27, A30] et 1 congrès [B14]. La soutenance est prévue à l'automne 2010.

Thèse en cours: Agnès DELAHAIES (début de la thèse en septembre 2008)
Titre provisoire de la thèse: Traitement et analyse de l'information en imagerie non conventionnelle. Applications aux domaines du biomédical et du végétal.
Encadrement : **50% D. ROUSSEAU**–CHAPEAU-BLONDEAU
Financement: Allocation de recherche du ministère flêchée sur thématique prioritaire et monitorat.
Situation actuelle du doctorant : elle est inscrite en deuxième année, 1 article [A32] et 2 congrès [B16, B18].

Stages de Master 2 (durée 6 mois)

• Jin CHEN, "Simulations dynamiques de forces de frottement avec retour d'effort", 2006-2007. Master2 SDS. Responsable du stage : E. RICHARD et **D. ROUSSEAU**. Aujourd'hui ingénieur en Chine.

• Thibault LEVRARD, "Une méthodologie de quantification multi-échelle du degré de dépendance de deux signaux-application aux signaux physiologiques", 2008-2009. Master 2 SDS. Respon-

sable du stage : **D. ROUSSEAU**, F. CHAPEAU-BLONDEAU. Embauché en sept. 2009 en tant qu'ingénieur R&D par l'entreprise de télémédecine Télévasc.

• Marouene KEFI, "Phénotypage du rosier buisson par traitement d'image et approche plante virtuelle", 2008-2009. Master 2 SDS Responsable du stage : P. RICHARD et **D. ROUSSEAU**. Financement par le projet PHENOTIC (décrit dans la section 4). Poursuite en thèse CIFRE avec Thalès au laboratoire LISA en sept. 2009.

• Frédéric AMIARD, "Imagerie par thermographie infrarouge, mise en oeuvre pour la détection de pathogène à la surface de feuilles de plantes"[B19], 2008-2009. Master 2 PSI. Responsable du stage : **D. ROUSSEAU**. Financement par le projet PHENOTIC (décrit dans la section 4). Recherche d'emploi d'ingénieur à partir de sept. 2009.

• Rohit BHAT, "Improved Bayesian Estimation of Weak Signals in Non-Gaussian Noise by Optimal Quantization", 2004-2005. Master de l'Indian Institute of Science. Responsable du stage : **D. ROUSSEAU**, G. V. ANAND. Il s'agit d'un stage que j'ai encadré lors d'un séjour en tant que professeur invité à l'Indian Institute of Science de Bangalore (Inde). Embauche dans une entreprise de télécommunication indienne en 2005.

Autres encadrements

Je citerai également les encadrements auxquel j'ai contribué de façon effective dans d'autres contextes comme :

• Stages post-doctoraux (ATER ou postdoctorat) : Aymeric HISTACE (ATER au laboratoire LISA 2005-2006) [A9], François Xavier INGLÈSE (ATER au laboratoire LISA 2007-2008) [A19], Etienne BELIN (Post-doctorant à l'INRA sur le projet PHENOTIC que je coordonne) [B19].

• Thèses en dehors d'un encadrement officiel : Jocelyn FIORINA (Thésard à SUPELEC 2004-2007) [A8], Benjamin BUARD (Thésard l'ESAIP 2007-2010)[A29,B11,B17].

• Projets étudiants de master 2 (100H), au rythme de 2 par ans depuis 10 ans, avec des sujets centrés sur les compétences de la section 63 du CNU et/ou liés à mes thématiques de recherche partant des capteurs ("Mesures physiques à partir du speckle optique","transmission d'image assistée par le bruit en imagerie cohérent" , "Etude du spectromètre à fibre SPID HR de la marque Ulice", "Etude de systèmes de lecture de code à barres", "Anémométrie laser Doppler") en passant par les convertisseurs analogiques-numériques ("Programmation d'une carte d'acquisition PCTV pour la conception d'un détecteur de mouvement", "Initiation au DSP TMS320C50", "Implémentation DSP TMS320C50 pour la réalisation de non linéarités statiques à saturation") et en allant jusqu'au traitement et la modélisation ("Réalisation d'une interface en DELPHI pour l'acquisition automatique d'intensité lumineuse", "Détection automatique de beats musicaux", "Evaluation du logiciel COMSIS sous les aspects codage et propagation de l'information dans une liaison optique").

2.5.3 Responsabilités

Management de la recherche : Depuis mars 2008, je suis **co-responsable** (montage scientifique et financier, animation scientifique et coordination, implication directe en recherche, représentation auprès des financeurs) d'un projet d'imagerie pour les sciences du végétal PHENOTIC de type pari scientifique régional. Le financement de ce projet a été accepté à hauteur de 300k euros pour une durée de 3 ans à compter de janvier 2009 (lien web : http://www.istia.univ-angers.fr/LISA/PHENOTIC/index.html). Le projet, que je coordonne avec Carolyne DÜRR (ingénieure INRA), rassemble plus de 30 enseignant-chercheurs ou chercheurs et inclut l'encadrement d'un post-doc (Etienn BELIN) de compétences STIC pour la durée du projet.

Rayonnement scientifique : Mon activité de recherche a permis d'établir des **coopérations** ayant donné lieu à publications.

✓ **Internationales**: avec l'Indian Institute of Science (Inde) [A11] et Qingdao University (Chine) [A1];
✓ **Nationales**: avec le Laboratoire des Equipes Traitement de l'Information et Systèmes (ETIS CNRS UMR 8051) de l'Université de Cergy-Pontoise [B4], avec le Département de Télécommunications du centre de Gif sur Yvette de SUPÉLEC [A8], avec le Laboratoire des Propriétés Optiques des Matériaux et Applications (POMA) de l'Université d'Angers [A14, A20, A23, A24, B3, B9, B16].

Relectures : Reviewer régulier pour différentes revues internationales dont IEEE Transactions on Signal Processing, IEEE Signal Processing Letters, Signal Processing Journal, International Journal on Bifurcation and Chaos. J'accepte de participer à ce travail pour 2 à 3 manuscrits par an, c'est environ la moitié du nombre d'articles que je soumets en tant qu'auteur.

Jury et commissions :

✓ Examinateur au jury de la soutenance de thèse de Cédric DUCHÊNE (Influence des fluctuations sur l'échantillonnage et la quantification dans le système visuel à l'INPG de Grenoble, juillet 2008).

✓ Membre du comité consultatif pour les section CNU 63-61-62-60 de l'Université d'Angers depuis 2008.
✓ Membre élu du conseil du laboratoire LISA depuis 2008.
✓ Membre du comité de pilotage de VEGEPOLYS pôle de compétitivité à vocation mondiale depuis 2009.

Invitations d'universités étrangères :

✓Du 1er juillet au 1er septembre 2004, j'ai été invité par le prof. G. V. Anand à l'Indian Institute of Science de Bangalore (Inde) pour un travail sur l'utilisation d'opérateurs non linéaires en vue d'améliorer les techniques actuelles de détection, d'estimation et localisation de sources sonores en acoustique sous-marine lorsque les bruits sont non-gaussiens.

✓Du 15 au 31 janvier 2006, j'ai été invité par le prof. Zhong-Ping JIANG à donner un cours sur la résonance stochastique appliquée au traitement d'image à Polytechnic University, New York, USA.

2.6 Liste des publications depuis la thèse

2.6.1 Articles dans des revues avec comité de lecture

[A1] **D. ROUSSEAU**, F. DUAN, J. ROJAS VARELA, and F. CHAPEAU-BLONDEAU. Evaluation of a nonlinear bistable filter for binary signal detection. *International Journal of Bifurcation and Chaos*, vol. 15:667–679, 2005.

[A2] **D. ROUSSEAU** and F. CHAPEAU-BLONDEAU. Constructive role of noise in signal detection from parallel arrays of quantizers. *Signal Processing*, vol. 85:571–580, 2005.

[A3] **D. ROUSSEAU** and F. CHAPEAU-BLONDEAU. Stochastic resonance and improvement by noise in optimal detection strategies. D*igital Signal Processing*, vol. 15:19–32, 2005.

[A4] F. CHAPEAU-BLONDEAU and **D. ROUSSEAU**. Constructive action of additive noise in optimal detection. *International Journal of Bifurcation and Chaos*, vol. 15:2985–2994, 2005.

[A5] F. CHAPEAU-BLONDEAU and **D. ROUSSEAU**. Nonlinear SNR amplification of harmonic signal in noise. *Electronics Letters*, vol. 41:618–619, 2005.

[A6] F. CHAPEAU-BLONDEAU and **D. ROUSSEAU**. Noise-aided SNR amplification by parallel arrays of sensors with saturation. *Physics Letters A*, vol. 351:231–237, 2006.

[A7] F. CHAPEAU-BLONDEAU and **D. ROUSSEAU**. Nonlinear devices acting as SNR amplifiers for a harmonic signal in noise. *Circuits, Systems and Signal Processing*, vol. 25:431–446, 2006.

[A8] J. FIORINA, **D. ROUSSEAU**, and F. CHAPEAU-BLONDEAU. Interferer rejection improved by noise in ultra-wideband telecommunications. *Fluctuation and Noise Letters*, vol. 6:L317–L328, 2006.

[A9] A. HISTACE and **D. ROUSSEAU**. Constructive action of noise for impulsive noise removal in scalar images. *Electronics Letters*, vol. 42:393–395, 2006.

[A10] F. CHAPEAU-BLONDEAU, S. BLANCHARD, and **D. ROUSSEAU**. Noise-enhanced Fisher information in parallel arrays of sensors with saturation. *Physical Review E*, vol. 74, 2006.

[A11] **D. ROUSSEAU**, G. V. ANAND, and F. CHAPEAU-BLONDEAU. Noise-enhanced nonlinear detector to improve signal detection in non-Gaussian noise. *Signal Processing*, vol. 86:3456–3465, 2006.

[A12] **D. ROUSSEAU** and F. CHAPEAU-BLONDEAU. Noise-improved Bayesian estimation with arrays of one-bit quantizers. *IEEE Transactions on Instrumentation and Measurement*, vol. 56:2658–2662, 2007.

[A13] S. BLANCHARD, **D. ROUSSEAU**, and F. CHAPEAU-BLONDEAU. Noise enhancement of signal transduction by parallel arrays of nonlinear neurons with threshold and saturation. *Neurocomputing*, vol. 71:333–341, 2007.

[A14] S. BLANCHARD, **D. ROUSSEAU**, D. GINDRE, and F. CHAPEAU-BLONDEAU. Constructive action of the speckle noise in a coherent imaging system. *Optics Letters*, vol. 32:1983–1985, 2007.

[A15] F. CHAPEAU-BLONDEAU and **D. ROUSSEAU**. Injecting noise to improve performance of optimal detector. *Electronics Letters*, vol. 43:897–898, 2007.

[A16] A. HUMEAU, F. CHAPEAU-BLONDEAU, **D. ROUSSEAU**, M. TARTAS, B. FROMY, and P. ABRAHAM. Multifractality in the peripheral cardiovascular system from pointwise Hölder exponents of laser Doppler flowmetry signals. *Biophysical Journal*, vol. 93:L59–L61, 2007.

[A17] A. HUMEAU, L. FIZANNE, J. ROUX, P. ASFAR, P. CALES, **D. ROUSSEAU**, and F. CHAPEAU-BLONDEAU. Laser Doppler flowmetry signals to quantify effects of isoflurane on the peripheral cardiovascular system of healthy rats. *Applied Physics Letters*, vol. 91, 2007.

[A18] A. HUMEAU, L. FIZANNE, J. ROUX, P. ASFAR, P. CALES, **D. ROUSSEAU**, and F. CHAPEAU-BLONDEAU. Linear and nonlinear analyses of laser Doppler flowmetry signals recorded during isoflurane-induced anaesthesia in healthy rats. *Journal of Vascular Research*, vol. 45 (suppl. 2):60, 2008.

[A19] F.-X. INGLESE and **D. ROUSSEAU**. Utilisation d'une manette de jeu vidéo pour des expériences de mécanique. *Le BUP, Le Bulletin de l'Union des Professeurs de Physique et de Chimie*, 902:427–434, 2008.

[A20] S. BLANCHARD, **D. ROUSSEAU**, D. GINDRE, and F. CHAPEAU-BLONDEAU. Benefits from a speckle noise family on a coherent imaging transmission. *Optics Communications*, 281:4173–4179, 2008.

[A21] F. CHAPEAU-BLONDEAU, S. BLANCHARD, and **D. ROUSSEAU**. Fisher information and noise-aided power estimation from one-bit quantizers. *Digital Signal Processing*, vol. 18:434–443, 2008.

[A22] A. HUMEAU, W. TRZEPIZUR, **D. ROUSSEAU**, F. CHAPEAU-BLONDEAU, and P. ABRAHAM. Fisher information and Shannon entropy for on-line detection of transient signal high-values in laser Doppler flowmetry signals of healthy subjects. *Physics in Medicine and Biology*, vol. 53:5061–5076, 2008.

[A23] F. CHAPEAU-BLONDEAU, D. GINDRE, R. BARILLE, and **D. ROUSSEAU**. Optical coherence of a scalar wave influenced by first-order and second-order statistics of its random phase. *Fluctuation and Noise Letters*, vol. 8:L95–L111, 2008.

[A24] F. CHAPEAU-BLONDEAU, **D. ROUSSEAU**, S. BLANCHARD, and D. GINDRE. Optimizing the speckle noise for maximum efficacy of data acquisition in coherent imaging. *Journal of the Optical Society of America A*, vol. 25:1287–1292, 2008.

[A25] A. HUMEAU, F. CHAPEAU-BLONDEAU, **D. ROUSSEAU**, P. ROUSSEAU, W. TRZEPIZUR, and P. ABRAHAM. Multifractality, sample entropy, and wavelet analyses for age-related changes in the peripheral cardiovascular system: preliminary results. *Medical Physics*, vol. 35:717–723, 2008.

[A26] F. CHAPEAU-BLONDEAU, **D. ROUSSEAU**. Raising the noise to improve performance in optimal processing. *Journal of Statistical Mechanics : Theory and Experiment*, P01003, 1–5, 2009.

[A27] F. CHAPEAU-BLONDEAU, J. CHAUVEAU, **D. ROUSSEAU**, P. RICHARD. Fractal structure in the color distribution of natural images. *Chaos, Solitons and Fractals*, vol. 42, 472–482, 2009.

[A28] A. HUMEAU, W. TRZEPIZUR, **D. ROUSSEAU**, F. CHAPEAU-BLONDEAU, P. ABRAHAM. Localization of transient signal high-values in laser Doppler flowmetry signals with an empirical mode decomposition. *Medical Physics* , vol. 36, 18–21, 2009.

[A29] A. HUMEAU, B. BUARD, F. CHAPEAU-BLONDEAU, **D. ROUSSEAU**, G. MAHE, P. ABRAHAM. Multifractal analysis of central (electrocardiography) and peripheral (laser Doppler flowmetry) cardiovascular time series from healthy human subjects. *Physiological Measurement*, vol. 30, 617–629, 2009.

[A30] J. CHAUVEAU and **D. ROUSSEAU** and F. CHAPEAU-BLONDEAU, Fractal capacity dimension of three-dimensional histogram from color images. *Multidimensional Systems and Signal Processing*, in press, DOI 10.1007/S11045-009-0097-0, 2009.

[A31] F. CHAPEAU-BLONDEAU, **D. ROUSSEAU**, The minimum description length principle for probability density estimation by regular histograms, *Physica A*, vol. 388, 3969–3984, 2009.

[A32] **D. ROUSSEAU**, A. DELAHAIES, F. CHAPEAU-BLONDEAU. Structural similarity measure to assess improvement by noise in nonlinear image transmission. *IEEE Signal Processing Letters*, vol. 17, 36–39, 2010.

[A33] **D. ROUSSEAU**, S. SOURISSEAU. Propositions pour la masterisation. *Le BUP, Le Bulletin de l'Union des Professeurs de Physique et de Chimie*, 104:225–230, 2010.

2.6.2 Conférences avec comité de lecture

[B1] **D. ROUSSEAU** and F. CHAPEAU-BLONDEAU. Amélioration par le bruit de la dynamique de capteurs à saturation. In *20e Colloque GRETSI sur le Traitement du Signal et des Images*, pages 595–598, Louvain-la-Neuve, Belgique, Septembre 2005.

[B2] **D. ROUSSEAU** and F. CHAPEAU-BLONDEAU. Noise improvement and stochastic resonance in parallel arrays of sensors with saturation. In 4th International Conference on Physics in Signal and Image Processing, pages 49–54, Toulouse, France, Janvier 2005.

[B3] S. BLANCHARD, **D. ROUSSEAU**, and F. CHAPEAU-BLONDEAU. Noise-assisted image transmission with speckle noise. In *5th International Conference on Physics in Signal and Image Processing*, Mulhouse, France, 5 pages, Janvier 2007.

[B4] A. HISTACE and **D. ROUSSEAU**. Noise-enhanced anisotropic diffusion for scalar image restoration. In *5th International Conference on Physics in Signal and Image Processing*, Mulhouse, France, 5 pages, Janvier 2007.

[B5] A. HUMEAU, P. ABRAHAM, **D. ROUSSEAU**, and F. CHAPEAU-BLONDEAU. Utilisation de l'effet Doppler laser pour l'analyse de la microcirculation sanguine. Traitement des signaux associés et modélisation non linéaire pour l'aide au diagnostic médical. In *Horizons de l'Optique*, pages 159–160, Saint Martin d'Hères, France, Juillet 2007.

[B6] A. HUMEAU, F. CHAPEAU-BLONDEAU, **D. ROUSSEAU**, and P. ABRAHAM. Numerical simulation of laser Doppler flowmetry signals based on a model of nonlinear coupled oscillators. Comparison with real data in the frequency domain. In *29th Annual International Conference of the IEEE Engineering in Medicine and Biology (SFGBM)*, pages 4068–4071, Lyon, France, Août 2007.

[B7] A. HUMEAU, F. CHAPEAU-BLONDEAU, **D. ROUSSEAU**, and P. ABRAHAM. Simulations numériques de signaux laser Doppler. Etude de l'influence des activités myogénique, neurogénique et endothéliale. In *Colloque "Diagnostic et Imagerie Optiques en Médecine" OPTDIAG 2007*, page 75, Paris, France, Mai 2007.

[B8] S. BLANCHARD, **D. ROUSSEAU**, and F. CHAPEAU-BLONDEAU. Using noise to improve measurement and information processing. In *4th International Conference on Informatics in Control, Automation and Robotics*, volume 3, pages 268–271, Angers, France, Mai 2007.

[B9] S. BLANCHARD, **D. ROUSSEAU**, D. GINDRE, and F. CHAPEAU-BLONDEAU. Transmission d'image assistée par le bruit en imagerie cohérente et incohérente. In *21ème Colloque GRETSI sur le Traitement du Signal et des Images*, pages 813–816, Troyes, France, Septembre 2007.

[B10] S. BLANCHARD, **D. ROUSSEAU**, D. GINDRE, and F. CHAPEAU-BLONDEAU. Utilisation de non-linéarités des capteurs pour optimiser l'acquisition d'images en imagerie cohérente. In *3èmes Journées Imagerie Optique Non Conventionnelle*, Paris, France, Mars 2008.

[B11] B. BUARD, A. HUMEAU, **D. ROUSSEAU**, F. CHAPEAU-BLONDEAU, and P. ABRAHAM. Laser Doppler flowmetry signals: pointwise Hölder exponents of experimental signals from young healthy subjects and numerically simulated data. In *4th European Congress for Medical and Biomedical Engineering*, volume 22, pages 221–225, Anvers, Belgique, Novembre 2008.

[B12] F. CHAPEAU-BLONDEAU and **D. ROUSSEAU**. Raising the noise to improve the performance of optimal processing. In *5th International Conference on Unsolved Problems on Noise and Fluctuations in Physics, Biology and High Technology*, Lyon, France, Juin 2008.

[B13] A. HUMEAU, B. HAUSSY, L. FIZANNE, J. ROUX, P. ASFAR, P. CALES, **D. ROUSSEAU**, and F. CHAPEAU-BLONDEAU. Laser Doppler flowmetry in healthy rats: impact of isoflurane anesthetic on signal complexity. In *16th Mediterranean Conference on Control and Automation*, pages 1330–1334, Ajaccio, France, Juin 2008.

[B14] J. CHAUVEAU, **D. ROUSSEAU**, F. CHAPEAU-BLONDEAU. Pair Correlation Integral for Fractal Characterization of Three-Dimensional Histograms from Color Images, ICISP 2008, 3rd International Conference on Image and Signal Processing, Cherbourg-Octeville, France, Lecture Notes in Computer Science 5099, 200-208, © Springer-Verlag Berlin Heidelberg 2008.

[B15] **D. ROUSSEAU**, G. V. ANAND, F. CHAPEAU-BLONDEAU. Overview of useful-noise effects in static nonlinear systems. In *Stochastic Resonance, ten years of continuous growth*, Perugia, Italie, Août 2008.

[B16] A. DELAHAIES, **D. ROUSSEAU**, D. GINDRE, F. CHAPEAU-BLONDEAU. Constructive Role of Sensors Nonlinearities in the Acquisition of Partially Polarized Speckle Images.

In *8th Euro-American Workshop on Information Optics*, Paris, France, DOI 10.1088/1742-6596/206/1/012020, Juillet 2009.
[B17] B. BUARD, W. TRZEPIZUR, G. MAHE, F. CHAPEAU-BLONDEAU, **D. ROUSSEAU**, F. GAGNADOUX, P. ABRAHAM, A. HUMEAU, Multifractal spectra of laser Doppler flowmetry signals in healthy and selep apnea syndrome subjects,In *European Conferences on Biomedical Optics*, Munich, Allemagne, Proceedings of SPIE, 7373, June 2009.
[B18] A. DELAHAIES, **D. ROUSSEAU**, J-M. BRETEAU, F. CHAPEAU-BLONDEAU, Un critère informationnel en imagerie pour l'échelle optimale d'observation d'une scène bruitée, *5ème Colloque Interdisciplinaire en Instrumentation*, Le Mans, France, 637-644, Janvier 2010.
[B19] T. BOUREAU, F. AMIARD, M-A. JACQUES, E. BELIN, S. POUSSIER, S. HANTEVILLE, V. GRIMAULT, S. PERROT, C. DURR, J-M. BRETEAU, F. CHAPEAU-BLONDEAU, **D. ROUSSEAU**. Utilisation de la thermographie pour localiser des microorganismes phytopathogénes dans des tissus végétaux de manière non-destructive, *9èmes Rencontres Phytobacteriologiques*, Aussois Janvier 2010.

Chapitre 3

Résonance stochastique

Je présente dans ce chapitre une synthèse de l'ensemble de mes travaux sur la résonance stochastique depuis mon recrutement en tant que maître de conférences en 2005.

3.1 Contexte, objectifs et méthodes

Contexte : Un de mes sujets de réflexion majeurs depuis mon travail de thèse est l'étude d'un effet non linéaire par lequel le traitement d'une information utile peut profiter de la présence du bruit. L'ensemble des situations qui peuvent donner lieu à un effet bénéfique du bruit est un secteur en constante évolution. L'ensemble des manifestations de ce phénomène est rassemblé, au profit d'une présentation unifiée, sous le terme de résonance stochastique. Cet effet paradoxal a originellement été introduit, au début des années 1980, dans le contexte de la physique non linéaire [10]. Progressivement, la résonance stochastique a été observée et analysée dans une variété grandissante de processus, incluant notamment des systèmes de traitement de l'information comme des circuits électroniques [5, 102, 103], des dispositifs optiques [91, 148], des systèmes neuronaux [104, 30]. Depuis son introduction, les études sur la résonance stochastique ont progressé dans de nombreuses directions à travers des variations et des extensions autour de quatre ingrédients essentiels :

(i) un signal utile ou cohérent $s(t)$;
(ii) un bruit $\eta(t)$;
(iii) un système ou un processus, en général non linéaire, qui reçoit $s(t)$ et $\eta(t)$ en entrée sous l'influence desquelles il produit le signal de sortie $y(t)$;
(iv) une mesure de performance qui quantifie l'efficacité du traitement ou de la transmission du signal d'entrée utile $s(t)$ vers la sortie $y(t)$ en présence du bruit $\eta(t)$.

$\Longrightarrow$ On parle de résonance stochastique chaque fois qu'il est possible d'augmenter la mesure de performance au moyen d'une augmentation du niveau du bruit $\eta(t)$.

À l'origine, et pendant relativement longtemps [62], la résonance stochastique et ses approfondissements se sont concentrés sur un seul type de signal, un signal cohérent périodique transmis par un système dynamique bistable. La mesure de performance standard était alors un rapport signal sur bruit en sortie, défini dans le domaine fréquentiel, comme la puissance contenue dans la raie cohérente à la fréquence fondamentale de l'entrée périodique divisée par la puissance contenue dans le fond continu de bruit autour de la fréquence fondamentale. Les

études visaient alors à analyser les circonstances par lesquelles le rapport signal sur bruit en sortie pouvait être augmenté en accroissant le niveau de bruit d'entrée [62]. Progressivement, il a été montré que la résonance stochastique pouvait être étendue à d'autres classes de signaux (apériodique, aléatoire). On trouve différénts types de synthèses sur la résonance stochastique avec des approches transdisciplinaires [62, 4] ou se restreignant à des domaines particuliers comme l'électricité [96, 97, 69] ou les neurones [105] ou encore se focalisant sur un mécanisme particulier de bruit utile [100]. La résonance stochastique apparaît donc desormais comme un phénomène non linéaire général.

Objectifs : Dans ce contexte, les études auxquelles je contribue depuis mes travaux de thèse, ont une double motivation. En tant que phénomène non linéaire général, la résonance stochastique amène un certain nombre de questions non triviales qu'il convient d'explorer pour faire progresser, sur un plan fondamental, la compréhension de l'influence du bruit dans les processus non linéaires. Ces études sont importantes conceptuellement, en ce qu'elles illustrent de façon précise et quantifiée les notions d'information tirée du bruit ou d'ordre tiré du désordre fréquemment évoquées au sujet des systèmes complexes. Ces études fondamentales, motivées par l'importance conceptuelle de l'effet, sont par ailleurs, vers l'aval, indispensables afin de pouvoir établir, en connaissance de cause, comment la résonance stochastique peut se prêter à des applications pratiques compétitives. Sur ce volet applicatif, un regard privilégié est porté en direction des processus neuronaux. Ils constituent en effet des systèmes non linéaires capables de remarquables performances pour le traitement du signal et de l'information et sont naturellement non linéaires dès le plus bas niveau de traitement ; ceci leur permet d'avoir accès à des phénomènes spécifiquement non linéaires comme la possibilité d'utiliser le bruit via la résonance stochastique. Comprendre les stratégies du codage neuronal de l'information constitue à la fois un enjeu pour des analyses fondamentales et une source d'inspiration pour de nouvelles générations de processus du traitement de l'information neuro-inspirées.

Méthode : La visée principale étant d'inventorier et d'analyser les formes et mécanismes sous lesquels une information utile interagissant non linéairement avec un bruit peut profiter de la présence de ce dernier, aucune restriction méthodologique n'était a priori fixée ce qui m'a permis de mobiliser et d'appréhender un large panel d'outils, de modèles et de représentations comme ceux de la théorie des signaux-systèmes, de la théorie des signaux aléatoires, de la théorie statistique de l'information, du traitement des images. A posteriori, on peut toutefois constater que sur la période (2005-2010) un choix méthodologique a été fait de se concentrer sur des systèmes non linéaires sans mémoire, c'est à dire statiques. L'intérêt de ces systèmes est qu'ils sont en un certain sens plus simples à manipuler que les systèmes non linéaires dynamiques ce qui autorise souvent à pousser plus avant des calculs sous forme analytique. Pour guider mes explorations, je me suis tout d'abord (2005-2008) naturellement inspiré des perspectives que j'avais dégagées durant ma thèse :

(j) Analyser avec un point de vue orienté capteur [132, 122] les effets de bruit utile dans les réseaux de non-linéarités comme ceux récemment introduits par N. G. STOCKS [143] et que j'avais commencé à étudier [130, 124].
(jj) Etendre les possibilités de résonance stochastique dans des traitements optimaux de l'information comme je l'avais montré pour du bruit de phase sur des tâches d'estimation et de détection [31, 33].
(jjj) En dehors du strict effet de résonance stochastique, étudier les propriétés utiles de systèmes non linéaires pour le traitement de l'information comme je l'avais fait pour le système dynamique

bistable qui a permis historiquement l'introduction de la résonance stochastique (dans un contexte de physique non linéaire), lorsqu'il est utilisé comme filtre non linéaire pour une tâche de détection [131, 55].

Progressivement (à partir de 2006), j'ai également initié et développé de nouvelles voies d'explorations pour la résonance stochastique en me concentrant notamment sur le domaine de l'imagerie et du traitement des images.

3.2 Bruit utile et réseaux de non-linéarités

Une voie d'exploration sur les effets de bruit utile a tout d'abord visé à poursuivre mes investigations sur l'étude de la résonance stochastique dans des réseaux de systèmes non linéaires identiques répliqués en architecture parallèle comme sur la Fig. 3.1.

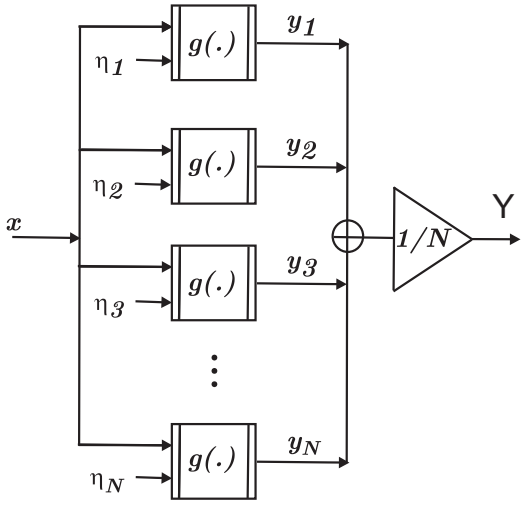

Figure 3.1 : Réseau parallèle de N composants identiques

Dans le réseau de la Fig. 3.1, chaque composant i de caractéristique entrée–sortie $g(\cdot)$ reçoit le même signal d'entrée x et un bruit η_i indépendant et identiquement distribué. Les sorties y_i de chacun des composants sont moyennées pour former la sortie $Y = \frac{1}{N}\sum_{i=1}^{N} y_i$ du réseau. En l'absence de bruit, chaque composant produit le même signal de sortie. Si on ajoute les bruits η_i de sorte que $y_i = g(x + \eta_i)$, chaque composant du réseau répond de manière distincte. En présence de caractéristique $g(\cdot)$ linéaire, le moyennage en sortie annule exactement l'effet des bruits en entrée. Ajouter des bruits en entrée, pour produire des réponses distinctes que l'on moyenne ensuite, n'apporte aucun bénéfice par rapport à un unique composant sans bruit d'entrée ajouté. Il n'en n'est plus de même lorsque la caractéristique $g(\cdot)$ des composants est non linéaire. Il existe des situations où l'ajout de bruits indépendants en entrée des non-linéarités conduit à un bénéfice en terme de traitement de l'information. Les bruits ajoutés permettent à chaque non-linéarité de répondre différemment à un même signal d'entrée. En moyennant les réponses sur le réseau, il apparaît que la réponse moyenne globale d'un réseau de non-linéarités bruités, peut être plus efficace que la réponse d'une unique non-linéarité sans bruit ajouté. C'est la diversité des réponses engendrées par les bruits en entrée qui est la source du bénéfice, et qui n'est plus annulée par moyennage en sortie pour des caractéristiques $g(\cdot)$ non linéaires.
Une motivation supplémentaire à l'étude de la résonance stochastique dans le système de la

Fig. 3.1 réside dans le fait qu'il peut constituer un modèle pour des systèmes réels dans des domaines très variés de traitement de l'information. Les réseaux parallèles d'éléments non linéaires sont des modèles pour les antennes SONAR [3], pour les convertisseurs analogique–numérique de type flash [98]. On retrouve aussi les architectures de réseaux parallèles dans le codage neuronal de l'information [146, 74], les implants cochléaires [145] la vision artificielle [99] où la possibilité d'amélioration par le bruit a été démontrée.

3.2.1 Résonance stochastique supraliminaire

Une première approche, dans la continuité de mes travaux de thèse, a consisté à considérer des réseaux où les N non-linéarités $g(\cdot)$ dans la Fig. 3.1 sont des comparateurs à seuil. Il s'agit de la configuration initialement introduite par [143, 144] dans un cadre de transmission d'information évaluée par une information mutuelle. J'ai étendu les études de la résonance stochastique dans ce réseau de comparateurs à d'autres problématiques de traitement du signal comme l'estimation (**[128]** et [27]) ou la détection de signaux noyés dans du bruit (**[117]**). Dans l'étude [27] que nous avons réalisée à l'occasion de la thèse de Solenna BLANCHARD, le signal d'entrée x de la Fig. 3.1 est un bruit dont on souhaite estimer la puissance σ^2 en sortie d'un quantifieur 1-bit de seuil θ isolé puis en sortie d'un réseau parallèle de quantifieurs 1-bit. Une mesure de performance adaptée ici est l'information de Fisher dont les évolutions sont visibles sur la Fig. 3.2 pour différentes tailles N du réseau en fonction du niveau de bruit volontairement injecté η_i. À bruit η_i nul, on observe sur la Fig. 3.2 que l'information de Fisher est nulle. Ceci signifie qu'il n'y a pas de possibilité d'estimer la puissance σ^2 quand le signal d'entrée $x(t)$ est centré et binarisé avec le seuil $\theta = 0$. Ainsi, pour un unique comparateur (N=1), l'injection des bruits dans le réseau n'a aucun effet. En revanche, dès que $N > 1$ sur la Fig. 3.2, il apparaît qu'un niveau non nul des bruits injectés permet de maximiser l'information de Fisher en sortie du réseau. Le maximum atteint au niveau du bruit optimal est d'autant plus élevé que la taille N du réseau est grande. Sur l'exemple de la Fig. 3.2, le signal x à estimer est, en l'absence des bruits de réseau η_i, mal positionné par rapport à la non-linéarité. Ce n'est cependant pas une condition pour que l'effet de bruit utile dans le réseau de non-linéarités puisse opérer. Au contraire, cette forme de la résonance stochastique dans des réseaux de composants non linéaires répliqués en parallèle révèle que le bénéfice apporté par le bruit n'est pas réservé à des signaux mal-positionnés par rapport à une non-linéarité. Cette propriété est spécialement intéressante car elle n'était généralement pas possible avec des non-linéarités isolées où le signal utile doit être mal positionné (trop petit pour franchir un seuil ou une barrière de potentiel) pour recevoir un bénéfice d'un ajout de bruit. Ce point est discuté et illustré dans l'article **[128]**.
Les résultats [128, 117, 27] qui complétaient ceux de ma thèse [124, 130, 126] avec de nouvelles mesures de performance (estimation bayésienne pour **[128]** et détection au sens de Neyman Pearson pour **[117]**) ou sur de nouvelles classes de signaux [27][1] ont contribué à démontrer que la résonance stochastique dans les réseaux de non-linéarités revêt une portée générale qui peut se manifester et être quantifiée de beaucoup de façons différentes.

Une autre approche sur l'étude des effets de bruit utile dans les réseaux de non-linéarités a été de s'intéresser à des réseaux impliquant d'autres types de non-linéarités que les simples seuils des comparateurs initialement introduits dans [143, 144]. Pour définir un périmètre à ces explorations et permettre de guider le choix de formes de non-linéarités, un point de vue orienté vers les capteurs a été adopté. Ainsi, des non-linéarités typiques de l'instrumentation [113]

[1] Une originalité de [27] en plus de l'aspect bruit utile dans les réseaux de non-linéarités est d'examiner pour la première fois la possibilité de résonance stochastique lorsque le signal d'entrée est un bruit.

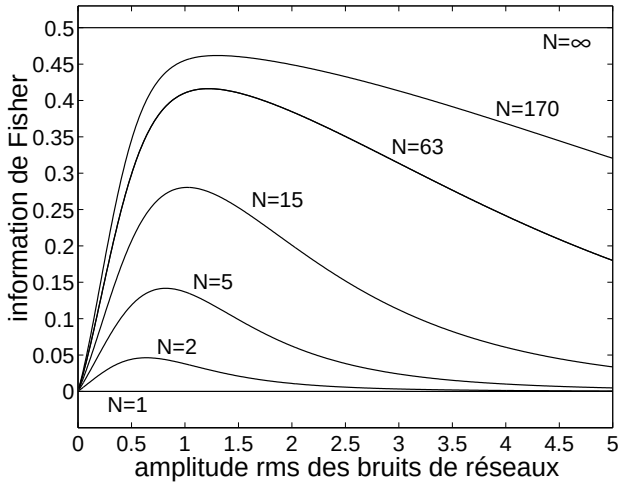

Figure 3.2 : Information de Fisher en fonction de l'amplitude efficace des bruits η_i volontairement injectés dans le réseau. Les η_i sont indépendants et identiquement distribués selon une loi gaussienne de moyenne nulle pour différentres tailles N, et le seuil de quantification θ est identique pour tous les quantifieurs $\theta = 0$. Le paramètre estimé est la puissance du signal d'entrée pris comme un bruit gaussien centré d'amplitude efficace 1.

comme des non-linéarités à saturation [125, 36, 26] ou des non-linéarités plus douces commes des polynômes [32] ont été testées. À l'occasion de la thèse de Solenna BLANCHARD, nous avons également appliqué cette démarche à des modèles de neurones sensoriels qui peuvent être vus comme des capteurs ou composants naturels avec des non-linéarités intrinsèques à dures (seuils et saturation) ou douces. Les neurones sont organisés en réseau, ils sont soumis aux bruits (d'origine externe ou interne), et sont capables de réaliser du traitement de l'information très performant. Dans **[14]**, nous étudions l'impact du bruit sur un réseau parallèle de neurones. L'étude est menée au moyen d'un modèle de neurone capable de rendre compte des principales non-linéarités des neurones réels. Nous montrons, en simulation, qu'il est théoriquement possible d'améliorer, par injection de bruit au sein du réseau, la transduction d'un signal d'entrée par ce réseau pour n'importe quelle position du signal, qu'il soit situé sous le seuil, dans la saturation ou même dans une partie curvilinéaire de la réponse neuronale.
Chacune des études [125, 36, 26, 32, 14] a montré la possibilité d'un effet de résonance stochastique dans les réseaux parallèles de non-linéarités ne présentant pas de seuils. Le nom historiquement proposé dans [143, 144] pour décrire l'effet bénéfique du bruit dans un réseau de comparateur à seuil était "suprathreshold stochastic résonance" que l'on peut traduire par résonance stochastique supraliminaire. Nos résultats ont ainsi contribué (comme le reconnaissent les auteurs de [143, 144] dans leur article dédié à la "suprathreshold stochastic resonance" sur http://www.scholarpedia.org) à démontrer sur des exemples d'intérêts pratiques que la classe de non-linéarités qui peut bénéficier d'un effet de bruit utile dans une architecture de réseau parallèle est beaucoup plus large que les non-linéarités à seuil.

3.2.2 Capteurs façonnés par le bruit

La phase décrite dans 3.2.1 visait à étendre les possibilités de la résonance stochastique dans les non-linéarités statiques associées en réseau en montrant la diversité des situations [130, 124, 32, 126, 125, 36, 26, 14] par lesquelles on peut bénéficier du bruit. Ce faisant, ces études m'ont

également permis de réaliser qu'un point de vue unificateur sur la résonance stochastique dans les non-linéarités statiques en présence de bruit additif était également possible. Je propose à présent cette démarche unificatrice dramatisée à la manière d'un problème de capteur [15, 119].

Considérons un capteur possédant une caractéristique entrée–sortie non linéaire $g(\cdot)$. Ce capteur est en charge de la transmission ou du traitement d'un signal utile s de façon à produire y avec

$$y = g(s) \ , \tag{3.1}$$

où les signaux d'entrée s et de sortie y peuvent être des fonctions du temps comme de l'espace. Nous allons supposer que la caractéristique entrée–sortie de notre capteur n'est pas optimalement adaptée pour transmettre ou traiter le signal d'entrée s. Partant de là, on peut chercher un autre capteur possédant une caractéristique entrée–sortie plus adaptée. Les études [124, 130, 126, 125, 36, 26, 32, 14] nous montrent que dans cette situation, il est parfois possible de modifier $g(\cdot)$ la caractéristique entrée–sortie d'un tel capteur sans avoir à modifier les paramètres physiques du capteur lui-même. On introduit un bruit η dans la relation entrée–sortie de l'Éq. (3.1) qui devient $y = g(s + \eta)$. Ce bruit η peut être natif c'est à dire lié à la physique du composant ou bien un bruit volontairement injecté en entrée du composant. Ainsi, puisque le composant n'est plus déterministe, une caractéristique entrée–sortie effective ou moyenne peut être définie comme $g_{\text{eff}}(\cdot)$ donnée par l'espérance

$$g_{\text{eff}}(s) = \mathrm{E}[y] = \int_{-\infty}^{+\infty} g(u) f_\eta(u - s) du \ , \tag{3.2}$$

avec $f_\eta(u)$ la fonction densité de probabilité du bruit η. En présence du bruit η, la forme de la caractéristique entrée–sortie du composant, $g_{\text{eff}}(\cdot)$ dans l'Éq. (3.2), est maintenant contrôlée par $g(\cdot)$ et par la fonction densité de probabilité $f_\eta(u)$. En conséquence, une modification de la réponse d'un capteur sans mémoire peut être obtenue grâce à la présence d'un bruit η qui permet de modifier la caractéristique entrée–sortie sans avoir à modifier le composant lui-même. En pratique, la caractéristique entrée–sortie effective, $g_{\text{eff}}(\cdot)$ du composant dans l'Éq. (3.2) n'est pas directement accessible. Néanmoins, il est possible d'avoir un composant présentant une approximation de la réponse de l'Éq. (3.2) en moyennant N acquisitions y_i avec $i \in \{1, \dots N\}$ pour produire

$$Y = \frac{1}{N} \sum_{i=1}^{N} y_i = \frac{1}{N} \sum_{i=1}^{N} g(s + \eta_i) \ , \tag{3.3}$$

où les N bruits η_i sont blancs, mutuellement indépendants et identiquement distribués avec la fonction densité de probabilité $f_\eta(u)$. Une implantation du processus de l'Éq. (3.3) peut être obtenue, avec la structure de la Fig. 3.1 via la réplication des composants associés en parallèle avec N bruits indépendants qui sont ajoutés en entrée de chaque composant, ou bien comme proposé dans [61] pour un signal constant en collectant la sortie d'un composant unique à N instants distincts. De façon similaire à ce que l'on trouve pour l'Éq. (3.2), la caractéristique entrée–sortie du processus de l'Éq. (3.3) est façonnée par la présence des N bruits η_i. On obtient ainsi

$$\mathrm{E}[Y] = \mathrm{E}[y_i] \ , \tag{3.4}$$

et pour tout i

$$\mathrm{E}[y_i] = \int_{-\infty}^{+\infty} g(s + u) f_\eta(u) du \ . \tag{3.5}$$

Les N bruits η_i apportent des fluctuations qui peuvent être quantifiés au moyen de la variance instationnaire $\mathrm{var}[Y] = \mathrm{E}[Y^2] - \mathrm{E}[Y]^2$, avec $\mathrm{E}[Y^2] = \mathrm{E}[y_i^2]/N + \mathrm{E}[Y]^2(N-1)/N$ et

$$\mathrm{E}[y_i^2] = \int_{-\infty}^{+\infty} g^2(s+u) f_\eta(u) du \; . \tag{3.6}$$

Pour les grandes valeurs N, $\mathrm{var}[Y]$ tend vers zéro. Dans ces conditions asymptotiques où N tend vers l'infini, le processus constitué par le composant $g(\cdot)$, les N bruits η_i et le moyennage de l'Éq. (3.3), devient un composant déterministe équivalent de caractéristique entrée–sortie donnée par l'Éq. (3.2). Pour les valeurs finies de N, la présence des N bruits η_i jouera un rôle constructif si l'amélioration apportée sur la transmission ou le traitement de s par la modification de la caractéristique du composant est plus grande que la nuisance due aux fluctuations résiduelles en sortie y.
Ainsi, le processus de l'Éq. (3.3) délimite un problème général : étant donné un composant de caractéristique $g(\cdot)$ et un nombre N d'échantillons pour le moyennage, comment peut-on choisir la fonction densité de probabilité des bruits η_i pour obtenir une réponse souhaitée. Ce problème inverse est, en général, difficile à résoudre. Un problème plus simple consiste à fixer une fonction densité de probabilité des bruits et agir uniquement sur l'amplitude efficace σ_η de ces bruits identiques. C'est exactement ce que l'on fait lors des études sur la résonance stochastique. Ainsi les études sur la résonance stochastique dans les non-linéarités statiques et bruit additif constituent une solution heuristique pragmatique au "problème de capteur" posé en début de cette section.
Comme illustration, donnons quelques exemples d'applications de ce processus de façonnage de l'Éq. (3.3). On considère un composant de caractéristique entrée–sortie $g(u)$ avec un régime linéaire délimité par un seuil et une saturation

$$g(u) = \begin{cases} 0 & \text{pour} \quad u \leq 0 \\ u & \text{pour} \quad 0 < u < 1 \\ 1 & \text{pour} \quad u \geq 1 \; . \end{cases} \tag{3.7}$$

La possibilité de façonner la réponse de tels composants par le bruit via l'Éq. (3.3) est montrée sur la Fig. 3.3. En l'absence de bruit, la caractéristique $g(u)$ présente des non-linéarités dures. Les bruits η_i injectés dans l'Éq. (3.3), arbitrairement choisis gaussien ici, tendent à adoucir ces non-linéarités pour étendre la gamme sur laquelle la caractéristique entrée–sortie effective $g_{\mathrm{eff}}(\cdot)$ de l'Éq. (3.2) est linéaire. La Fig. 3.4 représente la similarité entre les signaux d'entrée $s(t)$ et de sortie au moyen $y(t)$ l'intercovariance normalisée

$$C_{sy} = \frac{\langle s(t)\,\mathrm{E}[y(t)]\rangle - \langle s(t)\rangle\langle \mathrm{E}[y(t)]\rangle}{\sqrt{\left[\langle s(t)^2\rangle - \langle s(t)\rangle^2\right]\left[\langle \mathrm{E}[y^2(t)]\rangle - \langle \mathrm{E}[y(t)]\rangle^2\right]}} \; , \tag{3.8}$$

en fonction de l'amplitude efficace σ_η des bruits $\eta_i(t)$ ajoutés sur les capteurs, pour la transmission par le réseau de capteurs à saturation de l'Éq. (3.7) de signaux d'entrée apériodiques particuliers de grandes amplitudes. Pour chaque taille N du réseau présentée sur la Fig. 3.4, nous constatons que la transmission de signaux de grandes amplitudes qui font saturer les capteurs peut être améliorée par addition des bruits $\eta_i(t)$ sur les capteurs. Le façonnage de la caractéristique entrée–sortie effective $g_{\mathrm{eff}}(\cdot)$ se traduit par une augmentation de C_{sy} qui culmine pour un niveau optimal non nul des bruits ajoutés sur les capteurs $\eta_i(t)$. L'action du bruit permet une meilleure fidélité de transduction pour des signaux $s(t)$ de grandes amplitudes faisant saturer les capteurs. La dynamique du réseau de capteurs en présence des bruits $\eta_i(t)$ est donc plus étendue que celle d'un seul capteur sans bruit ajouté.

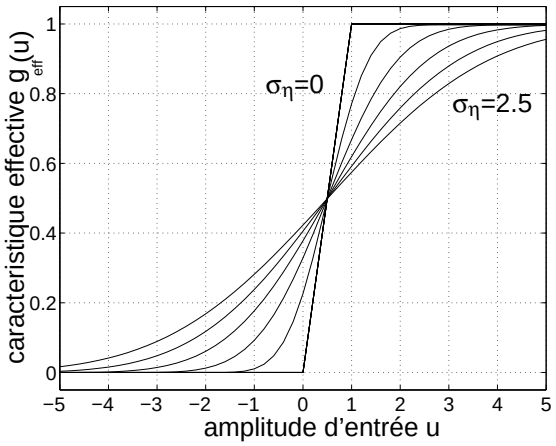

Figure 3.3 : Caractéristique entrée–sortie efficace $g_{\text{eff}}(\cdot)$ de l'Éq. (3.2) pour le capteur de l'Éq. (3.7) en présence de bruit gaussien centré d'amplitude efficace $\sigma_\eta = 0, 0.5, 1, 1.5, 2.5$.

La Fig. 3.4 montre que l'efficacité de l'amélioration par le bruit de l'intercovariance normalisée entrée–sortie C_{sy} est davantage prononcée à mesure que la taille du réseau N augmente. La valeur maximale de C_{sy}, obtenue pour un niveau de bruit non nul, tend d'ailleurs vers 1 lorsque N tend vers l'infini. De plus, la phase décroissante qui suit le passage par le niveau optimal de bruit s'étend à mesure que N augmente allant même jusqu'à disparaître pour un réseau de taille infini. Le "plateau" ainsi observé signifie que pour des réseaux de grandes tailles N, la distorsion due à la saturation peut être limitée pour une large gamme de valeurs de l'amplitude efficace des bruits $\eta_i(t)$. Cette observation est cohérente avec celle de la Fig. 3.3. Pour les réseaux de grandes tailles N, il existe un niveau de bruit minimal qui permet à la caractéristique équivalente de couvrir la dynamique du signal d'entrée permettant ainsi une distorsion entrée–sortie nulle. Augmenter le bruit au delà de cette valeur minimale étendra encore la gamme linéaire sans influence sur la mesure de similarité.

Le façonnage par le bruit ne se traduit pas toujours par une linéarisation de la caractéristique du capteur. Ainsi, dans la Fig. 3.2, pour $N = \infty$, l'information de Fisher ne dépend pas du niveau de bruit. Dans ce cas, l'effet du façonnage par le bruit fait passer la caractéristique du composant d'une forme non bijective (un quantifieur 1-bit à seuil pour la Fig. 3.2) à une forme bijective conservant l'information de Fisher intacte que la caractéristique effective en présence de bruit soit linéaire ou non. Enfin, dans l'article **[117]** le bruit injecté permet (comme clairement discuté dans la section conclusive de l'article) de façonner des caractéristiques effectives non linéaires utiles pour une détection en présence de bruit non gaussien. Il est à noter toutefois que toutes les modifications ne sont pas permises via un façonnage par le bruit. La caractéristique équivalente de l'Éq. (3.2) du capteur subit une convolution par la fonction densité de probabilité. Étant donné les formes des fonctions de densité de probabilité des bruits usuels, cette opération de convolution aura plutôt tendance à adoucir la caractéristique équivalente du capteur de l'Éq. (3.2). Aussi, puisque la fonction densité de probabilité est une fonction positive, la caractéristique équivalente de l'Éq. (3.2) sera croissante.

Cette partie a permis de proposer une vision synthétique rassemblant avec un point de vue orienté vers les capteurs, l'ensemble des effets de bruit utiles dans les non-linéarités statiques (associées en réseaux ou non) comme un effet de façonnage de la non-linéarité par un bruit additif. D'autres points de vue sont également possibles comme celui développé par [100] qui considère le réseau de comparateurs de la Fig. 3.1 comme un canal de communication. L'ajout

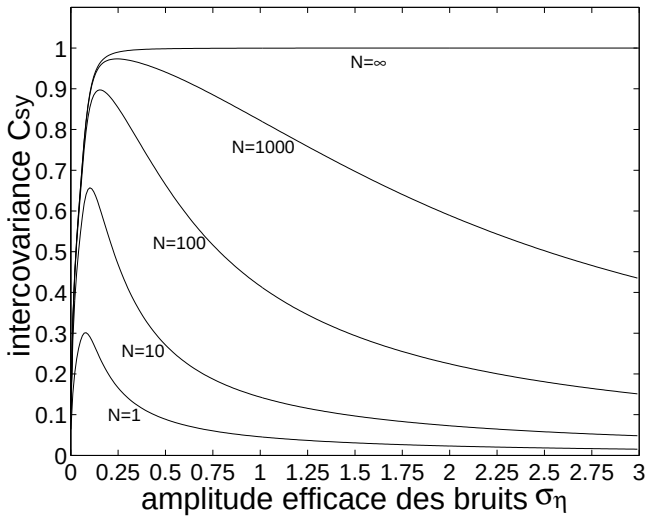

Figure 3.4 : Intercovariance normalisée entrée–sortie C_{sy} de l'Éq. (3.8), en fonction de l'amplitude efficace σ_η des bruits $\eta_i(t)$ choisis gaussiens. Le signal utile apériodique considéré est $s(t) = A + 0.2\,\sin\left(2\pi\frac{t}{T_s/2}\right) + 0.1\,\sin\left(2\pi\frac{t}{3T_s/2}\right)$, quand $t \in [0, T_s]$, et $s(t) = 0$ partout ailleurs. La composante $A = 1$ constante ne porte pas d'information. À bruit $\eta_i(t)$ nul, $\sigma_\eta = 0$, le signal $s(t)$ sature fortement à travers les capteurs $g(.)$ de l'Éq. (3.7) (essentiellement à cause de la composante A).

des bruits modifie alors le canal et l'interprétation de l'effet du bruit est alors plutôt centré sur la capacité informationnelle de ce canal plutôt qu'en terme de caractéristique effective de capteur. Dans [100], les auteurs en viennent aussi à considérer la question du choix du bruit optimal qui comme dans l'approche développée ici débouche sur un problème inverse en général difficile à résoudre analytiquement. Récemment, il a été montré que la résonance stochastique dans les réseaux de non-linéarités se manifeste avec d'autres types de non-linéarités que les non-linéarités statiques comme les systèmes dynamiques à saturation de [54], avec d'autres types de couplages non additifs entre le signal d'entrée et les bruits injectés dans le réseau [107], ou encore une diversité des caractéristiques des non-linéarités est introduite dans le schéma de la Fig. 3.1 [153]. Il serait intéressant de chercher à montrer si des mécanismes communs de ces effets de bruit utile peuvent là aussi être proposés.

On le voit, le schéma de la Fig. 3.1 peut encore constituer une source d'inspiration en explorant des variantes des quatre ingrédients principaux du paradigme de la résonance stochastique (signal utile, bruit, système non linéaire, mesure de performance) pour inventorier de nouvelles formes de bruit utile. Il est aussi possible d'imaginer d'autres architectures que celle de la Fig. 3.1 à base d'associations collective de non-linéarités. Les modèles d'opinions développés en sociophysique font souvent appels à des réseaux couplés de systèmes non linéaires identiques en présence de bruits et pourraient naturellement être transposés pour des études en résonance stochastique [147, 112]. Une ligne de conduite pour guider la créativité serait de ne pas perdre de vue l'importance d'arguments applicatifs pour les sciences de l'information et notamment en direction des neurones pour justifier l'intérêt des systèmes utilisés. La piste neuro-mimétique pourrait être testée expérimentalement en constituant un réseau parallèle de neurones biologiques pour y étudier le transfert d'information en présence du bruit naturellement présent. La réalisation de cette perspective dépend de façon critique de la possibité d'implanter

des architectures neuronales contrôlées. Les méthodes actuelles requièrent des techniques de salles blanches ou d'équipement coûteux. Notre équipe est associée à une collaboration entre des collègues physiciens et neurobiologistes sur l'Université d'Angers pour tester de façon exploratoire la possibilité d'utiliser des techniques moins onéreuses basées sur des principes d'auto-organisation de molécules pour guider la croissance de neurones.

3.3 Bruit utile, gains RSB et traitements optimaux

L'évolution des études sur les effets de bruits utile a été marquée par des avancées conceptuelles qui ont modifié le périmètre et la nature des situations où l'on pensait pouvoir tirer du bruit en présence de systèmes non linéaires. Chacune de ces avancées est en un sens a priori contre intuitive, jusqu'au point où historiquement la seule possibilité de ces avancées de la résonance stochastique a été considérée comme incertaine. Ainsi, il est desormais admis que la résonance stochastique permet par une augmentation de bruit l'amplification de signaux, l'amélioration d'un rapport signal sur bruit ou même encore un gain de rapport signal à bruit supérieur à un. Une avancée conceptuelle fondamentale obtenue dans mes travaux de thèse [31, 33] a été de montrer que les bénéfices à tirer parti du bruit pour le traitement d'information utile ne se limitent pas à des processus ou des traitements sous-optimaux, mais qu'ils peuvent aussi s'étendre à des processus ou traitements optimaux. Je présente dans cette section une synthèse des développements réalisés depuis ma thèse sur la question du bruit utile dans les traitement optimaux [127, 34, 38, 39] que j'articule pour commencer avec d'autres travaux liés aux gains en rapport signal sur bruit [35, 37, 14] et leur utilité **[11, 117]** en traitement de l'information.

3.3.1 Transformation non linéaire du rapport signal sur bruit

En parallèle de l'exploration du phénomène non linéaire de résonance stochastique, je me suis penché sur d'autres questions de traitement non linéaire du signal n'impliquant pas d'effet de bruit utile. J'ai ainsi étudié en dehors d'un strict effet de résonance stochastique, la transformation du rapport signal sur bruit entrée-sortie pour des signaux harmoniques par des filtres non linéaires. Les signaux harmoniques sont des signaux de base pour de nombreuses situations de traitement du signal, de codage ou de mesure d'information. Une composante harmonique peut être elle-même le signal d'intérêt ou elle peut porter une information utile via la modulation d'un de ses paramètres. C'est ainsi un problème courant très important dans de nombreux domaines des sciences expérimentales et des techniques d'avoir à retrouver un signal harmonique caché dans du bruit additif. C'est d'ailleurs sur une question de ce type qu'ont débuté historiquement, les études sur la résonance stochastique [10]. Un signal de fréquence ν_s ajouté à un bruit, constitue un mélange signal-bruit avec une signature très typée dans le domaine fréquenciel : son spectre de puissance est formé d'une raie spectrale fine à la fréquence ν_s, qui émerge hors d'un fond de bruit large bande. Pour quantifier dans le mélange signal-bruit la part du signal harmonique et celle du bruit, une mesure adaptée est un rapport signal sur bruit (RSB) défini à partir du spectre de puissance comme le rapport de la puissance contenu dans la raie spectrale ν_s divisée par la puissance contenue dans le fond de bruit situé autour de ν_s. Ce RSB mesure la façon dont la raie spectrale ν_s émerge du fond de bruit. Un filtre passe-bande centré sur ν_s utilisé pour extraire la composante harmonique a une efficacité qui est directement reliée avec le rapport signal sur bruit [49]. Ainsi, il semble intéressant, comme prétraitement, d'améliorer le RSB. Cependant, il est connu qu'aucun filtre linéaire n'est capable d'améliorer un tel rapport signal sur bruit. En effet, un filtre linéaire multipliera la raie spectrale et le fond de bruit à ν_s par le même facteur, le carré de sa fonction de transfert à ν_s [49]. En conséquence, tout filtre

linéaire, même dynamique, quelle que soit sa complexité et son ordre, laisse le rapport signal sur bruit inchangé [49]. En revanche, rien n'est connu a priori sur la transformation du rapport signal sur bruit si on considère la classe des filtres non linéaires.
Afin de restreindre le champ d'investigation (par définition infini avec les non–propriétés comme le non linéaire) j'ai choisi d'étudier des filtres non linéaires à base de simples composants non linéaires et facilement implantable en électronique. Un deuxième choix méthodologique a été de choisir la classe des composants sans mémoire à caractéristique entrée–sortie statique comme celle que j'avais étudié pour les effets de bruits. Ces composants sont particulièrement adaptés dans ce contexte puisque leur comportement est indépendant de la fréquence du signal d'entrée. Ainsi, si une transformation utile du rapport signal sur bruit est obtenue par un composant à caractéristique statique le bénéfice de cette transformation est garanti indépendemment de la fréquence ν_s du signal harmonique d'entrée [2]. Le calcul du rapport signal sur bruit de l'ensemble des non-linéarités statiques peut être mené de façon unifié [29] dans le cadre théorique suivant. On considère un mélange signal–bruit additif $x(t) = s(t)+\xi(t)$, où le signal utile $s(t)$ est constitué d'une seule composante harmonique $s(t) = A\cos(2\pi\nu_s t + \varphi)$,et $\xi(t)$ un bruit blanc stationnaire de fonction de répartition $F_\xi(u)$ et de densité de probabilité $f_\xi(u) = dF_\xi(u)/du$. Le bruit $\xi(t)$ est un bruit subit sur lequel nous ne souhaitons pas influer volontairement. Ce mélange $x(t)$ est appliqué en entrée d'un système non linéaire sans mémoire [9] de caractéristique entrée–sortie $g(\cdot)$ produisant la sortie

$$y(t) = g[s(t) + \xi(t)] \ . \tag{3.9}$$

Dans cette situation, $x(t)$ et $y(t)$ sont des signaux aléatoires cyclostationnaires [108] de période $T_s = 1/\nu_s$, dont les spectres de puissance sont une raie spectrale ν_s émergeant d'un fond de bruit large bande. Le rapport signal sur bruit peut alors s'exprimer comme

$$\mathcal{R}_{\text{out}} = \frac{\left|\langle \mathrm{E}[y(t)]\exp(-\imath 2\pi t/T_s)\rangle\right|^2}{\langle \mathrm{var}[y(t)]\rangle \Delta t \Delta B} \ . \tag{3.10}$$

avec l'espérance de sortie $\mathrm{E}[y(t)]$

$$\overline{Y}_1 = \left\langle \mathrm{E}[y(t)]\exp\Big(-\imath\frac{2\pi}{T_s}t\Big)\right\rangle \ , \tag{3.11}$$

où la moyenne temporelle s'écrit

$$\langle ... \rangle = \frac{1}{T_s}\int_0^{T_s} ...\, dt \ . \tag{3.12}$$

et la variance instationnaire à l'instant t $\mathrm{var}[y(t)] = \mathrm{E}[y^2(t)] - \mathrm{E}[y(t)]^2$ qui fait intervenir

$$\mathrm{E}[y(t)] = \int_{-\infty}^{+\infty} g(u) f_\xi[u - s(t)]du \ , \tag{3.13}$$

et

$$\mathrm{E}[y^2(t)] = \int_{-\infty}^{+\infty} g^2(u) f_\xi[u - s(t)]du \ . \tag{3.14}$$

[2] Cette indépendance vis à vis de la fréquence avec des composants statiques est vrai tant que l'hypothèse d'un bruit physique modélisable par un modèle de type bruit blanc est valide, c'est à dire tant que la durée de correlation du bruit physique est petite devant la période $T_s = 1/\nu_s$ et tout autre temps caractéristique du processus. Si l'hypothèse de bruit blanc n'est plus valide, l'amplification du gain en rapport signal sur bruit peut encore se produire mais la description théorique d'un tel gain sort du cadre de validité de l'Éq. (3.16) et est a priori plus compliqué à mener. D'autres limitations naturelles en fréquence peuvent se produire en pratique avec les limitations physiques des composants qui présentent tous une fréquence de coupure.

Dans l'Éq.(3.10), Δt représente la période d'échantillonnage de la mesure. Le bruit blanc modélise ici un bruit large bande avec une durée de corrélation beaucoup plus petite que les autres échelles de temps (T_s et Δt), et une variance finie σ_ξ^2. De façon similaire, le rapport signal sur bruit pour l'entrée $x(t)$ est

$$\mathcal{R}_{\text{in}} = \frac{A^2/4}{\sigma_\xi^2 \Delta t \Delta B} \,. \tag{3.15}$$

Le gain rapport signal sur bruit entrée–sortie à travers la non-linéarité $g(\cdot)$ s'exprime donc

$$G = \frac{\mathcal{R}_{\text{out}}}{\mathcal{R}_{\text{in}}} = \frac{\left|\langle \mathrm{E}[y(t)] \exp(-\imath 2\pi t/T_s)\rangle\right|^2}{\langle \mathrm{var}[y(t)]\rangle} \, \frac{\sigma_\xi^2}{A^2/4} \,, \tag{3.16}$$

Les Éqs. (3.12)–(3.14) donnent accès au gain RSB G de l'Éq. (3.16) pour une non-linéarité de forme arbitraire $g(\cdot)$ et une densité de bruit $f_\xi(u)$ de forme également arbitraire.
Illustrons le propos avec un quantifieur symétrique à 3 niveaux dont la caractéristique $g(\cdot)$ entrée–sortie s'écrit

$$g(u) = \left\{ \begin{array}{lll} -1 & \text{for} & u \leq -\lambda \,, \\ 0 & \text{for} & -\lambda < u < \lambda \,, \\ 1 & \text{for} & u \geq \lambda \,, \end{array} \right. \tag{3.17}$$

Dans ce cas, les Éqs. (3.13) et (3.14) s'ecrivent

$$\mathrm{E}[y(t)] = 1 - F_\xi[\lambda - s(t)] - F_\xi[-\lambda - s(t)] \,, \tag{3.18}$$

et

$$\mathrm{E}[y^2(t)] = 1 - F_\xi[\lambda - s(t)] + F_\xi[-\lambda - s(t)] \,. \tag{3.19}$$

Ceci conduit aux résultats de la Fig. 3.5 si $\xi(t)$ est un bruit centré gaussien. La Fig. 3.5

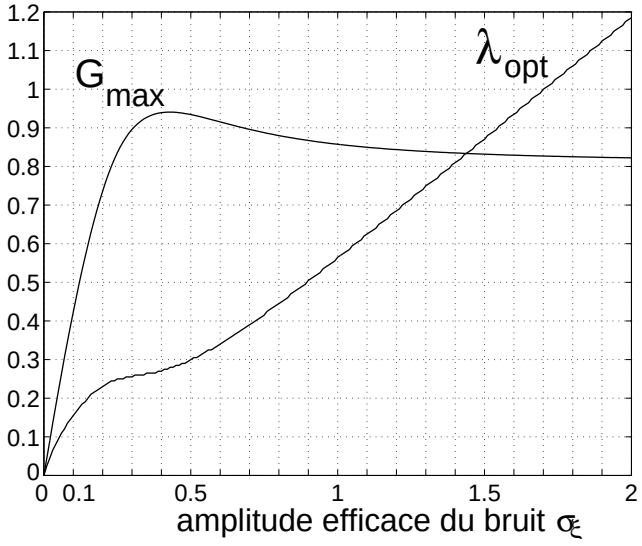

Figure 3.5 : Seuil optimal λ_{opt} pour le paramètre λ du quantifieur de l'Éq. (3.17), et le gain entrée–sortie du rapport signal sur bruit $G_{\max}$ à λ_{opt}, en fonction de l'amplitude efficace σ_ξ du bruit (en prenant l'amplitude maximum de la composante périodique $s(t)$ à $A = 1$) du bruit gaussien centré $\xi(t)$.

montre que la quantification du signal d'entrée $x(t)$ entraîne en présence de bruit gaussien

une dégradation systématique mais relativement faible (notamment à fort niveau σ_ξ de bruit) du rapport signal sur bruit quand le paramètre λ du quantifieur est optimisé. En présence de bruit non gaussien, les résultats de la Fig. 3.6 indiquent la possibilité cette fois de gain en rapport signal sur bruit supérieur à un. Ces résultats sont particulièrement intéressants puisqu'ils s'accompagnent d'une compression du signal d'entrée qui est ici quantifiée sur seulement 3 niveaux. Sur le même mode, les références [37] et **[35]** analysent les transformations du rapport

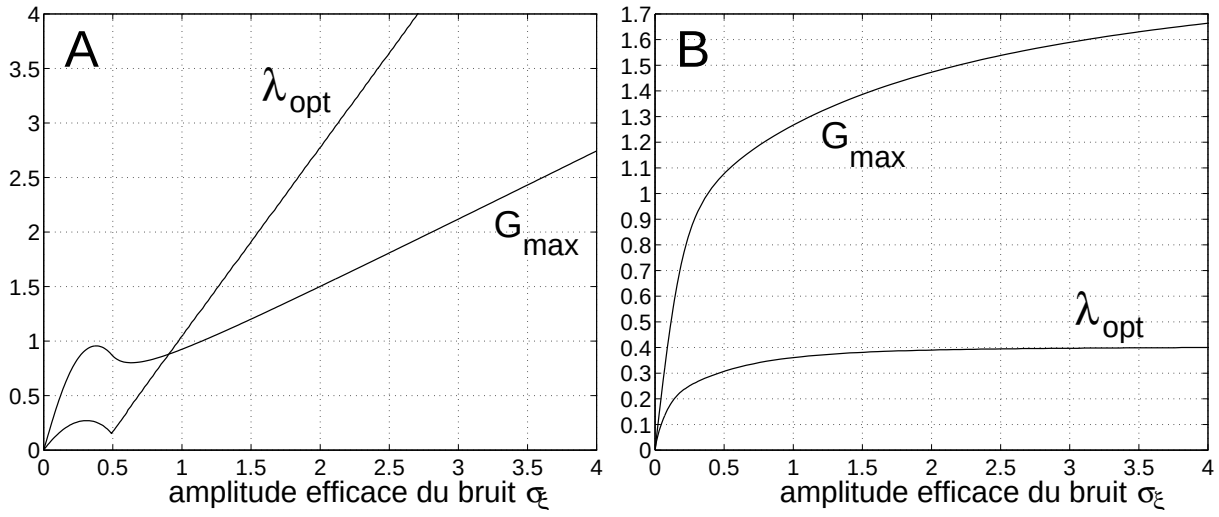

Figure 3.6 : Similaire à la Fig. 3.5, excepté pour la densité du bruit $f_\xi(u)$ qui est uniforme centré (A), centré laplacien (panel B).

signal sur bruit d'un signal périodique par d'autres non-linéarités statiques usuelles chez les composants électroniques comme les non-linéarités à saturation douce ou dure. Ces études sont systématiquement menées en observant l'influence du bruit pris gaussien ou non-gaussien. Un résultat étonnant que montre [37] et **[35]** est la possibilité en optimisant le paramètre de saturation d'obtenir un gain du rapport signal sur bruit entrée-sortie supérieur à 1 même en présence de bruit gaussien. Très peu de systèmes non linéaires sont capables d'amplifier le rapport signal sur bruit d'un sinus noyé dans un bruit blanc gaussien large bande comme décrit dans **[35]**. L'amplification du rapport signal sur bruit est une question qui a été soulevée très tôt en traitement du signal [48, 12]. Pour des conditions plus restreintes d'un bruit gaussien à bande étroite [48, 12] obtient un gain RSB maximum de 2 avec un comparateur. Dans le cadre moins restreint d'un bruit blanc gaussien large bande, les gains en RSB rapportés sont également modestes : [68] fait état d'un gain maximum en RSB de 1.2 avec un système non linéaire dynamique bistable, [24] rapporte un gain maximum en RSB 1.25 obtenu à l'aide d'un ensemble de systèmes non linéaires dynamiques bistables couplés en réseau. L'étude **[35]** montre que le gain en RSB peut culminer à 1.4 pour une simple non-linéarité statique à saturation optimalement ajustée.

L'amplification d'un sinus noyé dans du bruit dans [37, 35] est basée sur la sélection et l'optimisation de non-linéarités statiques. Alternativement, une autre approche qui peut aussi mener à l'amplification du rapport signal sur bruit dans des systèmes non linéaires est l'injection volontaire de bruit [68, 25, 32] via la résonance stochastique. La différence entre ces deux approches peut se présenter de la façon suivante. Pour une forme de non-linéarité donnée, et un niveau de bruit σ_ξ fixé, la meilleure chose à faire pour le rapport signal sur bruit, chaque fois que cela est possible, est de façonner la non-linéarité de façon optimum en jouant sur les paramètres ajustables (le seuil du

quantifieur, le niveau de saturation, ...). Si on a la possibilité de répliquer les non-linéarités en réseaux comme dans la Fig. 3.1, alors une injection volontaire de bruit peut permettre de façonner la caractéristique entrée–sortie du composant déterministe équivalent dans un sens qui améliore le rapport RSB comme je l'ai montré dans les études [36, 26, 32, 14] (voir **[14]**).

3.3.2 Utilisation de gain RSB supérieur à un

Une question naturelle une fois que l'on a établi la possibilité de gain en RSB porte sur l'utilité de ces gains dans des contextes applicatifs déterminés. Le rapport signal sur bruit tel que défini dans la sous-section précédente est un paramètre important en particulier parce qu'il est facilement mesurable en sciences expérimentales au moyen d'analyseurs de spectres. Pour autant, les mesures de performance en traitement de l'information ne s'expriment pas directement en terme de RSB. Ainsi, ma démarche a été de considérer des tâches classiques de traitement de l'information évaluées par des mesures de performances adaptées à ces tâches dans les conditions où j'avais démontré la possibilité de gains RSB supérieurs à un.

• L'étude **[11]** a été réalisée lors du stage de master de Rohit BHAT que j'ai encadré lors de mon séjour à l'Indian Institute of Sciences de Bangalore (Inde). Ce travail analyse un problème d'estimation bayésienne liée à la forme d'un signal noyé dans un bruit non-gaussien (du type de ceux de la Fig. 3.6). En présence de bruit gaussien, l'estimateur bayesien minimisant l'erreur quadratique moyenne d'estimation est le filtre de Wiener qui présente l'avantage d'être linéaire. Quand l'environnement de bruit est non-gaussien, l'estimateur optimal est souvent non linéaire et donc plus difficile à implanter et même parfois à déterminer explicitement. Nous analysons dans **[11]** comment un quantifieur symétrique à 3 niveaux comme celui de l'Éq. (3.17) placé en pré-traitement de l'estimateur optimal permet via une amplification du RSB d'améliorer les performances d'estimation du filtre de Wiener.

• L'étude **[117]** traite quant à elle d'une tâche de détection d'un sinus noyé dans un bruit non gaussien. Là aussi, les détecteurs optimaux, linéaires en milieu gaussien, sont souvent non linéaires en présence de bruit non gaussien. Une approche classique pour le design de détecteurs sous-optimaux [92] peut être de conserver le détecteur linéaire en appliquant un prétraitement non linéaire. Dans **[117]**, le prétraitement est un réseau de comparateur avec des bruits volontairement injectés comme dans la Fig. 3.1. On montre comment le bruit, en façonnant la caractéristique des comparateurs, peut améliorer la performance de détection du détecteur linéaire pour une large gamme de bruits non gaussien.

Ainsi, nous avons montré la possibilité d'utiliser en pratique les gains RSB supérieurs à un pour de l'estimation ou de la détection sous-optimale de signaux noyés dans des bruits non-gaussiens. Pour le cas important d'un sinus en présence de bruit blanc additif gaussien il n'en n'est pas de même. Prenons comme exemple la détection. Le détecteur optimal qui permet d'atteindre la plus petite probabilité d'erreur de détection d'un sinus dans du bruit blanc additif gaussien est le filtre adapté. Aucun traitement déterministe placé avant ce filtre ne peut améliorer les performances de la détection. Les performances du filtre adapté sont pourtant directement déterminées par le RSB. Néanmoins, après un prétraitement pour amplifier le rapport signal sur bruit, on est en présence d'un mélange non linéaire du sinus avec le bruit. Pour la détection du sinus à partir de ce mélange non linéaire, le détecteur optimal n'est plus le filtre adapté et la performance du détecteur optimal n'est plus forcément déterminée par le RSB. De cette façon, il est possible en présence de mélange signal-bruit non linéaire d'enregistrer une amplification du

RSB sans amélioration du détecteur optimal. Ces réflexions sur le RSB ont montré l'importance de considérer la finalité de la tâche de traitement de l'information pour apprécier l'impact d'une non-linéarité ou d'une augmentation de niveau de bruit sur une mesure de performance adaptée à cette tâche.

3.3.3 Surprobabilisation des traitements optimaux

Par essence, la spécification d'un traitement (estimation, détection, ...) optimal d'un signal noyé dans du bruit défini un processus qui est dépendant du bruit. Dans la plupart des cas (comme pour le filtre adapté en détection), la performance de ces traitements optimaux décroît de façon monotone lorsque le niveau de bruit augmente. Un fait intéressant que montre l'article **[39]** est qu'il existe des traitements optimaux qui se comportent différemment : leurs performances croîssent lorsque le niveau de bruit augmente. Ceci peut paraître paradoxal. C'est en fait en accord avec l'idée qu'un traitement optimal est une notion relative. Un traitement optimal dépend comme on vient de le rappeler d'un critère spécifique qu'il optimise et l'optimalité pour un gain en SNR par exemple peut très bien ne pas être optimale pour une performance de détection. Mais aussi, la solution optimale dépend de paramètres qui peuvent être pris comme ajustables et de ceux que l'on suppose fixés et non modifiables dans le critère d'optimisation. Une solution optimale est donc relative à un critère spécifique et aussi à un jeu défini de paramètres ajustables. Prenons l'exemple de la détection. Dans l'approche classique de la détection optimale, le bruit est supposé fixé, et les paramètres ajustables sont ceux qui définissent la fonction de décision qui opère sur les données mesurées. Les détecteurs optimaux sont alors ceux qui déterminent la meilleure paramétrisation de la fonction de décision en présence d'un niveau de bruit fixé. Les études sur la résonance stochastique nous incitent à élargir cette vision en explorant ce qu'implique de permettre à certains paramètres liés au bruit d'être considérés comme ajustables. L'article **[39]** présente une synthèse de nos travaux sur des exemples concrets [127, 34, 38] de traitements optimaux au sens de la théorie classique de la détection ou de l'estimation qui voient leurs performances s'améliorer quand le niveau de bruit augmente. Deux couplages signal-bruit ont essentiellement été identifiés :

• Les références [127, 38] considèrent une onde périodique de forme carrée ou sinusoïdale corrompue par un bruit de phase non gaussien ou gaussien et montre l'existence de conditions où la performance d'un détecteur optimal [127] ou d'un estimateur optimal [38] s'améliore quand le niveau de bruit de phase augmente, par exemple en bougeant de façon aléatoire la position du récepteur de l'onde.

• La référence [34] quant à elle considère un mélange signal–bruit additif avec un bruit non-gaussien. Pratiquement, le bruit non gaussien de [34] peut être vu comme la perturbation d'un transmetteur numérique qui émet des bits en basculant aléatoirement entre deux niveaux $\pm A$ eux-mêmes perturbés par un bruit Gaussien centré de variance σ_G^2. On s'autorise à faire varier séparément A et σ_G pour augmenter le niveau global du bruit additif non gaussien centré bimodal. Pour un signal constant en présence d'une source de bruit non gaussien de ce type, [34] montre la possibilité d'améliorer la performance d'un détecteur optimal en augmentant le niveau de bruit.

Ces résultats se présentent comme des preuves de faisabilité qui montrent sur la base d'exemples comment une augmentation du niveau de bruit peut modifier la probabilisation d'un traitement optimal et se traduire par une amélioration de la performance optimale. Notons que pour ces

exemples présentés dans [**39**], l'implantation du traitement optimal doit être modifié à chaque fois que le bruit est modifié. Pour autant, à la base, il s'agit toujours de la même tâche de traitement de l'information : même signal à estimer ou détecter en présence d'un bruit différent au sens où il est augmenté. Le changement de probabilisation d'un traitement optimal par une augmentation du bruit et autorisant des améliorations par le bruit de la performance optimale ouvre des perspectives d'explorations pour la résonance stochastique que décrit en détail [**39**].

3.4 Bruit utile et traitement des images

Dans un premier temps [62], les développements de la résonance stochastique se sont opérées sur un mode de preuve de faisabilité montrant la diversité des formes d'effets de bruit utile. Ceci a essentiellement été obtenu sur des traitements de signaux monodimensionnels. Pour autant, comme phénomène non linéaire général, la résonance stochastique n'est a priori pas limité à une dimension et doit pouvoir s'appliquer au domaine de l'image. Une approche innovante demande toutefois de mettre en évidence des formes de la résonance stochastique qui soient spécifiques aux images et non des transpositions triviales à l'échelle du pixel d'effets de bruit utile déjà connus en 1D. Il s'agit là d'une piste que j'ai initiée et développée à partir de 2006. Pour structurer mon questionnement, je me suis appuyé sur les 4 ingrédients rappelés dans la section 3.1 de ce chapitre qui avaient guidé les évolutions de la résonance stochastique sur les signaux 1D. Je me suis ainsi posé les questions suivantes :

• Existe-t-il des bruits spécifiques aux images ? Des effets de bruits utiles sont-ils possibles dans ces images naturellement bruitées lorsque des non-linéarités sont présentes ?

• Existe-t-il des processus non linéaires en traitement d'image qui impliquent naturellement des non-linéarités connues pour se prêter aux effets de bruit utiles ?

• Existe-t-il des mesures de performances spécifiques aux images ?

Cette section synthétise les éléments de réponses que j'ai apportés à ces interrogations à travers mes travaux [16, 13, 17, 41, 18, 51, 129, 72, 73].

3.4.1 Utilisation du speckle en imagerie cohérente

Un domaine où les images sont naturellement bruitées est l'imagerie cohérente avec le bruit de speckle. Ces fluctuations spatiales dans l'image s'observent lorsqu'une onde monochromatique éclaire la scène à imager avec une phase uniforme ou quasi-uniforme dans l'espace. En se réfléchissant ou en traversant, l'onde incidente voit sa phase perturbée par les variations microscopiques dues à la rugosité inhérente de la scène à l'échelle de la longueur d'onde. Sur un capteur d'image, certaines variations s'additionnent constructivement donnant de fortes intensités, d'autres interfèrent destructivement en donnant de faibles intensités. Il en résulte dans l'image cohérente des variations d'intensité d'apparence granuleuse que l'on appelle bruit de speckle. En optique (cohérente ou non) lorsqu'un faisceau parallèle de lumière traverse un milieu transparent, le profil de l'intensité du faisceau transmis est le produit de l'intensité du faisceau par la transparence spatiale du milieu. Ainsi, l'effet du bruit de speckle se modélise [66] comme la multiplication par un pattern 2D aléatoire $N(u, v)$ avec u et v les coordonnées spatiales des images. Il existe de multiples modèles de densité de probabilité de speckle suivant que l'onde est polarisée ou non, suivant la taille du grain de speckle devant la taille du pixel du

capteur d'image ou encore suivant l'homogénéité de la répartition des irrégularités à l'échelle de la longueur d'onde dans la scène à imager [65]. De tels modèles de densité de probabilité permettent de calculer des quantités utiles comme un contraste

$$C = \frac{\sigma_N}{\overline{N}} \, , \tag{3.20}$$

rapport entre l'écart-type σ_N du speckle et la valeur moyenne $\overline{N}$ ou encore un rapport signal sur bruit en calculant

$$S/B = \frac{1}{C} \, . \tag{3.21}$$

Un fait caractéristique des bruits de speckle est que les fluctuations mesurées par l'écart type σ_N sont du même ordre de grandeur que la moyenne $\overline{N}$. Ainsi, les quantités contraste C et rapport signal à bruit S/B sont en général indépendantes de l'amplitude du bruit de speckle. À titre d'illustration, considérons le modèle simple du speckle pleinement développé valide pour une scène uniforme, avec une onde incidente polarisée et une taille du pixel beaucoup plus petite que la taille d'un grain de speckle. La densité de probabilité du speckle pleinement développé s'exprime comme

$$p_N(j) = \frac{1}{\sigma_N} \exp\left(-\frac{j}{\sigma_N}\right) \, , \qquad j \geq 0 \, . \tag{3.22}$$

pour laquelle on a $\overline{N} = \sigma_N$ et donc $C = 1$ et $S/B = 1$ indépendamment de l'amplitude du speckle. Ce résultat, général pour une large variété de modèles de bruit de speckle, suppose que le capteur qui recueille les images specklées est parfaitement linéaire sans restriction d'échelle d'amplitude sur cette linéarité. En pratique, les capteurs ne peuvent pas être linéaires sur une gamme infinie d'échelle. Le seuil de détectabilité (lié par exemple au signal d'obscurité), la résolution (liée au pas de quantification du convertisseur analogique numérique associé au capteur), la saturation (liée à la dynamique nécessairement finie du capteur) visible sont autant de non-linéarités qui introduisent des échelles qui doivent a priori modifier les mesures de contrastes C ou de rapport signal sur bruit S/B de l'Éq. (3.22). Pour autant, j'ai constaté que ces impacts des non-linéarités des capteurs sur les images specklées avaient peu été analysés dans une perspective liée aux capteurs. Dans les études [16, 13, 17, 41, 18, 51] (voir **[16]** et **[41]**) que j'ai initiées et développées à l'occasion de la thèse de Solenna BLANCHARD, nous avons considéré une problématique de transmission d'images perturbées par du speckle en présence de non-linéarité à seuil ou à saturation. En présence de ces non-linéarités, nous avons analysé la dépendance de la qualité de la transmission des images specklées en fonction du niveau du bruit de speckle. Les explorations dans [16, 13, 17, 41, 18, 51] ont porté sur :

• le type de mesure de performance (information mutuelle [16], intercovariance [16, 41, 18], écart quadratique moyen [16, 17, 51].

• le type d'image à transmettre binaires [16, 41, 18] ou distribuées sur de multiples niveaux de gris [13].

• le type de modèle de speckle polarisé (avec capteur immobile [16, 13, 41] ou capteur en mouvement [18]), dépolarisé [51].

• le type de non-linéarité à seuil [16, 13, 18, 51] ou à saturation [41].

• le type de validation des résultats par confrontation de simulation numérique et de développements théorique allant jusqu'à l'établissement de résultats analytiques explicites [16, 13, 18] ou par l'apport supplémentaire d'une confrontation avec des résultats issus de l'expérimentation optique [16, 41].

L'ensemble des travaux [16, 13, 17, 41, 18, 51] montre qu'il existe des conditions pour lesquelles le niveau de bruit de speckle peut être ajusté optimalement afin de tirer des bénéfices des non-linéarités pour la transmission des images specklées. Il s'agit d'un effet non linéaire où, à la manière des études de résonance stochastique, une mesure de performance évolue de façon non monotone en fonction du niveau du bruit présent dans le processus de traitement de l'information en culminant pour un niveau de bruit non nul qui maximise la qualité du traitement. Il est possible de continuer à développer ces travaux dans différentes directions. Dans le domaine de l'imagerie cohérente, les mesures de performances utilisées sont des mesures générales de similarités dites de bas niveau de traitement de l'information. Il conviendrait d'analyser l'impact bénéfique des non-linéarités montré dans [16, 13, 17, 41, 18, 51] au moyen de mesures spécifiquement adaptées dans des contextes déterminés de plus haut niveau de traitement de l'information comme de la détection ou de la reconnaissance de forme en s'inspirant de la démarche que j'ai suivie pour les signaux 1D. Il existe d'autres domaines de l'imagerie où les images sont naturellement bruitées et définies par leurs propriétés statistiques. Je pense en particulier au domaine de l'imagerie par résonance magnétique où le couplage image-bruit n'est ni additif ni multiplicatif. Là aussi des non-linéarités sont présentes : inhomogénéité et saturation des bobines créant les champs magnétiques, saturation de l'antenne de réception ou du convertisseur analogique numérique en charge de l'acquisition dans le domaine de Fourier. L'impact de ces non-linéarités sur le traitement de l'image est peu connu. Il serait intéressant d'analyser s'il existe là aussi des régimes où il est possible de tirer profit des non-linéarités en jouant notamment sur le niveau de bruit. Il s'agit d'une piste que nous considérons dans le cadre de la thèse d'Agnès DELAHAIES [50].

3.4.2 Quantification psychovisuelle de la résonance stochastique

L'évaluation automatique de la qualité des images est une tâche importante pour de nombreux domaines du traitement des images. Les mesures traditionnelles habituellement utilisées comme mesures de qualité telles que l'écart quadratique moyen, ou encore le rapport signal sur bruit sont simples à implanter mais se cantonnent à fournir une indication très bas-niveau de traitement de l'information. Récemment, un indice sous l'acronyme d'indice SSIM (pour structural similarity) a été proposé comme nouvelle mesure de similarité [150, 151], avec des potentialités pour rendre compte de similarité structurelle évaluée par trois facteurs : la perte de corrélation, les distorsions de luminance et de contraste. Il a été montré que l'indice SSIM était pour certaines tâches de traitement des images (compression, recalage de dynamique, débruitage,...) plus proche de la perception humaine que les mesures traditionnelles tout en évitant une modélisation explicite complexe du système visuel humain [150, 151]. Pour autant, en tant que nouvelle mesure, les potentialités de l'indice SSIM restent à consolider. Pour ce faire, il est intéressant de tester l'indice SSIM dans de nouveaux contextes. La résonance stochastique a été enregistrée dans des expériences de psychovision où la mesure de performance est la perception humaine [141, 152, 111, 137]. Il nous a donc semblé intéressant de mettre l'indice SSIM à l'épreuve dans un cadre de résonance stochastique. Nous montrons dans **[129]** que l'indice SSIM est capable d'enregistrer l'amélioration apportée par le bruit lors d'une transmission non linéaire d'une image parfois même quand les mesures traditionnelles ne traduisent pas cet effet pourtant perçu par l'oeil

humain.
Les images dans [**129**] sont bruitées par un bruit additif. Il serait intéressant de considérer des couplages multiplicatifs comme ceux produits en imagerie cohérentes en présence de speckle. Au delà de ces extensions naturelles (voir également celles décrites en conclusion de [**129**]) l'étude [**129**] montre comment la résonance stochastique peut servir de banc de test pour de nouvelles mesures informationnelles. D'autres mesures de qualité des images pourraient être évaluées dans un contexte de résonance stochastique comme les mesures récentes de saillance proposées par [87]. On pourrait même imaginer de transposer cette approche à d'autres types de stimuli. La résonance stochastique a en effet également été montrée en psychoacoustique (en particulier pour les personnes équipées d'implantes cochléaires [42]). Ces expériences psychosensorielles sont fondamentales puisqu'elles montrent qu'au stade ultime d'intégration du système nerveux des effets de bruit utile existent. Une question ouverte est de connaître les méchanismes et échelles qui expliquent ces effets de bruits utiles observés sur nos propres sens. L'évaluation de mesures de qualité des images ou des sons inspirée à des degrés de complexité divers du système sensoriel dans le contexte de la résonance stochastique constitue une voie intéressante pour construire des éléments de réponse.

3.4.3 Diffusion non linéaire façonnée par le bruit

Le processus de diffusion non linéaire appliqué au traitement des images a été introduit historiquement par PERONA et MALIK [109]. Il s'agit d'un processus inspiré de la diffusion de la température dans lequel une image bruitée ψ_0 est restaurée en considérant la solution de l'équation aux dérivées partielles

$$\frac{\partial \psi}{\partial t} = div(g(\|\nabla\psi\|)\nabla\psi), \qquad \psi(x,y,t=0) = \psi_0 \ , \tag{3.23}$$

où le coefficient de diffusion est contrôlé par $g(\cdot)$ une fonction statique non linéaire décroissante de la norme du gradient $\nabla\psi$. Des exemples de fonction $g(\cdot)$ proposées dans [109] sont

$$g(u) = e^{-\frac{\|u\|^2}{k^2}} \ , \tag{3.24}$$

ou encore

$$g(u) = \frac{1}{1+\frac{\|u\|^2}{k^2}} \ , \tag{3.25}$$

avec le paramètre k qui peut être vu comme un seuil permettant d'ajuster l'amplitude des gradients qui sont préservés par le processus de diffusion. Le terme $g(\|\nabla\psi\|)$ joue en effet le rôle de coefficient de diffusion dans l'Éq. (3.23). Ainsi, les forts gradients de l'image se voient attribuer un faible coefficient de diffusion. Ils sont préservés. Les faibles gradients de l'image anticipés comme des bruits sont diffusés par le processus de l'Éq. (3.23). Les choix de la fonction non linéaire et du seuil étant arbitraires, on ne peut garantir leur optimalité qui dépend du contenu de l'image. Il est alors possible en partant d'un choix de fonction non linéaire et de paramètre k donnés de façonner la fonction non linéaire $g(\cdot)$ au moyen du bruit. Pour ce faire, on remplace la fonction $g(u)$ dans l'Éq. (3.23) par la fonction $g_\eta(u)$

$$g_\eta(u) = g(u+\eta(x,y)) \ , \tag{3.26}$$

où η est un bruit indépendant et identiquement distribué d'amplitude efficace σ_η. Contrairement au bruit originel dans ψ_0, le bruit η est volontairement injecté et on contrôle son niveau σ_η. La possibilité d'un effet bénéfique via le façonnage par le bruit du coefficient de diffusion est

présenté de façon condensée dans **[72]** pour une image bruitée ψ_0 par du bruit impulsionnel. L'effet bénéfique du bruit pour la diffusion non linéaire est en fait général et ne se restreint pas à ce type de couplage comme le montre visuellement les Fig. 3.7 et 3.8 extraites de [73]. L'intérêt de ces études était double. Il s'agissait d'illustrer le façonnage par le bruit exposé dans la section 3.1 de ce chapitre sur un exemple non trivial de traitement d'image. Cela m'a permis également de m'initier aux méthodes récentes d'équation aux dérivées partielles.

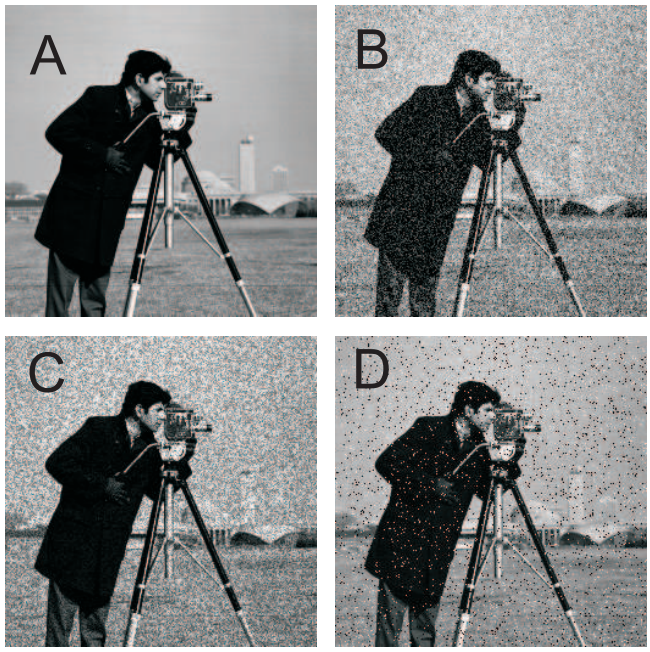

Figure 3.7 : Image originale non bruitée cameraman (A) perturbée par 3 types de bruits différents : (B) additif gaussien centré, (C) multiplicatif gaussien de moyenne unité, (D) impulsionnel. Les amplitudes efficaces de ces bruits sont ajustées séparémment de façon à avoir pour chacune des images (B,C,D) le même similarité (mesurée par l'intercovariance normalisée) avec l'image originale (d).

3.5 Conclusion

Ce chapitre a présenté comment mes recherches sur la résonance stochastique m'ont amené à travailler sur des systèmes physiques et des tâches de traitement de l'information variés. J'ai ainsi développé des compétences larges en physique non linéaire et en théorie de l'information appliquée aux signaux et aux images. Ceci m'a permis de m'interesser à des questions autres que celles liées aux effets de bruits utiles mais ayant comme point commun d'être situées à l'interface entre la physique et les sciences de l'information. Je donne une vision de ce cadre de physique de l'information dans le chapitre suivant.

Figure 3.8 : Comparaison visuelle des images débruitées par le processus de diffusion non linéaire de l'Éq. (3.23). La colonne de gauche donne les résultats optimaux (maximisant la similarité mesurée par l'intercovariance normalisée avec l'image originale non bruitée) pour le processus de l' Éq. (3.23). La colonne de droite donne les résultats optimaux pour la version stochastique du processus de diffusion de l'Éq. (3.23). En haut, le couplage additif; au milieu, le couplage multiplicatif et en bas le bruit impulsionnel décrits sur la Fig. 3.7. L'amélioration du processus de diffusion anisotrope par le bruit est visible sur l'information portée par des régions à faibles gradients comme la texture de l'herbe ou la présence du building en arrière plan.

Chapitre 4

Physique de l'information

Je présente dans ce chapitre le cadre étendu de physique de l'information dans lequel je conçois la suite de mon parcours de recherche.

4.1 Contexte, objectifs et méthodes

Contexte : La physique qui s'intéresse à comprendre, prédire et appliquer les lois et phénomènes de la nature nourrit et se nourrit des questions pratiques et fondamentales de chaque époque. Les progrès de la connaissance dans les domaines de l'électromagnétisme, de l'électronique et de la mécanique quantique ont permis l'essor au XX^{ème} siècle de sociétés centrées sur l'échange à haut débit d'informations. En retour, l'information, comme en d'autres temps le mouvement, la lumière ou l'énergie, se constitue comme une nouvelle grandeur et un nouveau champ d'investigation qui interroge la physique en tant que méthode c'est-à-dire appel à une physique de l'information. Il s'agit d'une dénomination peu commune [8]. Pourtant, on peut recenser différentes voies de recherche qui contribuent de façon significative à établir l'information comme une grandeur physique à part entière :

• *La physique des technologies de l'information* [63] pose des problèmes appliqués comme la compréhension et la modélisation de l'origine des bruits qui perturbent le transfert d'information ou encore comme le calcul des capacités informationnelles [140] des systèmes en charge de transmettre ou de stocker l'information. Les technologies de l'information amènent également des questions fondamentales et d'actualité comme leurs limites ultimes en termes de coût énergétique. Soulignons sur ces sujets les contributions de chercheurs phares comme Richard FEYNMAN [57] et Ralf LANDNAUER [93] auteur de la célèbre citation "information is physical". Les progrès notamment en optique permettent désormais de coder l'information sur l'état quantique de particules. Cette information quantique ouvre des champs nouveaux pour des applications (cryptograhie quantique par exemple) comme pour le développement de bases théoriques d'une théorie quantique de l'information [52].

• *Les liens de la physique avec les fondements des mesures informationnelles.* Un des premiers à avoir porté le point de vue du physicien sur l'information a été Léon BRILLOUIN [19] qui très tôt après l'introduction de la théorie statistique de l'information par Claude SHANNON a montré les liens de l'information au sens de Shannon et de l'entropie au sens de Boltzmann en physique statistique. D'autres entropies comme celle d'Alfred RÉNYI [116] fondées sur des questions informationnelles [23] ont également été reliées à des contextes de thermodynamique

pour l'étude de la turbulence par analyse multifractale [7]. Mentionnons également la thèse défendue sur de nombreux exemples [60] par Roy FRIEDEN du principe d'Extreme Physical Information qui montre comment l'ensemble des lois de la physique peut être vu comme sous-tendu par l'information de Fisher qui pose en théorie de l'estimation les limites fondamentales des performances de tout estimateur non biaisé.

• *Des analogies strictes entre physique et sciences de l'information.* Des travaux récents issus de la physique statistique ont montré des analogies formelles entre les transitions de phases dans les verres de spin en physique statistique, le problème informatique de calculabilité de type SAT (savoir s'il existe une solution à une série d'équations logiques données) et le design de codes correcteurs d'erreurs de types LDPC (pour low density parity-check) afin d'atteindre la limite de Shannon sur le codage de canal en théorie de l'information. La synthèse [101] de Marc MEZARD et Andréa MONTANARI sur le sujet illustre la possibilité d'un traitement unifié de ces problèmes fondamentaux qui sont au coeur de chacune de leurs disciplines.

• *Succès des méthodes bayésiennes.* Les sciences de l'information constituent l'ensemble des techniques qui permettent l'extraction et l'analyse de répétitions et de différences dans des données observables. La notion même d'information dépend des connaissances a priori (géométrique, physique, physiologiques ...) dont on dispose sur les données à observer. Ainsi, l'information est par essence liée à la physique au sens éthymologique du terme c'est à dire à la nature de la scène que l'on observe. Le succès des méthodes bayésiennes utilisant l'information a priori pour résoudre des problèmes heuristiques d'intérêt pratique comme la segmentation d'images bruitées [114, 66], la fusion de données (par exemple en imagerie [142, 46]), ou encore la séparation de sources illustrent à nouveau le bien-fondé des compétences du physicien pour le traitement de l'information.

Objectifs : Dans ce contexte qui situe les développements actuels vers des fondements d'une physique de l'information, ma démarche est celle d'une physique appliquée de l'information. J'organise mes explorations de façon à contribuer selon deux modalités.

• De nouvelles mesures informationnelles (similarités, contrastes, complexités, imprévisibilités, ...) sont continuellement proposées par les mathématiciens et les traiteurs de signaux-images et il convient de les évaluer puis de les appliquer dans des contextes originaux spécifiques pour en comprendre la portée.

• Les progrès récents (améliorations des technologies et baisse des coûts) dans les domaines des capteurs d'images, des composants optroniques de transmission, du traitement et du stockage de l'information, ont permis l'émergence de nouveaux types d'imagerie (l'imagerie de polarimétrie, l'imagerie multi- et hyperspectrale, etc.) non conventionnelle autrefois limitées par les capacités d'acquisition et de stockage des informations et l'apparition de domaines d'application non conventionnels (thermographie infrarouge, IRM) autrefois restreints en raison du coût des matériels. Ces imageries non conventionnelles renouvellent les problématiques classiques du traitement du signal et des images (détection, estimation, segmentation, compression,...). J'ai d'une certaine façon déjà développé de telles approches avec succès, via l'étude de la résonance stochastique et les effets de bruit utile, notamment en direction de l'imagerie cohérente en présence de bruit de speckle [16, 13, 17, 41, 18, 51]. Je cherche actuellement à les étendre et les appliquer aux imageries non conventionnelles citées ci-dessus.

Méthode : Le cours de théorie de l'information de niveau master 2 dont j'ai la charge depuis 2000 me permet de développer une dynamique enseignement-recherche (via des activités pédagogiques comme l'encadrement de projets, de stages ou la création d'études de cas). J'ai ainsi eu l'occasion de publier des travaux au moyen de mesures informationnelles [6] au sens large comme

• des mesures d'imprévisibilité : entropie de Shannon[132, 84, 50];
• des indicateurs de mesurabilité comme l'information de Fisher [130, 118, 26, 27];
• des indices de similarité visuelle : SSIM **[129]**;
• des mesures de complexité : information au sens de Rissanen **[40]** ou encore les outils de l'analyse fractale [43, 28, 44] et multifractale **[76]**;
• des analyses en échelle : décomposition empirique modale (EMD en anglais) [85] et aussi les outils de l'analyse fractales et multifractales.

Ces mesures sont autant d'outils, que j'ai pour l'instant essentiellement appliquées en recherche pour l'étude des effets de bruits utiles mais qui sont d'applicabilité large pour d'autres questions à l'interface de la physique et des sciences de l'information. Ainsi, depuis 2007, je mène en parallèle de la thématique sur la résonance stochastique des travaux liés à la question de l'analyse des signaux et des images à travers les échelles. Je présente une synthèse de ces travaux dans la section 1 de ce chapitre.
Au plan applicatif, je considère spécifiquement les domaines des sciences du vivant avec les domaines du biomédical (depuis 2007) et du biovégétal (depuis 2009), des domaines clés d'application des STIC, où les sciences de l'information jouent un rôle d'une importance grandissante. Je décris dans la section 2 de ce chapitre une vue d'ensemble des perspectives que je développe actuellement dans cette direction.

4.2 Analyse en échelle

Grâce aux progrès dans tous les domaines de la technique, il est aujourd'hui possible d'observer notre environnement à travers les échelles. Les satellites et leurs systèmes embarqués d'imagerie (visible, infrarouge, multi ou hyperspectral) à haute résolution permettraient dit-on de suivre un individu dans ses déplacements. Les microscopes à sondes locales (champ proche, AFM, STM) grâce à la précision micro voire nanométrique des actionneurs sont capables de nous donner à voir, à même résolution, des objets allant de quelques nm à quelques mm. De même en médecine, des scanners à haute résolution permettent, comme on peut le voir sur la Fig. 4.1, d'acquérir à la résolution maximale permise par le capteur imageur, des tissus occupant la totalité de la surface d'une lame de microscope. Les volumes importants des images produites par ces systèmes nouveaux (imagerie satellite, microscopes à sonde locale, scanner haute résolution) posent question : Avons-nous besoin de toutes ces données ? Pour une tâche définie de traitement de l'information, quelle est l'échelle optimale d'observation ? Supposons, à la manière d'une étude de cas, que l'on souhaite quantifier la surface de tissus pathologiques dans les images de la Fig. 4.1. Il est fort probable que le résultat de la quantification dépende de l'échelle d'observation. On observe sur la frise de la Fig. 4.1 que l'ambiguïté à classer le tissus dans une classe ou une autre évolue en fonction de l'échelle d'observation. Si on regarde de trop loin, le contour entre les deux classes risque d'être trop grossier, si on regarde de trop près il se peut que l'on ait du mal à distinguer la frontière entre les deux classes. Les performances d'un algorithme d'aide au diagnostic sont habituellement comparées à une vérité terrain réalisée par un expert. La question de l'échelle optimale s'exprime en terme de temps à passer pour l'expert, et en terme de temps de calcul pour l'algorithme. Enfin, il se peut que la notion même d'information dépende de

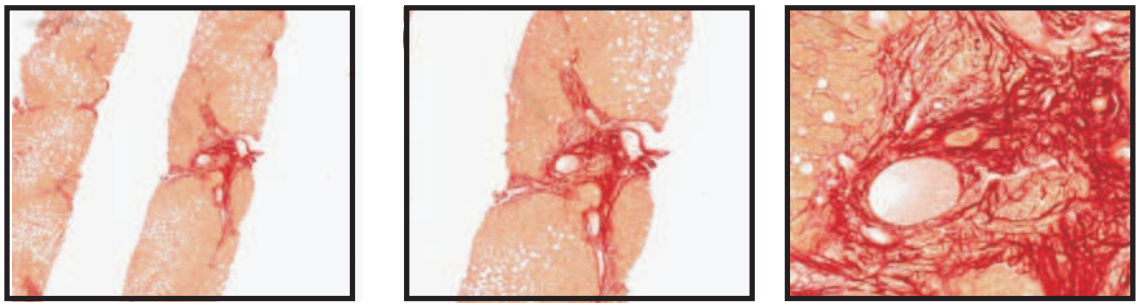

Figure 4.1 : Images de coupe de foie réalisées par Julien CHAIGNEAU du laboratoire HIFIH du CHU d'Angers à différentes échelles via un scanner à haute résolution dans le cadre d'une collaboration en cours avec l'équipe Signal-Image du Laboratoire LISA. Les parties fibreuses en rouges sont des tissus pathologiques et les zônes roses sont saines. L'ensemble de la zône visible dans l'image A est à la résolution de l'image C. Le poids brut de l'image A est de 100Mo.

l'échelle d'analyse. Pour l'expert, à l'échelle la plus grande, l'oeil opérant un moyennage spatial, l'information de texture fibreuse disparaît quelque peu pour laisser place à un simple "contraste" de densité de rouge. Au delà de l'exemple pratique de la Fig. 4.1, l'analyse en échelle est une question générique en sciences de l'information. En plus des mesures informationnelles générales, les mathématiques appliquées proposent des cadres spécialement adaptés pour donner un point de vue en échelle comme l'analyse multirésolution au moyen d'ondelettes ou encore comme les outils d'analyse fractale ou multifractale. Cette section donne à voir un échantillon de mes contributions et perspectives sur cette thématique.

4.2.1 Échelle optimale d'observation

Dans cette partie, je développe, à la manière d'un courte leçon, l'intérêt d'une approche physique de l'information où acquisition et traitement sont pensés conjointement. Pour cela, considérons une tâche informationnelle courante en imagerie qui consiste à dégager un objet d'un fond. En l'absence de bruit, l'objet se dégage parfaitement du fond et l'échelle optimale d'observation, celle qui permet par exemple d'estimer au mieux la surface de l'objet, est la plus petite échelle qui permet de voir entièrement l'objet. En présence de bruit, la distinction entre fond et objet est perturbée. Le sens commun prévoit qu'une échelle intermédiaire, ni trop large pour avoir suffisamment de résolution, ni trop petite pour que le fond soit suffisamment défini, soit à privilégier. Les outils issus de la théorie statistique de l'information permettent d'apporter une réponse quantifiée à ce problème expérimental interdisciplinaire.
En théorie statistique de l'information [47], un canal de communication est constitué d'une source qui délivre un message à un destinataire via un canal perturbé par du bruit. La capacité informationnelle d'un canal de communication est défini comme [47], $C = \max_{\Pr\{S\}} I(S;Y)$, où S est l'entrée du canal et Y sa sortie. $I(S;Y)$ est l'information mutuelle entrée–sortie $I(S;Y) = H(Y) - H(Y \mid S)$ avec $H(\cdot)$ l'entropie de Shannon [47]. La capacité informationnelle C est la borne supérieure sur la quantité d'information qui peut être transmise correctement via le canal informationnel. Le bruit étant imposé, la capacité est obtenue en ajustant le seul paramètre libre, la distribution de probabilité de l'entrée S. La modélisation de canaux de communication et le calcul de leur capacité informationnelle sont plutôt classiquement destinés aux contextes de télécommunication où les signaux transmis sont des signaux monodimmensionnels. Ici, $S(u,v)$ et

$Y(u,v)$ seront des images, où (u,v) sont les coordonnées spatiales. Nous modélisons la situation d'un objet seul sur un fond en choisissant l'image d'entrée $S(u,v)$ comme binaire. Notre scène est ainsi constituée d'un objet défini par un niveau de gris uniforme I_1 et un fond également uniforme à I_0. La densité de probabilité associée à $S(u,v)$ est $p_S(s) = p_1\delta(s-I_1)+p_0\delta(s-I_0)$ où $p_1 = 1-p_0$ est la fraction de pixels à I_1, c'est-à-dire la surface relative de l'objet dans l'image $S(u,v)$. Le paramètre clé de notre problème est donc p_1 qui représente bien l'échelle à laquelle l'objet est observé dans l'image. Ainsi, la valeur de p_1 qui permet d'obtenir la capacité C d'un canal modélisant un imageur, définit une échelle optimale à laquelle on observe le mieux (d'un point de vue informationnel) l'objet sur le fond. La Fig. 4.2 illustre la chaîne d'acquisition et de traitement des images que nous considérons comme un canal de communication tel qu'on le définit en théorie statistique de l'information [47]. Pour illustration, on choisit, pour des raisons méthodologiques,

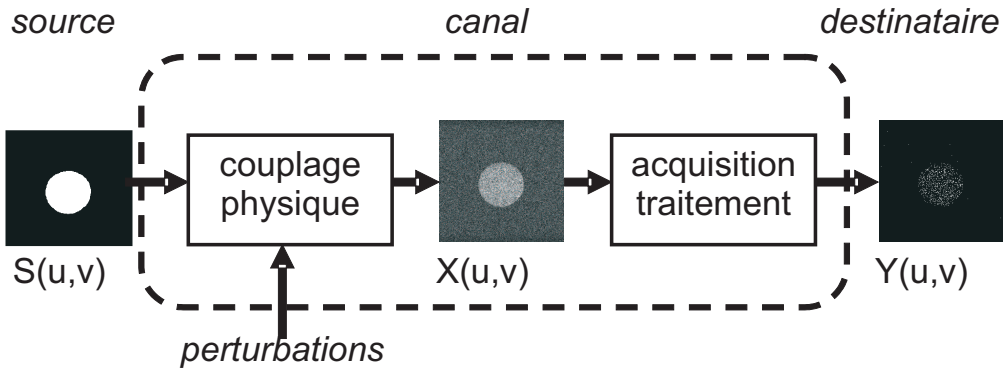

Figure 4.2 : Imagerie vue comme un canal de communication. X(u,v) est une image intermédiaire correspondant à l'image produite par la physique sur le capteur avant acquisition et traitement.

de modéliser un imageur simple où les images en sortie $Y(u,v)$, au niveau du capteur ou bien après traitement, sont binaires $Y(u,v) \in \{0,1\}$. Le canal de communication de la Fig. 4.2 est donc équivalent au canal binaire de la Fig. 4.3. L'information mutuelle entrée–sortie $I(S;Y)$ peut

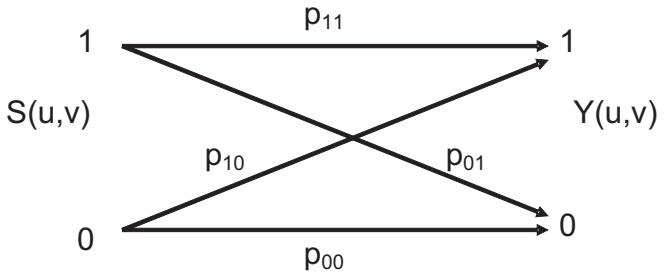

Figure 4.3 : Canal binaire.

être calculée à partir des entropies $H(Y) = h[p_{11}p_1+(1-p_{00})(1-p_1)]+h[(1-p_{11})p_1+p_{00}(1-p_1)]$ avec la fonction $h(u) = -u\log_2(u)$, et $H(Y\,|\,S) = (1-p_1)[h(p_{00})+h(1-p_{00})]+p_1[h(p_{11})+h(1-p_{11})]$ où $p_{ij} = Pr\{Y = i\,|\,S = I_j\}$. La dérivée de $I(S;Y)$ par rapport à l'échelle d'observation p_1 peut ensuite être calculée, et mène à l'échelle optimale d'observation p_1^* qui maximise $I(X;Y)$ et

atteint la capacité informationnelle C du canal binaire modélisant l'imageur. Ainsi, la question d'une échelle optimale d'observation d'un objet sur un fond trouve une solution analytique avec l'expression

$$p_1^* = \frac{ap_{00} - 1}{a(p_{00} + p_{11} - 1)} \ , \tag{4.1}$$

avec

$$a = 1 + \exp\left[\ln(2)\frac{h(p_{00}) + h(1 - p_{00}) - h(p_{11}) - h(1 - p_{11})}{p_{00} + p_{11} - 1}\right] . \tag{4.2}$$

Lorsque l'objet et le fond de la scène à imager présentent le même bruit, c'est-à-dire quand on a $p_{00} = p_{11}$, on obtient d'après l'Éq. (4.1) $p_1^* = 1/2$. L'échelle optimale d'observation est obtenue lorsque le fond représente la même surface que l'objet. Dans cette situation, le sens commun évoqué en introduction fonctionne. On rencontre cette situation en pratique lorsque le couplage signal–bruit est additif en présence par exemple de bruit d'origine thermique sur les capteurs. Le sens commun est mis en défaut à $p_1^* \neq 1/2$, lorsque $p_{00} \neq p_{11}$. Dans ce cas, l'échelle optimale d'observation, quantifiée par l'Éq. (4.1), revient à favoriser la surface relative accordée à l'item (objet ou fond) le moins bruité. On rencontre ces situations avec les bruits non additifs par exemple en imagerie cohérente avec le bruit de speckle ou encore en IRM avec du bruit Ricien qui sont communément [65] modélisés comme des bruits multiplicatifs. La modélisation de ces contextes applicatifs pluridisciplinaires dans le cadre de notre étude est obtenue directement en explicitant le couplage signal–bruit et en introduisant un seuil de binarisation en sortie du canal. Pour illustration, considérons l'image intermédiaire X(u,v) de la Fig. 4.2 comme étant l'image module obtenue lors d'une acquisition en IRM. Le bruit dans l'image module en IRM est usuellement modélisé comme un bruit Ricien de densité de probabilité

$$p_{X|s}(x) = \frac{x}{\sigma_N^2} \exp\left[-\frac{1}{2\sigma_N^2}(x^2 + 2s^2)\right] B_0\left(\frac{\sqrt{2}sx}{\sigma_N^2}\right) \ , \tag{4.3}$$

pour $x \geqslant 0$ et $p_{(X|s)}(x) = 0$ pour $x < 0$ avec $B_0(z) = \int_0^{2\pi} \frac{1}{2\pi} \exp(z\cos\theta)d\theta$. On peut ainsi calculer les probabilités conditionnelles p_{ii} du schéma de la Fig. 4.3 avec

$$p_{11} = 1 - F_{X|S=I_1}(\theta) \ , p_{00} = F_{X|S=I_0}(\theta) \ , \tag{4.4}$$

où $p_{ij} = 1 - p_{ii}$ la fonction de répartition

$$F_{X|S=I_i}(\theta) = \mathcal{Q}_{\chi'^2(\lambda)}\left(\frac{\theta}{\sigma_N}\right) \ , \tag{4.5}$$

avec $\lambda = \frac{2I_i^2}{\sigma_N^2}$ et $p_{ij} = 1 - p_{ii}$ et la fonction spéciale $\mathcal{Q}_{\chi'^2}(\cdot)$ telle que définie dans [92]. Le paramètre σ_N dans l'Éq. (4.5) est l'amplitude efficace du bruit gaussien centré qui intervient au niveau du récepteur, là où se produit l'échantillonnage avant la reconstruction par transformée de Fourier de $X(u, v)$. L'amplitude efficace σ_N du bruit peut être contrôlée par le réglage de la bande passante du récepteur. Plus cette bande passante est petite, plus σ_N est petit comme le montre le graphe de la Fig. 4.4. Sur la Fig. 4.5, on observe l'évolution de l'échelle optimale pour un seuil θ fixé en fonction de l'amplitude efficace σ_N. Suivant le niveau de bruit dans la scène, il faut parfois privilégier la surface accordée à l'objet $p_1^* > 0.5$ ou celle occupée par le fond $p_1^* < 0.5$. Cela montre que le choix d'une échelle d'observation n'est pas un paramètre expérimental sans conséquence d'un point de vue informationnel. Ainsi, une

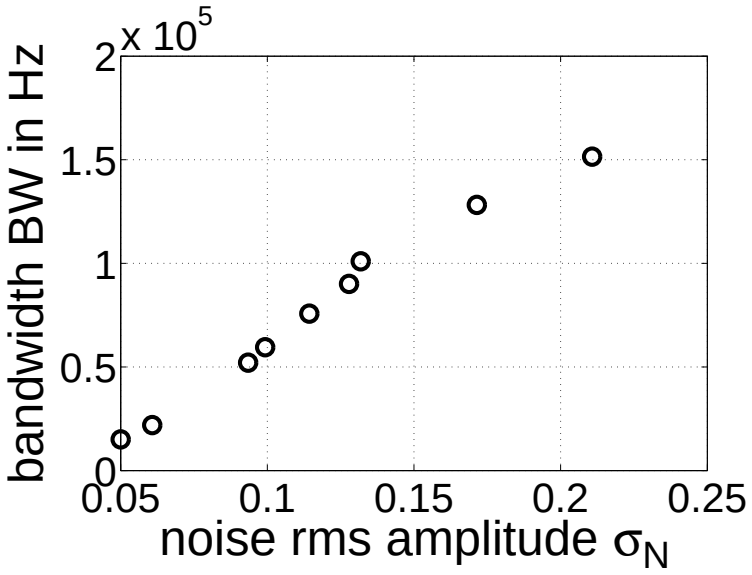

Figure 4.4 : Amplitude efficace du bruit σ_N de l'Éq. (4.3) en fonction de la bande passante de l'antenne réceptrice BW. σ_N est estimé à partir d'images d'IRM réalisées avec la collaboration de Florence FRANCONI (ingénieur de recherche à l'Université d'Angers) sur un imageur Bruker Avance DRX 7 tesla sur une séquence d'écho de spin classique dans un tube vide.

modélisation physique de la scène à imager peut être utilisée pour maximiser la transmission d'information lors du choix du grossissement d'un système imageur.

En imagerie, la question de l'échelle d'observation d'une scène est conventionnellement laissée à l'appréciation de l'expérimentateur qui a seul la charge du choix du grossissement du système imageur. De façon souvent découplée, le traiteur de données récupère les images après acquisition et, à partir de là, cherche à extraire au mieux les informations dans la scène. Nous venons de montrer comment la capacité informationnelle pouvait être utilisée pour appréhender la question expérimentale du choix d'une échelle d'observation. Pour illustration, nous avons pris des exemples simples d'images binaires perturbées par des bruits aux propriétés statistiques typiques de l'IRM. De nombreux développements possibles apparaissent. Je compte les mener à bien dans le cadre de la thèse d'Agnès DELAHAIES. Ainsi, la partie traitement se résumait ici en une simple classification binaire objet/fond. Nous avons montré qu'une expression analytique exacte est possible pour l'échelle optimale d'observation. Il serait toutefois possible à partir du cadre simplifié de ce travail de complexifier le traitement de classification (il suffit alors d'estimer les probabilités de transitions dans le canal), le nombre de classes (il suffit alors d'augmenter le nombre d'entrées et de sorties au canal), ou encore de considérer d'autres types d'imageries en environnement bruité (il suffit alors de reconsidérer la physique au niveau du capteur). Faire varier l'échelle d'observation revient expérimentalement à faire varier le grossissement du système imageur. Aux forts grossissements, il est courant que de nouvelles sources de bruit interviennent liées à des aberrations dues au système imageur (aberration géométrique en imagerie optique, inhomogénéité du champ magnétique en IRM par exemple). Ces bruits liés au grossissement n'ont pas été pris en compte ici et des développements dans cette direction constituent là aussi des perspectives intéressantes. Dans cette petite leçon sur la question d'une échelle optimale d'observation, nous avons examiné de façon conjointe des questions liées à l'acquisition et au traitement des données issues de l'acquisition. C'est une approche originale puisque ces deux

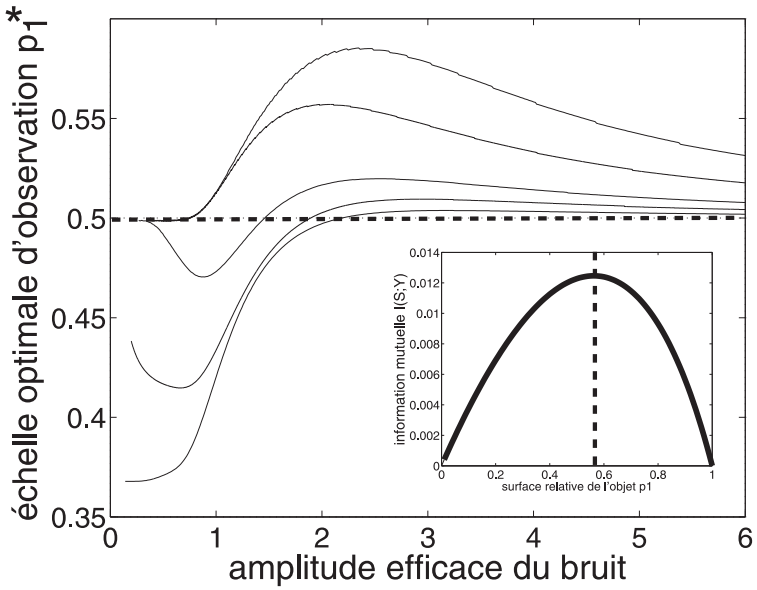

Figure 4.5 : Échelle optimale d'observation en fonction de l'amplitude efficace du bruit gaussien présent au niveau du récepteur de l'antenne d'un IRM. L'image binaire d'entrée S(u,v) porte les niveaux $I_0 = 0$ et différentes valeurs $I_1 = 0.5, 0.75, 1, 2, 4$ en allant de bas en haut. Le seuil de binarisation est fixé $\theta = 1$. En encart, l'information mutuelle entrée-sortie $I(S;Y)$ en fonction de l'échelle d'observation p_1 pour un niveau de bruit gaussien $\sigma_N = 3$ et $I_1 = 4$, $I_0 = 0$ on a $p_1^* = 0.57$.

étapes sont habituellement considérées séparément. D'autres critères informationnels pourraient être proposés sur la question de l'échelle optimale d'observation suivant la finalité du traitement envisagé. On pourrait par exemple utiliser comme dans **[40]** la complexité stochastique minimale [115] en détection ou encore l'information au sens de Fisher [60] pour de l'estimation. Pour les scènes considérées, nous avons supposé des objets simples occupant une surface bien définie. On pourrait également poser la question de l'échelle optimale d'observation sur des scènes comportant des objets aux structures plus complexes avec des propriétés d'invariances en échelle comme des objets "fractals" [67] qui donnent à voir les mêmes structures quelle que soit l'échelle d'observation. En pratique, pour les objets fractals que l'on rencontre dans la nature cette propriété d'invariance d'échelle existe uniquement sur une gamme d'échelle et il serait intéressant de regarder là aussi si une échelle optimale d'observation peut exister pour des tâches définies de traitement de l'information.
Cette conclusion me permet une transition douce vers les études [43, 28, 44] (voir **[28]**) réalisées dans le cadre de la thèse de Julien CHAVEAU où l'on s'intéresse à montrer un point de vue en échelle sur l'organisation des histogrammes multicomposantes comme ceux des images couleurs naturelles.

4.2.2 Analyse fractale en imagerie couleur

En traitement d'images, les histogrammes des valeurs des pixels sont utiles à divers égards [136]. Ils peuvent servir par exemple pour la caractérisation et la correction lors de l'acquisition des images, ou pour des opérations de segmentations, ou encore pour l'indexation d'images dans des bases de données. Pour des images en niveau de gris ou monocomposante, l'histogramme est

une structure monodimensionnelle aisée à visualiser et à manipuler. L'imagerie multicomposante avec les imageries multi-hyperspectrales ou encore en multimodalité est en plein développement. Les histogrammes des images multicomposantes sont par définition des structures de données multidimensionnelles qui peuvent montrer des organisations complexes [94]. Pour des images multicomposantes, une approche usuelle en traitement d'image est de considérer séparémment les histogrammes marginaux de chaque composante. Ceci mène à des traitements simples mais qui peuvent perdre une part importante de l'information contenue dans la dépendance entre les composantes. L'histogramme multidimmensionnel contient davantage d'information mais il est plus compliqué à manipuler et on en connaît finalement peu sur la structure multidimmensionnelle de ces histogrammes à commencer simplement par celles des images couleurs.

Dans les études [43, 28, 44], nous montrons que les histogrammes des images couleurs ont tendance à s'organiser selon des régularités non triviales à travers les échelles de l'espaces colorimétrique naturel RGB. L'identification d'invariants ou de régularités dans des classes données d'images est un résultat utile pour caractériser des images ou pour élaborer des modèles ou encore pour comprendre des processus liés à la vision. Les images naturelles sont connues pour montrer des régularités à travers les échelles dans leur organisation spatiale. Ceci se traduit par un spectre de fréquence spatiale qui évolue selon une loi de puissance en $1/f^{\alpha}$ avec f la fréquence spatiale [22, 58, 135, 134]. De façon équivalente une évolution en loi de puissance sur le spectre de fréquence est associée à une évolution selon une loi de puissance de la fonction de corrélation [134]. Ce type d'invariance en échelle a été rapporté à la présence de structures et de détails spatiaux à toutes les échelles dans les images naturelles avec des objets à de multiples tailles, des bords et des occlusions apparaissant sous différents angles [59, 134, 75]. Des régularités à travers les échelles apparaissent également dans les structures temporelles de séquences d'images vidéo. La dynamique temporelle d'images naturelles montre des évolutions en lois de puissance du spectre temporel de puissance [53]. Des objets de tailles très différentes, apparaissant à différentes profondeurs dans l'image, se déplacent à des vitesses très différentes pour l'observateur ce qui confère des structures invariantes à travers les échelles spatio-temporelles des images. Ces résultats montrent que les images naturelles n'évoluent pas de façon aléatoirement destructurées dans le temps et l'espace. Au contraire, les images dans le temps et l'espace montrent de la corrélation, des structures de la redondance. Et ces corrélations apparaissent auto-similaire ou invariantes à travers les échelles, ou aussi fractales selon le temps et l'espace. Dans les études [43, 28, 44], nous examinons un autres aspect de l'organisation des images naturelles : leur organisation colorimétrique. Et nous montrons dans [43, 28, 44] que dans le domaine colorimétrique, les images couleurs naturelles tendent également à s'organiser d'une façon que l'on peut qualifier de fractale.

Pour ce faire nous avons considéré des images couleurs où chacun des N_{pix} pixels est représenté par un triplet de composantes (R, G, B), chacune de ces composantes prenant une valeur entière dans $[0, Q-1]$ (par exemple $Q = 2^8 = 256$). L'espace colorimétrique tridimensionnel des coordonnées (R, G, B) possède donc Q^3 cases colorimétriques ou couleurs distinctes. Les Figs. 4.6 et 4.7 donnent deux exemples d'images naturelles avec leur histogramme couleur tri-dimensionnel dans le cube colorimétrique RGB. Pour caractériser l'organisation des histogrammes colorimétriques à travers les échelles nous avons testé différentes mesures classiques de l'analyse fractale que nous avons appliquées selon un paramètre d'échelle a :

• La méthode des boîtes (testée dans **[44]**) donne le nombre $N(a)$ de boîtes de taille r nécessaires pour couvrir tous les points P_n de l'histogramme tridimmensionel couleur. Cette mesure caractérise le support de l'histogramme c'est-à-dire la répartition de la palette des couleurs de l'image dans l'espace colorimétrique.

• L'"intégrale de corrélation" (testée dans [28]) fourni le nombre moyen $M(a)$ de voisins situés à l'intérieur d'une sphère de rayon a centré en un point de l'histogramme tri-dimensionnel couleur et totalement contenu dans le cube colorimétrique RGB.

• La mesure de "corrélation de paires" (testée dans [43]) évalue le nombre $C(a)$ de paires de points qui sont séparés par une distance $\leq a$.

Le tracé de $N(a)$, $M(a)$ et $C(a)$, en fonction de a dans un diagramme $\log - \log$ donne une vision de l'organisation en échelle de l'histogramme couleur. La méthode des boîtes caractérise le support de l'histogramme et les mesures de corrélation permettent d'apprécier la façon dont ce support est rempli. Une invariance en échelle est associée à une loi de puissance des mesures $N(a)$, $M(a)$ et $C(a)$. Parmi les comportements invariant en échelle, on qualifie de signature fractale l'existence d'un comportement linéaire de pente non entière sur une certaine gamme d'échelle du diagramme $\log - \log$ selon a. Comme le montre les études [43, 28, 44] et la Fig. 4.8, on observe chez les images couleurs la possibilité d'une signature fractale dans le diagramme $\log - \log$ pour les trois mesures $N(a)$, $M(a)$ et $C(a)$.

Figure 4.6 : Images couleurs RGB de taille 256×256 pixels et $Q = 256$ niveaux.

L'existence de possibles structures fractales dans la distribution des couleurs au sein des images naturelles est un fait nouveau que les résultats préliminaires [43, 44, 28] ont contribué à identifier. D'autres analyses et observations sur de larges banques d'images naturelles seraient nécessaires pour confirmer l'existence de propriétés colorimétriques fractales et pour apprécier leurs conditions d'existences et leurs possibles origines. Des hypothèses pour tenter d'expliquer l'origine de ces organisations fractales peuvent être proposées selon deux directions (possiblement reliées). L'organisation fractale des couleurs peut être reliée aux propriétés des scènes naturelles qui peuvent typiquement contenir de nombreuses structures et des objets de taille et de couleurs variées sous différents angles et différentes conditions d'éclairage. Ces ingrédients peuvent mener à l'existence dans des scènes naturelles, de plusieurs couleurs chacune affectées par de multiples facteurs de "modulation" qui construisent une organisation fractale des couleurs. Selon cette interprétation, la structure fractale de la distribution des couleurs aurait des origines communes avec d'autres propriétés fractales trouvées au niveau de l'organisation spatiale des images na-

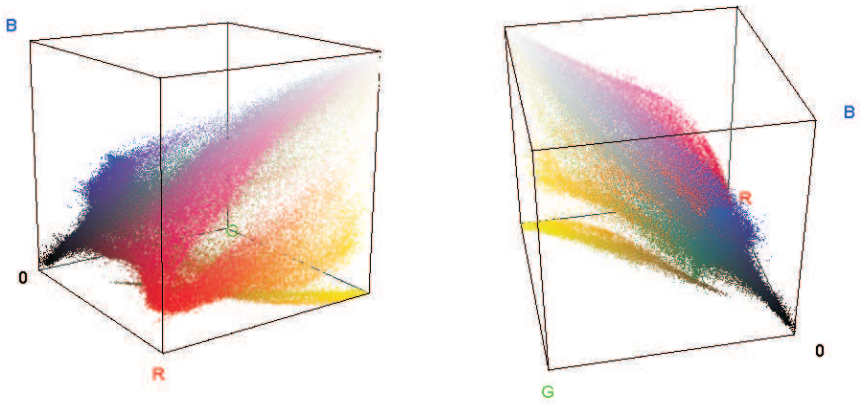

Figure 4.7 : Histogramme tri-dimensionel couleur dans le cube colorimétrique RGB $[0, 255]^3$ pour l'image Flowers de la Fig. 4.6 présenté sous deux angles de vue différents.

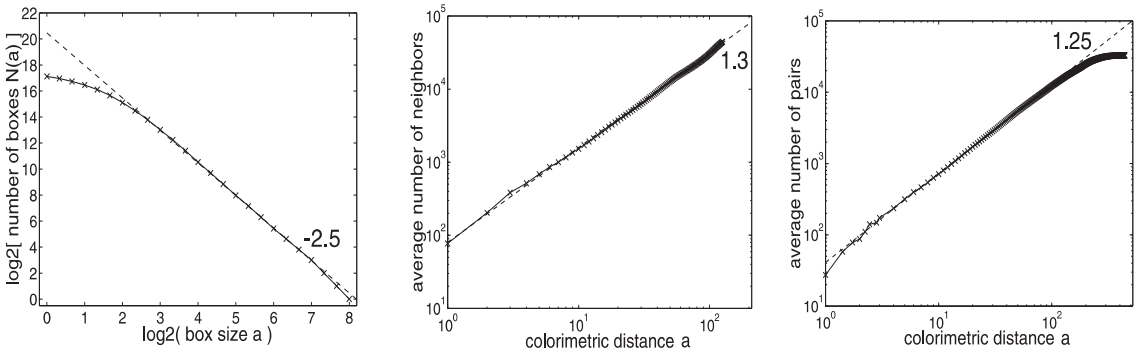

Figure 4.8 : Analyse en échelle de l'organisation de l'histograme couleur de l'image "Flowers" de la Fig. 4.7. *De gauche à droite*: mesures $N(a)$, $M(a)$, $C(a)$. Le nombre est la pente de la droite (en pointillés) ajustée manuellement pour coller aux mesures (en trait plein) sur la gamme d'échelle a la plus grande.

turelles. Dans une autre direction, l'organisation fractale des couleurs dans les scènes naturelles pourrait être reliée aux propriétés de codage de notre système visuel. Étant donné les propriétés statistiques spectrales de la lumière naturelle, le système visuel pourrait avoir évolué dans ses capacités de codage afin de permettre une représentation multiéchelle du spectre visible. Aux grandes échelles colorimétriques, on trouve des domaines très éloignés dans le spectre visible. Aux petites échelles, on a des couleurs qui sont proches comme dans le cas d'ombres portées qui créent autour d'une couleur donnée de subtils dégradés. Il y a aussi des échelles intermédiaires comme par exemple toutes les différences de verts et de marrons qui peuvent exister dans une forêt ou dans un paysage en extérieur ; et encore d'autres échelles. Pour permettre une discrimination efficace de ces multiples échelles, le système visuel pourrait avoir distribué ses capacités de codage sur toute les gammes d'échelle de couleurs contenant de l'information dans la nature. La structure fractale montrée dans [43, 44, 28] pourrait ainsi être une manifestation d'une telle stratégie de codage par le système visuel. Afin d'interroger les possibles origines d'une organisation fractale des couleurs, un moyen serait de considérer des images de synthèse produites par des techniques de rendu de sophistication croissante : une voie que nous explorons à l'occasion de la dernière année de thèse de Julien CHAUVEAU.

4.2.3 Analyse multifractale en imagerie couleur

Nous proposons de compléter notre point de vue sur l'organisation des histogrammes tridimensionnels à travers les échelles au moyen d'une analyse multifractale [56, 139, 149, 138] qui procède comme suit. Le cube colorimétrique $[0, Q-1]^3$ est recouvert par des boîtes cubiques jointives de côté a. Chacune de ces boîtes, d'indice i, reçoit une mesure $P_i \in [0,1]$ égale au nombre de pixels de l'histogramme contenus dans la boîte divisé par N_{pix}. Avec un paramètre $q \in \mathbb{R}$, on définit une fonction de partition

$$Z(q,a) = \sum_i P_i^q \ , \tag{4.6}$$

la somme sur i s'étendant à l'ensemble des boîtes de côté a (non vides) nécessaires pour recouvrir l'histogramme tridimensionnel. Pour une valeur fixée de l'exposant q, on répète l'évaluation de $Z(q,a)$ en variant le côté a des boîtes. L'exposant q joue un rôle de zoom sur la mesure P_i à l'échelle a, en distribuant différemment l'influence sur $Z(q,a)$ des diverses valeurs de la mesure. Ainsi, les $q > 1$ renforcent, en relatif, l'influence dans $Z(q,a)$ des fortes valeurs de P_i, alors que les $q < 1$ renforcent les faibles P_i. Tant que $q > 0$, la relation d'ordre des P_i est préservée ; les P_i forts contribuent davantage à $Z(q,a)$ que les P_i faibles, avec toutefois une pondération relative selon la valeur de $q > 0$. Si l'on passe aux $q < 0$, la relation d'ordre des P_i est renversée ; les P_i faibles contribuent davantage à $Z(q,a)$ que les P_i forts, avec une pondération relative selon la valeur de $q < 0$. Ainsi, selon l'exposant q, la fonction de partition $Z(q,a)$ est différemment influencée par la mesure P_i, offrant un point de vue multiple sur cette mesure.
Des propriétés remarquables à travers les échelles sont alors identifiées lorsque la fonction de partition $Z(q,a)$ présente une évolution en loi de puissance [139, 149] de la forme

$$Z(q,a) \sim a^{\tau(q)} \ , \tag{4.7}$$

avec l'exposant $\tau(q)$, appelé exposant de masse, une fonction du paramètre q qui offre une caractérisation condensée des propriétés multiéchelles de la structure analysée. Un comportement de référence (trivial) est la situation où les pixels de l'histogramme tridimensionnel se répartissent de façon uniforme dans le cube colorimétrique $[0, Q-1]^3$. Dans ce cas, la mesure de chaque boîte cubique est proportionnelle à son volume, c'est-à-dire $P_i \sim a^3$, et le nombre $N(a)$ de boîtes de côté a nécessaires pour recouvrir l'histogramme donne $N(a) \sim a^{-3}$. La fonction de partition de l'Éq. (4.6) donne alors $Z(q,a) \sim a^{3q-3}$, conduisant dans l'Éq. (4.7) à

$$\tau(q) = 3(q-1) \ . \tag{4.8}$$

Un $\tau(q)$ linéaire à l'instar de l'Éq. (4.7) est un comportement monofractal. L'existence de la loi de puissance de l'Éq. (4.7) associée à un exposant $\tau(q)$ s'écartant d'une loi linéaire comme l'Éq. (4.8) caractérise des organisations multiéchelles élaborées présentant un caractère multifractal. Notons que, comme conséquence de la normalisation à 1 de la mesure P_i, on a dans l'Éq. (4.6) l'identité $Z(q=1,a) = 1$ pour tout a ; la fonction $\tau(q)$ de l'Éq. (4.7) vérifie donc toujours $\tau(1) = 0$.
On définit une dimension fractale généralisée par [71]

$$D(q) = \frac{\tau(q)}{q-1} \ , \tag{4.9}$$

qui se réduit donc à la constante $D = 3$ dans le cas de l'histogramme tridimensionnel uniforme. La dimension généralisée $D(q)$ offre une autre caractérisation condensée des propriétés multiéchelles de la structure analysée. Un cas particulier intéressant survient pour $q = 0$, quand

$Z(q=0,a)$ de l'Éq. (4.6) se réduit à compter le nombre $N(a)$ de boîtes recouvrantes à l'échelle a. Alors l'Éq. (4.9) donne $D(0) = -\tau(0)$, et via l'Éq. (4.7) ce nombre de boîtes recouvrantes vérifie $N(a) \sim a^{-D(0)}$. La dimension $D(0)$ représente donc la dimension fractale de comptage de boîtes, ou dimension de Hausdorff, du support de l'histogramme tridimensionnel. Cette dimension vaut $D(0) = 3$ pour le support de l'histogramme tridimensionnel uniforme ; elle pourra être inférieure à 3 pour des histogrammes lacunaires présentant des zones vides de pixels sur toute une gamme d'échelles. D'autres valeurs de q sont associées à des dimensions fractales particulières possédant une interprétation concrète simple [71]. Ainsi $D(q=1)$ est reliée à la dimension informationnelle et $D(q=2)$ à la dimension de corrélation de la structure analysée. La dimension de corrélation pour caractériser les histogrammes tridimensionnels d'images couleur a été étudiée dans [43, 44, 28] et nous considérons maintenant l'ensemble du spectre de dimension fractale généralisée $D(q)$ qui représente une série en principe infinie de dimensions fractales [71], et qui constitue une caractérisation poussée de l'organisation à travers les échelles.

• Cascade multiplicative

Pour comparaison, il est possible de distribuer les pixels de l'histogramme couleur tridimensionnel selon une mesure synthétique multifractale, au moyen du procédé suivant [56]. Le cube colorimétrique $[0, Q-1]^3$ se voit assigné une mesure initiale uniforme de 1. En bissectant également selon chacun des trois axes de coordonnées, le cube colorimétrique est découpé en huit sous-cubes égaux. Chacun de ces huit sous-cubes voit sa mesure initiale (1/8) multipliée par un facteur de pondération $m_i \in]0,1[$ avec la normalisation de la pondération $\sum_{i=1}^{8} m_i = 1$. On itère le processus, en découpant en huit chacun des sous-cubes, et en redistribuant la mesure initiale de chaque sous-cube via la pondération par les m_i fixés. Le processus ainsi itéré constitue une cascade multiplicative qui converge vers une mesure multifractale sur le cube colorimétrique $[0, Q-1]^3$, dont les caractéristiques sont déterminées par les facteurs de pondération m_i. On a en particulier l'exposant de masse $\tau(q)$ de l'Éq. (4.7) qui est

$$\tau(q) = -\log_2 \left(\sum_{i=1}^{8} m_i^q \right) , \tag{4.10}$$

et la dimension fractale généralisée $D(q)$ découle de l'Éq. (4.9). Notamment, on a toujours pour ce type de cascade multiplicative $D(q=0) = 3$, en cohérence avec le support de la mesure multifractale qui est le cube colorimétrique tout entier, donc un support de dimension 3.

• Analyse des images

Nous présentons maintenant la fonction de partition $Z(q,a)$ de l'Éq. (4.6) évaluée numériquement sur trois types d'images couleur de taille $N_{\text{tot}} = 512 \times 512 = 2^{18}$ pixels avec $Q = 256 = 2^8$ niveaux pour chacune des trois composantes R, G et B. Le premier type est constitué par des images aléatoires où, en chaque pixel, les trois composantes R, G et B sont tirées au hasard uniformément sur $[0, Q-1 = 255]$. Le deuxième type correspond à des images où les pixels se répartissent dans le cube colorimétrique $[0, 255]^3$ conformément à la mesure multifractale résultant de la cascade multiplicative. Le troisième type contient des images naturelles standard, typiquement comme montré sur la Fig. 4.6.

Sur les graphes log–log de la fonction de partition $Z(q,a)$ des Figs. 4.9–4.12, les comportements en loi de puissance selon l'Éq. (4.7) sont identifiés par des portions de droites. Des droites caractéristiques de lois de puissance apparaîssent nettement sur les Figs. 4.9–4.12, avec toutefois de façon fréquente un comportement dit de "crossover", c'est-à-dire, pour une échelle identifiée, un changement de pente dans la loi de puissance [1, 95, 106]. Ces observations sur les Figs. 4.9–

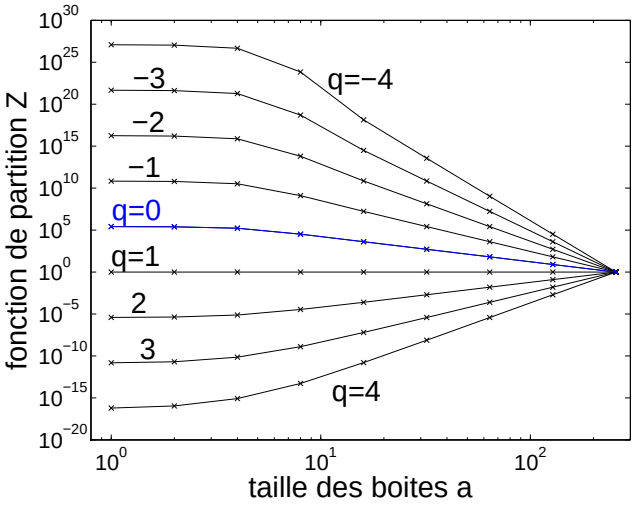

Figure 4.9 : Fonction de partition $Z(q, a)$ de l'Éq. (4.6) en fonction du côté a des boîtes cubiques, pour une image aléatoire uniforme.

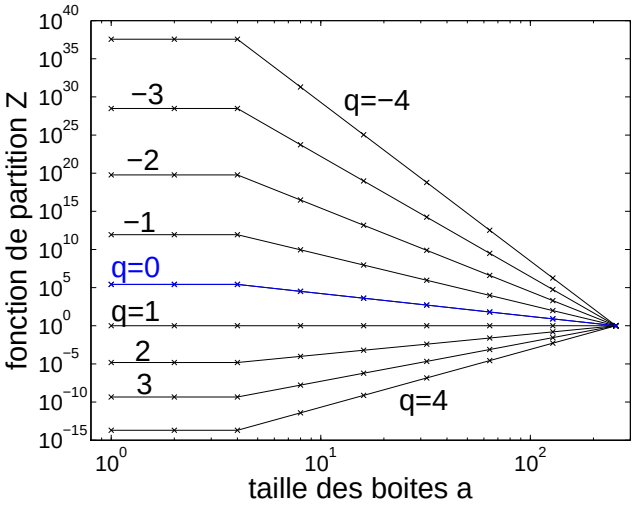

Figure 4.10 : Fonction de partition $Z(q, a)$ de l'Éq. (4.6) en fonction du côté a des boîtes cubiques, pour une image cascade multiplicative.

4.12 peuvent s'interpréter comme suit, en se rappelant que les graphes de $Z(q, a)$ caractérisent la structure de l'histogramme couleur de l'image, c'est-à-dire la façon dont les pixels de l'image prennent leurs couleurs dans le cube colorimétrique, en fonction de l'échelle, selon les couleurs proches (petites échelles) jusqu'aux couleurs très distinctes (grandes échelles).
Pour l'image aléatoire de la Fig. 4.9, $N_{\text{tot}} = 2^{18}$ pixels prennent leurs couleurs uniformément au hasard dans le cube colorimérique $[0, Q-1]^3$. Avec $Q = 256 = 2^8$, le cube colorimétrique comporte 2^{24} couleurs distinctes ou cellules élémentaires d'étendue $1 \times 1 \times 1$. La répartition au hasard des $N_{\text{tot}} = 2^{18}$ pixels dans ces 2^{24} cellules colorimétriques donne une densité moyenne de $1/2^6$ pixel par cellule. Ainsi, dans le voisinage d'un pixel donné de l'histogramme couleur, en dessous d'une distance linéaire de 2^2 on ne trouve en moyenne aucun autre pixel. Le nombre de pixels ne commence à croître qu'au delà d'un voisinage d'extension linéaire 2^2. Autrement dit, dans le proche voisinage d'une couleur présente dans l'image aléatoire, il n'y a pas d'autre

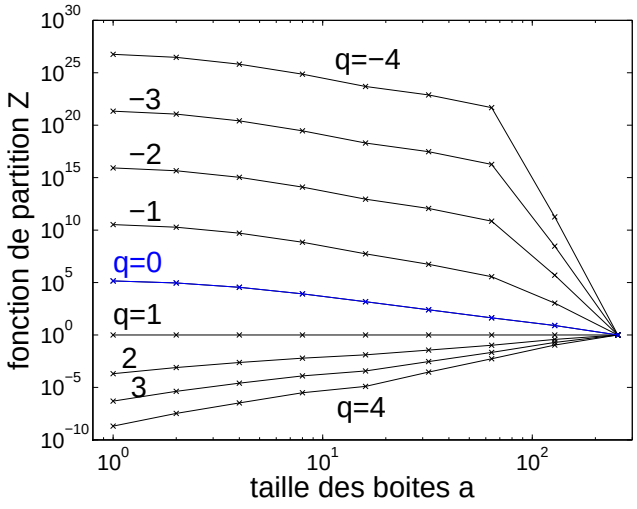

Figure 4.11 : Fonction de partition $Z(q, a)$ de l'Éq. (4.6) en fonction du côté a des boîtes cubiques, pour l'image "Flowers" de la Fig. 4.6.

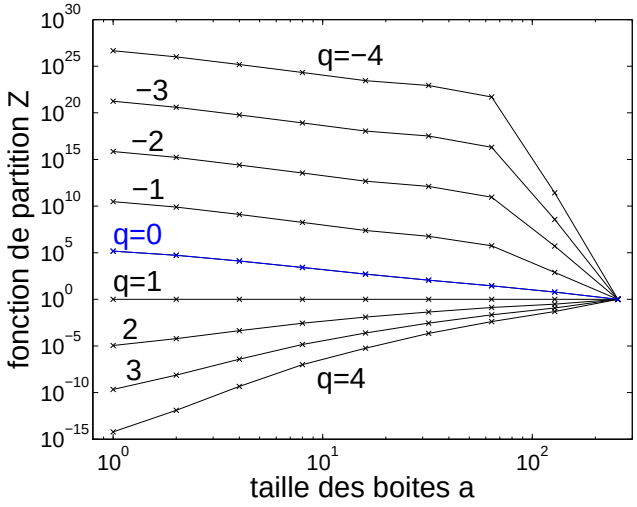

Figure 4.12 : Fonction de partition $Z(q, a)$ de l'Éq. (4.6) en fonction du côté a des boîtes cubiques, pour l'image "Lena" de la Fig. 4.6.

couleur employée dans l'image, il faut accéder à des couleurs suffisamment distantes pour les trouver représentées dans l'image. C'est une caractérisation de la structure colorimétrique de l'image. Ces propriétés sont manifestées par le crossover dans $Z(q, a)$ autour de l'échelle $a = 2^2$ sur la Fig. 4.9. Il faut atteindre des échelles plus grandes que $a = 2^2$ pour que le compte des pixels augmente dans l'histogramme ; en deçà de cette échelle $a = 2^2$ le compte ne varie pas et $Z(q, a)$ reste constant. Au delà du crossover, la variation de $Z(q, a)$ sur la Fig. 4.9 se produit selon la pente $\tau(q) = 3(q-1)$ de l'Éq. (4.8), comme montré sur la Fig. 4.13. Ceci caractérise une distribution uniforme de la répartition des couleurs dans l'histogramme au delà de l'échelle de crossover $a = 2^2$. Conformément, la dimension fractale généralisée $D(q)$ est la constante $D = 3$, comme montré sur la Fig. 4.14.
Pour l'image de la Fig. 4.10 associée à la cascade multiplicative, un crossover comparable existe à l'échelle $a = 2^2$. La raison en est similaire. La cascade multiplicative est itérée jusqu'à garnir

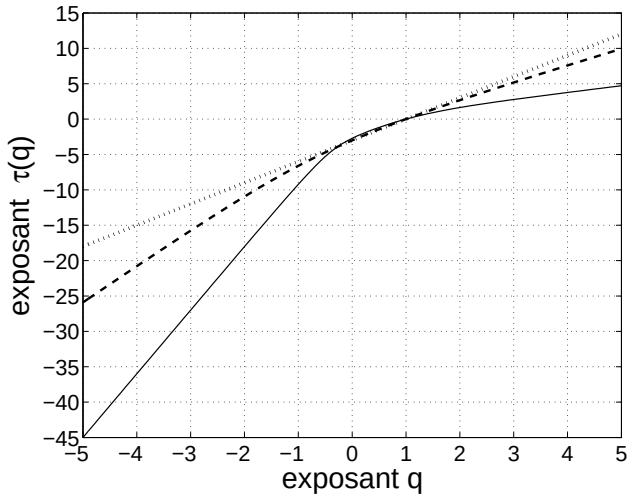

Figure 4.13 : Exposant de masse $\tau(q)$ de l'Éq. (4.7) en fonction de l'exposant q appliqué à la mesure. Trait pointillé : image uniforme coïncidant avec la prévision théorique de l'Éq. (4.8). Tirets : image cascade multiplicative coïncidant avec la prévision théorique de l'Éq. (4.10). Trait plein image "Flowers" de la Fig. 4.6.

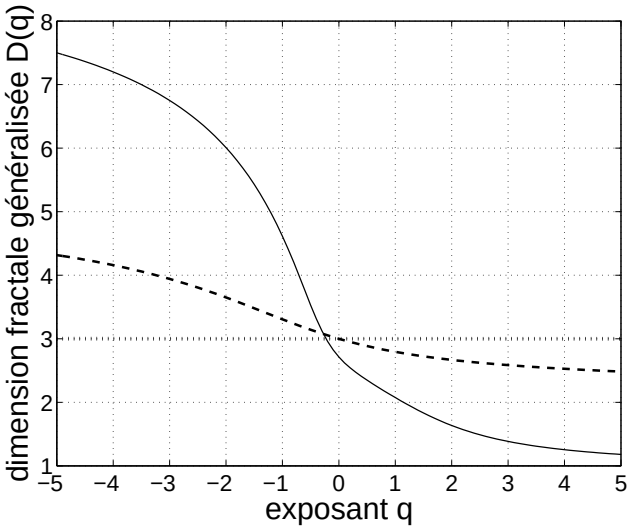

Figure 4.14 : Dimension fractale généralisée $D(q)$ de l'Éq. (4.9) en fonction de l'exposant q appliqué à la mesure. Trait pointillé : image uniforme coïncidant avec la prévision théorique $D(q) = 3, \forall q$. Tirets : image cascade multiplicative. Trait plein image "Flowers" de la Fig. 4.6.

2^{18} sous-cubes du cube colorimétrique initial $[0, 255]^3$, correspondant aux $N_{\text{tot}} = 2^{18}$ pixels des images considérées. L'échelle linéaire $a = 2^2$ est donc là aussi une échelle de transition. Sous cette échelle de crossover, il n'y a plus de variations des populations de pixels ni donc de $Z(q, a)$; au dessus du crossover $a = 2^2$, sur la Fig. 4.10, $Z(a, q)$ varie en loi de puissance selon la pente $\tau(q)$ montrée sur la Fig. 4.13. La dimension fractale généralisée $D(q)$ correspondante est présentée sur la Fig. 4.14. On observe avec la cascade multiplicative pour l'histogramme couleur, un comportement bien différent de l'histogramme uniforme de la Fig. 4.9. Sur la Fig. 4.10 pour la cascade, $Z(q, a)$ au dessus du crossover varie selon un pente $\tau(q)$ bien différente de celle de

l'histogramme uniforme. La Fig. 4.13 montre ainsi un $\tau(q)$ non linéaire pour la cascade. C'est la marque de la nature multifractale de l'histogramme de la cascade de la Fig. 4.10. Pour cet histogramme, il n'existe pas d'échelle où la mesure s'uniformise. Au contraire, à toutes les échelles, la mesure ne cesse de varier de façon significative dans l'espace colorimétrique, avec toutefois une forme d'autosimilarité en échelle des variations existantes. C'est ce que manifeste l'existence des loi de puissance pour $Z(q,a)$, avec des pentes $\tau(q)$ différant significativement des pentes issues de l'histogramme uniforme comme l'indique la Fig. 4.13.

Notons que sur les Figs. 4.13 et 4.14, les exposants de masse $\tau(q)$ et dimensions fractales généralisées $D(q)$ qui sont évalués numériquement sur des histogrammes tridimensionnels, coïncident exactement avec les prévisions théoriques attendues des Éqs. (4.8)–(4.10), pour l'image uniforme et pour l'image associée à la cascade multiplicative multifractale. Ceci constitue une validation, sur des situations de référence, de la procédure d'évaluation numérique.

Pour les images couleur naturelles des Figs. 4.11–4.12, une interprétation peut être proposée au moyen des comportements de référence précédents. Des lois de puissance apparaissent également sur les Figs. 4.11–4.12 pour les images naturelles. Et, pour les q négatifs, un crossover émerge graduellement pour les q progressant vers $-\infty$. Le crossover est observé cette fois à une échelle plus élevée $a = 2^6$. Ce crossover repère une transition dans la répartition des pixels de l'histogramme couleur. Aux grandes échelles $a \geq 2^6$, on caractérise les couleurs largement distinctes de l'image, leurs poids relatifs et la façon dont elles se distribuent dans l'espace colorimétrique. Aux petites échelles $a < 2^6$, on caractérise les couleurs proches de l'image, c'est-à-dire des variations fines ou nuances de couleurs. On note que, contrairement aux Figs. 4.9–4.10, sous le crossover $a = 2^6$ des Figs. 4.11–4.12 la fonction de partition $Z(q,a)$ continue de varier. Ceci révèle que dans les images naturelles, aux faibles distances d'une couleur peuplée dans l'histogramme, il existe en général toujours d'autres couleurs représentées dans l'image, ceci jusqu'aux échelles les plus fines de l'espace colorimétrique. C'est une caractéristique des images naturelles, une grande richesse de nuances de couleurs, manifestée par les graphes de $Z(q,a)$. D'une façon schématique, dans les graphes des Figs. 4.11–4.12, au-delà du crossover on caractérise les couleurs largement distinctes, en-deçà on caractérise les nuances de couleurs. Les répartitions de ces couleurs présentent une forme d'autosimilarité à travers les échelles, traduite par les lois de puissance, mais avec des exposants (des pentes) distincts de part et d'autre du crossover. Il apparaît donc que les couleurs basiques et les nuances se répartissent différemment dans l'espace colorimétrique, quoique toutes deux de façon autosimilaire. Par ailleurs, on peut vérifier que si l'on réduit les images couleur RGB comme celles de la Fig. 4.6 en images indexées vers une table de couleurs contenant uniquement les couleurs dominantes, il apparaît qu'aux petites échelles les graphes de $Z(q,a)$ cessent de varier, et deviennent constants comme sur les Figs. 4.9–4.10 : on a perdu les nuances en ne gardant que les couleurs dominantes. On accède ainsi, par les graphes de $Z(q,a)$ comme ceux des Figs. 4.11–4.12, à une caractérisation quantitative de l'organisation colorimétrique, qui apparaît riche pour les images naturelles.

Pour les images couleur naturelles, la Fig. 4.13 présente les pentes $\tau(q)$, avec pour les $q < 0$ les $\tau(q)$ évaluées aux grandes échelles au delà du crossover, pour comparaison avec les conditions des Figs. 4.9–4.10. La dimension fractale généralisée $D(q)$ correspondante est montrée sur la Fig. 4.14. Les caractérisations condensées offertes par les Figs. 4.13 et 4.14 révèlent pour l'organisation colorimétrique des images naturelles un caractère très différent de l'image aléatoire uniforme, voire même de l'image multifractale de la cascade multiplicative. Notamment, l'exposant de masse $\tau(q)$ de la Fig. 4.13 présente un aspect non linéaire plus prononcé que la cascade multifractale. Également, la dimension fractale généralisée $D(q)$ sur la Fig. 4.14, prend des valeurs dans un domaine plus large pour l'image naturelle que pour l'image de la cascade multiplicative et a fortiori que pour l'image uniforme. Ceci qui traduit une plus grande

complexité colorimétrique des images naturelles au vu de l'analyse multifractale. De plus, on observe sur la Fig. 4.14 en $q = 0$ une dimension $D(q = 0) = 3$ à la fois pour l'image uniforme et pour l'image de la cascade multiplicative. Ceci exprime que la dimension du support de l'histogramme couleur de ces deux types d'images est 3, ce qui est attendu de par leur constitution homogène sur l'ensemble du cube colorimétrique, même pour l'image multifractale. Par contre, l'image naturelle "Flowers" sur la Fig. 4.14 possède $D(q = 0) = 2.7$; et pour l'image "Lena" de la Fig. 4.6 on trouve $D(q = 0) = 2.4$. Ceci exprime que la dimension du support de l'histogramme des images naturelles est non entière, inférieure à 3. Il s'agit d'une dimension fractale traduisant le caractère lacunaire du support de l'histogramme tridimensionnel, avec des vides de toute une gamme de tailles ou d'échelles ne contenant aucune couleur employée dans l'image, comme illustré sur la Fig. 4.7. Le support de l'histogramme constitue la palette des couleurs employées dans l'image, indépendamment des populations de pixels occupant ces couleurs. Ce support présente un caractère fractal pour les images naturelles, au vu de la dimension généralisée $D(q = 0)$ qui est non entière. Les autres caractéristiques, à $q \neq 0$, elles, sont sensibles à l'influence des populations de pixels dans l'histogramme.

• **Petites et grandes échelles** Nous complétons sur les Figs. 4.15–4.16 avec les exposants de masse $\tau(q)$ et les dimensions fractales généralisées $D(q)$ évalués également aux petites échelles à partir des graphes de $Z(q, a)$ de la Fig. 4.11. Pour les exposants $q \geq 0$, les valeurs de $\tau(q)$ et $D(q)$ ne diffèrent pas significativement lorsqu'évaluées aux petites ou aux grandes échelles. On a un comportement homogène à travers les échelles, avec une loi de puissance régulière pour $Z(q, a)$ sans crossover. Par contre, pour les exposants $q < 0$, on voit sur les Figs. 4.15–4.16 les valeurs de $\tau(q)$ et $D(q)$ s'écarter et devenir distinctes lorsqu'évaluées aux petites ou aux grandes échelles. Il est encore difficile d'obtenir une interprétation complète assurée sur l'origine de ce comportement aux $q < 0$ donnant naissance au crossover. Une raison en est qu'aux $q < 0$ ce sont les plus petites valeurs de la mesure à travers l'histogramme qui tendent à dominer la fonction de partition $Z(q, a)$ de l'Éq. (4.6), et que donc l'influence d'un bruit de mesure peut ici devenir significative. Toutefois, les valeurs les plus communément interprétables des paramètres multifractals comme la dimension généralisée $D(q)$ sont habituellement associées aux $q \geq 0$. On a ainsi $D(0)$ qui donne la dimension fractale du support de l'histogramme, $D(1)$ qui constitue sa dimension d'information, et $D(2)$ est liée à sa dimension de corrélation. Les paramètres $\tau(q)$ et $D(q)$ issus de l'analyse multifractale contiennent donc des caractérisations riches de l'histogramme tridimensionnel et donc de l'organisation colorimétrique des images à travers les échelles.
Notons que les observations rapportées ici au sujet des images de la Fig. 4.6 sont typiques des résultats observés lors de l'analyse multifractale que nous avons réalisée sur de nombreuses images couleur naturelles. En particulier, l'allure des graphes de $Z(q, a)$ comme sur les Figs. 4.11–4.12, avec un crossover apparaissant pour les $q < 0$ uniquement, est retrouvée de façon quasi systématique sur les nombreuses images couleur naturelles que nous avons testées. Les graphes de $Z(q, a)$ des Figs. 4.11–4.12 sont en cela typiques, ainsi que les formes d'évolutions de $\tau(q)$ et $D(q)$ des Figs. 4.15–4.16. Au delà des formes similaires, ce sont les valeurs numériques précises de $\tau(q)$ et $D(q)$ qui vont différer d'une image à l'autre et être spécifiques. Ainsi par exemple pour l'image "Flowers" de la Fig. 4.6 on a la dimension fractale du support $D(q = 0) = 2.7$, la dimension d'information $D(q = 1) = 2.1$, et reliée à la dimension de corrélation $D(q = 2) = 1.6$; alors que pour l'image "Lena" il vient ici $D(q = 0) = 2.4$, $D(q = 1) = 1.8$ et $D(q = 2) = 1.5$.

• **Discussion**
Les approches multiéchelles offrent des moyens pouvant contribuer à la caractérisation de struc-

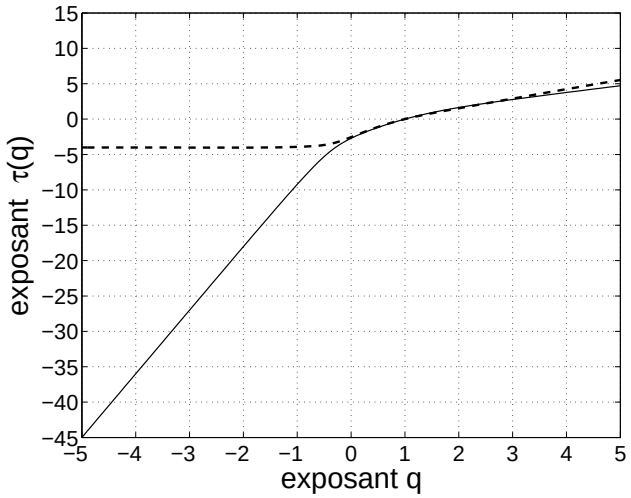

Figure 4.15 : Exposant de masse $\tau(q)$ de l'Éq. (4.7) en fonction de l'exposant q pour l'image "Flowers" des Figs. 4.6 et 4.11. Trait plein : aux grandes échelles $a \in [2^6, 2^8]$. Tirets : aux petites échelles $a \in [1, 2^6]$.

tures complexes comme les images naturelles. Dans cette direction, nous avons réalisé ici une analyse multifractale des histogrammes tridimensionnels issus d'images numériques couleur. Les résultats gardent un caractère préliminaire. Ils doivent être étendus à de plus grandes séries d'images, afin d'interpréter parfaitement leur signification et ce qu'ils révèles sur l'organisation colorimétrique des images naturelles. Des extensions peuvent également être réalisées sur des images multicomposantes présentant plus de trois composantes.

Soulignons que les analyses multifractales développées ici ne nécessitent pas d'hypothèse a priori sur la structure des données auxquelles elles sont appliquées. En particulier, les fonctions de partition $Z(q, a)$ comme sur les Figs. 4.9–4.12 peuvent toujours être calculées. On est ensuite en mesure de juger de l'existence de comportements en loi de puissance selon l'Éq. (4.7), ainsi que les domaines d'échelle sur lesquels de telles lois peuvent exister. On obtient ainsi déjà un point de vue sur les propriétés en échelle des données analysées. Si l'on observe des lois de puissance dans $Z(q, a)$ sur des domaines d'échelle significatifs, ceci permet d'extraire les pentes $\tau(q)$ dans l'Éq. (4.7), puis la dimension fractale généralisée $D(q)$ via l'Éq. (4.9). On a ainsi avec $\tau(q)$ et $D(q)$ une caractérisation condensée de propriétés en échelle de l'histogramme tridimensionnel (ou multidimensionnel). Les graphes de $\tau(q)$ et $D(q)$ reflètent l'organisation colorimétrique des images à travers les échelles. Ils peuvent ainsi servir différentes finalités du traitement des images.

Il serait possible de pousser plus loin une analyse multifractale, moyennant cette fois des hypothèses spécifiques à faire sur les données. On suppose que la mesure locale P_i à l'échelle a utilisée dans l'Éq. (4.6) peut s'exprimer comme $P_i \sim a^\alpha$, où α définit un exposant de singularité local ou encore exposant de Hölder. On suppose de plus que, à l'échelle a, le nombre de points de données où l'exposant de Hölder possède une valeur α spécifiée, peut s'exprimer comme $N(\alpha, a) \sim a^{-f(\alpha)}$; et en faisant ainsi on met en jeu $f(\alpha)$ qui représente la dimension fractale de l'ensemble des points d'exposant de Hölder valant α, ou encore spectre multifractal. Le formalisme mathématique multifractal [56, 149, 138] permet alors d'établir que, dans des conditions bien spécifiques, l'exposant de masse $\tau(q)$ que nous avons évalué, peut donner accès au spectre multifractal $f(\alpha)$. Ceci est possible dans des conditions bien spécifiques, qui ne sont pas forcément garanties chez tout jeu de données présentant des structurations multiéchelles

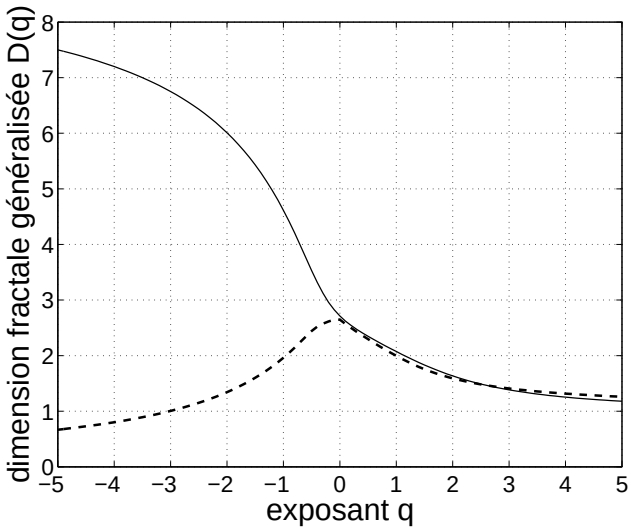

Figure 4.16 : Dimension fractale généralisée $D(q)$ de l'Éq. (4.9) en fonction de l'exposant q pour l'image "Flowers" des Figs. 4.6 et 4.11. Trait plein : aux grandes échelles $a \in [2^6, 2^8]$. Tirets : aux petites échelles $a \in [1, 2^6]$.

complexes. Notamment, il est nécessaire pour l'application de ce formalisme mathématique multifractal, que les hypothèses faites plus haut et qui mettent en jeu α et $f(\alpha)$, soient vérifiées jusqu'aux plus petites échelles $a \to 0$. Cette condition mathématique, exploitée pour relier $f(\alpha)$ et $\tau(q)$, pose notamment une difficulté d'application pratique, car les échelles $a \to 0$ ne sont pas physiquement accessibles à la mesure. Par ailleurs, le formalisme mathématique multifractal permet de relier $f(\alpha)$ et $\tau(q)$ lorsque ces deux fonctions sont convexes ($\cap$), se trouvant liées par une transformation de Legendre. Toutefois en pratique, ces deux fonctions $\tau(q)$ et $f(\alpha)$, lorsqu'elles peuvent être définies, ne sont pas nécessairement toujours convexes, pour un jeu de données empiriques présentant des structurations multiéchelles complexes. Il semble que ce soit la situation des histogrammes tridimensionnels des images couleur naturelles étudiés ici. Pour ces raisons, il semble pour l'instant malaisé pour les histogrammes tridimensionnels couleur, de pousser l'analyse multifractale jusqu'à définir un spectre multifractal $f(\alpha)$ et de chercher à y accéder par l'observation de la fonction $\tau(q)$, via le formalisme multifractal standard. Il semble que les histogrammes tridimensionnels couleur aient une structure multiéchelle plus complexe, allant au-delà des hypothèses primitives où le formalisme multifractal permet d'accéder simplement à un spectre $f(\alpha)$ à partir de l'exposant $\tau(q)$. Il est donc approprié dans l'état actuel des observations, de limiter l'analyse multifractale à l'évaluation des fonctions $\tau(q)$ et $D(q)$ comme nous l'avons fait ici, les hypothèses permettant de pousser jusqu'à un spectre multifractal $f(\alpha)$ n'étant pas positivement établies. Comme nous l'avons dit, l'évaluation des fonctions $\tau(q)$ et $D(q)$ ne nécessite pas d'hypothèses a priori sur les données. À elles seules, elles apportent une contribution utile dans l'analyse et la caractérisation multiéchelle de nombreuses données empiriques complexes, comme cela a été illustré dans bien des contextes jusque par les études les plus récentes [90].

4.3 Applications aux sciences du vivant

Dans mes études sur la résonance stochastique ou l'analyse en échelle, la démarche de recherche est celle d'un paradigme que l'on inventorie ou que l'on explore. La dimension applicative vient en quelque sorte en second lieu : soit comme une justification à considérer tel ou tel dispositif physique dans le cadre du paradigme soit comme une perspective applicative à envisager une fois que le paradigme (effet de bruit utile ou comportement non trivial à travers les échelles) a été établi. Une façon d'enrichir cette démarche de recherche consisterait à partir de problématiques applicatives physiques pour développer ou tester de nouveaux outils de traitement de l'information. Les sciences du vivant actuellement en plein essor constituent un domaine privilégié d'application pour la physique et les sciences de l'information. La compréhension des mécanismes de développement, de régulation ou de dérégulation des organismes vivants posent des questions fondamentales qui peuvent tirer profit des nouvelles méthodes de mesure, des outils de caractérisation ou de modélisation. Ces questions rencontrent également des enjeux sociétaux urgents liés à la santé et l'environnement qui les élèvent au rang de priorités scientifiques nationales. Je développe une partie croissante de mon activité en direction de ces domaines depuis 2007.

4.3.1 Microcirculation sanguine et fluctuations des signaux laser Doppler

Le traitement des signaux cardiovasculaires est une thématique d'intérêt pour la recherche et les applications cliniques. L'électrocardiogramme (ECG) et les signaux qui en découlent comme le signal d'intervalle R-R à partir duquel on calcule le taux de variabilité du cœur HRV (pour heart rate variability) fournissent des informations sur l'état physiologique du cœur qui peuvent aider dans le diagnostic et l'anticipation de problèmes cardiaques. Ces signaux (ECG, interval R-R, HRV) donnent un point de vue sur le système cardiovasculaire central. Une analyse d'un point de vue du système périphérique est également utile. Le système cardiovasculaire périphérique peut être étudié de façon non invasive au moyen de différentes techniques comme la thermographie, la photopléthysmographie, la capillaroscopie, le suivi d'isotope ou encore la fluxmétrie laser Doppler (LDF). Depuis 2007, je participe au sein de l'équipe Signal-Image du LISA à une collaboration avec des médecins du CHU visant à l'utilisation de cette technique LDF pour l'étude de la microcirculation. Mon engagement dans ce travail se positionne actuellement à la marge du reste de mon activité de recherche. Ma contribution personnelle se situe pour l'instant au sein de l'équipe dirigée par Anne HUMEAU (professeure au Laboratoire LISA) au niveau du mode de questionnement, de proposition d'explorations, de l'établissement de protocoles expérimentaux ou encore de la relecture critique des résultats obtenus ainsi que de leur mise en forme. Les interactions se déroulent dans le cadre de la thèse de Benjamin BUARD (soutenance prévue avant fin 2010). Je résume dans cette partie les choix méthodologiques, les résultats principaux et les perspectives de notre action sur ce volet applicatif biomédical lié à la microcirculation sanguine.

La fluxmétrie laser Doppler repose sur le principe de l'effet Doppler généré par le battement temporel entre des photons directement issus d'un laser et ceux réfléchis par des particules en mouvement. Lorsque une sonde LDF est orientée vers la peau, le faisceau laser est rétro-diffusé par des particules en mouvement via le flux sanguin comme les globules rouges. La technique (LDF) permet alors de recueillir une information liée à la microcirculation sanguine à la surface de la peau. La recherche et les applications sur les signaux (LDF) pour l'étude de la microcirculation sanguine sont liées à des pathologies vasculaires périphériques, le diabète, des maladies de peau, ... Dans toutes les applications actuelles, la grandeur analysée sur les signaux LDF

est la moyenne du signal calculée empiriquement sur une fenêtre temporelle. Qu'en est-il des fluctuations des signaux laser Doppler autour de ces valeurs moyennes ? C'est la question que nous considérons. Pour apporter des éléments de réponse, nous avons déployé le questionnement suivant :

• Les fluctuations des signaux LDF de la circulation microvasculaires portent-elles la trace d'activités physiologiques ? Parmi les processus physiologiques susceptibles d'influencer les signaux LDF, on trouve les battements du cœur, la respiration et les activités myogénique, neurogénique et endotheliale. Ces processus présentent une périodicité avec des ordres de grandeurs respectifs de 1.1 Hz, 0.36 Hz, 0.1 Hz, 0.04 Hz, et 0.01 Hz pour un organisme humain "normal". Nous avons cherché la trace de ces activités dans les signaux expérimentaux comme le relate **[78]**. Seule l'activité cardiaque ressort systématiquement du bruit. L'étude **[78]** compare des signaux expérimentaux avec le seul modèle d'inspiration physiologique actuellement proposé. Implicitement, **[78]** montre les limites de cette approche de modélisation empirico-inductiviste que nous avons pour l'instant abandonnée.

• Les fluctuations sont-elles reliées aux fluctuations observées au niveau du système vasculaire central sur les signaux HRV ? Les signaux du système vasculaire central comme les signaux HRV traduisent des fluctuations aux dynamiques complexes dans le temps. Ces fluctuations ont été étudiées intensément au moyen de nombreux outils d'analyse en lien ou non avec des démarches de modélisation du cœur par des systèmes dynamiques capables de transcrire certaines signatures de ces fluctuations [2]. Parmi les outils proposés, on trouve des mesures de "complexité" comme l'analyse multifractale. Des observations récentes (par exemple [70, 89, 88, 45]) ont montré que les résultats fournis par l'analyse multifractale peuvent évoluer de façon saillante pour discriminer des états pathologiques ou physiologiques disctincts. Ceci nous a motivé pour procéder à des analyses multifractales des signaux LDF. L'article **[76]** donne un état de nos explorations sur le sujet à la suite des études [80, 79, 81, 82, 20, 77, 21, 83].

• Quelle est la part dans les fluctuations des signaux LDF de la microcirculation et des bruits liés à l'appareil lui-même ? C'est une étude en cours où nous en venons à considérer les signaux délivrés par l'appareil lorsqu'on ne lui présente aucune cible, ou une cible réfléchissante immobile ou encore un tuyau siège d'un écoulement laminaire au débit connu. Ces mesures nous permettront d'avoir des ordres de grandeurs du bruit d'obscurité lié à l'appareil ou à la sonde à placer en regard des fluctuations observées en mesure clinique.

4.3.2 Phénotypage et imagerie du végétal

L'acquisition de caractéristiques phénotypiques c'est-à-dire de grandeurs observables des plantes comme la forme, le développement, les propriétés biochimiques ou physiologiques est une activité importante en biologie. Le phénotypage consiste à collecter, sur un grand nombre d'individus, un ensemble de données phénotypiques dont la variabilité est analysée en fonction du patrimoine génétique et des conditions environnementales de production. Le phénotypage est souvent limité par la capacité en temps de travail humain à réaliser les observations dans le temps limite imposé par l'état du végétal à caractériser. Etant donné les moyens de génotypage (identification de parties du génome d'individus) ou encore en matière de protéomique (étude d'ensembles de protéines exprimées par un génome) actuellement disponibles, le phénotypage de grandes séries d'individus constitue un verrou majeur de l'étude des relations génotype-phénotype. Ainsi, augmenter la

capacité à collecter des données sur des végétaux dans un temps limité tout en améliorant la nature et la précision des mesures est d'un intérêt primordial comme le souligne l'INRA dans son projet de priorité scientifique pour la période 2010-2014 (voir http://www.inra2014.fr/). Ainsi, après le biomédical, le biovégétal avec la problématique du phénotypage de grandes populations de plante apparaît comme un nouveau domaine applicatif nécessitant la collaboration étroite entre spécialistes du végétal et des sciences et technologies de l'information et de la communication. Des plateforme de phénotypage fleurissent actuellement à travers le monde (par exemple http://www.apf.edu.au/ en Australie ou http://www.fz-juelich.de/icg/icg-3/jppc en Europe) en adaptant les techniques d'acquisitions aux objets et échelles d'études spécifiques dans chacun de ces centres. Au sein de la région Pays de la Loire, un secteur important et original de production concerne le végétal spécialisé (semences et horticulture au sens large). Dans ce contexte, une plateforme spécifiquement dédiée à l'imagerie du végétal spécialisé est actuellement en cours de développement sur le site d'Angers. C'est l'objet du projet PHENOTIC dont j'ai la responsabilité en tant que coordinateur principal pour la partie sciences de l'information avec Carolyne DÜRR (ingénieure INRA) pour la partie sciences du végétale. Trois supports d'étude ont été retenus pour ce projet : la croissance d'une plantule depuis la semence jusqu'à la reprise de la photosynthèse; la mise en place de l'architecture d'un rosier ; le développement d'un pathogène dans différents tissus. Le projet porte sur le développement de nouvelles techniques d'imagerie adaptées à ces différents objets végétaux, de tailles variant du millimètre au mètre, et placés dans des environnements très variés. Le descriptif des voies envisagées et le détail des avancées sont visibles sur le site web (http://www.istia.univ-angers.fr/LISA/PHENOTIC/index.html). Ce travail part clairement d'une demande de type ingénierie qui ne s'exprime pas directement en terme de recherche. Afin de rester dans le cadre de mes missions d'enseignement et de recherche. J'ai choisi d'utiliser ces demandes pour proposer des sujets de projet ou de stage de master aux étudiants. Il s'agit d'un choix délibéré décidé dès le montage du projet puisque 10 bourses de stages de master ont été demandées sur la durée 2009-2011 (anticipant ainsi l'obligation de gratification des stages légiférée en 2010). Ces travaux m'ont amené à proposer et explorer certaines pistes innovantes à l'occasion de partenariats initiés par mes soins :

• Test de la microscopie holographique pour ausculter sans contact et de façon non destructive la surface des feuilles lors du développement de champignons (réalisé en partenariat avec l'Ecole Polytechnique Fédérale de Lausanne voir Fig. 4.18A).

• Test de l'IRM pour caractériser la quantité d'eau chez les feuilles atteintes de pathologies (réalisé en partenariat avec le service commun d'analyses de l'université d'Angers voir Fig. 4.18B).

• Test de scanner biomédical pour acquérir l'architecture complète d'un rosier (réalisé en partenariat avec le CHU d'Angers voir Fig. 4.18C).

Je me suis aussi engagé (directement ou en tant qu'encadrant) dans la réalisation effective de différents prototypes :

• Création d'une visionneuse pour la détection manuelle et automatique de défauts de graine en imagerie par rayons X.

• Agencement d'un plateau tournant pour l'acquisition et le traitement d'images de rosier en vue d'en extraire l'enveloppe externe.

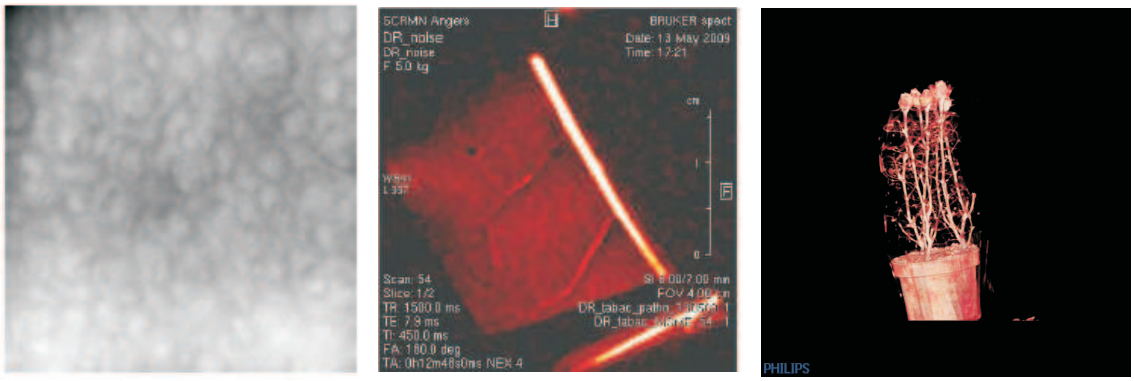

Figure 4.17 : Observations innovantes de végétaux à différentes échelles. (A) Image de phase en microscopie holographique de chloroplastes à la surface d'une feuille de choux. Le côté de l'image fait 600 μm. (B) IRM d'un limbe de feuille de tabac après inoculation par un pathogène (le point noir sur l'image). La zone visible fait environ 2 cm de côté. (C) Vision 2D d'un scanner d'un rosier d'ornement de 60 cm de hauteur.

• Détournement de scanners commerciaux rendus autonomes pour permettre des scans de feuilles en serre et réalisation d'une banque d'images de symptômes de pathogènes avec vérité expert.

• Constitution d'un banc d'imagerie par thermographie infrarouge et visible synchronisé et recalé pour la détection précoce du développement de pathogène dans les feuilles.

Au bout d'un an de travail, des questions génériques et spécifiques aux sciences de l'information commencent à émerger comme la compression des données, le recalage et la fusion entre différentes modalités d'imageries ou la segmentation d'images. Sur ce dernier point, les analyses en échelle au moyen d'outils de l'analyse fractale dont l'utilité est bien connue pour la représentation de l'organisation spatiale des plantes [64] pourraient s'avérer utiles pour la segmentation de zones nécrosées à la surface des feuilles comme celles de la Fig. 4.19.
La Fig. 4.20 montre une analyse en échelle des images de la Fig. 4.19. L'exposant fractal correspondant à la pente du comportement en loi de puissance observées sur les trois images de la Fig. 4.20 pourrait fournir un paramètre utile pour caractériser de façon concise l'organisation complexe d'images couleur dans leur espace colorimétrique. Cet exposant pourrait servir pour des tâches de reconnaissance, de classification ou d'indexation. Si une structure fractale existe dans l'histogramme, cela signifie qu'il tend à exister de nombreux groupes de couleur de plein de tailles différentes dans l'espace colorimétrique. À l'inverse une structure simple serait caractérisée par un petit nombre de couleurs dominantes facilement délimitables en clusters.

4.4 Conclusion

Ce chapitre m'a permis de présenter le cadre étendu de physique de l'information dans lequel je souhaite faire évoluer mon activité de recherche. Ce cadre inclut la résonance stochastique mais aussi d'autres questions auxquelles je m'intéresse desormais également comme les analyses en échelles et les applications aux sciences du vivant.

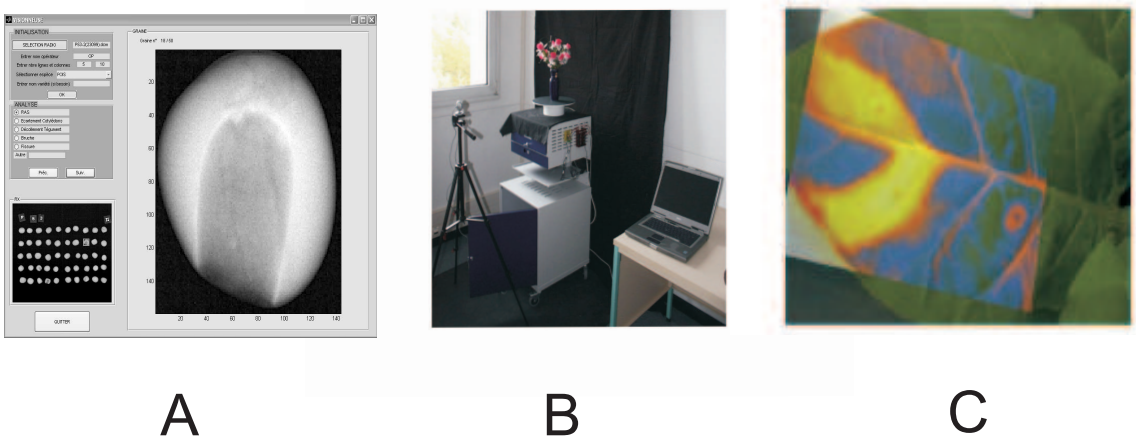

Figure 4.18 : Exemples de prototypes opérationnels réalisés en 2009 dans le cadre du projet PHENOTIC. (A) Interface permettant la visualisation et la notation expert de radiographies de graines. (B) Banc photo permettant l'acquisition automatique d'images de plantes en rotation autour de leur axe principal. (C) Recalage automatique d'une image visible et de l'image thermique d'une feuille de tabac infectée par des pathogènes.

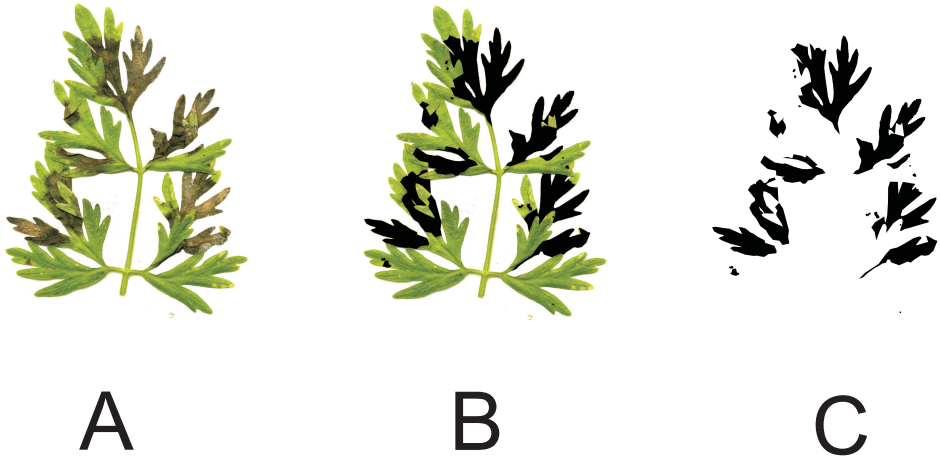

Figure 4.19 : Images de feuilles nécrosées de carottes. (A) Image scannée avec un scanner à plat. (B) Référence terrain numérique réalisée manuellement. (C) Masque binaire de la partie nécrosée seule.

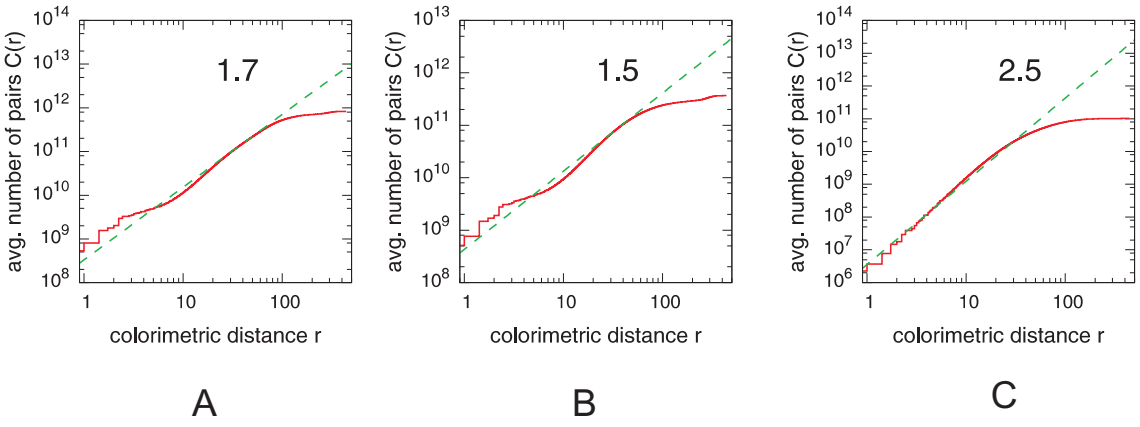

Figure 4.20 : Nombre moyen de paires de points qui sont séparés par une distance colorimétrique $\leq r$ (trait plein). (A) pour l'image (A) de la Fig. 4.19, (B) pour la partie non nécrosée de l'image (A) de la Fig. 4.19 et (C) partie nécrosée de l'image (A) de la Fig. 4.19. L'exposant indiqué correspond à la pente de la droite en pointillé ajustée sur la plus grande gamme d'échelles possibles.

Bibliographie

[1] A. Adrover, W. Schwalm, M. Giona et D. Bachand : Scaling and scaling crossover for transport on anisotropic fractal structures. *Physical Review E*, vol. 55:7304–7312, 1997.

[2] M. Akay : *Nonlinear Biomedical Signal Processing.* IEEE Pres, New York, 2000.

[3] V. C. Anderson : Digital array phasing. *Journal of the Acoustical Society of America*, 32:867–870, 1960.

[4] B. Andò et S. Graziani : *Stochastic Resonance: Theory and Applications.* Kluwer Academic Publishers, Boston, 2000.

[5] V. S. Anishchenko, M. A. Safonova et L. O. Chua : Stochastic resonance in the nonautonomous Chua's circuit. *Journal of Circuits, Systems and Computers*, 3:553–578, 1993.

[6] C. Arndt : *Information Measures: Information and Its Description in Science and Engineering.* Springer, Berlin, 2003.

[7] A. Arnéodo, F. Argoul, Bacry E., E. Elezgaray et J.-F. Muzy : *Ondelettes, multifractales et turbulences.* Diderot, Paris, 1995.

[8] F. A. Bais et J. D. Farmer : The physics of information. *In* P. Adriaans et J. van Benthem, éditeurs : *Philosophy of Information (Handbook of the Philosophy of Science)*, chapitre 5b. North Holland, Amsterdam, 2008. (also arXiv:0708.2837v2).

[9] J. S. Bendat : *Nonlinear Systems Techniques and Applications.* Wiley, New York, 1998.

[10] R. Benzi, A. Sutera et A. Vulpiani : The mechanism of stochastic resonance. *Journal of Physics A*, 14:L453–L458, 1981.

[11] P.R. Bhat, D. Rousseau et G. V. Anand : **Improved Bayesian Estimation of Weak Signal in Non-Gaussian Noise by Optimal Quantization**. *In IEEE 7th SPCOM, International Conference on Signal Processing and Communications*, Bangalore, India, décembre 2004.

[12] N. M. Blachman : The output signal-to-noise ratio of a power-law device. *Journal of Applied Physics*, 24:783–785, 1953.

[13] S. Blanchard, D. Rousseau et F. Chapeau-Blondeau : Noise-assisted image transmission with speckle noise. *In 5th International Conference on Physics in Signal and Image Processing*, Mulhouse, France, janvier 2007.

[14] S. Blanchard, D. Rousseau et F. Chapeau-Blondeau : **Noise Enhancement of Signal Transduction by Parallel Arrays of Nonlinear Neurons with Threshold and Saturation**. *Neurocomputing*, 71:333–341, 2007.

[15] S. Blanchard, D. Rousseau et F. Chapeau-Blondeau : Using noise to improve measurement and information processing. *In 4th International Conference on Informatics in Control, Automation and Robotics*, volume 3, pages 268–271, Angers, France, mai 2007.

[16] S. Blanchard, D. Rousseau, D. Gindre et F. Chapeau-Blondeau : **Constructive Action of the Speckle Noise in a Coherent Imaging System**. *Optics Letters*, 32:1983–1985, 2007.

[17] S. Blanchard, D. Rousseau, D. Gindre et F. Chapeau-Blondeau : Transmission d'image assistée par le bruit en imagerie cohérente et incohérente. *In 21ème Colloque GRETSI sur le Traitement du Signal et des Images*, pages 813–816, Troyes, France, septembre 2007.

[18] S. Blanchard, D. Rousseau, D. Gindre et F. Chapeau-Blondeau : Benefits from a speckle noise family on a coherent imaging transmission. *Optics Communications*, vol. 281:4173–4179, 2008.

[19] L. Brillouin : *Science And Information Theory*. Masson, Paris, 1959.

[20] B. Buard, A. Humeau, D. Rousseau, F. Chapeau-Blondeau et P. Abraham : Laser Doppler flowmetry signals: pointwise Hölder exponents of experimental signals from young healthy subjects and numerically simulated data. *In 4th European Congress for Medical and Biomedical Engineering*, volume 22, pages 221–225, Anvers, Belgique, novembre 2008. J. Vander Sloten, P. Verdonck, M. Nyssen, J. Haueisen (Eds.), ECIFMBE 2008, IFMBE Proceedings.

[21] B. Buard, G. Mahe, F. Chapeau-Blondeau, D. Rousseau, P. Abraham et A. Humeau : Etude des variations spatiales des spectres multifractals de signaux laser Doppler. *In OPT-DIAG 2009 : Septième colloque Diagnostic et imagerie optiques en médecine*, page 24, Paris, France, mai 2009.

[22] G. J. Burton et I. R. Moorhead : Color and spatial structure in natural scenes. *Applied Optics*, 26:157–170, 1987.

[23] L. L. Campbell : A coding theorem and rényi's entropy. *Information and Control*, 8:423–429, 1965.

[24] J. M. Casado, J. Gómez Ordóñez et M. Morillo : Stochastic resonance of collective variables in finite sets of interacting identical subsystems. *Physical Review E*, 73:011109,1–8, 2006.

[25] J. Casado-Pascual, C. Denk, J. Gómez-Ordóñez, M. Morillo et P. Hänggi : Gain in stochastic resonance: Precise numerics versus linear response theory beyond the two-mode approximation. *Physical Review E*, 67:036109,1–10, 2003.

[26] F. Chapeau-Blondeau, S. Blanchard et D. Rousseau : Noise-enhanced Fisher information in parallel arrays of sensors with saturation. *Physical Review E*, 74:031102,1–10, 2006.

[27] F. Chapeau-Blondeau, S. Blanchard et D. Rousseau : Fisher information and noise-aided power estimation from one-bit quantizers. *Digital Signal Processing*, 18:434–443, 2008.

[28] F. Chapeau-Blondeau, J. Chauveau, D. Rousseau et P. Richard : Fractal structure in the color distribution of natural images. *Chaos, Solitons & Fractals*, 42:472–482, 2009.

[29] F. Chapeau-Blondeau et X. Godivier : Theory of stochastic resonance in signal transmission by static nonlinear systems. *Physical Review E*, 55:1478–1495, 1997.

[30] F. Chapeau-Blondeau, X. Godivier et N. Chambet : Stochastic resonance in a neuron model that transmits spike trains. *Physical Review E*, 53:1273–1275, 1996.

[31] F. Chapeau-Blondeau et D. Rousseau : Noise improvements in stochastic resonance: From signal amplification to optimal detection. *Fluctuation and Noise Letters*, 2:L221–L233, 2002.

[32] F. Chapeau-Blondeau et D. Rousseau : Enhancement by noise in parallel arrays of sensors with power-law characteristics. *Physical Review E*, 70:060101(R),1–4, 2004.

[33] F. Chapeau-Blondeau et D. Rousseau : Noise enhanced performance for an optimal bayesian estimator. *IEEE Transactions on Signal Processing*, 52:1327–1334, 2004.

[34] F. Chapeau-Blondeau et D. Rousseau : Constructive action of additive noise in optimal detection. *International Journal of Bifurcation and Chaos*, 15:2985–2994, 2005.

[35] F. Chapeau-Blondeau et D. Rousseau : **Nonlinear SNR Amplification of a Harmonic Signal in Noise**. *Electronics Letters*, 41:618–619, 2005.

[36] F. Chapeau-Blondeau et D. Rousseau : Noise-aided SNR amplification by parallel arrays of sensors with saturation. *Physics Letters A*, 351:231–237, 2006.

[37] F. Chapeau-Blondeau et D. Rousseau : Nonlinear devices acting as SNR amplifiers for a harmonic signal in noise. *Circuits, Systems and Signal Processing*, 25:431–446, 2006.

[38] F. Chapeau-Blondeau et D. Rousseau : Injecting noise to improve performance of optimal detector. *Electronics Letters*, 43:897–898, 2007.

[39] F. Chapeau-Blondeau et D. Rousseau : **Raising the Noise to Improve Performance in Optimal Processing**. *Journal of Statistical Mechanics: Theory and Experiment*, P01003:1–15, 2009.

[40] F. Chapeau-Blondeau et D. Rousseau : **The minimum description length principle for probability density estimation by regular histograms**. *Physica A*, vol. 388:3969–3984, 2009.

[41] F. Chapeau-Blondeau, D. Rousseau, S. Blanchard et D. Gindre : **Optimizing the speckle noise for maximum efficacy of data acquisition in coherent imaging**. *Journal of the Optical Society of America A*, vol. 25:1287–1292, 2008.

[42] M. Chatterjee et M. E. Robert : Noise enhances modulation sensitivity in cochlear implant listeners: Stochastic resonance in a prosthetic sensory system ? *Journal of the Association for Research in Otolaryngology*, 2:159–171, 2001.

[43] J. Chauveau, D. Rousseau et F. Chapeau-Blondeau : Pair correlation integral for fractal characterization of three-dimensional histograms from color images. *In Lecture Notes in Computer Science*, volume LNCS 5099, pages 200–208. Springer, Berlin, 2008.

[44] J. Chauveau, D. Rousseau et F. Chapeau-Blondeau : **Fractal capacity dimension of three-dimensional histogram from color images**. *Multidimensional Systems and Signal Processing*, 2009. In press DOI 10.1007/s11045-009-0097-0, 2010.

[45] E. Ching et Y. Tsang : Multifractality and scale invariance in human heartbeat dynamics. *Physical Review E*, vol. 76:041910, 2007.

[46] C. Collet, F. Flitti, S. Bricq et A. Jalobeanu : *Inverse Problems in Imaging and Vision : Fusion and Multi-modality*, chapitre 13, pages 457–479. Traité IC2, ISBN : 978-2-7462-1997-7. Edited by Ali Mohammad-Djafari, John Wiley and Sons, 2010.

[47] T. M. Cover et J. A. Thomas : *Elements of Information Theory*. Wiley, New York, 1991.

[48] W. B. Davenport : Signal-to-noise ratios in band-pass limiters. *Journal of Applied Physics*, 24:720–727, 1953.

[49] W. B. Davenport et W. L. Root : *An Introduction to the Theory of Random Signals and Noise*. Wiley, New York, 1987.

[50] A. Delahaies, D. Rousseau, J-M. Breteau et F. Chapeau-Blondeau : Un critère informationnel en imagerie pour l'échelle optimale d'observation d'une scène bruitée. *In 5ème Colloque Interdisciplinaire en Instrumentation*, pages 637–644, Le Mans, France, janvier 2010.

[51] A. Delahaies, D. Rousseau, D. Gindre et F. Chapeau-Blondeau : Constructive role of sensors nonlinearities in the acquisition of partially polarized speckle images. *In 8th Euro American Workshop on Information Optics (WIO'09)*, pages DOI 10.1088/1742–6596/206/1/012020, Paris, France, juillet 2009.

[52] E. Desurvire : *Classical and Quantum Information Theory: An Introduction for the Telecom Scientist*. Cambridge University Press, Cambridge, 2009.

[53] D. W. Dong et J. J. Atick : Statistics of natural time-varying images. *Network: Computation in Neural Systems*, 6:345–358, 1995.

[54] F. Duan, F. Chapeau-Blondeau et D. Abbott : Noise-enhanced SNR gain in parallel array of bistable oscillators. *Electronics Letters*, 42:1008–1009, 2006.

[55] F. Duan, D. Rousseau et F. Chapeau-Blondeau : Residual aperiodic stochastic resonance in a bistable transmitting a suprathreshold binary signal. *Physical Review E*, 69, 011109:1–10, 2004.

[56] C. J. G. Evertsz et B. B. Mandelbrot : Multifractal measures. *In* H. O. Peitgen, H. Jürgens et D. Saupe, éditeurs : *Chaos and Fractals – New Frontiers of Science*, pages 921–953. Springer, Berlin, 1992.

[57] R. Feynman : *Feynman Lectures on Computation*. Perseus Books, New York, 2000.

[58] D. J. Field : Relations between the statistics of natural images and the response properties of cortical cells. *Journal of the Optical Society of America A*, 4:2379–2394, 1987.

[59] D. J. Field : What is the goal of sensory coding? *Neural Computation*, 6:559–601, 1994.

[60] R. B. Frieden : *Physics From Fisher Information: A Unification*. Cambridge University Press, Cambridge (MA), 1998.

[61] L. Gammaitoni : Stochastic resonance and the dithering effect in threshold physical systems. *Physical Review E*, 52:4691–4698, 1995.

[62] L. Gammaitoni, P. Hänggi, P. Jung et F. Marchesoni : Stochastic resonance. *Reviews of Modern Physics*, 70:223–287, 1998.

[63] N. Gershenfeld : *The Physics of Information Technology*. Cambridge University Press, Cambridge, 2000.

[64] C. Godin : *Introduction aux structures multi-échelles : Application à la représentation des plantes*. Habilitation à Diriger des Recherches, 2003.

[65] J. W. Goodman : *Speckle Phenomena in Optics: Theory and Applications*. Roberts & Company, Englewood, 2006.

[66] F. Goudail et P. Réfrégier : *Statistical Image Processing Techniques for Noisy Images*. Kluwer, New York, 2004.

[67] J. F. Gouyet : *Physics and Fractal Structures*. Springer, Berlin, 1996.

[68] P. Hänggi, M. E. Inchiosa, D. Fogliatti et A. R. Bulsara : Nonlinear stochastic resonance : The saga of anomalous output-input gain. *Physical Review E*, 62:–, 2000.

[69] G. P. Harmer, B. R. Davis et D. Abbott : A review of stochastic resonance: Circuits and measurement. *IEEE Transactions on Instrumentation and Measurement*, 51:299–309, 2002.

[70] S. Havlin, L. A. N. Amaral, Y. Ashkenazy, A. L. Goldberger, P. Ch. Ivanov, C. K. Peng et H. E. Stanley : Multifractality and scale invariance in human heartbeat dynamics. *Physica A*, vol. 274:99–110, 1999.

[71] H. G. E. Hentschel et I. Procaccia : The infinite number of generalized dimensions of fractals and strange attractors. *Physica D*, 8:435–444, 1983.

[72] A. Histace et D. Rousseau : **Constructive Action of Noise for Impulsive Noise Removal in Scalar Images**. *Electronics Letters*, 42:393–395, 2006.

[73] A. Histace et D. Rousseau : Noise-enhanced anisotropic diffusion for scalar image restoration. *In 5th International Conference on Physics in Signal and Image Processing*, Mulhouse, France, janvier 2007.

[74] T. Hoch, G. Wenning et K. Obermayer : Optimal noise-aided signal transmission through population of neurons. *Physical Review E*, 68, 011911:1–11, 2004.

[75] W. H. Hsiao et R. P. Millane : Effects of occlusion, edges, and scaling on the power spectra of natural images. *Journal of the Optical Society of America A*, 22:1789–1797, 2005.

[76] A. Humeau, B. Buard, F. Chapeau-Blondeau, D. Rousseau, G. Mahe et P. Abraham : **Multifractal analysis of central (electrocardiography) and peripheral (laser Doppler flowmetry) cardiovascular time series from healthy human subjects**. *Physiological Measurement*, vol. 30:617–629, 2009.

[77] A. Humeau, B. Buard, D. Rousseau, F. Chapeau-Blondeau et P. Abraham : Multifractal analysis of laser Doppler flowmetry signals: partition function and generalized dimensions of data recorded before and after local heating. *In 105th International Center for Biocybernetics Seminar "Light and optics in medical diagnosis"*, Varsovie, Pologne, septembre 2009.

[78] A. Humeau, F. Chapeau-Blondeau, D. Rousseau et P. Abraham : **Numerical simulation of laser Doppler flowmetry signals based on a model of nonlinear coupled oscillators. Comparison with real data in the frequency domain**. *In 29th Annual International Conference of the IEEE Engineering in Medicine and Biology Society in conjunction with the biennial Conference of the French Society of Biological and Medical Engineering (SFGBM)*, volume IEEE Catalog Number 07CH37852C, ISBN : 1-4244-0788, pages 4068–4071, Lyon, France, août 2007.

[79] A. Humeau, F. Chapeau-Blondeau, D. Rousseau, P. Rousseau, W. Trzepizur et P. Abraham : Multifractality, sample entropy, and wavelet analyses for age-related changes in the peripheral cardiovascular system: preliminary results. *Medical Physics*, vol. 35:717–723, 2008.

[80] A. Humeau, F. Chapeau-Blondeau, D. Rousseau, M. Tartas, B. Fromy et P. Abraham : Multifractality in the peripheral cardiovascular system from pointwise Hölder exponents of laser Doppler flowmetry signals. *Biophysical Journal*, vol. 93:L59–L61, 2007.

[81] A. Humeau, L. Fizanne, J. Roux, P. Asfar, P. Cales, D. Rousseau et F. Chapeau-Blondeau : Linear and nonlinear analyses of laser Doppler flowmetry signals recorded during isoflurane-induced anaesthesia in healthy rats. *Journal of Vascular Research*, vol. 45 (suppl. 2):60, 2008.

[82] A. Humeau, B. Haussy, L. Fizanne, J. Roux, P. Asfar, P. Cales, D. Rousseau et F. Chapeau-Blondeau : Laser Doppler flowmetry in healthy rats: impact of isoflurane anesthetic on signal complexity. *In 16th Mediterranean Conference on Control and Automation*, volume IEEE Catalog Number : CFP08MED-CDR, ISBN : 978-1-4, pages 1330–1334, Ajaccio, France, juin 2008.

[83] A. Humeau, G. Mahe, B. Buard, F. Chapeau-Blondeau, D. Rousseau et P. Abraham : Spectres multifractals de signaux laser Doppler acquis au cours d'un chauffage cutané local. *In OPT-DIAG 2009 : Septième colloque "Diagnostic et imagerie optiques en médecine"*, page 78, Paris, France, mai 2009.

[84] A. Humeau, W. Trzepizur, D. Rousseau, F. Chapeau-Blondeau et P. Abraham : Fisher information and Shannon entropy for on-line detection of transient signal high-values in laser Doppler flowmetry signals of healthy subjects. *Physics in Medicine and Biology*, vol. 53:5061–5076, 2008.

[85] A. Humeau, W. Trzepizur, D. Rousseau, F. Chapeau-Blondeau et P. Abraham : Localization of transient signal high-values in laser Doppler flowmetry signals with an empirical mode decomposition. *Medical Physics*, vol. 36:18–21, 2009.

[86] F.-X. Inglese et D. Rousseau : Utilisation d'un manette de jeu vidéo pour des expériences de mécanique. *Le BUP, Le Bulletin de l'Union des Professeurs de Physique et de Chimie*, vol. 902:427–434, 2008.

[87] L. Itti, C. Koch et E. Niebur : A model of saliency-based visual attention for rapid scene analysis. *Transactions on Pattern Analysis and Machine Intelligence*, 20:1254–1259, 1998.

[88] P. C. Ivanov, L. A. N. Amaral, A. L. Goldberger, S. Havlin, M. G. Rosenblum, H. E. Stanley et Z. R. Struzik : From 1/f noise to multifractal cascades in heartbeat dynamics. *Chaos*, vol. 11:641–693, 2001.

[89] P. C. Ivanov, L. A. N. Amaral, A. L. Goldberger, S. Havlin, M. G. Rosenblum, Z. R. Struzik et H. E. Stanley : Multifractality in human heartbeat dynamics. *Nature*, vol. 399:461–466, 1999.

[90] P. C. Ivanov, Q. D. Ma, R. P. Bartsch, J. M. Hausdorff, Nunes Amaral L. A., Schulte-Frohlinde V., Stanleyn H. E. et Yoneyama M. : Levels of complexity in scale-invariant neural signals. *Physical Review E*, vol. 79:041920, 2009.

[91] B. M. Jost et B. E. A. Saleh : Signal-to-noise ratio improvement by stochastic resonance in a unidirectional photorefractive ring resonator. *Optics Letters*, 21:287–289, 1996.

[92] S. Kay : *Fundamentals of Statistical Signal Processing: Detection Theory*. Prentice Hall, Englewood Cliffs, 1998.

[93] R. Landauer : *Feynman and computation: exploring the limits of computers*. Perseus Books, New York, 1999.

[94] D. Landgrebe : Hyperspectral image data analysis. *IEEE Signal Processing Magazine*, 19(1):17–28, Jan. 2002.

[95] M. Liljenstam et A. T. Ogielski : Crossover scaling effects in aggregated TCP traffic with congestion losses. *ACM SIGCOMM Computer Communication Review*, vol. 32:89–100, 2002.

[96] D. G. Luchinsky, R. Mannella, P. V. E. McClintock et N. G. Stocks : Stochastic resonance in electrical circuits – I: Conventional stochastic resonance. *IEEE Transactions on Circuits and Systems – II: Analog and Digital Signal Processing*, 46:1205–1214, 1999.

[97] D. G. Luchinsky, R. Mannella, P. V. E. McClintock et N. G. Stocks : Stochastic resonance in electrical circuits – II: Nonconventional stochastic resonance. *IEEE Transactions on Circuits and Systems – II: Analog and Digital Signal Processing*, 46:1215–1224, 1999.

[98] V. K. Madisetti et D. B. Williams : *The Digital Signal Processing Handbook*. CRC Press, Boca Raton, 1999.

[99] M. D. McDonnell et D. Abbott : Open questions for suprathreshold stochastic resonance in sensory neural models for motion detection using artificial insect vision. *AIP Conference Proceedings*, 665:L51–L58, 2003.

[100] M. D. McDonnell, N. G. Stocks, C. E. M. Pearce et D. Abbott : *Stochastic Resonance: From Suprathreshold Stochastic Resonance to Stochastic Signal Quantization.* Cambridge University Press, Cambridge, 2008.

[101] M. Mézard et A. Montanari : *Information, Physics, and Computation.* Oxford University Press, Oxford, 2009.

[102] S. Morfu, J. M. Bilbault et J. C. Comte : Noise-enhanced propagation in a dissipative chain of triggers. *International Journal of Bifurcation and Chaos*, 12:1–5, 2002.

[103] S. Morfu, J. M. Bilbault et J. C. Comte : Digital information receiver based on stochastic resonance. *International Journal of Bifurcation and Chaos*, 13:233–236, 2003.

[104] F. Moss, J. K. Douglass, L. Wilkens, D. Pierson et E. Pantazelou : Stochastic resonance in an electronic Fitzhugh-Nagumo model. *Annals of New York Academy of Sciences*, 706:26–41, 1993.

[105] F. Moss, L. M. Ward et W. G. Sannita : Stochastic resonance and sensory information processing: a tutorial and review of application. *Clinical Neurophysiology*, 115(2):267–281, 2004.

[106] A. Muñoz-Diosdado, L. Guzmán-Vargas, A. Ramírez-Rojas, J. L. Del Río-Correa et Angulo-Brown F. : Some cases of crossover behavior in heart interbeat and electroseismic times series. *Fractals*, vol. 13:253–263, 2005.

[107] A. Nikitin, N. G. Stocks et R. P. Morse : Enhanced information transmission with signal-dependent noise in an array of nonlinear elements. *Physical Review E*, 75, 021121:1–8, 2007.

[108] A. Papoulis : *Probability, Random Variables, and Stochastic Processes.* McGraw-Hill, New York, 1991.

[109] P. Perona et J. Malik : Scale-space and edge detection using anistropic diffusion. *IEEE Transcations on Pattern Analysis and Machine Intelligence*, 12(7):629–639, 1990.

[110] P. Perrenoud : *Développer la pratique réflexive dans le métier d'enseignant : professionnalisation et raison pédagogique.* PU Polytechnique, Issy-les-Moulineaux, 2001.

[111] M. Piana, M. Canfora et M. Riani : Role of noise in image processing by the human perceptive system. *Physical Review E*, 62:1104–1109, 2000.

[112] A. Pinada et R. Toral : Noise continuous-opinion dynamics. *Journal of Statistical Mechanics: Theory and Experiment*, P08001, 2009.

[113] D. Placko : *De la Physique du Capteur au Signal Électrique.* Hermes, Paris, 2000.

[114] P. Réfrégier : *Théorie du Bruit et Applications en Physique.* Hermès, Paris, 2002.

[115] J. Rissanen : *Stochastic Complexity in Statistical Inquiry.* World Scientific, Singapore, 1989.

[116] A. Rényi : On measures of entropy and information. *In Proc. 4th Berkeley Sympos. Math. Statist. and Prob.*, Berkeley, USA, 1961.

[117] D. Rousseau, G. V. Anand et F. Chapeau-Blondeau : **Noise-Enhanced Nonlinear Detector to Improve Signal Detection in Non-Gaussian Noise**. *Signal Processing*, 86:3456–3465, 2006.

[118] D. Rousseau, G. V. Anand et F. Chapeau-Blondeau : Nonlinear estimation from quantized signals: Quantizer optimization and stochastic resonance. *In Proceedings* 3*rd International Symposium on Physics in Signal and Image Processing*, pages 89–92, Grenoble, France, 28–31 Jan. 2003.

[119] D. Rousseau, G.V. Anand et F. Chapeau-Blondeau : Overview of useful-noise effects in static nonlinear systems. *In Stochastic Resonance, 1998SR2008, ten years of continuous growth*, Perugia, Italie, août 2008.

[120] D. Rousseau et F. Chapeau-Blondeau : Various forms of improvement by noise in nonlinear system. *In Proceedings Complex Systems Intelligence and Modern Technology Application*, Cherbourg, France, 19–22 Sept. 2004.

[121] D. Rousseau et F. Chapeau-Blondeau : Résonance stochastique et performance améliorée par le bruit pour un estimateur optimal. *In Proceedings 19è Colloque GRETSI sur le Traitement du Signal et des Images*, pages 50–54 vol 3, Paris, France, 2003.

[122] D. Rousseau et F. Chapeau-Blondeau : Neuronal signal transduction aided by noise at threshold and saturation. *Neural Processing Letters*, 20:71–83, 2004.

[123] D. Rousseau et F. Chapeau-Blondeau : Stochastic resonance and improvement by noise in optimal detection strategies. *Digital Signal Processing*, 15:19–32, 2004.

[124] D. Rousseau et F. Chapeau-Blondeau : Suprathreshold stochastic resonance and signal-to-noise ratio improvement in arrays of comparators. *Physics Letters A*, 321:280–290, 2004.

[125] D. Rousseau et F. Chapeau-Blondeau : Amélioration par le bruit de la dynamique de capteurs à saturation. *In 20e Colloque GRETSI sur le Traitement du Signal et des Images*, pages 595–598, Louvain-la-Neuve, Belgique, septembre 2005.

[126] D. Rousseau et F. Chapeau-Blondeau : Noise-improved detection via suprathreshold stochastic resonance in arrays of quantizers. *Signal Processing*, 85:571–580, 2005.

[127] D. Rousseau et F. Chapeau-Blondeau : Stochastic resonance and improvement by noise in optimal detection strategies. *Digital Signal Processing*, 15:19–32, 2005.

[128] D. Rousseau et F. Chapeau-Blondeau : Noise-improved Bayesian estimation with arrays of one-bit quantizers. *IEEE Transactions on Instrumentation and Measurement*, 56:2658–2662, 2007.

[129] D. Rousseau, A. Delahaies et F. Chapeau-Blondeau : **Structural similarity measure to assess improvement by noise in nonlinear image transmission**. *IEEE Signal Processing Letters*, vol. 17:36–39, 2010.

[130] D. Rousseau, F. Duan et F. Chapeau-Blondeau : Suprathreshold stochastic resonance and noise-enhanced Fisher information in arrays of threshold devices. *Physical Review E*, 68:031107,1–10, 2003.

[131] D. Rousseau, F. Duan, J. Rojas Varela et F. Chapeau-Blondeau : Evaluation of a nonlinear bistable filter for binary detection. *International Journal of Bifurcation and Chaos*, 15:667–679, 2005.

[132] D. Rousseau, J. Rojas Varela et F. Chapeau-Blondeau : Stochastic resonance for nonlinear sensors with saturation. *Physical Review E*, 67:021102,1–6, 2003.

[133] D. Rousseau et S. Sourisseau : Propositions pour la masterisation. *Le BUP, Le Bulletin de l'Union des Professeurs de Physique et de Chimie*, vol. 104:225–230, 2010.

[134] D. L. Ruderman : Origins of scaling in natural images. *Vision Research*, 37:3385–3398, 1997.

[135] D. L. Ruderman et W. Bialek : Statistics of natural images: Scaling in the woods. *Physical Review Letters*, 73:814–817, 1994.

[136] J. C. Russ : *The Image Processing Handbook*. CRC Press, Boca Raton, 1995.

[137] H. Sasaki, M. Todorokihara, T. Ishida, J. Miyachi, T. Kitamura et R. Aoki : Effect of noise on the contrast detection threshold in visual perception. *Neuroscience Letters*, 408:94–97, 2006.

[138] A. Saucier : *Méthodes multifractales pour l'analyse d'images et de signaux," in* Lois d'Échelle, Fractales et Ondelettes*, (P. Abry, P. Gonçalvès, and J. Lévy Véhel, eds.), pp. 165–206.* Hermès, Paris, 2002.

[139] M. Schroeder : *Fractals, Chaos, Power Laws*. Freeman, New York, 1999.

[140] C. E. Shannon : A mathematical theory of communication. *Bell System Technical Journal*, 27:379–423, 1948.

[141] E. Simonotto, M. Riani, C. Seife, M. Roberts, J. Twitty et F. Moss : Visual perception of stochastic resonance. *Physical Review Letters*, 78:1186–1189, 1997.

[142] T. Stathaki : *Image Fusion: Algorithms and Applications*. Academic Press, New York, 2008.

[143] N. G. Stocks : Suprathreshold stochastic resonance in multilevel threshold systems. *Physical Review Letters*, 84:2310–2313, 2000.

[144] N. G. Stocks : Information transmission in parallel threshold arrays: Suprathreshold stochastic resonance. *Physical Review E*, 63:041114,1–9, 2001.

[145] N. G. Stocks, D. Allingham et R. P. Morse : The application of suprathreshold stochastic resonance to cochlear implant coding. *Fluctuation and Noise Letters*, 2:L169–L181, 2002.

[146] N. G. Stocks et R. Mannella : Generic noise-enhanced coding in neuronal arrays. *Physical Review E*, 64:030902,1–4, 2001.

[147] C. Tessone, C. Mirasso, R. Toral et J.D. Gunton : Diversity-induced resonance. *Physical Review Letters*, 97:194101, 2006.

[148] F. Vaudelle, J. Gazengel, G. Rivoire, X. Godivier et F. Chapeau-Blondeau : Stochastic resonance and noise-enhanced transmission of spatial signals in optics: The case of scattering. *Journal of the Optical Society of America B*, 15:2674–2680, 1998.

[149] J. Lévy Véhel et C. Tricot : *Analyse fractale et multifractale en traitement des signaux," in* Lois d'Échelle, Fractales et Ondelettes," in *Lois d'Échelle, Fractales et Ondelettes, (P. Abry, P. Gonçalvès, and J. Lévy Véhel, eds.) pp. 165–206.* Hermès, Paris, 2002.

[150] Z. Wang et A. C. Bovik : A universal image quality index. *IEEE Signal Processing Letters*, 9:81–84, 2002.

[151] Z. Wang, A. C. Bovik, H. R. Sheikh et E. P. Simoncelli : Image quality assessment: From error visibility to structural similarity. *IEEE Transactions on Image Processing*, 13:600–612, 2004.

[152] T. Yang : Adaptively optimizing stochastic resonance in visual system. *Physics Letters A*, 245:79–86, 1998.

[153] S. Zozor, P.-O. Amblard et C. Duchêne : On pooling networks and fluctuation in suboptimal detection framework. *Fluctuation and Noise Letters*, 7:39–60, 2007.

Chapitre 5

Annexe : recueil de publications

p. 78 : D. ROUSSEAU and F. CHAPEAU-BLONDEAU. Noise-improved Bayesian estimation with arrays of one-bit quantizers. *IEEE Trans. on Instrum. and Meas.*, vol. 56:2658–2662, 2007.

p. 84 : D. ROUSSEAU, G. V. ANAND, and F. CHAPEAU-BLONDEAU. Noise-enhanced nonlinear detector to improve signal detection in non-Gaussian noise. *Signal Processing*, vol. 86:3456–3465, 2006.

p. 95 : S. BLANCHARD, D. ROUSSEAU, and F. CHAPEAU-BLONDEAU. Noise enhancement of signal transduction by parallel arrays of nonlinear neurons with threshold and saturation. *Neurocomputing*, vol. 71:333–341, 2007.

p. 105 : F. CHAPEAU-BLONDEAU and D. ROUSSEAU. Nonlinear SNR amplification of harmonic signal in noise. *Electronics Letters*, vol. 41:618–619, 2005.

p. 108 : P. R. BHAT and D. ROUSSEAU and G. V. ANAND. Improved Bayesian Estimation of Weak Signal in Non-Gaussian Noise by Optimal Quantization. IEEE 7th SPCOM, Bangalore, India, dec 2004.

p. 114 : F. CHAPEAU-BLONDEAU and D. ROUSSEAU. Raising the noise to improve performance in optimal processing. *Journal of Statistical Mechanics : Theory and Experiment*, P01003, 1–5, 2009.

p. 130 : S. BLANCHARD, D. ROUSSEAU, D. GINDRE, and F. CHAPEAU-BLONDEAU. Constructive action of the speckle noise in a coherent imaging system. *Optics Letters*, vol. 32:1983–1985, 2007.

p. 134 : F. CHAPEAU-BLONDEAU, D. ROUSSEAU, S. BLANCHARD, and D. GINDRE. Optimizing the speckle noise for maximum efficacy of data acquisition in coherent imaging. *Journal of the Optical Society of America A*, vol. 25:1287–1292, 2008.

p. 141 : D. ROUSSEAU, A. DELAHAIES, F. CHAPEAU-BLONDEAU. Structural similarity measure to assess improvement by noise in nonlinear image transmission. *IEEE Signal Processing Letters*, vol. 17, 36–39, 2010.

p. 146 : A. HISTACE and D. ROUSSEAU. Constructive action of noise for impulsive noise removal in scalar images. *Electronics Letters*, vol. 42:393–395, 2006.

p. 149 : F. CHAPEAU-BLONDEAU, D. ROUSSEAU, The minimum description length principle for probability density estimation by regular histograms, *Physica A*, vol. 388, 3969–3984, 2009.

p. 166 : J. CHAUVEAU and D. ROUSSEAU and F. CHAPEAU-BLONDEAU, Fractal capacity dimension of three-dimensional histogram from color images. *Multidimensional Systems and Signal Processing*, in press, DOI 10.1007/S11045-009-0097-0, 2009.

p. 179 : A. HUMEAU, F. CHAPEAU-BLONDEAU, D. ROUSSEAU, and P. ABRAHAM. Numerical simulation of laser Doppler flowmetry signals based on a model of nonlinear coupled oscillators. Comparison with real data in the frequency domain. In *29th Annual International Conference of the IEEE Engineering in Medicine and Biology (SFGBM)*, pages 4068–4071, Lyon, France, Août 2007.

p. 184 :A. HUMEAU, B. BUARD, F. CHAPEAU-BLONDEAU, D. ROUSSEAU, G. MAHE, P. ABRAHAM. Multifractal analysis of central (electrocardiography) and peripheral (laser Doppler flowmetry) cardiovascular time series from healthy human subjects. *Physiological Measurement*, vol. 30, 617–629, 2009.

D. ROUSSEAU and F. CHAPEAU-BLONDEAU. Noise-improved Bayesian estimation with arrays of one-bit quantizers. *IEEE Transactions on Instrumentation and Measurement*, vol. 56:2658–2662, 2007.

Noise-Improved Bayesian Estimation With Arrays of One-Bit Quantizers

David Rousseau and François Chapeau-Blondeau

***Abstract*—A noisy input signal is observed by means of a parallel array of one-bit threshold quantizers, in which all the quantizer outputs are added to produce the array output. This parsimonious signal representation is used to implement an optimal Bayesian estimation from the output of the array. Such conditions can be relevant for fast real-time processing in large-scale sensor networks. We demonstrate that, for input signals of arbitrary amplitude, the performance in the estimation can be improved by the addition of independent noises onto the thresholds in the array. These results constitute a novel instance of the phenomenon of suprathreshold stochastic resonance in arrays, by which nonlinear transmission or processing of signals with arbitrary amplitude can be improved through cooperative coupling with noise.**

***Index Terms*—Estimation, noise, nonlinear arrays, quantizer, sensor arrays, stochastic resonance (SR).**

I. Introduction

MULTISENSOR arrays are currently an area of active research: Nonlinear arrays, microarrays or nanoarrays, intelligent sensing arrays incorporating preprocessing of data, and arrays drawing inspiration from sensory neurons constitute interesting lines of research in this area [1], [2]. In the present paper, we consider parallel arrays of threshold comparators or one-bit quantizers. Such simple devices can be useful in building large-scale arrays that are very efficient in terms of resources and time for data processing, storage, and communication, and in terms of energy supply, with a possibly high density of integration in solid-state realizations. Such arrays of comparators have similarities with flash analog-to-digital converters or with digital sonar arrays [3]. Such arrays of threshold devices also mimic, in a crude way, the nonlinear behavior, which can be present in networks of sensory neurons [4]. These arrays are therefore specially appealing in devising novel strategies based on multisensor networks for nonlinear signal and information processing.

A specific interest of such parallel arrays of comparators is that they have recently been shown to lend themselves to the phenomenon of suprathreshold stochastic resonance (SR). SR is a nonlinear phenomenon by which the action of noise can improve the performance of signal-processing or measurement systems [5]–[12]. Since its introduction some 20 years ago, SR has gradually been shown to be feasible under several different forms, with various types of systems, signals, and indexes of performance receiving improvement from the noise [10], [13]–[21]. Most occurrences of SR known today involve a signal which is, by itself, too small or ill-conditioned to elicit a strong response from a nonlinear system. Injection of noise then, through a cooperative interaction, brings assistance to the small signal in eliciting a more efficient response from the nonlinear system, for instance, by overcoming a threshold or a potential barrier.

Recently, an interesting new form of SR has been introduced under the name of suprathreshold SR since it is not restricted to a small, subthreshold, or ill-conditioned signal [22], [23]. Suprathreshold SR relies on a parallel array of identical nonlinear devices. At the location of each device, an independent noise is injected in the process. The result is to make each one of the identical devices elicit a distinct output in response to a same common input signal. When the individual outputs are collected or averaged over the array to produce a global response, it turns out that a net improvement can be obtained compared to the response of a single device with no noise injected. Qualitatively, its benefit comes from the diversity induced by the injected noises in the responses of the individual nonlinear devices over the array. This suprathreshold SR does not involve a small signal receiving assistance from the noise to elicit a more efficient response from a single isolated nonlinear system. As such, suprathreshold SR can be viewed as a specifically distinct mechanism under which an improvement by noise can take place.

Since its recent introduction in [22], suprathreshold SR has been shown to be possible in various conditions, with different types of signals and indexes of performance, including Shannon mutual information [3], [22], [23], input–output cross correlation [24], Fisher information [25], or signal-to-noise ratio [26]. Suprathreshold SR has also been applied to arrays of sensory neurons [27], to motion detectors [28], and to cochlear implants [29]. The most simple systems which have been reported to give way to suprathreshold SR and which have been exploited to investigate its properties are the parallel arrays of threshold comparators or quantizers mentioned earlier. A very recent study [30] demonstrates that such arrays can show detection capabilities that are improved by noise via suprathreshold SR. In the present paper, we extend the investigation of the capabilities of these arrays for noise-improved information processing or measurement via suprathreshold SR. We use these arrays for a Bayesian estimation task, and we demonstrate the possibility of conditions where the estimation performance is augmented by injection of noise in the array.

II. Estimation From a Nonlinear Parallel Array

A signal $x_a(t)$ is dependent upon parameter a, whose possible values are distributed according to the prior probability

Manuscript received October 18, 2005; revised April 2, 2007.

The authors are with the Laboratoire d'Ingénierie des Systèmes Automatisés (LISA), Université d'Angers, 49000 Angers, France.

Digital Object Identifier 10.1109/TIM.2007.908125

density function (pdf) $p_a(u)$. This signal $x_a(t)$ is observed by means of a parallel array of N threshold comparators or one-bit quantizers, following the setting of [3] and [22]. We arrange for the possibility of a noise $\eta_i(t)$, which is independent of $x_a(t)$, to be added to $x_a(t)$ before quantization by quantizer i. The N threshold noises $\eta_i(t)$ are taken as white, mutually independent, and identically distributed with cumulative distribution function $F_\eta(u)$. Quantizer i, with a threshold θ_i, delivers the output

$$y_i(t) = U\left[x_a(t) + \eta_i(t) - \theta_i\right], \qquad i = 1, 2, \ldots, N \tag{1}$$

where $U(u)$ is the Heaviside function, i.e., $U(u) = 1$ if $u > 0$ and is zero otherwise. The response $Y(t)$ of the array is obtained by summing the outputs of all the quantizers, as

$$Y(t) = \sum_{i=1}^{N} y_i(t). \tag{2}$$

The array output of (2) is measured at M distinct times t_j, for $j = 1$ to M, so as to provide M data points $Y_j = Y(t_j)$. We then want to use the data $\boldsymbol{Y} = (Y_1, \ldots, Y_M)$ to estimate the value of a that produced the observation. Once $\boldsymbol{Y}$ is observed, a posterior pdf $p(a|\boldsymbol{Y})$ for parameter a can be defined. A given estimator $\widehat{a}(\boldsymbol{Y})$ for a achieves a mean-square estimation error defined [31] as the expectation (conditioned by observation $\boldsymbol{Y}$)

$$\mathcal{E}(\boldsymbol{Y}) = E\left[(a - \widehat{a})^2|\boldsymbol{Y}\right] = \int_{-\infty}^{\infty} [a - \widehat{a}(\boldsymbol{Y})]^2 p(a|\boldsymbol{Y}) da. \tag{3}$$

It is easy to show that $\mathcal{E}(\boldsymbol{Y})$ of (3) can equivalently be expressed as

$$\mathcal{E}(\boldsymbol{Y}) = \left[\widehat{a} - \mathrm{E}(a|\boldsymbol{Y})\right]^2 + \mathrm{var}(a|\boldsymbol{Y}) \tag{4}$$

with $E(a|\boldsymbol{Y}) = \int_{-\infty}^{\infty} a p(a|\boldsymbol{Y}) da$ and $\mathrm{var}(a|\boldsymbol{Y}) = \int_{-\infty}^{\infty} [a - E(a|\boldsymbol{Y})]^2 p(a|\boldsymbol{Y}) da$.

Since $\mathrm{var}(a|\boldsymbol{Y})$ in (4) is nonnegative and independent of $\widehat{a}$, the optimal Bayesian estimator that minimizes error $\mathcal{E}(\boldsymbol{Y})$, for any given observation $\boldsymbol{Y}$, comes out as

$$\widehat{a}_{\mathrm{B}}(\boldsymbol{Y}) = \mathrm{E}(a|\boldsymbol{Y}) = \int_{-\infty}^{\infty} a p(a|\boldsymbol{Y}) da \tag{5}$$

and its performance is measured by the minimal error

$$\mathcal{E}_{\mathrm{B}}(\boldsymbol{Y}) = \mathrm{var}(a|\boldsymbol{Y}) = \int_{-\infty}^{\infty} \left[a - E(a|\boldsymbol{Y})\right]^2 p(a|\boldsymbol{Y}) da. \tag{6}$$

A model that shows how $x_a(t)$, and then $\boldsymbol{Y}$ via (1) and (2), are related to parameter a allows one to define the conditional probabilities $\Pr\{\boldsymbol{Y}|a\}$ of observing one specific $\boldsymbol{Y}$ among the $(N+1)^M$ accessible states, given a. With the prior information summarized by $p_a(a)$, the Bayes rule then provides access to the posterior pdf under the form

$$p(a|\boldsymbol{Y}) = \frac{\Pr\{\boldsymbol{Y}|a\} p_a(a)}{\Pr\{\boldsymbol{Y}\}} \tag{7}$$

with the total probability $\Pr\{\boldsymbol{Y}\} = \int_{-\infty}^{\infty} \Pr\{\boldsymbol{Y}|a\} p_a(a) da$.

For any given observation $\boldsymbol{Y}$, the optimal Bayesian estimator $\widehat{a}_{\mathrm{B}}(\boldsymbol{Y})$ from (5) achieves the minimum $\mathcal{E}_{\mathrm{B}}(\boldsymbol{Y})$ from (6) of the error $\mathcal{E}(\boldsymbol{Y})$ from (3). Consequently, $\widehat{a}_{\mathrm{B}}(\boldsymbol{Y})$ also achieves the minimum $\overline{\mathcal{E}}_{\mathrm{B}}$ of error $\mathcal{E}(\boldsymbol{Y})$ averaged over every possible observation $\boldsymbol{Y}$, i.e., $\widehat{a}_{\mathrm{B}}(\boldsymbol{Y})$ minimizes $\sum_{\boldsymbol{Y}} \mathcal{E}(\boldsymbol{Y}) \Pr\{\boldsymbol{Y}\}$, and the minimum that is reached is

$$\overline{\mathcal{E}}_{\mathrm{B}} = \sum_{\boldsymbol{Y}} \mathrm{var}(a|\boldsymbol{Y}) \Pr\{\boldsymbol{Y}\} \tag{8}$$

where the sums on $\boldsymbol{Y}$ run over the $(N+1)^M$ accessible states, from $\boldsymbol{Y} = (Y_1 = 0, \ldots, Y_M = 0)$ to $\boldsymbol{Y} = (Y_1 = N, \ldots, Y_M = N)$.

To proceed, at any time t_j, for a fixed given value x_a of the input signal $x_a(t_j)$, we have the conditional probability $\Pr\{y_i(t_j) = 0|x_a\}$ which is also $\Pr\{x_a + \eta_i(t_j) \le \theta_i\}$. This amounts to

$$\Pr\{y_i(t_j) = 0|x_a\} = F_\eta(\theta_i - x_a). \tag{9}$$

In the same way, we have $\Pr\{y_i(t_j) = 1|x_a\} = 1 - F_\eta(\theta_i - x_a)$.

To show the possibility of a noise-improved estimation, we assume, as done in [23], the simplest configuration of the array, where all the thresholds θ_i share the same value $\theta_i = \theta$ for all i. The conditional probability $\Pr\{Y(t_j) = Y_j|x_a\}$, for any accessible value $Y_j = 0$ to N, then follows, according to the binomial distribution, as

$$\begin{aligned}\Pr\{Y(t_j) = Y_j|x_a\} &\\ = C_{Y_j}^N \left[1 - F_\eta(\theta - x_a)\right]^{Y_j} &F_\eta(\theta - x_a)^{N - Y_j}\end{aligned} \tag{10}$$

where $C_{Y_j}^N$ is the binomial coefficient.

For the sake of definiteness, concerning the parametric dependence of $x_a(t)$ on a, we shall consider the broad class of processes, where $x_a(t)$ is formed by the additive mixture $x_a(t) = \xi(t) + s_a(t)$. The signal $\xi(t)$ is a random input noise, which is white and independent of a and of η_is, with pdf $f_\xi(u)$. Signal $s_a(t)$ is deterministic for a fixed value of a. For instance, $s_a(t)$ may be the constant signal $s_a(t) \equiv a$ or the periodic signal $s_a(t) = \sin(at)$, or any other signal of known deterministic form that is parameterized by a. At time t, the pdf for the values of $x_a(t)$ given a is thus given as $f_\xi[u - s_a(t)]$, and we therefore obtain the conditional probability

$$\begin{aligned}\Pr\{Y(t_j) = Y_j|a\} = \int_{-\infty}^{\infty} C_{Y_j}^N \left[1 - F_\eta(\theta - u)\right]^{Y_j} &\\ \times F_\eta(\theta - u)^{N - Y_j} f_\xi\left(u - s_a(t_j)\right) du.&\end{aligned} \tag{11}$$

Since the noises $\xi(t)$ and $\eta_i(t)$ are white and mutually independent, the conditional probability of (7) factorizes as

$$\Pr\{\boldsymbol{Y}|a\} = \prod_{j=1}^{M} \Pr\left\{Y(t_j) = Y_j|a\right\}. \tag{12}$$

Equations (11) and (12), through (7), will enable an explicit evaluation of the optimal Bayesian estimator of (5) and of its performance measured by (6) or (8). This will be obtainable,

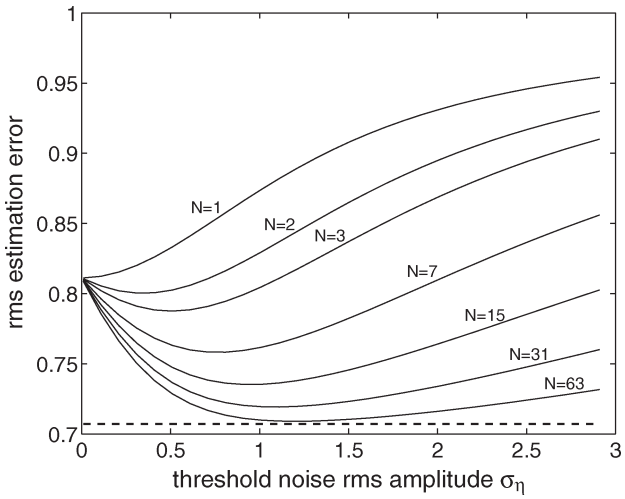

Fig. 1. RMS error of the optimal Bayesian estimator as a function of the rms amplitude σ_η of the threshold noises $\eta_i(t)$ chosen zero-mean Gaussian. The input noise $\xi(t)$ is a zero-mean Gaussian with an rms amplitude $\sigma_\xi = 1$. The prior pdf $p_a(u)$ is a zero-mean Gaussian with an rms amplitude $\sigma_a = 1$. All the thresholds in the array are set to $\theta = 0$, with $M = 1$. The solid lines are $\overline{\mathcal{E}}_{\rm B}^{1/2}$ from the theory of (8). The dashed line is the estimation error $\sigma_{\rm Bin}$ from (13) of the same optimal (minimal error) estimator operating directly on the input-signal–noise mixture $x_a(t)$.

possibly through numerical integration, for any definite conditions concerning the following: 1) the input signal via $s_a(t)$ and $p_a(u)$; 2) the input white noise via $f_\xi(u)$, and 3) the measuring array via θ, N, and $F_\eta(u)$. We shall now use this theory to illustrate the existence of conditions where enhancement of the threshold noises $\eta_i(t)$ results in an improved performance for the optimal Bayesian estimator of a from $\boldsymbol{Y}$.

III. Noise-Improved Estimation

For illustration of the possibility of a noise-improved estimation via suprathreshold SR, we consider the simple case of a constant input signal $s_a(t) \equiv a$. The input noise $\xi(t)$ is taken with zero mean and rms amplitude σ_ξ. The common threshold in the array is set at the input mean, i.e., $\theta = E[x_a(t)]$, which is known as soon as $p_a(u)$ and $f_\xi(u)$ are specified. Fig. 1 then shows the evolution of the rms estimation error $\overline{\mathcal{E}}_{\rm B}^{1/2}$ from (8) as a function of the rms amplitude σ_η of the threshold noises for various sizes N of the array when both the input noise $\xi(t)$ and the threshold noises $\eta_i(t)$ are zero-mean Gaussian.

In Fig. 1, the choice $\theta = E[x_a(t)]$ ensures that the input-signal–noise mixture $x_a(t)$ is suprathreshold, in the sense that $x_a(t)$ evolves on both sides of the threshold θ and can cross θ without assistance from the threshold noises $\eta_i(t)$. As a consequence, if the array is reduced to a single device ($N = 1$), the added threshold noise $\eta_1(t)$ does not improve the performance, and its increase monotonically degrades the estimation error $\overline{\mathcal{E}}_{\rm B}^{1/2}$, as shown in Fig. 1. When $N > 1$, in the absence of the threshold noises $\eta_i(t)$, all the quantizers in the array switch in unison, acting like a single quantizer. In this case, at $\sigma_\eta = 0$, the performance of the array does not depend on size N of the array. At $N > 1$, application of the threshold noises $\eta_i(t)$ then allows for the quantizers to differently respond. This is the source of the richer response of the array with threshold noises. For the estimation task performed from the array output, this translates into a possibility of improving the performance measured by the estimation error $\overline{\mathcal{E}}_{\rm B}^{1/2}$, with, for each $N > 1$, a nonzero optimal amount of the threshold noises that minimizes $\overline{\mathcal{E}}_{\rm B}^{1/2}$, as shown in Fig. 1. This is the suprathreshold SR effect, which is reported here in a Bayesian estimation task.

For comparison of the optimal Bayesian estimation from the array output that is addressed in Fig. 1, it is interesting to consider the same optimal estimator (the minimal-error estimator) that would directly operate on the input-signal–noise mixture $x_a(t)$ rather than on its quantized representation by the array. By applying on $x_a(t)$ the principles of optimal Bayesian estimation similar to those exposed in Section II, it comes out that, when the input noise $\xi(t)$ is zero-mean Gaussian, the optimal Bayesian estimator [31] operating directly on $x_a(t)$ is $\widehat{a}_{\rm Bin}$, which achieves the rms estimation error $\sigma_{\rm Bin}$, verifying

$$\frac{1}{\sigma_{\rm Bin}^2} = \frac{1}{\sigma_a^2} + \frac{M}{\sigma_\xi^2} \tag{13}$$

with the estimator itself reading

$$\widehat{a}_{\rm Bin} = \frac{\sigma_{\rm Bin}^2}{\sigma_a^2}{\rm E}(a) + M\frac{\sigma_{\rm Bin}^2}{\sigma_\xi^2}\overline{x}_a \tag{14}$$

with the empirical mean of the measurements $\overline{x}_a = M^{-1}\sum_{j=1}^{M} x_a(t_j)$.

In Fig. 1, the rms estimation error $\sigma_{\rm Bin}$ from (13) is represented by the dashed line. It is shown in Fig. 1 that, in the optimal Bayesian estimation from the array output, the minimal value reached by the estimation error $\overline{\mathcal{E}}_{\rm B}^{1/2}$ at the optimal level of the threshold noises, as N increases, tends to the performance $\sigma_{\rm Bin}$ of the optimal Bayesian estimator operating directly on the input-signal–noise mixture $x_a(t)$. This proves that the optimal Bayesian estimator $\widehat{a}_{\rm B}$ from the output of the array of one-bit quantizers, as the array becomes large, is able to perform as efficiently as the optimal Bayesian estimator $\widehat{a}_{\rm Bin}$ operating directly on the input-signal–noise mixture $x_a(t)$. At the same time, Fig. 1 shows that, with relatively modest sizes N, the performance of the array comes close to the best performance $\sigma_{\rm Bin}$ at the input. Advantages afforded by the array lie in the parsimony of the representation and simplicity of operation (possibly associated to rapidity), working on a few bits collected by the comparators, as opposed to the infinite number of bits, in principle, associated with the analog input $x_a(t)$. In addition, in various circumstances, it may be the case that the analog input $x_a(t)$ is not directly accessible when no linear transducers are available to form a direct image of $x_a(t)$ that is manageable by the signal-processing system.

Fig. 2 represents the evolution of the rms estimation error $\overline{\mathcal{E}}_{\rm B}^{1/2}$ in the same conditions as in Fig. 1, except for the number of data points $M = 2$. As usual, in Bayesian estimation, the theoretical calculation of the rms estimation error gets more and more computationally demanding as the number of data points M increases. This is because the rms error results from an average (expressed by multiple sums or integrals) over all

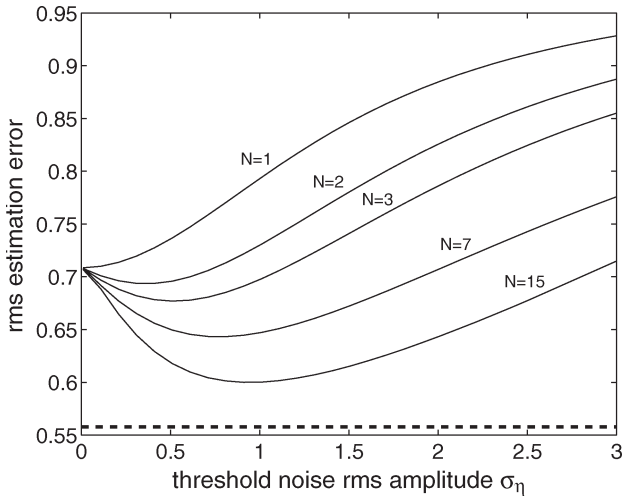

Fig. 2. Same as in Fig. 1, except that $M = 2$.

possible configurations of the data, with the number of that configurations exponentially growing with the number of data points M. This is the computational price to pay to have access to the theoretical performance of a Bayesian estimator. However, the practical application of the estimator itself on one observed data set is much more direct since this does not require averaging over all the data configurations. This explains why our calculation of the rms estimation error in Figs. 1 and 2 remains limited to small values of M. Nevertheless, the important point with Fig. 2 is to verify that the possibility of improvement by noise of the rms error $\overline{\mathcal{E}}_{\mathrm{B}}^{1/2}$ is preserved when the number M of data points increases. The minimal rms error (shown in Fig. 2 in arrays with size $N > 1$) is always achieved at a nonzero level of the added threshold noises $\eta_i(t)$, which is the SR effect.

IV. Discussion and Conclusion

To summarize, we have considered simple threshold comparators for estimation in a Bayesian framework. When such simple binary sensors are used in isolation, a rather crude estimation capability results. We have shown that, by associating these simple sensors into arrays, an enhanced estimation capability is obtained, owing to the action of added noises, through the SR phenomenon. The present results contribute to the inventory and analysis of SR, especially through the specific mechanism of SR in parallel uncoupled arrays. They also contain significance in the direction of novel architectures and processes for sensing arrays.

The results that are shown in Figs. 1 and 2 represent a new manifestation of suprathreshold SR, which is applied here for the first time to a Bayesian estimation task. The evolutions of the estimation error obtained in Figs. 1 and 2 are quite reminiscent of the evolutions of other performance indexes obtained in different instances of suprathreshold SR, namely, the Shannon mutual information in [23], the correlation coefficient in [24], the Fisher information in [25], a signal-to-noise ratio in [26], or a probability of detection error in [30]. This is an important point to note because all these indexes of performance are different and relate to distinct signal-processing tasks. This contributes to establish SR, which is understood as a possibility of noise-improved signal processing, as a general nonlinear phenomenon which can be obtained in many contexts under many distinct forms, with the ability to enhance many different performance indexes. The specific structure considered here for Bayesian estimation, i.e., parallel arrays of one-bit quantizers, can be considered as realizing a suboptimal estimator. The central contribution of the present study is to demonstrate the feasibility in this structure, for improvement by noise of Bayesian estimation. A common feature with many other forms of SR previously reported is the suboptimal character of the processor which receives improvement by noise, as stressed, for instance, in [32]. However, some optimal processors have also been shown to lend themselves to a form of SR, with a performance for the optimal processor which can improve when the optimal processor operates at a higher level of noise. This possibility of SR has been shown with optimal detectors [33]–[35] and optimal estimators [12], and the mechanism of SR in parallel arrays, as studied here, could be investigated for further improvement in this direction.

The present approach is based on SR for improvement by addition of the noises $\eta_i(t)$ to one-bit quantizers with a fixed common threshold. The procedure can also be viewed as quantization with a distribution of random thresholds. By contrast, the common approach to quantization would be to select a nonrandom distribution of the thresholds in order to optimize a specific design criterion, and many studies have been conducted along this line for optimal quantization [36]. However, finding optimal distributions of the thresholds is, generally, a difficult optimization problem; moreover, the solutions are likely to vary with the properties of the input signal $s_a(t)$ and input noise $\xi(t)$. Addition of the noises $\eta_i(t)$ with a common threshold can be considered as an SR-based alternative that dispenses one from facing the difficult and specific determination of the optimal distribution of the quantization thresholds. A good performance can, nevertheless, be obtained by this SR-based approach with a common threshold and added noises $\eta_i(t)$, as proved by the behavior of the performance of the array compared to the overall best performance given by σ_{Bin} in Figs. 1 and 2. The SR-based estimation might also reveal more robust to variations in the input $x_a(t)$ with respect to the nominal conditions of an optimal distribution of the quantization thresholds. Finally, situations may exist due to hardware limitations, where the thresholds θ_i are not separately adjustable; this could be the case, for instance, with nanodevices or with sensory neurons. However, the more complex conditions with distributed thresholds θ_i could be explicitly investigated through an extension of the present approach to uncover how the specific properties and potentialities of the noise-improved estimation evolve. Multiple parameter estimation could also be addressed as an extension to the present approach.

Compared to linear sensors, the present approach is based on quite simple nonlinear devices producing a very parsimonious one-bit representation of the signal. Estimation aided by noise with such one-bit quantizers can be specially appealing in the context of measurement for real-time processing with large-scale sensor networks. In addition, in various circumstances, the

analog input may not be accessible when no linear transducers are available for this. It will be the case, for instance, with sensory neurons, which form a thresholded all-or-nothing type of representation of an analog signal from the physical environment, bearing similarities with the representation by the present array of comparators [27], [29], [37]. This will also be the case with nanodevices with intrinsic nonlinearities and usable in building sensor microarrays [38]. The estimation aided by noise that we have described in arrays can be specially relevant in these contexts of intrinsically nonlinear sensing networks. This can provide a basis for devising novel unconventional intelligent sensing arrays that are capable of exploiting the noise.

REFERENCES

[1] O. Kanoun and H. R. Tränkler, "Sensor technology advances and future trends," *IEEE Trans. Instrum. Meas.*, vol. 53, no. 6, pp. 1497–1501, Dec. 2004.

[2] J. S. Wilson, *Sensor Technology Handbook*. Boston, MA: Newnes, 2004.

[3] M. D. McDonnell, D. Abbott, and C. E. M. Pearce, "An analysis of noise enhanced information transmission in an array of comparators," *Microelectron. J.*, vol. 33, no. 12, pp. 1079–1089, Dec. 2002.

[4] M. A. Arbib, *The Handbook of Brain Theory and Neural Networks*. Cambridge, MA: MIT Press, 2002.

[5] L. Gammaitoni, P. Hänggi, P. Jung, and F. Marchesoni, "Stochastic resonance," *Rev. Modern Phys.*, vol. 70, no. 1, pp. 223–287, Jan. 1998.

[6] B. Andò, S. Baglio, S. Graziani, and N. Pitrone, "Optimal improvement in bistable measurement device performance via stochastic resonance," *Int. J. Electron.*, vol. 86, no. 7, pp. 791–806, Jul. 1999.

[7] B. Andò and S. Graziani, *Stochastic Resonance: Theory and Applications*. Boston, MA: Kluwer, 2000.

[8] B. Andò, S. Baglio, S. Graziani, and N. Pitrone, "Measurements of parameters influencing the optimal noise level in stochastic systems," *IEEE Trans. Instrum. Meas.*, vol. 49, no. 5, pp. 1137–1143, Oct. 2000.

[9] B. Andò and S. Graziani, "Adding noise to improve measurement," *IEEE Instrum. Meas. Mag.*, vol. 4, no. 1, pp. 24–30, Mar. 2001.

[10] G. P. Harmer, B. R. Davis, and D. Abbott, "A review of stochastic resonance: Circuits and measurement," *IEEE Trans. Instrum. Meas.*, vol. 51, no. 2, pp. 299–309, Apr. 2002.

[11] A. Nikitin, N. G. Stocks, and A. R. Bulsara, "Signal detection via residence times statistics: Noise-mediated minimization of the measurement error," *Phys. Rev. E, Stat. Phys. Plasmas Fluids Relat. Interdiscip. Top.*, vol. 68, no. 3, pp. 036 133-1–036 133-4, Sep. 2003.

[12] F. Chapeau-Blondeau and D. Rousseau, "Noise-enhanced performance for an optimal Bayesian estimator," *IEEE Trans. Signal Process.*, vol. 52, no. 5, pp. 1327–1334, May 2004.

[13] S. Mitaim and B. Kosko, "Adaptive stochastic resonance," *Proc. IEEE*, vol. 86, no. 11, pp. 2152–2183, Nov. 1998.

[14] G. P. Harmer and D. Abbott, "Simulation of circuits demonstrating stochastic resonance," *Microelectron. J.*, vol. 31, no. 7, pp. 553–559, Jul. 2000.

[15] J. J. Collins, C. C. Chow, and T. T. Imhoff, "Stochastic resonance without tuning," *Nature*, vol. 376, no. 6537, pp. 236–238, Jul. 1995.

[16] Z. Gingl, L. B. Kiss, and F. Moss, "Non-dynamical stochastic resonance: Theory and experiments with white and arbitrarily coloured noise," *Europhys. Lett.*, vol. 29, no. 3, pp. 191–196, Jan. 1995.

[17] M. E. Inchiosa and A. R. Bulsara, "Signal detection statistics of stochastic resonators," *Phys. Rev. E, Stat. Phys. Plasmas Fluids Relat. Interdiscip. Top.*, vol. 53, no. 3, pp. R2 021–R2 024, Mar. 1996.

[18] X. Godivier, J. Rojas-Varela, and F. Chapeau-Blondeau, "Noise-assisted signal transmission via stochastic resonance in a diode nonlinearity," *Electron. Lett.*, vol. 33, no. 20, pp. 1666–1668, Sep. 1997.

[19] D. G. Luchinsky, R. Mannella, P. V. E. McClintock, and N. G. Stocks, "Stochastic resonance in electrical circuits—I: Conventional stochastic resonance," *IEEE Trans. Circuits Syst. II*, vol. 46, no. 9, pp. 1205–1214, Sep. 1999.

[20] F. Chapeau-Blondeau, "Noise-assisted propagation over a nonlinear line of threshold elements," *Electron. Lett.*, vol. 35, no. 13, pp. 1055–1056, Jun. 1999.

[21] S. Zozor and P. O. Amblard, "On the use of stochastic resonance in sine detection," *Signal Process.*, vol. 82, no. 3, pp. 353–367, Mar. 2002.

[22] N. G. Stocks, "Suprathreshold stochastic resonance in multilevel threshold systems," *Phys. Rev. Lett.*, vol. 84, no. 11, pp. 2310–2313, Mar. 2000.

[23] N. G. Stocks, "Information transmission in parallel threshold arrays: Suprathreshold stochastic resonance," *Phys. Rev. E, Stat. Phys. Plasmas Fluids Relat. Interdiscip. Top.*, vol. 63, no. 4, pp. 041114-1–041114-9, Apr. 2001.

[24] M. D. McDonnell, D. Abbott, and C. E. M. Pearce, "A characterization of suprathreshold stochastic resonance in an array of comparators by correlation coefficient," *Fluctuation Noise Lett.*, vol. 2, no. 3, pp. L205–L220, 2002.

[25] D. Rousseau, F. Duan, and F. Chapeau-Blondeau, "Suprathreshold stochastic resonance and noise-enhanced Fisher information in arrays of threshold devices," *Phys. Rev. E, Stat. Phys. Plasmas Fluids Relat. Interdiscip. Top.*, vol. 68, no. 3, pp. 031107-1–031107-10, Sep. 2003.

[26] D. Rousseau and F. Chapeau-Blondeau, "Suprathreshold stochastic resonance and signal-to-noise ratio improvement in arrays of comparators," *Phys. Lett. A*, vol. 321, no. 5/6, pp. 280–290, Feb. 2004.

[27] N. G. Stocks and R. Mannella, "Generic noise-enhanced coding in neuronal arrays," *Phys. Rev. E, Stat. Phys. Plasmas Fluids Relat. Interdiscip. Top.*, vol. 64, no. 3, pp. 030902-1–030902-4, Sep. 2001.

[28] G. P. Harmer and D. Abbott, "Motion detection and stochastic resonance in noisy environments," *Microelectron. J.*, vol. 32, no. 12, pp. 959–967, Dec. 2001.

[29] N. G. Stocks, D. Allingham, and R. P. Morse, "The application of suprathreshold stochastic resonance to cochlear implant coding," *Fluctuation Noise Lett.*, vol. 2, no. 3, pp. L169–L181, 2002.

[30] D. Rousseau and F. Chapeau-Blondeau, "Constructive role of noise in signal detection from parallel arrays of quantizers," *Signal Process.*, vol. 85, no. 3, pp. 571–580, Mar. 2005.

[31] S. M. Kay, *Fundamentals of Statistical Signal Processing: Estimation Theory*. Englewood Cliffs, NJ: Prentice-Hall, 1993.

[32] S. Kay, "Can detectability be improved by adding noise?" *IEEE Signal Process. Lett.*, vol. 7, no. 1, pp. 8–10, Jan. 2000.

[33] F. Chapeau-Blondeau, "Stochastic resonance for an optimal detector with phase noise," *Signal Process.*, vol. 83, no. 3, pp. 665–670, Mar. 2003.

[34] D. Rousseau and F. Chapeau-Blondeau, "Stochastic resonance and improvement by noise in optimal detection strategies," *Digit. Signal Process.*, vol. 15, no. 1, pp. 19–32, Jan. 2005.

[35] F. Chapeau-Blondeau and D. Rousseau, "Constructive action of additive noise in optimal detection," *Int. J. Bifurc. Chaos*, vol. 15, no. 9, pp. 2985–2994, 2005.

[36] R. M. Gray and D. L. Neuhoff, "Quantization," *IEEE Trans. Inf. Theory*, vol. 44, no. 6, pp. 2325–2383, 1998.

[37] M. D. McDonnell and D. Abbott, "Open questions for suprathreshold stochastic resonance in sensory neural models for motion detection using artificial insect vision," in *Proc. AIP Conf.*, 2003, vol. 665, pp. L51–L58.

[38] I. Y. Lee, X. Liu, B. Kosko, and C. Zhou, "Nanosignal processing: Stochastic resonance in carbon nanotubes that detect subthreshold signals," *Nano Lett.*, vol. 3, no. 12, pp. 1683–1686, 2003.

David Rousseau was born in Le Mans, France, in 1973. He received the M.S. degree in acoustics and signal processing from the Institut de Recherche Coordination Acoustique et Musique, Paris, France, in 1996 and the Ph.D. degree in nonlinear signal processing from the Université d'Angers, Angers, France, in 2004.

He is currently a Maître de Conférences with the Université d'Angers.

François Chapeau-Blondeau was born in France in 1959. He received the Engineer Diploma from ESEO, Angers, France, in 1982, the Ph.D. degree in electrical engineering from University Paris 6, Paris, France, in 1987, and the Habilitation degree from the Université d'Angers in 1994.

In 1988, he was a Research Associate with the Department of Biophysics, Mayo Clinic, Rochester, MN, working on biomedical ultrasonics. Since 1990, he has been with the Université d'Angers, where he is currently a Professor of electronic and information sciences. His research interests include nonlinear systems and signal processing, and the interface between physics and information sciences.

D. ROUSSEAU, G. V. ANAND, and F. CHAPEAU-BLONDEAU. Noise-enhanced nonlinear detector to improve signal detection in non-Gaussian noise. *Signal Processing*, vol. 86:3456–3465, 2006.

Available online at www.sciencedirect.com
ScienceDirect
Signal Processing 86 (2006) 3456–3465
SIGNAL PROCESSING
www.elsevier.com/locate/sigpro

Noise-enhanced nonlinear detector to improve signal detection in non-Gaussian noise

David Rousseau[a,*], G.V. Anand[b], François Chapeau-Blondeau[a]

[a]*Laboratoire d'Ingénierie des Systèmes Automatisés (LISA), Université d'Angers, 62 avenue Notre Dame du Lac, 49000 Angers, France*
[b]*Department of Electrical Communication Engineering, Indian Institute of Science, Bangalore 560012, India*

Received 1 September 2005; received in revised form 23 January 2006; accepted 8 March 2006
Available online 30 May 2006

Abstract

We compare the performance of two detection schemes in charge of detecting the presence of a signal buried in an additive noise. One of these is the correlation receiver (linear detector), which is optimal when the noise is Gaussian. The other detector is obtained by applying the same correlation receiver to the output of a nonlinear preprocessor formed by a summing parallel array of two-state quantizers. We show that the performance of the collective detection realized by the array can benefit from an injection of independent noises purposely added on each individual quantizer. We show that this nonlinear detector can achieve better performance compared to the linear detector for various situations of non-Gaussian noise. This occurs for both Bayesian and Neyman–Pearson detection strategies with periodic and aperiodic signals.

Keywords: Detection; Quantizer; Nonlinear arrays; Suprathreshold stochastic resonance

1. Introduction

In presence of non-Gaussian noise, optimal detectors (in the standard Bayesian or Neyman–Pearson sense) are often nonlinear. Techniques, based on Hilbert space formalism, like in [1], can be used to derive optimal detectors in non-Gaussian noise. Yet, since optimal nonlinearities are rarely standard devices, these optimal detectors can be difficult to implement or time consuming to compute. In a context where simple processes are required to maintain fast real-time processing, one can seek a tradeoff between simplicity and efficacy by designing some suboptimal detectors. These suboptimal detectors are expected to be almost as simple to compute as the linear detector used in Gaussian noise with performances that should at least overcome the performances of the linear detector and hopefully come as close as possible to the optimal detector performances when the noise is non-Gaussian. In this suboptimal detection context, a classical approach [2,3] is to implement a nonlinear scheme composed of a nonlinear preprocessor followed by the linear scheme that would be used in a Gaussian noise.

In this article, following the approach of [2,3], we study a specific nonlinear preprocessor. We propose to design a simple suboptimal detector in non-Gaussian noise with a parallel array of two-state

*Corresponding author. Tel.: +33 241226511; fax: +33 241226561.
E-mail address: david.rousseau@univ-angers.fr (D. Rousseau).

0165-1684/$ - see front matter © 2006 Elsevier B.V. All rights reserved.
doi:10.1016/j.sigpro.2006.03.008

quantizers. Classically, the design of the input–output characteristic of such arrays is done by optimizing the distribution of the threshold of the quantizers among the array [4–8]. Here, we propose another strategy to design the input–output characteristic of our parallel array of two-state quantizers. Instead of considering a distribution of threshold, a single threshold value is shared by all the two-state quantizers of the array. Then, some independent noises are purposely injected at the input of each two-state quantizer. These noises injected onto the two-state quantizers, induce more variability and a richer representation capability in the individual responses collected over the array. We give a theoretical analysis which allows one to determine the optimal amount of the quantizer noises, this with arbitrary choices concerning the probability densities of the input and quantizer noises, the shape of the signals to be detected, and the configuration and size of the array of quantizers.

This non-standard strategy to design suboptimal detectors based on two-state quantizers benefits from recent studies on the use of stochastic resonance and the constructive role of noise in nonlinear processes [9–14]. This paradoxical nonlinear phenomenon, has been intensively studied during the last two decades. Stochastic resonance has been reported with nonlinear systems under the form of isolated two-state quantizers [15,16]. In these circumstances, the mechanism of improvement, qualitatively, is that the noise assists small signals in overcoming the threshold of the two-state quantizer. Recently, another form of stochastic resonance was proposed in [9,10], with parallel arrays of two-state quantizers, under the name of suprathreshold stochastic resonance. This form in [9–14] applies to signals of arbitrary amplitude, which do not need to be small and subthreshold, whence the name. Different measures of performance have been studied to quantify the suprathreshold stochastic resonance: general information measures like the input–output Shannon mutual information [9], the input–output correlation coefficient [11], signal-to-noise ratios [11,13], in an estimation context with the Fisher information contained in the array output [12] or in a detection context with a probability of error [14].

The first occurrence of the suprathreshold stochastic resonance effect in a detection context has been reported in [14]. The nonlinear detector under study in [14] is a Bayesian optimal detector based on the data set obtained at the output of the same nonlinear array of two-state quantizers considered here. As stated in [14], this detector is highly time consuming to compute and was more given as a first proof of feasibility of the suprathreshold stochastic resonance effect in the context of detection. By contrast, the present study proposes a more practical use of the suprathreshold stochastic resonance effect since the nonlinear detector detailed here is almost as fast as a linear detector to compute.

2. Two detection procedures

We consider the classical problem of detecting the presence of a known deterministic signal $s(t)$ buried in an additive input noise $\xi(t)$. One is to decide whether the signal $s(t)$ is present in noise (hypothesis H_1) or not (hypothesis H_0):

$$\text{hypothesis } H_1: x(t) = s(t) + \xi(t), \tag{1}$$

$$\text{hypothesis } H_0: x(t) = \xi(t). \tag{2}$$

The observable signal $x(t) = s(t) + \xi(t)$ is uniformly sampled to provide N data points $x(t_j) = x(j\tau)$ with $j = 0, 1, \ldots, N-1$ and τ the sampling step. The noise samples $\xi(t_j) = \xi(j\tau)$ are assumed independent and identically distributed with cumulative distribution $F_\xi(u)$, probability density function (pdf) $f_\xi(u) = \mathrm{d}F_\xi/\mathrm{d}u$ and rms amplitude σ_ξ. We first consider a Bayesian detection strategy where the probabilities (P_0, $P_1 = 1 - P_0$) of both hypotheses (respectively, H_0, H_1) are known. We tackle this detection problem with two distinct procedures presented in Fig. 1 that we shall describe in detail in this section.

2.1. A linear detector

In the procedure of Fig. 1a, the decision between (hypothesis H_1) and (hypothesis H_0) is directly based on the linear signal–noise mixture, the observable data set $\mathbf{x} = (x(t_0), x(t_1), \ldots, x(t_N))$. The minimum probability of error detection procedure based on $\mathbf{x}$ leads to the maximum a posteriori probability (MAP) test

$$\frac{\Pr\{H_1|\mathbf{x}\}}{\Pr\{H_0|\mathbf{x}\}} \underset{H_0}{\overset{H_1}{\gtrless}} 1. \tag{3}$$

When the input noise $\xi(t)$ is Gaussian, the MAP test of Eq. (3) takes the form of the detection procedure described in Fig. 1a [2]: a correlation receiver which computes the statistic $T(\mathbf{x}) = \sum_{j=0}^{N-1} x(t_j)s(t_j)$ is

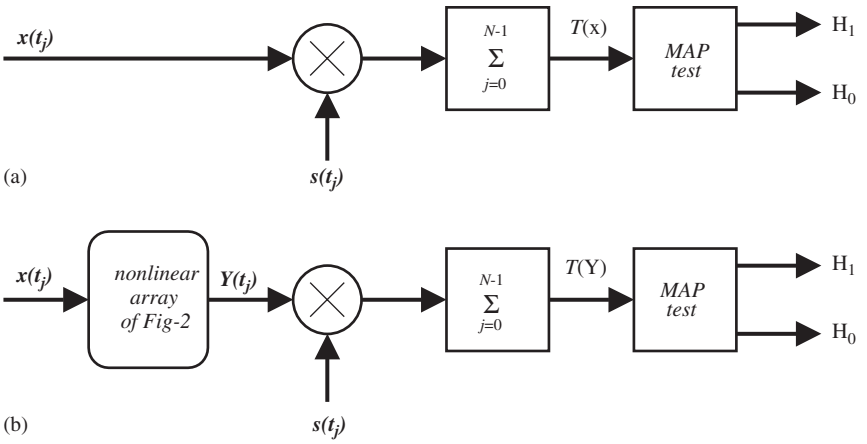

Fig. 1. Two detectors that we shall compare in terms of performance. The linear detector (a) is a standard procedure optimal for Gaussian noise. The nonlinear detector (b) is a new procedure keeping the same architecture of (a) with the introduction of a nonlinear preprocessor detailed in Fig. 2.

followed by the MAP test based on this statistic $T(\mathbf{x})$:

$$T(\mathbf{x}) \underset{\mathrm{H}_0}{\overset{\mathrm{H}_1}{\gtrless}} \frac{1}{2}\sum_{j=0}^{N-1} s(t_j)^2 + \sigma_\xi^2 \log(P_0/P_1) = x_T. \tag{4}$$

The performance of the detection procedure of Fig. 1a can be assessed by the overall probability of error minimized by Eq. (4) which is expressed as

$$P_{\mathrm{er}} = \frac{1}{2}\left[1 + P_1 \operatorname{erf}\left(\frac{x_T - m_1}{\sqrt{2}\,\sigma_1}\right) - P_0 \operatorname{erf}\left(\frac{x_T - m_0}{\sqrt{2}\,\sigma_0}\right)\right], \tag{5}$$

with $\operatorname{erf}(u) = \int_{-\infty}^{u} (1/\sqrt{2\pi}) \exp(-v^2/2)\,\mathrm{d}v$, means $m_0 = E[T(\mathbf{x})|\mathrm{H}_0]$, $m_1 = E[T(\mathbf{x})|\mathrm{H}_1]$ and variances $\sigma_0^2 = \operatorname{var}[T(\mathbf{x})|\mathrm{H}_0]$, $\sigma_1^2 = \operatorname{var}[T(\mathbf{x})|\mathrm{H}_1]$.[1] When the input noise $\xi(t)$ is non-Gaussian, the optimal detector minimizing the probability of error, in general, is more difficult to design and the MAP test of Eq. (3) does not lead to a simple test as simple as in Eq. (4). However, the detection procedure of Eq. (4) although suboptimal when the input noise is non- Gaussian is often chosen for its simplicity. By the central limit theorem, the statistic $T(\mathbf{x})$ is approximately Gaussian for large data set length N. Therefore, when the input noise $\xi(t)$ is non-Gaussian, the performance of the detector of Eq. (4) and Fig. 1a given in Eq. (5) remains valid.

[1]Note that, in this context of additive signal–noise mixture of Eqs. (1) and (2) $\sigma_0 = \sigma_1 = \sigma_\xi$, $m_0 = \sum_{j=0}^{N-1} s(t_j)E[\xi(t_j)]$ and $m_1 = \sum_{j=0}^{N-1} s(t_j)^2$.

2.2. A nonlinear detector

The detection procedure of Fig. 1b is similar to the procedure of Fig. 1a except that the data set $\mathbf{x}$ obtained from the linear signal–noise mixture $x(t) = s(t) + \xi(t)$ is not directly observable. The data set $\mathbf{x} = (x(t_1), \ldots, x(t_N))$ is first applied at the input of a nonlinear preprocessor which produces a vector $\mathbf{Y} = (Y(t_1), \ldots, Y(t_N))$ on which we shall base the decision between (hypothesis H_1) and (hypothesis H_0). The detection procedure of Fig. 1b is then composed of a correlation receiver which computes the statistic $T(\mathbf{Y}) = \sum_{j=0}^{N-1} Y(t_j)s(t_j)$ followed by the MAP test based on this statistic $T(\mathbf{Y})$,

$$\frac{\Pr\{\mathrm{H}_1|T(\mathbf{Y})\}}{\Pr\{\mathrm{H}_0|T(\mathbf{Y})\}} \underset{\mathrm{H}_0}{\overset{\mathrm{H}_1}{\gtrless}} 1. \tag{6}$$

The nonlinear preprocessor involved in the detection procedure of Fig. 1b is a parallel array of M identical two-state quantizers which has an architecture similar to the one also considered in [9,17,18]. In this array of Fig. 2, we choose to fix all the quantizer threshold θ_i to a common value $\theta_i = \theta$ for any i. Then, a noise $\eta_i(t)$, independent of $x(t)$, is added to $x(t)$ at each two-state quantizer i. Whereas the input noise $\xi(t)$ is considered as a noise imposed by the external environment, the quantizer noises $\eta_i(t)$ are considered as purposely added noises applied to influence the operation of the array. Accordingly, each quantizer i produces the output signal,

$$\begin{aligned} y_i(t_j) &= \operatorname{sign}[x(t_j) + \eta_i(t_j) - \theta_i] \\ &= \pm 1, \quad i = 1, 2, \ldots M. \end{aligned} \tag{7}$$

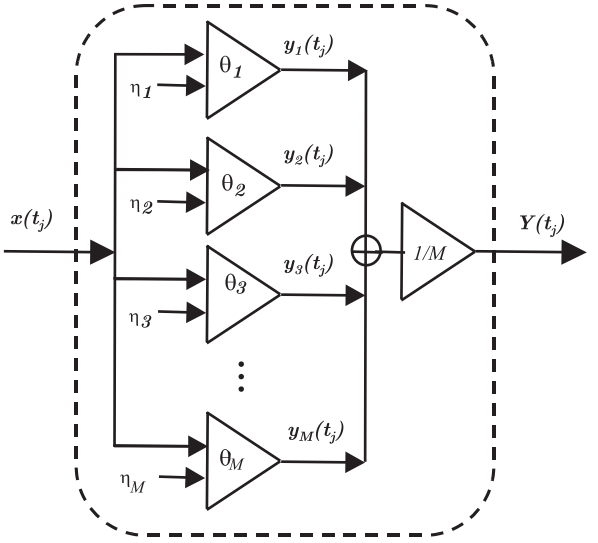

Fig. 2. Nonlinear array used as preprocessor in the detection scheme of Fig. 1b.

The M quantizer noises $\eta_i(t)$ are white, mutually independent and identically distributed with cumulative distribution function $F_\eta(u)$ and pdf $f_\eta(u) = \mathrm{d}F_\eta(u)/\mathrm{d}u$. The response $Y(t_j)$ of the array is obtained by averaging the outputs of all the quantizers as

$$Y(t_j) = \frac{1}{M}\sum_{i=1}^{M} y_i(t_j). \tag{8}$$

At the scale of the individual quantizer, the presence of the quantizer noises $\eta_i(t)$ can be interpreted as a source of variability which enable a richer representation capability when individual responses are collected over the array. Another complementary interpretation is possible with a collective point of view. Consider the array as a single device with input–output characteristic $g(.)$. Within this perspective, the quantizer noises $\eta_i(t)$ are modifying the input–output characteristic of the array $g(.)$. Naturally, the M quantizers noises $\eta_i(t)$ also bring fluctuations. But, for sufficiently large values of M these fluctuations will tend to zero. In these asymptotic conditions where M tends to infinity, the parallel array of noisy quantizers given in Eq. (8) becomes a deterministic equivalent device with input–output characteristic given by $g(x) = E[Y(t)|x]$. Therefore, the purposely added noises $\eta_i(t)$ can be seen as a mean to shape the input–output characteristic $g(.)$ of the array of comparators without having to change any physical parameter of the comparators.

In the following, we are going to compare the two detection procedures presented in Fig. 1 and show the specific interest of the nonlinear array of Fig. 2 for detection purposes. Owing to the presence, in Eq. (4), of the linear correlation receiver acting on the linear signal–noise mixture in the detection procedure of Fig. 1a, we decide to call linear detector this detection procedure. By comparison, the detection procedure of Fig. 1b, which involves the nonlinear preprocessor described in Fig. 2, will be called the nonlinear detector.

3. Assessing performances of the nonlinear detector

In this section, we give the expression of the performance (in terms of probability of error) of the nonlinear detector of Fig. 1b and Eq. (6). By Bayes' rule, the MAP test of Eq. (6) is equivalent to

$$\frac{\Pr\{T(\mathbf{Y})|\mathrm{H}_1\}}{\Pr\{T(\mathbf{Y})|\mathrm{H}_0\}} \underset{\mathrm{H}_0}{\overset{\mathrm{H}_1}{\gtrless}} \frac{P_0}{P_1}, \tag{9}$$

with the conditional probabilities $\Pr\{T(\mathbf{Y})|\mathrm{H}_1\}$ and $\Pr\{T(\mathbf{Y})|\mathrm{H}_0\}$ that we shall now address. The statistic $T(\mathbf{Y})$, defined through Eqs. (7) and (8) has mean

$$\begin{aligned} m_k &= E[T(\mathbf{Y})|\mathrm{H}_k] \\ &= \sum_{j=0}^{N-1} s(t_j) E[Y(t_j)|\mathrm{H}_k], \quad k \in \{0,1\}, \end{aligned} \tag{10}$$

with

$$E[Y(t_j)|\mathrm{H}_k] = \int_{-\infty}^{+\infty} E[Y(t_j)|x;\mathrm{H}_k] f_\xi(x - s(t_j))\,\mathrm{d}x, \tag{11}$$

and, since the quantizer noises $\eta_i(t)$ are i.i.d.,

$$E[Y(t_j)|x;\mathrm{H}_k] = E[y_i(t_j)|x;\mathrm{H}_k] = 1 - 2F_\eta(\theta - x). \tag{12}$$

Similarly, the variance of $T(\mathbf{Y})$ under hypothesis $k \in \{0,1\}$ can be expressed as

$$\begin{aligned} \sigma_k^2 &= \mathrm{var}[T(\mathbf{Y})|\mathrm{H}_k] \\ &= \sum_{j=0}^{N-1} s(t_j)^2 (E[Y^2(t_j)|\mathrm{H}_k] - E[Y(t_j)|\mathrm{H}_k]^2) \end{aligned} \tag{13}$$

with

$$\begin{aligned} &E[Y^2(t_j)|\mathrm{H}_k] \\ &= \int_{-\infty}^{+\infty} E[Y^2(t_j)|x;\mathrm{H}_k] f_\xi(x - s(t_j))\,\mathrm{d}x \end{aligned} \tag{14}$$

and

$$E[Y^2(t_j)|x;\mathrm{H}_k] = \frac{1}{M}E[y_i^2(t_j)|x;\mathrm{H}_k] + \frac{M-1}{M}E^2[y_i(t_j)|x;\mathrm{H}_k] \quad (15)$$

and, because of Eq. (7), one has for any i

$$E[y_i^2(t_j)|x;\mathrm{H}_k] = 1. \quad (16)$$

When N is large, thanks to the central limit theorem, $T(\mathbf{Y})$ gets normally distributed. The conditional probabilities in Eq. (9) are then given by

$$\Pr\{T(\mathbf{Y})|\mathrm{H}_k\} = \frac{1}{\sigma_k\sqrt{2\pi}}\exp\left[-\frac{(T(\mathbf{Y})-m_k)^2}{2\sigma_k^2}\right], \quad (17)$$

and the loglikelihood-ratio test derived from Eq. (6) follows as

$$\log\left(\frac{\sigma_0 P_1}{\sigma_1 P_0}\right) + \frac{(T(\mathbf{Y})-m_0)^2}{2\sigma_0^2} - \frac{(T(\mathbf{Y})-m_1)^2}{2\sigma_1^2} \underset{\mathrm{H}_0}{\overset{\mathrm{H}_1}{\gtrless}} 0. \quad (18)$$

With the only condition of a large data set (i.e. when N is large[2]), the performance of the nonlinear detector of Fig. 1b can be calculated with the algorithm of Fig. 3. This algorithm has already been described in [19] for specific conditions (constant signal $s(t) \equiv s_0$ or s_1 and a statistic performed on a 1-bit representation of the input signal x). Although not highlighted in [19], the algorithm of Fig. 3 can, in fact, be applied generically to any situation of detection, with no restriction on the signal to be detected.

If $\sigma_0 > \sigma_1$
  Let $\sigma_2 = \sqrt{\sigma_0^2 - \sigma_1^2}$
  If $(m_1 - m_0)^2 + 2\sigma_2^2 \ln[(\sigma_0 P_1)/(\sigma_1 P_0)] > 0$
    Let $m_2 = \sqrt{(m_1 - m_0)^2 + 2\sigma_2^2 \ln[(\sigma_0 P_1)/(\sigma_1 P_0)]}$
    Let $Y_{T1} = (\sigma_0^2 m_1 - \sigma_1^2 m_0 - \sigma_0\sigma_1 m_2)/\sigma_2^2$
    Let $Y_{T2} = (\sigma_0^2 m_1 - \sigma_1^2 m_0 + \sigma_0\sigma_1 m_2)/\sigma_2^2$
    If $Y_{T1} < T(\mathbf{Y}) < Y_{T2}$ **decide** H_1 Else **decide** H_0 End If
    $P_{\mathrm{er}} = \frac{1}{2}\left[\mathrm{erf}\left(\frac{Y_{T2}-m_0}{\sqrt{2}\sigma_0}\right) - \mathrm{erf}\left(\frac{Y_{T1}-m_0}{\sqrt{2}\sigma_0}\right)\right]P_0 + \left[1 + \frac{1}{2}\mathrm{erf}\left(\frac{Y_{T1}-m_1}{\sqrt{2}\sigma_1}\right) - \frac{1}{2}\mathrm{erf}\left(\frac{Y_{T2}-m_1}{\sqrt{2}\sigma_1}\right)\right]P_1$
  Else
    decide H_0
    $P_{\mathrm{er}} = P_1$
  End If
Else If $\sigma_0 < \sigma_1$
  Let $\sigma_2 = \sqrt{\sigma_1^2 - \sigma_0^2}$
  If $(m_1 - m_0)^2 + 2\sigma_2^2 \ln[(\sigma_1 P_0)/(\sigma_0 P_1)] > 0$
    Let $m_2 = \sqrt{(m_1 - m_0)^2 + 2\sigma_2^2 \ln[(\sigma_1 P_0)/(\sigma_0 P_1)]}$
    Let $Y_{T1} = (\sigma_1^2 m_0 - \sigma_0^2 m_1 - \sigma_0\sigma_1 m_2)/\sigma_2^2$
    Let $Y_{T2} = (\sigma_1^2 m_0 - \sigma_0^2 m_1 + \sigma_0\sigma_1 m_2)/\sigma_2^2$
    If $Y_{T1} < T(\mathbf{Y}) < Y_{T2}$ **decide** H_0 Else **decide** H_1 End If
    $P_{\mathrm{er}} = \left[1 + \frac{1}{2}\mathrm{erf}\left(\frac{Y_{T1}-m_0}{\sqrt{2}\sigma_0}\right) - \frac{1}{2}\mathrm{erf}\left(\frac{Y_{T2}-m_0}{\sqrt{2}\sigma_0}\right)\right]P_0 + \frac{1}{2}\left[\mathrm{erf}\left(\frac{Y_{T2}-m_1}{\sqrt{2}\sigma_1}\right) - \mathrm{erf}\left(\frac{Y_{T1}-m_1}{\sqrt{2}\sigma_1}\right)\right]P_1$
  Else
    decide H_1
    $P_{\mathrm{er}} = P_0$
  End If
Else If $\sigma_0 = \sigma_1$
  Let $Y_T = \frac{m_0+m_1}{2} + \frac{\sigma_0^2}{m_1-m_0}\ln(P_0/P_1)$
  If $T(\mathbf{Y}) > Y_T$ **decide** H_1 Else **decide** H_0 End If
  $P_{\mathrm{er}} = \frac{1}{2}\left[1 + P_1\,\mathrm{erf}\left(\frac{Y_T-m_1}{\sqrt{2}\sigma_0}\right) - P_0\,\mathrm{erf}\left(\frac{Y_T-m_0}{\sqrt{2}\sigma_0}\right)\right]$
End If

Fig. 3. Detection algorithm to compute and assess the performance of the nonlinear detector which is the MAP test based on the statistic $T(\mathbf{Y})$. The algorithm takes as input the set of quantities $\{T(\mathbf{Y}),\ m_0 = E[T(\mathbf{Y})|\mathrm{H}_0],\ m_1 = E[T(\mathbf{Y})|\mathrm{H}_1],\ \sigma_0^2 = \mathrm{var}[T(\mathbf{Y})|\mathrm{H}_0],\ \sigma_1^2 = \mathrm{var}[T(\mathbf{Y})|\mathrm{H}_1]\}$ and gives as output the theoretical performance P_{er} and the result of the decision for a given numerical trial for the nonlinear detector of Fig. 1b.

4. Comparing performances of the linear and nonlinear detector

We now come to compare the probability of detection error P_{er} of the nonlinear detector of Fig. 1b (given in Fig. 3) and the linear detector of Fig. 1a (given in Eq. (5)) for various conditions concerning the input noise $\xi(t)$ and the type of signals to be detected.

We first consider the case where the input noise $\xi(t)$ is zero-mean Gaussian. Fig. 4 shows the evolution of the probability of error P_{er} of Fig. 3, as a function of the rms amplitude σ_η of the quantizer noises $\eta_i(t)$, for various sizes M of the array. In these conditions, where $\xi(t)$ is Gaussian, the linear detector represents the optimal detector (in terms of lowest probability of error P_{er}) based on the data set $\mathbf{x}$. Therefore, in Fig. 4, the nonlinear detector cannot produce a lower P_{er}. Nevertheless, the performance of the nonlinear detector comes close to that of the best detector. As demonstrated at the origin of Fig. 4, this is already the case when no noise is present in the array $\sigma_\eta = 0$ although requiring only a parsimonious 1-bit representation of each data sample x_i. This observation is consistent with the one given in [19]. The new

[2]We will discuss in the next section what is the order of magnitude required to have this large data set condition fulfilled.

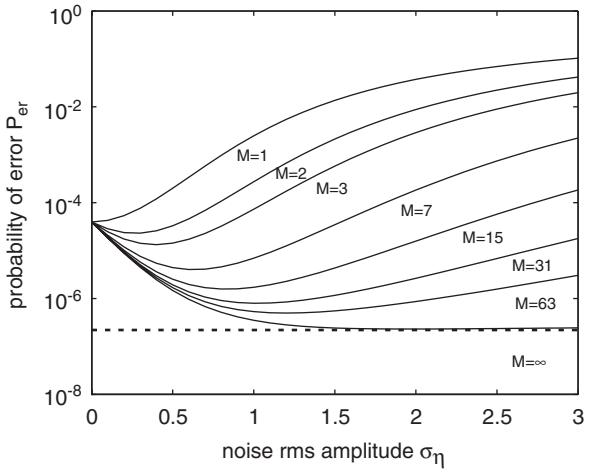

Fig. 4. Probability of detection error P_{er}, as a function of the rms amplitude σ_η of the uniform zero-mean white noises $\eta_i(t)$ purposely added to the quantizer input. The solid lines are the theoretical P_{er} of the nonlinear detector of Fig. 1b calculated from the algorithm in Fig. 3, for various size M of the array of two-state quantizer, when the input noise $\xi(t)$ is chosen Gaussian. The dashed line is the performance of the linear detector of Fig. 1a given in Eq. (4). The other parameters are $s(t) = A$ with $A/\sigma_\xi = 1$, $P_0 = 0.5$ and $N = 100$.

feature here is that it is possible to improve the performance of the nonlinear detector for a single two-state quantizer. This improvement is obtained by simply replicating the two-state quantizer and then by injecting a certain amount of independent noises in the array of quantizers. At $M>1$, application of the quantizer noises $\eta_i(t)$ allows the quantizers to respond differently. For the nonlinear detector, this translates into a possibility of minimizing P_{er} with a non-zero optimal amount of the quantizer noises. The benefit from noise is especially visible in Fig. 4, when the size of the array M increases. The explicit computation of the asymptotic behavior in large arrays is available from Eq. (15) by considering M tending to ∞. If the array size M tends to ∞, and if the optimal amount of noise is added in the array, the performance of the nonlinear detector asymptotically reaches the overall minimum probability of error P_{er} of the linear detector. This last statement, concerning the convergence of the nonlinear detector toward the linear detector, can be proved explicitly in the case of Fig. 4. As previously explained, when M tends to ∞, the array of noisy quantizers acts like a deterministic single device with input–output characteristic $g(x) = E[Y|x] = 1 - 2F_\eta(\theta - x)$ according to Eq. (12). In Fig. 4, the quantizer noises $\eta_i(t)$,

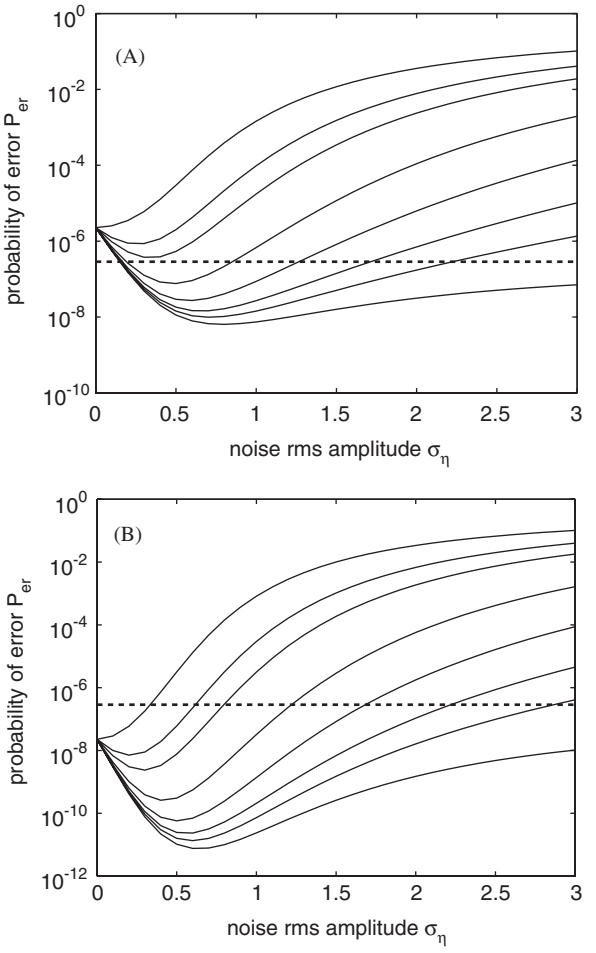

Fig. 5. Influence of the density $f_\xi(u)$ of the input noise $\xi(t)$. Panel A: same as Fig. 4 but the input noise $\xi(t)$ is zero-mean Laplacian, i.e. $\xi(t)$ is generalized Gaussian with exponent $\alpha = 1$. Panel B: same as panel A but the input noise $\xi(t)$ is a zero-mean mixture of Gaussian with parameters $\alpha = 0.8$ and $\beta = 4$. In both panels (A,B), the dashed lines stand for the performance of the linear detector given by Eq. (5).

chosen uniform, linearize the input–output characteristic $g(.)$ of the array.

When the input noise $\xi(t)$ is non-Gaussian, the linear detector is suboptimal and represents the best detection when basing the detection on $T(\mathbf{x})$ only. In this case, the nonlinear detector can produce lower P_{er} as shown in Fig. 5. This is the case when $\xi(t)$ is non-Gaussian and belongs to the generalized Gaussian noise family or the mixture of Gaussian noise family. The generalized Gaussian noise family is expressed as $f_\xi(u) = f_{gg}(u/\sigma_\xi)/\sigma_\xi$, using the standardized density

$$f_{gg}(u) = A\exp(-|bu|^\alpha), \tag{19}$$

where $b=[\Gamma(3/\alpha)/\Gamma(1/\alpha)]^{1/2}$, $A=(\alpha/2)[\Gamma(3/\alpha)]^{1/2}/[\Gamma(1/\alpha)]^{3/2}$ are parameterized by the positive exponent α. This family includes the Gaussian case ($\alpha=2$) but also enables leptokurtic noise densities whose tails are either heavier ($\alpha<2$) or lighter ($\alpha>2$) than that of the Gaussian noise. The mixture of Gaussian pdf is expressed as $f_\xi(u)=f_{\mathrm{mg}}(u/\sigma_\xi)/\sigma_\xi$, using the standardized density

$$f_{\mathrm{mg}}(u)=\frac{c}{\sqrt{2\pi}}\left[\alpha\exp\left(-\frac{c^2u^2}{2}\right)+\frac{1-\alpha}{\beta}\exp\left(-\frac{c^2u^2}{2\beta^2}\right)\right], \tag{20}$$

where $c=[\alpha+(1-\alpha)(\beta^2)]^{1/2}$; $\alpha\in[0,1]$ is the mixing parameter and $\beta>0$ is the ratio of the standard deviations of the individual contributions. All the pdf of the mixture of Gaussian noise family have Gaussian tails. This family of pdf's has practical implication since it is a subclass of Middleton's class which is widely used to model ocean acoustic noise [20]. As illustrated in Fig. 5, our analysis establishes that the superiority of the nonlinear detector over the linear detector especially occurs for various situations of non-Gaussian noises $\xi(t)$ having Gaussian or heavy tails.

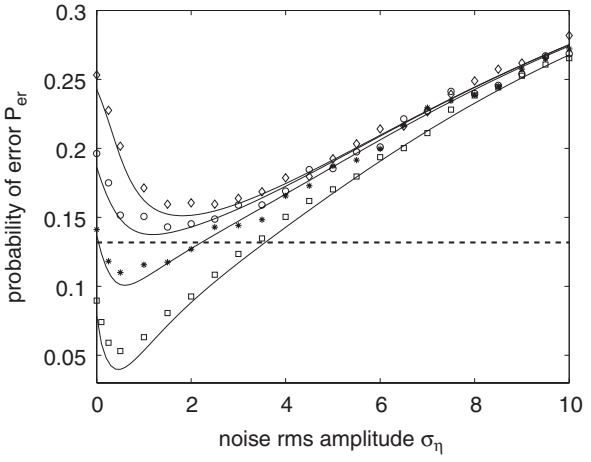

Fig. 6. Probability of detection error P_{er}, as a function of the rms amplitude σ_η of the Gaussian zero-mean white noise $\eta_i(t)$ purposely added to the quantizer input. The solid lines are the theoretical P_{er} of the nonlinear detector of Fig. 1b calculated from the algorithm in Fig. 3, with a quantizer array of fixed size $M=63$, for various probability densities of the input noise $\xi(t)$ according to Eq. (19). The discrete data points are the corresponding numerical estimations of P_{er} over 10^4 trials with: ($\diamond$) $\alpha=\infty$ (ξ uniform), ($\circ$) $\alpha=2$ (ξ Gaussian), ($*$) $\alpha=1$ (ξ Laplacian), ($\square$) $\alpha=\frac{1}{2}$. The dashed line is the performance of the linear detector scheme based on the linear statistic $T(\mathbf{x})$ of Eq. (4) given by the same algorithm in Fig. 3. The other parameters are $s(t)=A\cos(2\pi t/T_s)$, $A/\sigma_\xi=1$, $P_0=0.5$, $\tau=T_s/10$ and $N=10$.

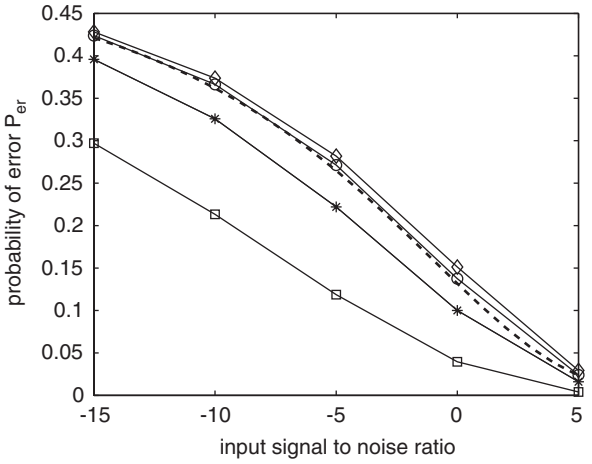

Fig. 7. Best performance of the nonlinear detector error as a function of the input signal-to-noise ratio in dB. For each discrete point the rms amplitude σ_η of the Gaussian zero-mean white noise $\eta_i(t)$ purposely added to the quantizer input is fixed in order to minimize the probability of error. Same conditions as in Fig. 6 except the solid lines which are just guides for the eye. In the context of Fig. 6, the input signal-to-noise ratio in dB is $10\log_{10}((A^2/2)/\sigma_\xi^2)$.

Fig. 6 offers a validation of the nonlinear detection algorithm of Fig. 3 through the numerical evaluation of P_{er}. The results of Fig. 3 are obtained on data sets of size $N=10$. They show that the algorithm of Fig. 3 and the associated expressions of P_{er} although valid in principle in the large N limit, also constitute a very good approximation for small N. Therefore, the superiority observed for the nonlinear detector over the linear detector (due to the presence of the nonlinear array used as preprocessor) and the performance gain brought by the injection of independent noises in the array are robustly preserved for small data sets N. Fig. 7 demonstrates that this superiority of the nonlinear detector over the linear detector is available over a large range of input signal-to-noise ratio.

5. Enlarging to a Neyman–Pearson detection strategy

In this section, we show that the usefulness of the nonlinear array of Fig. 2, when the input noise $\xi(t)$ is non-Gaussian, can easily be extended to another detection strategy. Until now, we have compared the detection performance of the linear detector and the nonlinear detector of Fig. 1 assessed by the

probability of error (expected as small as possible). This Bayesian detection strategy requires that probabilities (P_0, $P_1 = 1 - P_0$) of both hypotheses (respectively, H_0, H_1) of Eq. (2) are known. This assumption, typically valid in the domain of telecommunication, is not possible in other applications such as sonar or radar [2]. When P_0 and P_1 are unknown, if the decision between (hypothesis H_1) and (hypothesis H_0) is directly based on the linear signal–noise mixture, the observable data set $\mathbf{x}$, a strategy to implement an optimal detection is to seek to maximize the probability of detection

$$P_D = \int_{\mathscr{R}_1} p(\mathbf{x}|H_1)\,d\mathbf{x}, \tag{21}$$

while keeping the probability of false alarm

$$P_F = \int_{\mathscr{R}_1} p(\mathbf{x}|H_0)\,d\mathbf{x} \tag{22}$$

no larger than a prescribed level $P_{F,sup}$. This constrained maximization is achieved by the optimal Neyman–Pearson detector, which also implements a likelihood-ratio test. When the input noise $\xi(t)$ is Gaussian the best detector in the Neyman–Pearson sense takes a form very similar to the linear detector described in Fig. 1a [2]: a correlation receiver which computes the statistic $T(\mathbf{x}) = \sum_{j=0}^{N-1} x(t_j)s(t_j)$ is followed by the Neyman–Pearson likelihood-ratio test based on this statistic $T(\mathbf{x})$,

$$L(T(\mathbf{x})) \underset{H_0}{\overset{H_1}{\gtrless}} \mu(P_{F,sup}), \tag{23}$$

with a threshold $\mu(P_{F,sup})$, a function of $P_{F,sup}$, which is found from Eq. (22) by imposing $P_F \leqslant P_{F,sup}$. The probability of detection of this Neyman–Pearson linear detector is given by

$$P_D = \mathrm{erfc}\left(\mathrm{erfc}^{-1}(P_{F,sup})\frac{\sigma_0}{\sigma_1} - \frac{m_1 - m_0}{\sigma_0}\right) \tag{24}$$

with, for $k \in \{0,1\}$, means $m_k = E[T(\mathbf{x})|H_k]$, variance $\sigma_k^2 = \mathrm{var}[T(\mathbf{x})|H_k]$ and $\mathrm{erfc}(u) = \int_u^{+\infty}(1/\sqrt{2\pi})\exp(-v^2/2)\,dv$. When the input noise $\xi(t)$ is non-Gaussian, the optimal detector in the Neyman–Pearson, in general, is difficult to design. The same nonlinear array of Fig. 2 can be used again as preprocessor to design a simple suboptimal nonlinear detector capable of outperforming the Neyman–Pearson linear detector when the input noise $\xi(t)$ is non-Gaussian. Therefore, this Neyman–Pearson nonlinear detector first applies the observable data set $\mathbf{x} = (x(t_1), \ldots, x(t_N))$ at the input of the nonlinear array of Fig. 2 which produces a vector $\mathbf{Y} = (Y(t_1), \ldots, Y(t_N))$. The Neyman–Pearson nonlinear detector is then composed of a correlation receiver which computes the statistic $T(\mathbf{Y}) = \sum_{j=0}^{N-1} Y(t_j)s(t_j)$ followed by the likelihood-ratio test based on this statistic $T(\mathbf{Y})$,

$$L(T(\mathbf{Y})) \underset{H_0}{\overset{H_1}{\gtrless}} \mu(P_{F,sup}). \tag{25}$$

The performance of the Neyman–Pearson nonlinear detector of Eq. (23) is given by Eq. (24) with, for $k \in \{0,1\}$, $m_k = E[T(\mathbf{Y})|H_k]$, variance $\sigma_k^2 = \mathrm{var}[T(\mathbf{Y})|H_k]$, which have been given in Section 3. Fig. 8 shows that the Neyman–Pearson nonlinear detector can produce larger P_D than the one produced by the Neyman–Pearson linear detector when the noise is non-Gaussian. This observation, consistent with the result presented in Figs. 5 and 6 for another detection strategy, enlarges the usefulness of the nonlinear array of Fig. 2 as preprocessor for detection purposes.

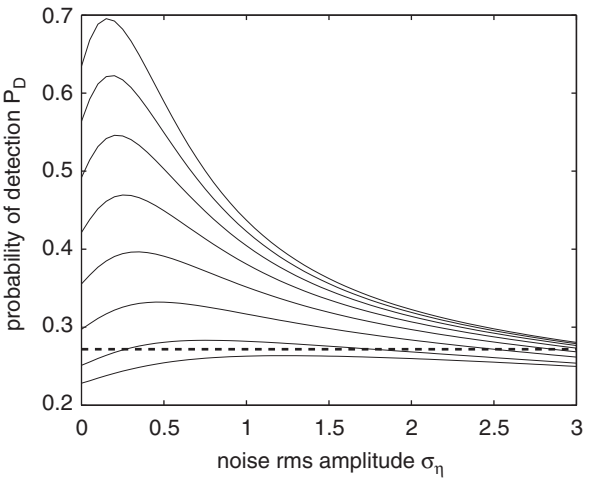

Fig. 8. Probability of correct detection P_D for a fixed probability of false alarm $P_{F,sup} = 0.1$, as a function of the rms amplitude σ_η of the Gaussian zero-mean white noise $\eta_i(t)$ purposely added to the quantizer input. The solid lines are the theoretical P_D of the Neyman–Pearson nonlinear detector of Eq. (25) calculated from Eq. (24), with a quantizer array of fixed size $M = 63$, for various probability densities of the input noise $\xi(t)$ according to Eq. (20). From up to bottom, the input noise $\xi(t)$ is a mixture of Gaussian with parameters $\alpha = 0.8$ and $\beta = 8, 7, 6, 5, 4, 3, 2, 1$. The dashed line is the performance of the Neyman–Pearson linear detector of Eq. (25) given by Eq. (24). The other parameters are $s(t) = A\exp(-vt)\cos(2\pi t/T_s)$, $A/\sigma_\xi = 1$, $v = 100/T_s$, $\tau = T_s/20$ and $N = 100$.

6. Discussion

We have studied the usefulness of a specific nonlinear preprocessor, a parallel array of two-state quantizers, to design simple suboptimal detectors in non-Gaussian noise. To do so, we have considered a standard two hypotheses detection problem and we have assessed the performance of two kinds of detectors:

(i) Standard linear detectors, optimal in Gaussian noise, composed of a correlation receiver followed by a binary test.
(ii) Nonlinear detectors, composed of the nonlinear preprocessor under study followed by a structure identical to the one of the linear detectors.

The performance of these linear and nonlinear detectors have been compared in a Bayesian and in a Neyman–Pearson detection strategy when the signal to be detected and the native non-Gaussian noise are known a priori. This comparison is meaningful since the linear detectors are often used even when the noise is a priori known to be non-Gaussian. This suboptimal choice is specially made for fast real-time hard processing, to maintain a simple test statistic on which to base the detection. The nonlinear detector considered here is almost as fast to compute as the linear detector. In addition of being compatible with a fast real-time hard implementation, we have shown that this nonlinear detector can achieve better performance compared to the linear detector for various non-Gaussian noise of practical interest. As illustrated in this article, this occurs for both Bayesian and Neyman–Pearson detection strategy with a large range of input signal $s(t)$ amplitude with various types including constant signals (in Figs. 4 and 5), periodic signals (in Fig. 6) and aperiodic signals (in Fig. 8).

These results have been obtained with a non-standard configuration of the parallel array quantizers. Instead of adopting a classical distributed-threshold configuration, we have used a simpler common-threshold configuration in which some noise have purposely been injected in order to shape the input–output characteristic of the array seen as a single device. The resulting input–output characteristic of the array depends on the choice of the injected noises and quantizer characteristics. In this article, we have chosen to study an array of two-state quantizers associated with noises in the array that were uniform or Gaussian. Many other associations could be investigated with variations concerning the type of noises injected in the array or the characteristic of the quantizers. It is remarkable to note that the simple associations tested in this study can be useful to design suboptimal detectors for the variety of non-Gaussian noise pdf that we have explored here. Such simple associations of standard noises and existing electronic devices which can easily be replicated, at a micro- or nano-scale, to constitute large arrays, could also exist for other detection problem in non-Gaussian noises of practical interest (like speckle noise in coherent imaging). These research could benefit from the theoretical framework of this study since it allows to consider any kind of static nonlinearity. Another possible interesting extension would be to draw the design of adaptive procedures, which would extend those introduced for conventional stochastic resonance [21] and which would let the array automatically increase the array noises above zero until an optimal efficacy is reached.

At a general level, this report contributes to extend our understanding of noise enhanced signal processing. The idea that an addition of a certain controlled amount of noise can be useful in the processing of information carrying signals by static quantizers is not new in itself. All occurrences of this phenomenon in static quantizers are often thought to illustrate the dithering effect [22]. In this well-known dithering effect, a noise induces threshold crossing and linearizes on average the quantizer characteristic. This is clearly not the case here since when the input noise has a non-Gaussian pdf, averaging the individual independent response of the two-state quantizers leads to a collective detection performance that outperforms the linear detector applied to the original analog data. This proves that the noise-enhanced detection performance reported here cannot be interpreted as a noise-induced linearization of a nonlinear system. Many counter-intuitive contributions of noise in nonlinear signal processing may still be uncovered and ought to be analyzed in detail.

References

[1] D.L. Duttweiler, T. Kailath, RKHS approach to detection and estimation problems—part IV: non-Gaussian detection, IEEE Trans. Inform. Theory 19 (1973) 19–28.
[2] S. Kay, Fundamentals of Statistical Signal Processing: Detection Theory, Prentice-Hall, Englewood Cliffs, NJ, 1998.

[3] N.H. Lu, B.A. Einstein, Detection of weak signals in non-Gaussian noise, IEEE Trans. Inform. Theory IT-27 (1981) 755–771.
[4] S. Kassam, Optimum quantization for signal detection, IEEE Trans. Comm. 25 (1977) 479–484.
[5] H.V. Poor, J.B. Thomas, Applications of Ali–Silvey distance measures in the design of generalized quantizers for binary decision systems, IEEE Trans. Comm. 25 (1977) 893–900.
[6] B. Aazhang, H.V. Poor, On optimum and nearly optimum data quantization for signal detection, IEEE Trans. Comm. 32 (1984) 745–751.
[7] B. Picinbono, P. Duvaut, Optimum quantization for detection, IEEE Trans. Comm. 36 (1988) 1254–1258.
[8] C. Duchene, P.-O. Amblard, S. Zozor, Quantizer-based suboptimal detectors: noise-enhanced performance and robustness, International Symposium on Fluctuations and Noise (FN'05), Proceedings of the SPIE, vol. 5847, Austin, TX, USA, 23–26 May 2005, pp. 100–110.
[9] N.G. Stocks, Suprathreshold stochastic resonance in multilevel threshold systems, Phys. Rev. Lett. 84 (2000) 2310–2313.
[10] N.G. Stocks, Information transmission in parallel threshold arrays: suprathreshold stochastic resonance, Phys. Rev. E 63 (2001) 041114,1–9.
[11] M.D. McDonnell, D. Abbott, C.E.M. Pearce, A characterization of suprathreshold stochastic resonance in an array of comparators by correlation coefficient, Fluctuation Noise Lett. 2 (2002) L205–L220.
[12] D. Rousseau, F. Duan, F. Chapeau-Blondeau, Suprathreshold stochastic resonance and noise-enhanced Fisher information in arrays of threshold devices, Phys. Rev. E 68 (2003) 031107,1–10.
[13] D. Rousseau, F. Chapeau-Blondeau, Suprathreshold stochastic resonance and signal-to-noise ratio improvement in arrays of comparators, Phys. Lett. A 321 (2004) 280–290.
[14] D. Rousseau, F. Chapeau-Blondeau, Constructive role of noise in signal detection from parallel arrays of quantizers, Signal Processing 85 (2005) 571–580.
[15] X. Godivier, F. Chapeau-Blondeau, Noise-assisted signal transmission in a nonlinear electronic comparator: experiment and theory, Signal Processing 56 (1997) 293–303.
[16] L. Gammaitoni, P. Hänggi, P. Jung, F. Marchesoni, Stochastic resonance, Rev. Mod. Phys. 70 (1998) 223–287.
[17] E. Pantazelou, F. Moss, D. Chialvo, Noise sampled signal transmission in an array of Schmitt triggers, in: P.H. Handel, A.L. Chung (Eds.), Noise in Physical Systems and $1/f$ Fluctuations, AIP Conference Proceedings, vol. 285, New York, 1993, pp. 549–552.
[18] J.J. Collins, C.C. Chow, T.T. Imhoff, Stochastic resonance without tuning, Nature 376 (1995) 236–238.
[19] F. Chapeau-Blondeau, Nonlinear test statistic to improve signal detection in non-Gaussian noise, IEEE Signal Process. Lett. 7 (2000) 205–207.
[20] F.W. Machell, C.S. Penrod, G.E. Ellis, Statistical characteristics of ocean acoustic noise process, in: E.J. Wegman, S.C. Schwartz, J.B. Thomas (Eds.), Topics in Non-Gaussian Signal Processing, Springer, Berlin, 1989, pp. 29–57.
[21] B. Kosko, S. Mitaim, Robust stochastic resonance: signal detection and adaptation in impulsive noise, Phys. Rev. E 64 (2001) 051110,1–11.
[22] L. Gammaitoni, Stochastic resonance and the dithering effect in threshold physical systems, Phys. Rev. E 52 (1995) 4691–4698.

S. BLANCHARD, D. ROUSSEAU, and F. CHAPEAU-BLONDEAU. Noise enhancement of signal transduction by parallel arrays of nonlinear neurons with threshold and saturation. *Neurocomputing*, vol. 71:333–341, 2007.

Available online at www.sciencedirect.com
ScienceDirect
Neurocomputing 71 (2007) 333–341
NEUROCOMPUTING
www.elsevier.com/locate/neucom

Noise enhancement of signal transduction by parallel arrays of nonlinear neurons with threshold and saturation

Solenna Blanchard, David Rousseau, François Chapeau-Blondeau*

Laboratoire d'Ingénierie des Systèmes Automatisés (LISA), Université d'Angers, 62 avenue Notre Dame du Lac, 49000 Angers, France

Received 2 June 2006; received in revised form 7 November 2006; accepted 7 December 2006
Communicated by V. Jirsa
Available online 20 February 2007

Abstract

A classic model neuron with threshold and saturation is used to form parallel uncoupled neuronal arrays in charge of the transduction of a periodic or aperiodic noisy input signal. The impact on the transduction efficacy of added noises is investigated. In isolated neurons, improvement by noise is possible only in the subthreshold and in the strongly saturating regimes of the neuronal response. In arrays, improvement by noise is always reinforced, and it becomes possible in all regimes of operation, i.e. in the threshold, in the saturation, and also in the intermediate curvilinear part of the neuronal response. All the configurations of improvement by noise apply equally to periodic and to aperiodic signals. These results extend the possible forms of stochastic resonance or improvement by noise accessible in neuronal systems for the processing of information.

Keywords: Neuronal transduction; Stochastic resonance; Array; Saturation; Threshold; Noise

1. Introduction

Neurons interconnected in networks are very efficient for signal and information processing, through detailed modalities and mechanisms which are still under intense investigation. Neurons are intrinsically nonlinear devices. It is now known that in nonlinear processes, the presence or even the injection of noise, can play a beneficial role for signal and information processing. This type of useful-noise phenomena have been widely investigated under the denomination of stochastic resonance [15,1]. Many forms of stochastic resonance or improvement by noise have been reported in various nonlinear systems involved in diverse signal processing operations. Several forms of stochastic resonance have been reported in neural processes (see for instance [14,12] for early experimental demonstrations, and [21] for a recent overview). At the level of the nonlinear neuron, many reported instances of stochastic resonance essentially rely on the threshold or excitable dynamics inherent to the neuron. In such situations, there is usually a small information-carrying signal, which is by itself too weak to elicit an efficient response from the threshold or excitable dynamics. The noise then cooperates constructively with the small signal, in such a way as to elicit a more efficient neuronal response.

Recently, a new mechanism of stochastic resonance has been exhibited when threshold or excitable nonlinearities are assembled into an uncoupled parallel array. This new form has been introduced under the name of suprathreshold stochastic resonance in [25,26], because in the array, addition of noise can improve the transmission of an input signal with arbitrary amplitude, not necessarily a small subthreshold signal. A parallel array is a common architecture for neuron assemblies, especially in sensory systems in charge of the transduction of noisy signals from the environment. Stochastic resonance has been shown possible in neuronal parallel arrays, with various models for the threshold or excitable nonlinear dynamics of the neuron. In neuronal arrays, Collins et al. [11], Chialvo et al. [9], and Hoch et al. [18,19] show stochastic resonance essentially with a subthreshold input signal, while Stocks [24], Stocks and Mannella [27], and Hoch et al. [17] show the novel form of suprathreshold stochastic resonance.

*Corresponding author.
E-mail address: chapeau@univ-angers.fr (F. Chapeau-Blondeau).

0925-2312/$ - see front matter © 2007 Elsevier B.V. All rights reserved.
doi:10.1016/j.neucom.2006.12.014

In the neuronal arrays, suprathreshold stochastic resonance is shown in [24,17] with simple threshold binary neurons, meanwhile Collins et al. [11], and Stocks and Mannella [27] for this investigate an excitable FitzHugh–Nagumo model in its subthreshold and suprathreshold regimes.

For isolated nonlinear systems, it has recently been shown that stochastic resonance can also operate in threshold-free nonlinearities with saturation, where the noise has the ability to reduce the distortion experienced by a signal because of the saturation [23], with an extension to arrays of threshold-free sensors with saturation given in [8]. Saturation is also a feature present in the neuronal response, and this effect of stochastic resonance at saturation has been shown to occur [22] in the transmission by a nonlinear neuron in its saturating region. More detailedly, Rousseau and Chapeau-Blondeau [22] demonstrate that in signal transmission by an isolated neuron, improvement by noise can take place both in the region of the threshold and in the region of the saturation; in between, when the neuron operates in the intermediate region avoiding both the threshold and the saturation, then improvement by noise does not take place. In the present paper, we shall consider the same type of neuron model with saturation as in [22]; we shall assemble these neurons into a parallel array, and investigate the impact of added noise in the array. We shall exhibit that different occurrences of stochastic resonance take place in the array. We shall show in the array that stochastic resonance is present in the threshold and in the saturation regimes of the neuronal response, just like in the case of an isolated neuron, but always with an increased efficacy brought in by the array. In addition, we shall show that in the array, stochastic resonance also takes place in the intermediate regime of operation that avoids both the threshold and the saturation of the neuron. Stochastic resonance does not arise in isolated neurons in this regime, but the property becomes possible in neuronal arrays through a truly specific array effect.

2. The model of neuronal array

We consider the neuron model of [22]. The input signal to the neuron, at time t, is taken as the total somatic current $I(t)$. This input current $I(t)$ may result from presynaptic neuronal activities, or also from an external stimulus of the environment for sensory neurons, a situation to which stochastic resonance effects are specially relevant. The output response of the neuron is taken as the short-term firing rate $f(t)$ at which action potentials are emitted in response to $I(t)$. A classic modeling of the integrate-and-fire dynamics of the neuron leads to an input–output firing function $g(.)$, under the so-called Lapicque form [20,4]

$$f(t) = g[I(t)] = \begin{cases} 0 & \text{for } I(t) \leqslant I_{\text{th}}, \\ \dfrac{1/T_{\text{r}}}{1-(\tau_{\text{m}}/T_{\text{r}})\ln[1-I_{\text{th}}/I(t)]} & \text{for } I(t) > I_{\text{th}}. \end{cases} \tag{1}$$

In the firing function of Eq. (1), a threshold current arises as $I_{\text{th}} = V_{\text{th}}/R_{\text{m}}$, with V_{th} the standard firing potential of the neuron, and R_{m} its total membrane resistance. Also in Eq. (1), τ_{m} is the membrane time constant, and T_{r} the neuron refractory period. We take the typical values as in [22]: $V_{\text{th}} = 10\,\text{mV}$ above the neuron resting potential, $R_{\text{m}} = 100\,\text{M}\Omega$ leading to $I_{\text{th}} = 0.1\,\text{nA}$, and $\tau_{\text{m}} = 10\,\text{ms}$ and $T_{\text{r}} = 1\,\text{ms}$. The resulting neuron firing function of Eq. (1) is depicted in Fig. 1.

Although resulting from a very simplified description of the neuronal dynamics, the firing function of Eq. (1) is able to capture essential features of the neuron response [20,4] characterized by the presence of a threshold, a saturation, and in between a smooth curvilinear part.

A number N of identical neurons modeled as Eq. (1) and labeled with index $i = 1$ to N, are assembled into an uncoupled parallel array. Each neuron i in the array receives a common input signal $I(t)$. There is also, at the level of each neuron i, a local noise $\eta_i(t)$, independent of $I(t)$, which adds to $I(t)$ and leads to the response of neuron i as

$$f_i(t) = g[I(t) + \eta_i(t)], \quad i = 1, 2, \ldots, N. \tag{2}$$

The N noises $\eta_i(t)$ are assumed white, mutually independent and identically distributed (i.i.d.) with probability density function $p_\eta(u)$. The response $y(t)$ of the array can be taken as the sum $\sum_{i=1}^{N} f_i(t)$ or as the average $N^{-1}\sum_{i=1}^{N} f_i(t)$ of the N neuron outputs, and both quantities would behave in the same way in the present study; for the sequel we will consider

$$y(t) = \frac{1}{N}\sum_{i=1}^{N} f_i(t). \tag{3}$$

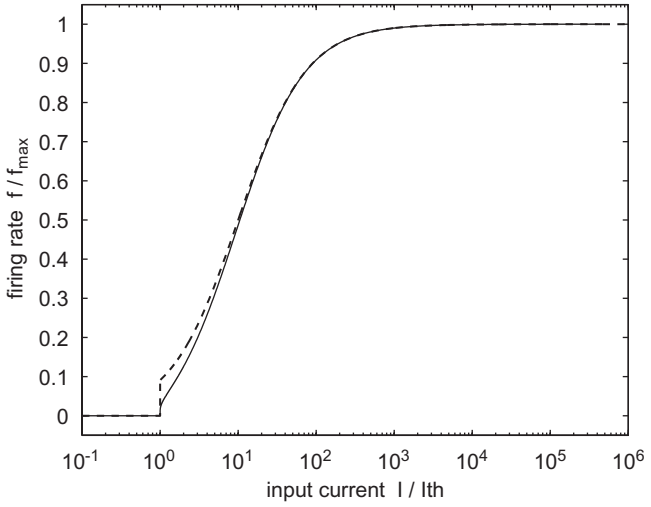

Fig. 1. Output firing rate $f(t)$ in units of $f_{\text{max}} = 1/T_{\text{r}}$, as a function of the input somatic current $I(t)$ in units of I_{th}, in typical conditions with $\tau_{\text{m}} = 10\,\text{ms}$, $T_{\text{r}} = 1\,\text{ms}$ and $I_{\text{th}} = 0.1\,\text{nA}$, according to the neuron firing function Eq. (1) (solid line) and its approximation Eq. (17) (dashed line).

3. Assessing nonlinear transmission by the array

To demonstrate a neuronal transmission aided by noise, we consider that the input current $I(t)$ to the array is formed as

$$I(t) = s(t) + \xi(t). \tag{4}$$

In Eq. (4), $s(t)$ is our information-carrying signal, which will be successively considered to be a periodic and an aperiodic component. $s(t)$ conveys an image of the information coming from presynaptic neurons or from the external world for sensory cells. Also in Eq. (4), $\xi(t)$ is a white noise, independent of $s(t)$ and of the $\eta_i(t)$, with probability density function $p_\xi(u)$. This noise $\xi(t)$ may have its origin in random activities of presynaptic neurons, or in the external environment. The input signal-plus-noise mixture $I(t) = s(t) + \xi(t)$ is transmitted by the neuronal array to produce the corresponding output $y(t)$ via Eqs. (2)–(3). We will now study the impact of the array noises $\eta_i(t)$ on the efficacy of transmission of $s(t)$ by the array.

3.1. Periodic signal transmission

To assess the transmission efficacy, when $s(t)$ is a periodic signal with period T_s, a standard measure in stochastic resonance studies is the signal-to-noise ratio (SNR), defined in the frequency domain [5,15]. At the output, the SNR measures in $y(t)$ the power contained in the coherent spectral line existing at $1/T_s$ divided by the power contained in the noise background in a small frequency band ΔB around $1/T_s$, and reads [5]

$$\mathscr{R}_{\text{out}} = \frac{|\langle \mathrm{E}[y(t)]\, \exp(-\imath 2\pi t/T_s)\rangle|^2}{\langle \mathrm{var}[y(t)]\rangle \Delta t\, \Delta B}. \tag{5}$$

In Eq. (5), a time average is defined as

$$\langle \cdots \rangle = \frac{1}{T_s}\int_0^{T_s} \cdots \mathrm{d}t, \tag{6}$$

$\mathrm{E}[y(t)]$ and $\mathrm{var}[y(t)] = \mathrm{E}[y^2(t)] - \mathrm{E}^2[y(t)]$ represent the expectation and variance of $y(t)$ at a fixed time t; and Δt is the time resolution of the measurement (i.e. the signal sampling period in a discrete time implementation), throughout this study we take $\Delta t\, \Delta B = 10^{-3}$.

At time t, for a fixed given value I of the input current $I(t)$, according to the linearity of Eq. (3), one has the conditional expectations

$$\mathrm{E}[y(t)|I] = \mathrm{E}[f_i(t)|I] \tag{7}$$

and

$$\mathrm{E}[y^2(t)|I] = \frac{1}{N}\mathrm{E}[f_i^2(t)|I] + \frac{N-1}{N}\mathrm{E}^2[f_i(t)|I], \tag{8}$$

which are both independent of i since the $\eta_i(t)$, and therefore the $f_i(t)$, are i.i.d. From Eq. (2), one has for every i,

$$\mathrm{E}[f_i(t)|I] = \int_{-\infty}^{+\infty} g(I+u)p_\eta(u)\,\mathrm{d}u \tag{9}$$

and

$$\mathrm{E}[f_i^2(t)|I] = \int_{-\infty}^{+\infty} g^2(I+u)p_\eta(u)\,\mathrm{d}u. \tag{10}$$

Since $I(t) = s(t) + \xi(t)$, the probability density for $I(t)$ is $p_\xi(I - s(t))$, and one obtains

$$\mathrm{E}[y(t)] = \int_{-\infty}^{+\infty} \mathrm{E}[y(t)|I]p_\xi(I - s(t))\,\mathrm{d}I, \tag{11}$$

and

$$\mathrm{E}[y^2(t)] = \int_{-\infty}^{+\infty} \mathrm{E}[y^2(t)|I]p_\xi(I - s(t))\,\mathrm{d}I, \tag{12}$$

which completes the relations needed for evaluation of the output SNR $\mathscr{R}_{\text{out}}$ of Eq. (5).

3.2. Aperiodic signal transmission

When the information-carrying input signal $s(t)$ is aperiodic, a standard measure in stochastic resonance studies is the normalized input–output cross-covariance, which quantifies the similarity between input $s(t)$ and output $y(t)$ in a way which is insensitive to both scaling and offsetting in signal amplitude [10,23]. When $s(t)$ is a deterministic aperiodic signal existing over the duration T_s, we introduce the signals centered around their time-averaged statistical expectation,

$$\widetilde{s}(t) = s(t) - \langle s(t)\rangle \tag{13}$$

and

$$\widetilde{y}(t) = y(t) - \langle \mathrm{E}[y(t)]\rangle, \tag{14}$$

with the time average again defined by Eq. (6). The normalized time-averaged cross-covariance is

$$C_{sy} = \frac{\langle \mathrm{E}[\widetilde{s}(t)\widetilde{y}(t)]\rangle}{\sqrt{\langle \mathrm{E}[\widetilde{s}^2(t)]\rangle \langle \mathrm{E}[\widetilde{y}^2(t)]\rangle}}, \tag{15}$$

or equivalently, since $s(t)$ is deterministic,

$$C_{sy} = \frac{\langle s(t)\mathrm{E}[y(t)]\rangle - \langle s(t)\rangle\langle \mathrm{E}[y(t)]\rangle}{\sqrt{[\langle s(t)^2\rangle - \langle s(t)\rangle^2][\langle \mathrm{E}[y^2(t)]\rangle - \langle \mathrm{E}[y(t)]\rangle^2]}}, \tag{16}$$

with $\mathrm{E}[y(t)]$ and $\mathrm{E}[y^2(t)]$ again given by Eqs. (11) and (12).

With the measures of performance $\mathscr{R}_{\text{out}}$ of Eq. (5) and C_{sy} of Eq. (16), we are now in a position to quantify the impact of the array noises $\eta_i(t)$ on the efficacy of transmission of a periodic or an aperiodic $s(t)$ by the neuronal array.

4. Array transmission aided by noise

Direct numerical evaluations of $\mathscr{R}_{\text{out}}$ and C_{sy} can be realized through numerical integration of the integrals of Eqs. (9)–(12). Alternatively, to push further the analytical treatment, it is possible to consider the following situation. The Lapicque function $g(.)$ of Eq. (1) can be approximated for $I(t)$ sufficiently above the threshold I_{th} by using

$\ln(1 - I_{\rm th}/I) \approx -I_{\rm th}/I$, yielding the approximation

$$f(t) = g[I(t)] = \begin{cases} 0 & \text{for } I(t) \leqslant I_{\rm th}, \\ \dfrac{1/T_{\rm r}}{1 + (\tau_{\rm m}/T_{\rm r})(I_{\rm th}/I(t))} & \text{for } I(t) > I_{\rm th}, \end{cases} \tag{17}$$

which is also depicted in Fig. 1. Eq. (17) constitutes an interesting approximation that only departs slightly from Eq. (1) for $I(t)$ immediately above the threshold $I_{\rm th}$, and it preserves the qualitative features of the existence of a threshold, a saturation and an intermediate curvilinear part in the response. This approximation, when associated to a probability density $p_\eta(u)$ uniform over $[-a, a]$ authorizes an analytical evaluation of integrals (9)–(10), as

$$\mathrm{E}[f_i(t)|I] = \begin{cases} 0 & \text{for } I \leqslant I_{\rm th} - a, \\ \dfrac{1}{T_{\rm r}}\dfrac{I_{\rm th}}{2a}[\Phi_1(I + a) - \Phi_1(I_{\rm th})] & \text{for } I_{\rm th} - a < I < I_{\rm th} + a, \\ \dfrac{1}{T_{\rm r}}\dfrac{I_{\rm th}}{2a}[\Phi_1(I + a) - \Phi_1(I - a)] & \text{for } I \geqslant I_{\rm th} + a, \end{cases} \tag{18}$$

and

$$\mathrm{E}[f_i^2(t)|I] = \begin{cases} 0 & \text{for } I \leqslant I_{\rm th} - a, \\ \left(\dfrac{1}{T_{\rm r}}\right)^2\dfrac{I_{\rm th}}{2a}[\Phi_2(I + a) - \Phi_2(I_{\rm th})] & \text{for } I_{\rm th} - a < I < I_{\rm th} + a, \\ \left(\dfrac{1}{T_{\rm r}}\right)^2\dfrac{I_{\rm th}}{2a}[\Phi_2(I + a) - \Phi_2(I - a)] & \text{for } I \geqslant I_{\rm th} + a, \end{cases} \tag{19}$$

with the two functions

$$\Phi_1(u) = \frac{u}{I_{\rm th}} - \frac{\tau_{\rm m}}{T_{\rm r}}\ln\left(\frac{u}{I_{\rm th}} + \frac{\tau_{\rm m}}{T_{\rm r}}\right) \tag{20}$$

and

$$\Phi_2(u) = \frac{u}{I_{\rm th}} - 2\frac{\tau_{\rm m}}{T_{\rm r}}\ln\left(\frac{u}{I_{\rm th}} + \frac{\tau_{\rm m}}{T_{\rm r}}\right) - \frac{(\tau_{\rm m}/T_{\rm r})^2}{(u/I_{\rm th}) + (\tau_{\rm m}/T_{\rm r})}. \tag{21}$$

To illustrate noise-aided transmission by the neuronal array, we choose as in [22], the periodic input

$$s(t) = I_0 + I_1 \sin(2\pi t/T_{\rm s}) \quad \forall t, \tag{22}$$

to be assessed by the SNR $\mathscr{R}_{\rm out}$ of Eq. (5), and the transient aperiodic input

$$s(t) = \begin{cases} I_0 + I_1 \sin(2\pi t/T_{\rm s}) & \text{for } t \in [0, T_{\rm s}], \\ 0 & \text{otherwise}, \end{cases} \tag{23}$$

to be assessed by the cross-covariance C_{sy} of Eq. (16). The parameters I_0 (offset) and I_1 (amplitude) of the coherent input $s(t)$ of Eqs. (22) or (23) will be varied, in order to solicit the array in various operation ranges of the nonlinearity of Fig. 1, successively the threshold region, the intermediate curvilinear part, and the saturation region.

4.1. Transmission at threshold

We consider here the situation of a small information-carrying signal $s(t)$ which permanently evolves, for every t, below the threshold $I_{\rm th}$. The input noise $\xi(t)$ which adds to $s(t)$ is also small, in such a way that the input signal–noise mixture $I(t) = s(t) + \xi(t)$ practically never reaches the neuron firing threshold $I_{\rm th}$. Thus $I(t)$ alone is unable to trigger an efficient response at the output, and consequently the measures of transmission efficacy $\mathscr{R}_{\rm out}$ and C_{sy} remain essentially at zero. From this situation, Fig. 2 shows the action of the added array noises $\eta_i(t)$ to enhance the transmission.

In an isolated neuron, at $N = 1$ in Fig. 2, the added noise $\eta_1(t)$ cooperates with the subthreshold input $I(t)$ to reach the firing threshold $I_{\rm th}$ and to induce variations at the neuron output that will be correlated with the information-carrying input $s(t)$. This cooperative effect is observed for both a periodic (Fig. 2A) and an aperiodic (Fig. 2B) input $s(t)$. For the efficacy of the transmission, measured by the output SNR $\mathscr{R}_{\rm out}$ in Fig. 2A and by the input–output cross-covariance C_{sy} in Fig. 2B, the effect gives rise to a nonmonotonic evolution culminating at a maximum for a nonzero level of the added noise $\eta_1(t)$. This is a standard effect of stochastic resonance in a threshold nonlinearity, also observed in the same model of a single isolated neuron in [22].

We next show here that the noise-aided transmission of a subthreshold $s(t)$, already present in a single neuron, is reinforced when the neurons are associated into a parallel array. This is visible in Fig. 2 at $N > 1$, where both measures of efficacy $\mathscr{R}_{\rm out}$ and C_{sy} are always enhanced by the action of the added array noises $\eta_i(t)$. With no noises $\eta_i(t)$ added in the array, i.e. at $\sigma_\eta = 0$ in Fig. 2, all the neurons respond in unison as a single one, and therefore the performance is the same at $\sigma_\eta = 0$ for any N. Addition of the array noises $\eta_i(t)$ then always entails an enhancement of the efficacy of the neural transmission compared to the efficacy of a single isolated neuron, and the enhancement gets more and more important as the array size N increases as seen in Fig. 2. At the limit of large arrays, $N = \infty$ in Fig. 2, both measures $\mathscr{R}_{\rm out}$ and C_{sy} reach a plateau at large values of the rms amplitude σ_η of the array noises $\eta_i(t)$. The behavior of the array with the added noises $\eta_i(t)$, and especially the presence of the plateau, is consistent with a similar behavior observed in [11] with arrays of Fitz-Hugh–Nagumo neuron models for an input–output correlation measure and an aperiodic noise-free input signal. Here, for the input signal–noise mixture $I(t) = s(t) + \xi(t)$, the input SNR defined according to Eqs. (5) and (22) is $\mathscr{R}_{\rm in} = I_1^2/(4\sigma_\xi^2 \Delta t\, \Delta B)$, while the normalized cross-covariance between $s(t)$ and $I(t)$ defined according to Eqs. (16) and (23) is $C_{sI} = 1/[1 + 2\sigma_\xi^2/I_1^2]^{1/2}$. Precisely, in Fig. 2 at $N = \infty$ and large σ_η, the plateau

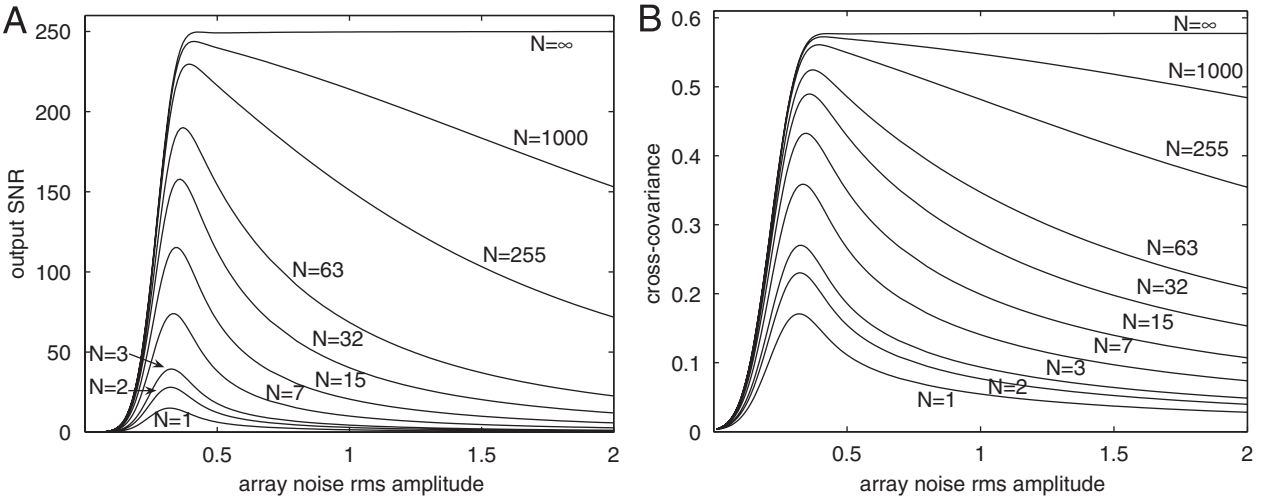

Fig. 2. Transmission at threshold by the neuronal array of size N, as a function of the rms amplitude $\sigma_\eta/I_{\text{th}}$ of the array noises $\eta_i(t)$, with a zero-mean Gaussian input noise $\xi(t)$ of rms amplitude $\sigma_\xi = 0.1I_{\text{th}}$, and signal parameters $I_0 = 0.5I_{\text{th}}$ and $I_1 = 0.1I_{\text{th}}$: (A) output SNR $\mathscr{R}_{\text{out}}$ of Eq. (5) for the T_s-periodic input $s(t)$ of Eq. (22); (B) input–output cross-covariance C_{sy} of Eq. (16) for the aperiodic input $s(t)$ of Eq. (23).

reached by the SNR $\mathscr{R}_{\text{out}}$ is $\mathscr{R}_{\text{in}}$, and the plateau reached by the cross-covariance C_{sy} is C_{sI}. This means that the arrays with added noises $\eta_i(t)$, which always enhance the transmission efficacy of an isolated neuron, have also the ability, at large size N, to restore the transmission efficacy as it would be if a direct observation of the input $I(t) = s(t) + \xi(t)$ were accessible instead of its observation by neurons with inherent thresholds.

A complementary point of view on the improvement by noise in the array is provided by Fig. 3 in the time domain. Fig. 3 considers a large array whose input is the same subthreshold sinusoid in noise as in Fig. 2. For the array output $y(t)$, Fig. 3 which depicts the mean E[$y(t)$] and standard deviation std[$y(t)$], shows that the beneficial effect of adding noise in the array is two-fold. When moving from Fig. 3A to B by addition of the array noises $\eta_i(t)$: (i) on average the output $y(t)$ resembles more the input sinusoid, (ii) the fluctuation std[$y(t)$] relative to E[$y(t)$] is reduced. In short, the output signal is less noisy and resembles more the input sinusoid. These aspects are properly quantified by the measures of Fig. 2, and can be visually appreciated in Fig. 3.

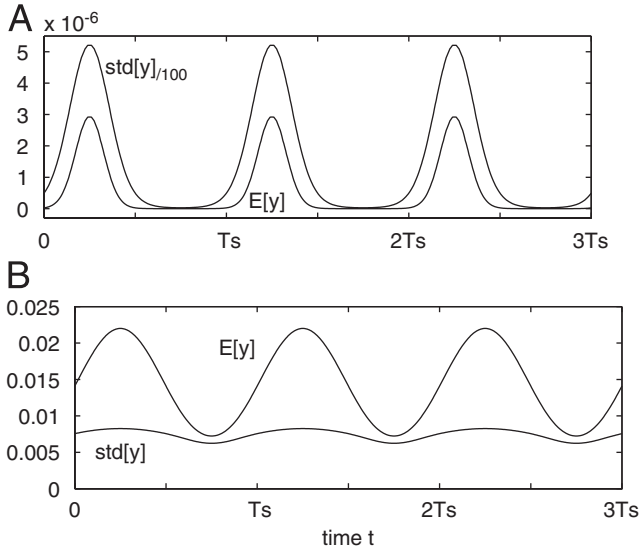

Fig. 3. For the array output $y(t)$: its mean E[$y(t)$] and standard deviation std[$y(t)$], in units of $f_{\max} = 1/T_r$. The input signal is the noisy sinusoid of Eq. (22) with the same parameter values as in Fig. 2, applied to a large array of size $N \to \infty$: (A) is at $\sigma_\eta = 0$, i.e. with no added noises $\eta_i(t)$ in the array; (B) is at $\sigma_\eta = 0.4I_{\text{th}}$, i.e. with a nonzero level close to the optimum for the added array noises $\eta_i(t)$. (In (A), std[$y(t)$] is shown divided by 100, so that it fits nicely in the graph along with E[$y(t)$].)

4.2. Transmission at medium range

Another interesting capability of the noisy arrays arises in the transmission of an input signal $s(t)$ which is large enough (but not too large) to permanently evolve, for every t, above the neuron firing threshold I_{th}, while at the same time avoiding to operate the neuron characteristic of Fig. 1 in its saturation region. In this situation of a medium signal $s(t)$, the behavior of the neuronal array is presented in Fig. 4.

In an isolated neuron, at $N = 1$ in Fig. 4, enhancement by noise of the transmission efficacy does not occur, as expressed by the monotonic decay of the SNR $\mathscr{R}_{\text{out}}$ and of the cross-covariance C_{sy} when the level of noise σ_η grows. This is because a medium $s(t)$, permanently above the threshold and below the saturation, has the ability by itself to trigger an efficient response from an isolated neuron. No assistance by noise, for instance to overcome a threshold or be shifted away of a saturation, is needed by a medium $s(t)$. In this condition, addition of noise is felt as a pure nuisance and always degrades the transmission efficacy of an isolated neuron. This same behavior of no stochastic resonance was also observed in the same model of a single isolated neuron in [22].

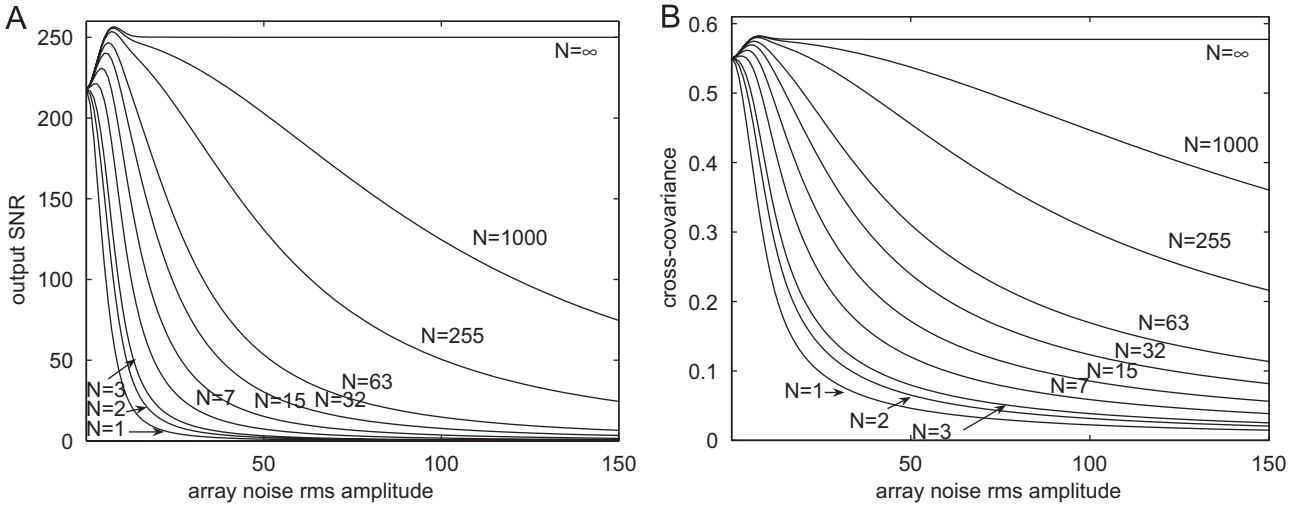

Fig. 4. Transmission at medium range by the neuronal array of size N, as a function of the rms amplitude $\sigma_\eta/I_{\rm th}$ of the array noises $\eta_i(t)$, with a zero-mean Gaussian input noise $\xi(t)$ of rms amplitude $\sigma_\xi = 5I_{\rm th}$, and signal parameters $I_0 = 10I_{\rm th}$ and $I_1 = 5I_{\rm th}$: (A) output SNR $\mathscr{R}_{\rm out}$ of Eq. (5) for the $T_{\rm s}$-periodic input $s(t)$ of Eq. (22); (B) input–output cross-covariance C_{sy} of Eq. (16) for the aperiodic input $s(t)$ of Eq. (23).

We demonstrate here that the picture is quite different when the neurons are assembled into a parallel array with added noises. In this case, Fig. 4 shows that with array sizes N sufficiently above 1, the array with added noises $\eta_i(t)$ always has the ability to improve the efficacy of transmission of a medium signal $s(t)$, compared to the efficacy achieved by an isolated neuron with no added noise $\eta_1(t)$. This constructive action of the added noises $\eta_i(t)$ in the array is again expressed by a possibility of increasing $\mathscr{R}_{\rm out}$ in Fig. 4A and C_{sy} in Fig. 4B by raising the noise level σ_η. The constructive action of the noise is more and more pronounced as the array size N gets larger. In the limit of an infinite array $N = \infty$ in Fig. 4, the input performances $\mathscr{R}_{\rm out} = \mathscr{R}_{\rm in}$ and $C_{sy} = C_{sI}$ are again recovered, on the plateaus at large σ_η, as if the array of nonlinear neurons was turned into a purely linear device.

Moreover, sufficiently large arrays even have the possibility, in a small range of the noise level σ_η, of improving the measures of efficacy $\mathscr{R}_{\rm out}$ and C_{sy} above their values $\mathscr{R}_{\rm in}$ and C_{sI} at the input. This is a small effect here, as visible in Fig. 4, where $\mathscr{R}_{\rm out}$ and C_{sy} slightly peak above the large-σ_η plateaus. Yet, this proves, in principle, that some nonlinear sensors, possibly aided by noise, can outperform a putative purely linear system providing direct access to the input signal. Such a direct linear observation is not available to isolated sensory neurons which have to cope with their inherent threshold and saturation; but it becomes possible, as shown here, when neurons are assembled in arrays with added noises. But beyond, as shown by Fig. 4, the neuronal arrays with added noises can sometimes outperform the performance of a strict linearization of the process. It is a remarkable property that arrays of neuronal nonlinearities with threshold and saturation can amplify the efficacies $\mathscr{R}_{\rm out}$ and C_{sy} above their input values $\mathscr{R}_{\rm in}$ and C_{sI}, because this property is shared by very few systems.

It is well known that linear systems, even dynamic linear systems of arbitrarily high order, are incapable[1] of amplifying the output SNR $\mathscr{R}_{\rm out}$ of Eq. (5) above the input SNR $\mathscr{R}_{\rm in}$. Very few nonlinear systems are capable of amplifying the SNR of a sinusoid in broadband white Gaussian noise as in Fig. 4. SNR amplification is a problem which has been addressed very early for signal processing [13,2]. For the less stringent condition of a *narrowband* noise addressed in [13,2], maximum SNR gains of 2 are reported, and achieved with hard-threshold or Heaviside nonlinearities. In the more stringent condition of a *broadband white* noise, the SNR gains effectively reported are also modest: Hänggi et al. [16] report a maximum SNR gain of 1.2 achieved by an isolated bistable dynamic system, Casado et al. [3] report a maximum SNR gain of 1.25 achieved by a fully coupled network of bistable dynamic systems, Chapeau-Blondeau and Rousseau [7] report a maximum SNR gain of 1.4 achieved by an optimally tuned static nonlinearity with saturation. It seems that, in nonlinearities capable of amplifying the SNR, a moderate amount of saturation, as in the case of [7] and also of neuronal nonlinearities as considered here, might be an interesting feature, due to its clipping capability on the input signal–noise mixture that could reduce the noise more than the coherent signal. Beyond the uncoupled parallel arrays of Fig. 4, more efficient arrangements of neuronal nonlinearities could be tested to specifically amplify the SNR for instance. Yet, this is not

[1]Any linear system leaves the SNR unchanged, because in the output spectrum it multiplies both the coherent line at $1/T_{\rm s}$ and the noise background around $1/T_{\rm s}$ by the same factor, the squared modulus of its transmittance.

precisely the scope of the present study, which rather aims at demonstrating a constructive impact of added noises in simple uncoupled parallel neuronal arrays in different regimes of operation (at threshold, at medium range and at saturation, with periodic or aperiodic signal).

Fig. 5 offers a complementary point of view, in the time domain, on the improvement by noise in the array. For the same medium-range input sinusoid in noise as in Fig. 4, Fig. 5 shows again a two-fold beneficial action of the noise. When moving from Fig. 5A to B by addition of the array noises $\eta_i(t)$, on average the output $y(t)$ resembles more (slightly here) the input sinusoid, and the fluctuation std[$y(t)$] is reduced.

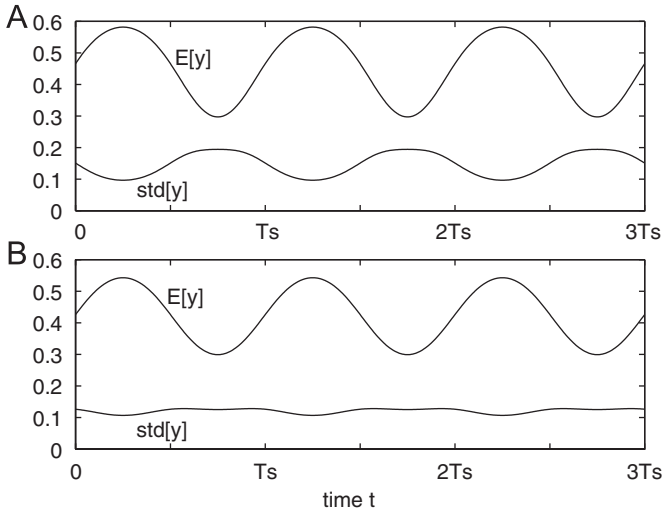

Fig. 5. For the array output $y(t)$: its mean E[$y(t)$] and standard deviation std[$y(t)$], in units of $f_{\max} = 1/T_r$. The input signal is the noisy sinusoid of Eq. (22) with the same parameter values as in Fig. 4, applied to a large array of size $N \to \infty$: (A) is at $\sigma_\eta = 0$, i.e. with no added noises $\eta_i(t)$ in the array; (B) is at $\sigma_\eta = 7I_{\text{th}}$, i.e. with a nonzero level close to the optimum for the added array noises $\eta_i(t)$.

4.3. Transmission at saturation

The conditions of Fig. 6 concern the operation of the array in the regime of strong saturation of the neuronal firing function. In an isolated neuron, at $N = 1$ in Fig. 6, the added noise $\eta_1(t)$ already is capable of inducing an improvement in the transmission efficacy of both a periodic and an aperiodic signal. A similar improvement at $N = 1$ was also present in Fig. 2 in the threshold region, but absent in Fig. 4 in the intermediate curvilinear region of the neuronal characteristic. This illustrates the ability of the added noise to bring some shift in the neuronal response, when needed, in order to displace it away of an unfavorable strongly nonlinear region (a threshold or a saturation) into a more favorable region (the curvilinear part) of the characteristic. Again, this behavior in a single isolated neuron was also observed in [22].

Next we show here that the noise-aided transmission in the saturation regime, already present in an isolated neuron at $N = 1$, is strongly enhanced when the neurons are assembled in an array at $N > 1$ in Fig. 6. The enhancement by noise applies to both periodic (Fig. 6A) and aperiodic (Fig. 6B) signals. Again the enhancement is more and more important as the array size N grows. At array sizes $N \to \infty$ and a sufficient amount of the added noises $\eta_i(t)$, the output of the nonlinear array recovers the performance as at the input.

Fig. 7 in the time domain shows again the two-fold beneficial action of the noises added to the array, for the large input sinusoid in noise of Fig. 6: on average the output $y(t)$ resembles more, with reduced saturation, the input sinusoid; and the fluctuation is decreased.

5. Discussion

The results presented here can be viewed as extensions concerning the various forms of stochastic resonance or

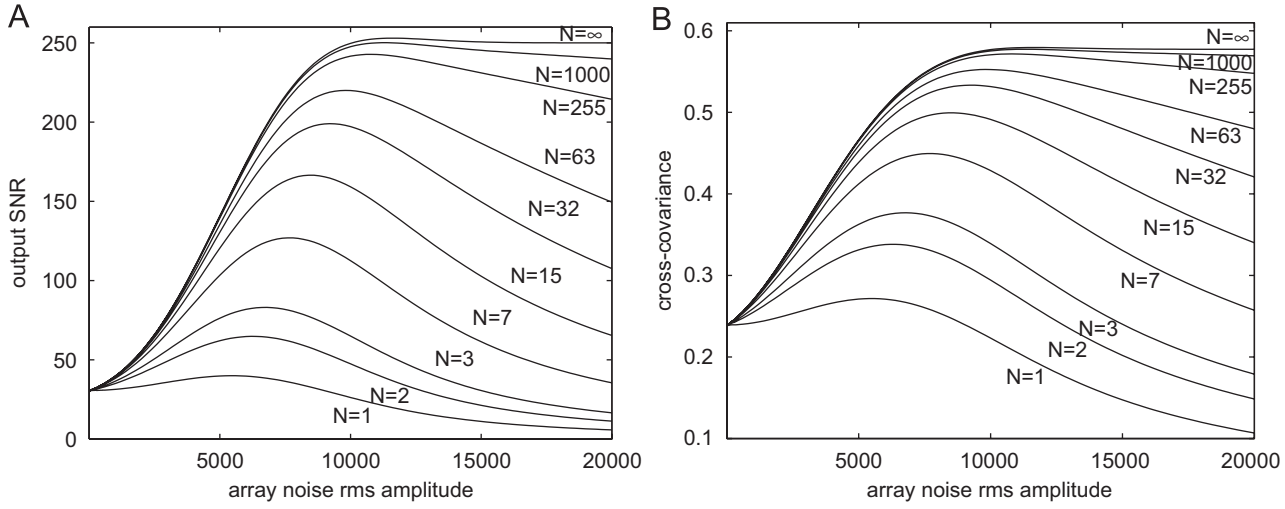

Fig. 6. Transmission at saturation by the neuronal array of size N, as a function of the rms amplitude $\sigma_\eta/I_{\text{th}}$ of the array noises $\eta_i(t)$, with a zero-mean Gaussian input noise $\xi(t)$ of rms amplitude $\sigma_\xi = 5 \times 10^3 I_{\text{th}}$, and signal parameters $I_0 = 10^4 I_{\text{th}}$ and $I_1 = 5 \times 10^3 I_{\text{th}}$: (A) output SNR $\mathscr{R}_{\text{out}}$ of Eq. (5) for the T_s-periodic input $s(t)$ of Eq. (22); (B) input–output cross-covariance C_{sy} of Eq. (16) for the aperiodic input $s(t)$ of Eq. (23).

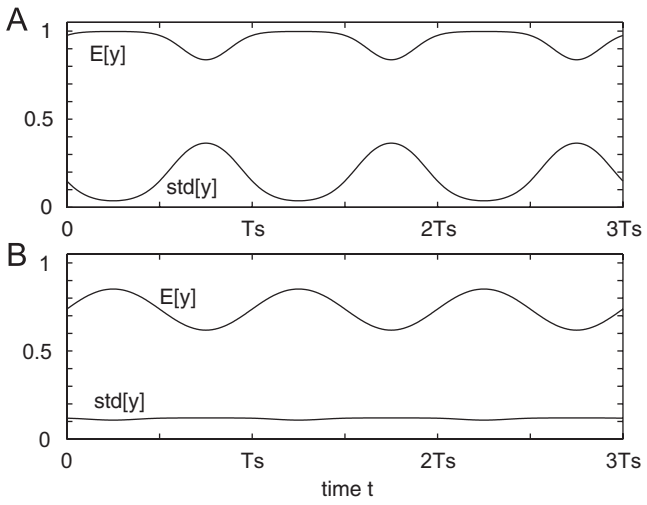

Fig. 7. For the array output $y(t)$: its mean $\mathrm{E}[y(t)]$ and standard deviation $\mathrm{std}[y(t)]$, in units of $f_{\max} = 1/T_r$. The input signal is the noisy sinusoid of Eq. (22) with the same parameter values as in Fig. 6, applied to a large array of size $N \to \infty$: (A) is at $\sigma_\eta = 0$, i.e. with no added noises $\eta_i(t)$ in the array; (B) is at $\sigma_\eta = 12 \times 10^3 I_{\mathrm{th}}$, i.e. with a nonzero level close to the optimum for the added array noises $\eta_i(t)$.

improvement by noise in signal transduction by neurons. In this context, stochastic resonance has been widely studied for noise-enhanced signal transmission by neurons operating in the region of the threshold of activity. Here, by contrast, we have also investigated signal transmission away of the threshold, in the curvilinear part of the neuronal response, and beyond in the saturation region. For isolated neurons, we observed that improvement by noise of the transmission can occur both in the threshold and in the saturation of the response, but does not take place in the intermediate curvilinear part, as it was also found in [22]. Beyond, we have focused here on the situation of a common basic architecture for neuronal assemblies, i.e. parallel arrays of neurons, and the impact of independent noises injected in such arrays. We have observed that the stochastic resonance effect is always reinforced in the arrays with a sufficient amount of the added noises, compared to the situation of isolated neurons. Moreover, in arrays stochastic resonance becomes possible in the intermediate curvilinear part of the neuronal response, where it was not feasible in isolated neurons. Altogether in neuronal arrays, improvement by noise of signal transduction is possible for any regime of operation of the transmission, in the threshold, or in the intermediate, or in the saturation part of the neuronal response. This is afforded by the distinct mechanism of stochastic resonance in arrays, where the added noises force individual neurons to respond differently to a common input signal. This is the source of richer representation capabilities by the neuronal outputs that when collected over the array result in enhanced transduction of the input signal. This enhanced transduction obtained by gathering distinct nonlinear outputs, does not specifically require threshold-like or saturation-like nonlinearities, and curvilinear nonlinearities also lend themselves to this effect as visible here. By contrast, in isolated neurons, the mechanism of improvement by noise can be interpreted as a form of biasing by noise, where the noise assists a signal hidden below a threshold or squeezed in a saturation to access a more favorable region of the characteristic. This mechanism, inherently, relies on threshold or saturation nonlinearities, and does not apply to smooth curvilinear ones. Both mechanisms of improvement by noise, in isolated neurons and in arrays, operate in conjunction in Figs. 2 and 6 at threshold and at saturation, while only one mechanism (the array one) operates in the intermediate condition of Fig. 4. Also here, all the configurations of improvement by noise have been verified, with standard measures of efficacy, to apply equally to periodic and to aperiodic signals. This illustrates the wide versatility of the forms of improvement by noise in neuronal structures.

An alternative interpretation of the constructive action of noise, which has been employed especially in threshold systems, resorts sometimes to a mechanism of linearization by noise of the input–output characteristic. First, a linearized characteristic may not be uniformly meaningful, nor even definable, for distinct time-varying signals as considered here. Second, clearly here there is more than a linearization, since the action of noise, as visible in Fig. 4, can increase the efficacy for signal transduction above that of a purely linear device.The present neuronal nonlinearities aided by noise, as also verified by other nonlinear systems [6,8], implement an ''intelligent'' preprocessing capable of reaching efficacies that no linear systems can achieve.

The various forms of neuronal transduction aided by noise in arrays, were shown here with a very simple neuron model based on Eq. (1). Yet, as it has been pointed out in many other neuronal studies [20], this model of Eq. (1) is able to capture essential features of the neuronal transmission, i.e. the presence of both threshold and saturation and in-between an intermediate curvilinear response. At the same time, it is known that stochastic resonance is usually a general and robust nonlinear phenomenon, which persists over many variations in the nonlinearities. More elaborate neuron models, with possibly couplings in the arrays, could next be tested to investigate how the basic properties exposed here are preserved or evolved, and how they could play a part in the highly efficient processing of information accomplished by neural systems.

References

[1] B. Andò, S. Graziani, Stochastic Resonance: Theory and Applications, Kluwer Academic Publishers, Boston, 2000.
[2] N.M. Blachman, The output signal-to-noise ratio of a power-law device, J. Appl. Phys. 24 (1953) 783–785.
[3] J.M. Casado, J. Gómez Ordóñez, M. Morillo, Stochastic resonance of collective variables in finite sets of interacting identical subsystems, Phys. Rev. E 73 (2006) 011109, 1–8.

[4] F. Chapeau-Blondeau, G. Chauvet, Dynamic properties of a biologically motivated neural network model, Int. J. Neural Syst. 3 (1992) 371–378.
[5] F. Chapeau-Blondeau, X. Godivier, Theory of stochastic resonance in signal transmission by static nonlinear systems, Phys. Rev. E 55 (1997) 1478–1495.
[6] F. Chapeau-Blondeau, D. Rousseau, Enhancement by noise in parallel arrays of sensors with power-law characteristics, Phys. Rev. E 70 (2004) 060101(R), 1–4.
[7] F. Chapeau-Blondeau, D. Rousseau, Nonlinear SNR amplification of a harmonic signal in noise, Electron. Lett. 41 (2005) 618–619.
[8] F. Chapeau-Blondeau, D. Rousseau, Noise-aided SNR amplification by parallel arrays of sensors with saturation, Phys. Lett. A 351 (2006) 231–237.
[9] D.R. Chialvo, A. Longtin, J. Mullergerking, Stochastic resonance in models of neuronal ensembles, Phys. Rev. E 55 (1997) 1798–1808.
[10] J.J. Collins, C.C. Chow, T.T. Imhoff, Aperiodic stochastic resonance in excitable systems, Phys. Rev. E 52 (1995) R3321–R3324.
[11] J.J. Collins, C.C. Chow, T.T. Imhoff, Stochastic resonance without tuning, Nature 376 (1995) 236–238.
[12] J.J. Collins, T.T. Imhoff, P. Grigg, Noise-enhanced information transmission in rat SA1 cutaneous mechanoreceptors via aperiodic stochastic resonance, J. Neurophysiol. 76 (1996) 642–645.
[13] W.B. Davenport, Signal-to-noise ratios in band-pass limiters, J. Appl. Phys. 24 (1953) 720–727.
[14] J.K. Douglass, L. Wilkens, E. Pantazelou, F. Moss, Noise enhancement of information transfer in crayfish mechanoreceptors by stochastic resonance, Nature 365 (1993) 337–340.
[15] L. Gammaitoni, P. Hänggi, P. Jung, F. Marchesoni, Stochastic resonance, Rev. Mod. Phys. 70 (1998) 223–287.
[16] P. Hänggi, M.E. Inchiosa, D. Fogliatti, A.R. Bulsara, Nonlinear stochastic resonance: the saga of anomalous output–input gain, Phys. Rev. E 62 (2000) 6155–6163.
[17] T. Hoch, G. Wenning, K. Obermayer, Adaptation using local information for maximizing the global cost, Neurocomputing 52–54 (2003) 541–546.
[18] T. Hoch, G. Wenning, K. Obermayer, Optimal noise-aided signal transmission through populations of neurons, Phys. Rev. E 68 (2003) 011911, 1–11.
[19] T. Hoch, G. Wenning, K. Obermayer, The effect of correlations in the background activity on the information transmission properties of neural populations, Neurocomputing 65–66 (2005) 365–370.
[20] C. Koch, Biophysics of Computation: Information Processing in Single Neurons, Oxford University Press, New York, 1999.
[21] F. Moss, L.M. Ward, W.G. Sannita, Stochastic resonance and sensory information processing: a tutorial and a review of application, Clin. Neurophysiol. 115 (2004) 267–281.
[22] D. Rousseau, F. Chapeau-Blondeau, Neuronal signal transduction aided by noise at threshold and at saturation, Neural Process. Lett. 20 (2004) 71–83.
[23] D. Rousseau, J. Rojas Varela, F. Chapeau-Blondeau, Stochastic resonance for nonlinear sensors with saturation, Phys. Rev. E 67 (2003) 021102, 1–6.
[24] N.G. Stocks, Optimizing information transmission in model neuronal ensembles: the role of internal noise, in: J.A. Freund, T. Poschel (Eds.), Stochastic Processes in Physics, Chemistry and Biology, Lecture Notes in Physics, vol. 557, Springer, Berlin, 2000, pp. 150–159.
[25] N.G. Stocks, Suprathreshold stochastic resonance in multilevel threshold systems, Phys. Rev. Lett. 84 (2000) 2310–2313.
[26] N.G. Stocks, Information transmission in parallel threshold arrays: suprathreshold stochastic resonance, Phys. Rev. E 63 (2001) 041114, 1–9.
[27] N.G. Stocks, R. Mannella, Generic noise-enhanced coding in neuronal arrays, Phys. Rev. E 64 (2001) 030902, 1–4.

Solenna Blanchard received a M.Sc. degree in Signal Processing in 2004 and a M.Sc. degree in Electronics in 2005, both from the University of Rennes, France. She is currently a Ph.D. student in the field of nonlinear signal processing and stochastic resonance at the University of Angers, France.

David Rousseau was born in 1973 in France. He received the Master degree in acoustics and signal processing from the *Institut de Recherche Coordination Acoustique et Musique* (IRCAM), Paris, France in 1996. He received, in 2004, the Ph.D. degree in nonlinear signal processing and stochastic resonance at the *Laboratoire d'Ingénierie des Systèmes Automatisés* (LISA), University of Angers where he is currently a *Maître de Conférences* of physics and information sciences.

François Chapeau-Blondeau was born in France in 1959. He received the Engineer Diploma from ESEO, Angers, France, in 1982, the Ph.D. degree in electrical engineering from University Paris 6, Paris, France, in 1987, and the *Habilitation* degree from the University of Angers, France, in 1994. In 1988, he was a research associate in the Department of Biophysics at the Mayo Clinic, Rochester, Minnesota, USA, working on biomedical ultrasonics. Since 1990, he has been with the University of Angers, France, where he is currently a professor of electronic and information sciences. His research interests are nonlinear systems and signal processing, and the interactions between physics/biophysics and information processing, including neural information processing.

F. CHAPEAU-BLONDEAU and D. ROUSSEAU. Nonlinear SNR amplification of harmonic signal in noise. ***Electronics Letters*****, vol. 41:618–619, 2005.**

Nonlinear SNR amplification of harmonic signal in noise

F. Chapeau-Blondeau and D. Rousseau

The SNR of a harmonic signal in additive white noise is computed after transformation by an arbitrary memoryless nonlinearity. With a simple saturating nonlinearity having direct electronic implementation, an amplification of the SNR can be obtained, an outcome which is inaccessible with linear devices.

Assessing the presence of a harmonic signal hidden in additive noise is a very common problem in many areas of experimental sciences and technologies. This type of signal–noise mixture has a very characteristic signature in the frequency domain: its power spectrum is formed by a sharp spectral line at the harmonic frequency v_s, emerging out of a broadband background contributed by the noise. A signal-to-noise ratio (SNR) $\mathcal{R}$ is conveniently defined as the ratio of the power contained in the spectral line at v_s divided by the power contained in the noise background in a small reference frequency band ΔB around v_s. This SNR quantifies how well the spectral line at v_s emerges out of the noise background. A narrowband filter at v_s used to extract the harmonic component, will have an efficacy directly increasing with this SNR [1]. As a pre-processing, it is known that no linear filter is able to improve (increase) such an SNR $\mathcal{R}$. This is because a linear filter multiplies both the spectral line and the noise background at v_s by the same factor (the squared modulus of its transfer function at v_s), and therefore leaves the SNR $\mathcal{R}$ unchanged [1]. On the contrary, we will show that very simple nonlinear devices can act as an SNR amplifier providing an enhancement of $\mathcal{R}$.

We consider the signal–noise mixture $x(t) = s(t) + \xi(t)$, with the harmonic component $s(t) = A\cos(2\pi v_s t + \varphi)$, and $\xi(t)$ a stationary white noise with probability density function $f_\xi(u)$. This signal $x(t)$ is fed into a memoryless (nonlinear) system [2] with input–output characteristic $g(.)$ producing the output

$$y(t) = g[s(t) + \xi(t)] \tag{1}$$

In this case, both $x(t)$ and $y(t)$ are cyclostationary random signals with period $T_s = 1/v_s$, both showing a power spectrum with a sharp spectral line at v_s emerging out of a broadband noise background. The SNR, as defined above, for the output $y(t)$ can be expressed as [3]

$$\mathcal{R}_{\text{out}} = \frac{|\langle \mathrm{E}[y(t)] \exp(-i2\pi t/T_s)\rangle|^2}{\langle \mathrm{var}[y(t)]\rangle \Delta t \Delta B} \tag{2}$$

In (2), a time average is defined as

$$\langle \ldots \rangle = \frac{1}{T_s}\int_0^{T_s} \ldots dt \tag{3}$$

$\mathrm{E}[y(t)]$ and $\mathrm{var}[y(t)] = \mathrm{E}[y^2(t)] - \mathrm{E}^2[y(t)]$ represent the expectation and variance of $y(t)$ at a fixed time t; and Δt is the time resolution of the measurement (i.e. the signal sampling period in a discrete time implementation). The white noise assumption here models a broadband physical noise with a correlation duration much shorther than the other relevant time scales, i.e. T_s and Δt, and finite variance σ_ξ^2 [3].

From (1), one has

$$\mathrm{E}[y(t)] = \int_{-\infty}^{+\infty} g(u) f_\xi[u - s(t)]du \tag{4}$$

and

$$\mathrm{E}[y^2(t)] = \int_{-\infty}^{+\infty} g^2(u) f_\xi[u - s(t)]du \tag{5}$$

In a similar way, the SNR for the input $x(t)$ is

$$\mathcal{R}_{\text{in}} = \frac{A^2/4}{\sigma_\xi^2 \Delta t \Delta B} \tag{6}$$

We then consider for $g(.)$ a very simple nonlinearity, easily implementable with an operational amplifier, the linear-limiting saturation

$$g(u) = \begin{cases} -\lambda & \text{for } u \le -\lambda \\ u & \text{for } -\lambda < u < \lambda \\ \lambda & \text{for } u \ge \lambda \end{cases} \tag{7}$$

with the 'clipping' parameter $\lambda > 0$. With $f_\xi(u)$ a zero-mean Gaussian density associated to the cumulative distribution function $F_\xi(u)$, (4) and (5) give

$$\mathrm{E}[y(t)] = \lambda + (-\lambda - s(t))F_\xi(-\lambda - s(t)) - (\lambda - s(t)) \times F_\xi(\lambda - s(t)) + \sigma_\xi^2[f_\xi(-\lambda - s(t)) - f_\xi(\lambda - s(t))] \tag{8}$$

and

$$\mathrm{E}[y^2(t)] = \lambda^2 + (\lambda^2 - s^2(t) - \sigma_\xi^2)[F_\xi(-\lambda - s(t)) - F_\xi(\lambda - s(t))] + \sigma_\xi^2[(-\lambda - s(t))f_\xi(\lambda - s(t)) - (\lambda - s(t))f_\xi(-\lambda - s(t))] \tag{9}$$

In these conditions, we can analyse the behaviour of the input–ouput SNR gain $G = \mathcal{R}_{\text{out}}/\mathcal{R}_{\text{in}}$. It turns out that there is a broad range of values for λ, both $>A$ or $<A$ depending on the noise level σ_ξ, where the SNR gain G is above unity. Qualitatively, the clipping device (7) on the signal–noise mixture $x(t) = s(t) + \xi(t)$, is able to reduce the noise $\xi(t)$ more than the harmonic signal $s(t)$, this resulting in an improved SNR. Furthermore, at each noise level σ_ξ, it is possible to find the optimal clipping λ_{opt} that maximises the SNR gain G, as presented in Fig. 1. Fig. 1 shows that the optimal clipping λ_{opt} is not necessarily at the signal amplitude A; depending on the noise level, λ_{opt} can be below or above A. Also, for any noise level σ_ξ, at the optimal clipping λ_{opt}, the SNR gain G is always above unity, although it returns (from above) to unity at large noise when $\lambda_{\text{opt}} \to \infty$ (linearity of $g(.)$ is recovered as the optimal processor).

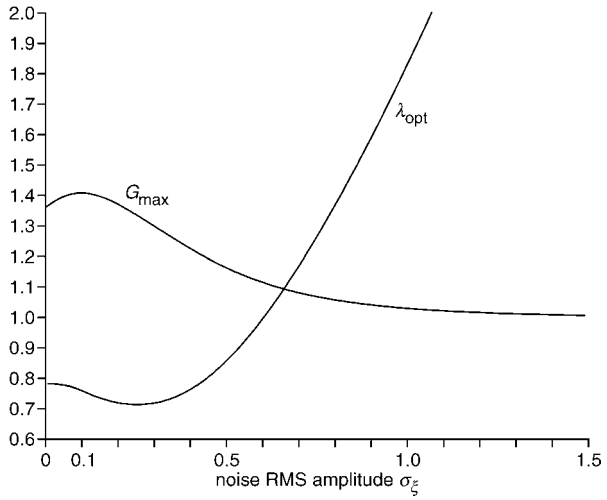

Fig. 1 *Optimal clipping λ_{opt} in (7) and maximum input–ouput SNR gain G_{max} at λ_{opt} against function of RMS amplitude σ_ξ (in units of $A = 1$) of zero-mean Gaussian noise $\xi(t)$*

The present analysis establishes that simple nonlinear devices can be used as SNR amplifiers for a harmonic signal in noise, an outcome which is inaccessible with linear devices. The present treatment is general in $g(.)$ (and also in the noise density f_ξ); we have tested here the simple $g(.)$ of (7), the electronic implementation of which is easy; but other nonlinearities $g(.)$ can be tested for an SNR amplification $G > 1$. Power-law nonlinearities tested in [4] exhibit a similar property of $G > 1$ but with a more complex physical implementation. Additionally, application of the present treatment shows that hard-threshold nonlinearities, like signum or Heaviside functions for $g(.)$, do not allow $G > 1$ with Gaussian noise. Other common nonlinearities encountered, for instance in semiconductor devices, could also be tested for SNR amplification. Such simple nonlinear operators offer a useful complement to linear techniques for signal processing and sensors.

23 March 2005
Electronics Letters online no: 20051065
doi: 10.1049/el:20051065

F. Chapeau-Blondeau and D. Rousseau (*Laboratoire d'Ingénierie des Systèmes Automatisés (LISA), Université d'Angers, 62 avenue Notre Dame du Lac, 49000 Angers, France*)

E-mail: chapeau@univ-angers.fr

References

1 Davenport, W.B., and Root, W.L.: 'An introduction to the theory of random signals and noise' (Wiley, New York, 1987)
2 Bendat, J.S.: 'Nonlinear systems techniques and applications' (Wiley, New York, 1998)
3 Chapeau-Blondeau, F., and Godivier, X.: 'Theory of stochastic resonance in signal transmission by static nonlinear systems', *Phys. Rev. E*, 1997, **55**, pp. 1478–1495
4 Chapeau-Blondeau, F., and Rousseau, D.: 'Enhancement by noise in parallel arrays of sensors with power-law characteristics', *Phys. Rev. E*, 2004, **70**, pp. 060101(R), 1–4

P.R. BHAT and D. ROUSSEAU and G. V. ANAND. Improved Bayesian Estimation of Weak Signal in Non-Gaussian Noise by Optimal Quantization. IEEE 7th SPCOM, International Conference on Signal Processing and Communications. Bangalore, India, dec 2004.

IMPROVED BAYESIAN ESTIMATION OF WEAK SIGNALS IN NON-GAUSSIAN NOISE BY OPTIMAL QUANTIZATION

P. R. BHAT [1*], *D. ROUSSEAU* [2*], *G. V. ANAND* [3]

[1] Department of Electrical Engineering
Indian Institute of Technology MADRAS, CHENNAI, India.
[2] Laboratoire d'Ingénierie des Systémes Automatisés (LISA, CNRS, 2656)
Université d'Angers, 62 avenue Notre Dame du Lac, 49000 ANGERS, France.
[3] Department of Electrical Communication Engineering
Indian Institute of Science, BANGALORE 560012, India.
e-mail: anandgv@ece.iisc.ernet.in

ABSTRACT

In this paper, we present a new improved method for signal shape estimation in non-Gaussian noise with low signal to noise ratio. We combine a nonlinear preprocessing with Wiener £ltering. In the proposed method, the data received is £rst quantized by a symmetric 3–level quantizer before processing by the Wiener £lter. A complete theoretical analysis of this quantizer–estimator is worked out under low signal to noise ratio conditions. In this framework, we show that if the noise is suf£ciently non-Gaussian and the quantizer thresholds are optimally chosen, the quantization, although limited to 3–levels, leads to an enhancement of the estimation performed by the Wiener £lter. Numerical results comparing the quantizer–estimator with the Wiener £lter applied alone are presented to con£rm the theory. Non-Gaussian noise distributions speci£cally relevant for an underwater acoustic environment are chosen for illustration.

1. INTRODUCTION

Shape estimation of a signal buried in noise is a problem of great interest for many signal processing applications [1]. In presence of Gaussian noise, the optimal Bayesian estimator minimizing the estimation mean square error is the Wiener £lter that has the advantage of being linear. In non-Gaussian noisy environment, the optimal estimators are usually nonlinear and hence more dif£cult to implement and, sometimes, even to determine explicitly. Non-Gaussian noise can be found in many practical situations like, for example, in the £eld of ocean acoustics [2]. Therefore, there is a need to develop simple nonlinear estimators capable of outperforming the Wiener estimator with non-Gaussian noise. Such estimators would be especially useful when the signal to be estimated is very weak compared to the noise; indeed in these conditions the estimation performance of the optimal linear estimator is very poor and really needs to be enhanced. In this paper, we describe, analyze and evaluate a new simple nonlinear estimator capable of outperforming the Wiener £lter under conditions of weak signal and non-Gaussian noise.

* First and second authors performed the work while at [3]

This work was supported by the Defense Research and Development Organisation under the DRDO-IISc Joint Programme on Advanced Research in Mathematical Engineering.

2. AN ESTIMATION PROBLEM

We consider the problem of estimating the shape of a weak signal $s(t)$ buried in an additive noise $\eta(t)$. The observable signal $x(t) = s(t) + \eta(t)$ is uniformaly sampled to provide N data points $x_i = x(i \times T)$ with $i = 0, 1, \ldots, N-1$ and $1/T$ the sampling rate. From the data set $\mathbf{x} = (x_1, \ldots x_N)$ the N-dimensional vector $\mathbf{s} = (s_1, \ldots s_N)$ is to be estimated. The noise samples η_i are assumed independent and identically distributed with cumulative distribution $F_\eta(u)$, and probability density function (pdf) $f_\eta(u) = dF_\eta/du$, with zero mean and unit variance.

$$\mathrm{E}\left[\eta_i\right] = 0; \qquad \mathrm{E}\left[\eta_i \eta_j\right] = \delta_{ij}, \tag{1}$$

where $\delta_{ij} = 1$ if $j = i$ and 0 otherwise. The signal s is assumed to be a random wide-sense stationary process with exponentially decaying autocorrelation. The signal samples s_i are assumed identically distributed with cumulative distribution $F_s(u)$, pdf $f_s(u) = dF_s/du$, with zero mean and variance σ_s^2. Therefore we have

$$\mathrm{E}\left[s_j\right] = 0; \qquad \mathrm{E}\left[s_i s_j\right] = \sigma_s^2 \rho_{ij} \ , \tag{2}$$

with

$$\rho_{ij} = \exp(-\zeta |i-j|). \tag{3}$$

It is assumed that the signal $\mathbf{s}$ is weak, so that $\sigma_s^2 \ll 1$.

The linear minimum mean square error estimator $\hat{\mathbf{s}}$ of the signal $\mathbf{s}$ is given by the well known Wiener £lter [1]

$$\hat{\mathbf{s}} = \mathbf{C_{sx}}\mathbf{C_{xx}^{-1}}\mathbf{x} \ , \tag{4}$$

where $\mathbf{C_{xx}}$ is the covariance matrix of $\mathbf{x}$ and $\mathbf{C_{sx}}$ is the cross-covariance matrix of $\mathbf{s}$ and $\mathbf{x}$. As $\mathbf{C_{sx}} = \mathbf{C_{ss}}$ and $\mathbf{C_{xx}} = \mathbf{C_{ss}} + \mathbf{C}_{\boldsymbol{\eta\eta}}$ with $\mathbf{C}_{\boldsymbol{\eta\eta}} = \mathbf{I}$, the estimated signal $\hat{\mathbf{s}}$ is given by

$$\hat{\mathbf{s}} = \mathbf{C_{ss}}(\mathbf{C_{ss}} + \mathbf{I})^{-1}\mathbf{x} \ . \tag{5}$$

Using the weak signal approximation, $\sigma_s^2 \ll 1$, we get

$$\hat{\mathbf{s}} = \mathbf{C_{ss}}\mathbf{x} \ . \tag{6}$$

When the additive noise $\boldsymbol{\eta}$ is Gaussian the linear Wiener Filter turns out to be the overall (among all linear or nonlinear classes) optimal estimator minimizing the mean square error of the estimated signal $\hat{\mathbf{s}}$ with respect to the original signal $\mathbf{s}$. But, as soon as one departs from the case of a Gaussian noisy environment, the optimality of the Wiener £lter is no longer assured. Still, because of its simplicity of implementation, due to its linear property, the Wiener £lter is often used even in the presence of non-Gaussian noise. However, the performance of the Wiener £lter in such non-Gaussian noisy conditions can be quite poor.

For our estimation task, we will speci£cally consider $\boldsymbol{\eta}$ to be non-Gaussian noise. For illustration, we examine two noise famillies: generalized Gaussian noise, and mixture of Gaussian noise.The pdf of the generalized Gaussian noise is expressed as $f_\eta(u) = f_{gg}(u/\sigma_\eta)/\sigma_\eta$, using the standardized density

$$f_{gg}(u) = A\exp(-\mid bu \mid^p) \ , \tag{7}$$

where σ_η^2 is the variance, $b = [\Gamma(3/p)/\Gamma(1/p)]^{1/2}$ and $A = (p/2)[\Gamma(3/p)]^{1/2}/[\Gamma(1/p)]^{3/2}$ are parameterized by the positive exponent p. This family is interesting in the present situation for it includes the Gaussian case ($p = 2$). Furthermore, generalized Gaussian densities enable one to study noise whose tails are either heavier ($p < 2$) or lighter ($p > 2$) than that of the Gaussian noise. The mixture of Gaussian pdf is expressed as $f_\eta(u) = f_{mg}(u/\sigma_\eta)/\sigma_\eta$, using the standardized density

$$\begin{aligned} f_{mg}(u) \quad = \quad & \frac{c}{\sqrt{2\pi}}\left[\alpha\exp\left(-\frac{c^2u^2}{2}\right)\right. \\ & \left. + \frac{1-\alpha}{\beta}\exp\left(-\frac{c^2u^2}{2\beta^2}\right)\right] , \end{aligned} \tag{8}$$

where $c = [\alpha + (1-\alpha)(\beta^2)]^{1/2}$; σ_η^2 is the variance, $\alpha \in [0,1]$ is the mixing parameter and $\beta > 0$ is the ratio of the standard deviations of the individual contributions. This family of pdf's is a subclass of Middleton's class wich is also widely used to model ocean acoustic noise [2]. In the next section, we introduce a simple nonlinear estimator and compare its performance with that of the Wiener £lter in the presence of generalized Gaussian or mixture of Gaussian noise.

3. THE QUANTIZER–ESTIMATOR

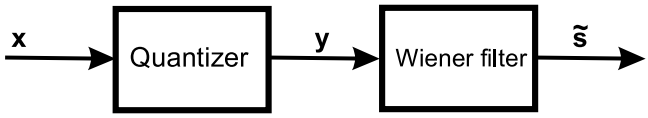

Fig. 1. Block diagram of the quantizer–estimator.

We consider a nonlinear estimator composed of a quantizer followed by the Wiener £lter. A block diagram of this nonlinear estimator is shown in Fig. 1, where $\mathbf{y} = Q(\mathbf{x})$ is the quantized version of the observable data set $\mathbf{x}$ and

$$\tilde{\mathbf{s}} = \mathbf{C_{sy}}\mathbf{C_{yy}^{-1}}\mathbf{y} \ , \tag{9}$$

is the estimation given by the nonlinear estimator. It is now well established [3, 4] that static memoryless nonlinear systems like quantizers can lead to signal to noise ratio (SNR) gain greater than unity and that such quantizers can be used to design nonlinear detectors which can outperform optimal linear detectors in non-Gaussian noise. In particular, a recent study [4] has shown that SNR gain exceeding unity is available for a large number of noise pdf's belonging to the families of Eqs. (7) and (8); a striking point is that these SNR gains [5, 4] can be obtained using a simple symmetric 3–level quantizer with only a very limited loss of performance in comparison with higher number of quantization levels. In the following, we choose for illustration the quantizer $Q(.)$ as a symmetric 3–level quantizer de£ned by

$$y_i = \begin{cases} -1 & \text{for } x_i \le -\gamma \\ 0 & \text{for } -\gamma < x_i \le \gamma \\ 1 & \text{for } x_i > \gamma \end{cases} \ , \tag{10}$$

where y_i and x_i are the i^{th} elements of vectors $\mathbf{y}$ and $\mathbf{x}$ and γ is the threshold of the quantizer. We are going to show that the use of quantizers for detection purposes can be extended to signal estimation.

3.1. Analytical expression for weak signal estimator

Performance analysis of the quantizer estimator $\tilde{\mathbf{s}}$ of Eq. (9) requires the determination of the covariance matrices $\mathbf{C_{sy}}$

and $\mathbf{C_{yy}}$. We shall present a detailed analysis to obtain analytical expressions for these two matrices $\mathbf{C_{sy}}$ and $\mathbf{C_{yy}}$.

To derive the expression for $\mathbf{C_{sy}}$, let the random variable u_{ij} be de£ned as $u_{ij} = s_i y_j$, with $i, j = 0, 1, \ldots, N-1$. By symmetry of pdf's of the noise $\boldsymbol{\eta}$ and signal $\boldsymbol{s}$, the pdf of u_{ij} is given by

$$f_{u_{ij}}(u) = 2\frac{d}{du}\Pr\{\mathrm{s_i} \le \mathrm{u}, \mathrm{x_j} > \gamma\} + \Pr\{|\mathrm{x_j}| < \gamma\}\delta(\mathrm{u}) , \quad (11)$$

where $\delta(u)$ is the Dirac delta function. The joint probability $\Pr\{\mathrm{s_i} \le \mathrm{u}, \mathrm{x_j} > \gamma\}$ is given by

$$\Pr\{\mathrm{s_i} \le \mathrm{u}, \mathrm{x_j} > \gamma\} = \left[\int_{-\infty}^{u}\int_{-\infty}^{\infty}[1 - F_\eta(\gamma - s_j)] \times f_{s_i s_j}(s_i, s_j)ds_i ds_j\right] . \quad (12)$$

In view of the weak signal assumption, $F_\eta(\gamma - s_j)$ may be replaced by the truncated Taylor series

$$F_\eta(\gamma - s_j) = F_\eta(\gamma) - s_j f_\eta(\gamma) + \frac{1}{2}s_j^2 f'_\eta(\gamma) , \quad (13)$$

to obtain the following expression

$$\Pr\{\mathrm{s_i} \le \mathrm{u}, \mathrm{x_j} > \gamma\} = \left[\int_{-\infty}^{\mathrm{u}}\{[1 - \mathrm{F}_\eta(\gamma)] + f_\eta(\gamma)\,\mathrm{E}\,[s_j|s_i] - \frac{1}{2}f'_\eta(\gamma)\,\mathrm{E}\,[s_j^2|s_i]\}f_s(s_i)ds_i\right] . \quad (14)$$

Assuming the conditional expectations $\mathrm{E}\,[s_j|s_i]$ and $\mathrm{E}\,[s_j^2|s_i]$ to be polynomials of s_i and determining the coef£cients so as to reducing the mean square error, the following expressions are obtained

$$\mathrm{E}\,[s_j|s_i] = \rho_{ij}s_i + O(s_i^3) , \quad (15)$$

$$\mathrm{E}\,[s_j^2|s_i] = \sigma_s^2(1 - K) + Ks_i^2 + O(s_i^3) , \quad (16)$$

where

$$K = \frac{\mathrm{E}\,[s_i^2 s_j^2] - \sigma_s^4}{\mathrm{E}\,[s_i^4] - \sigma_s^4} . \quad (17)$$

Substituting Eqs. (15)–(17) into Eq. (14), differentiating with respect to u, and neglecting terms of third and higher powers in u, we get

$$\frac{d}{du}[\Pr\{\mathrm{s_i} \le \mathrm{u}, \mathrm{x_j} > \gamma\}] = \mathrm{f_s(u)} \times \left[1 - \mathrm{F}_\eta(\gamma) - \frac{1}{2}f'_\eta(\gamma)\sigma_s^2(1-K) + f_\eta(\gamma)\rho_{ij}u - \frac{1}{2}f'_\eta(\gamma)Ku^2\right] . \quad (18)$$

Substituting Eq. (18) into Eq. (11) and considering the expectation of $s_i y_j$ the following result is obtained

$$\mathrm{E}\,[s_i y_j] = \mathrm{E}\,[u_{ij}] = 2f_\eta(\gamma)\rho_{ij}\sigma_s^2 . \quad (19)$$

An element of the covariance matrice $\mathbf{C_{sy}}$ is de£ned by $cov(s_i, y_j) = \mathrm{E}\,[s_i y_j] - \mathrm{E}\,[s_i]E[y_j]$ and since $\mathrm{E}\,[s_i] = 0$, we have

$$\mathbf{C_{sy}} = 2f_\eta(\gamma)\mathbf{C_{ss}} . \quad (20)$$

To derive the expression for $\mathbf{C_{yy}}$, we use the same approximations as in the derivation of $\mathbf{C_{sy}}$ i.e. the weak signal assumption (the second and higher power terms of σ_s are ignored in the Taylor series development of $F_\eta(\gamma - s_j)$) and the assumptions of symmetry of pdf's of the signal $\mathbf{s}$ and noise $\boldsymbol{\eta}$. The following expression for $\mathbf{C_{yy}}$ is obtained

$$\mathbf{C_{yy}} = 2[1 - F_\eta(\gamma)]\mathbf{I} . \quad (21)$$

Using Eqs. (20) and (21) in Eq. (9) the following expression is obtained for the estimator of a weak signal

$$\tilde{\mathbf{s}} = \frac{f_\eta(\gamma)}{1 - F_\eta(\gamma)} \times \mathbf{C_{ss}}\mathbf{y} . \quad (22)$$

In Eq. (22), a noticeable characteristic of the quantizer–estimator is its simplicity which is comparable to that of the Wiener £lter of Eq. (6) under the weak signal assumption. Furthermore, we are going to show that under the weak signal assumption the quantizer–estimator can outperform the Wiener £lter when the noise $\boldsymbol{\eta}$ belongs to the generalized Gaussian or mixture of Gaussian noise families. We will explain how to design this 3–level quantizer by optimizing the threshold γ to enhance the quantizer-estimator performance.

3.2. Performance Analysis

In this section, we derive an asymptotic analysis of the performance of the quantizer–estimator of the previous section valid under the weak signal assumption. In the context of shape estimation that we are considering, a meaningful measure of the estimator performance is provided by the normalized cross-covariance between the signal and its estimate; This is a similarity measure insensitive to both scaling and translation in signal amplitude. Since $\mathrm{E}[s] = \mathrm{E}[\hat{s}] = 0$, the normalized cross-covariance of $\mathbf{s}$ and $\hat{\mathbf{s}}$ is

$$\mathbf{Cor_{s\hat{s}}} = \frac{\mathrm{E}\left[\mathbf{s}^{\mathrm{T}}\hat{\mathbf{s}}\right]}{\sqrt{\mathrm{E}[\mathbf{s}^{\mathrm{T}}\mathbf{s}]\,\mathrm{E}[\hat{\mathbf{s}}^{\mathrm{T}}\hat{\mathbf{s}}]}} , \quad (23)$$

where T stands for the transposition operator. Similarly the normalized cross-covariance for $\mathbf{s}$ and $\tilde{\mathbf{s}}$ is

$$\mathbf{Cor_{s\tilde{s}}} = \frac{\mathrm{E}\left[\mathbf{s}^{\mathrm{T}}\tilde{\mathbf{s}}\right]}{\sqrt{\mathrm{E}[\mathbf{s}^{\mathrm{T}}\mathbf{s}]\,\mathrm{E}[\tilde{\mathbf{s}}^{\mathrm{T}}\tilde{\mathbf{s}}]}} . \quad (24)$$

Let us de£ne the improvement in performance of the quantizer–estimator over that of the Wiener £lter alone as estimation gain

$$G_{est} = \frac{\mathbf{Cor}_{\mathbf{s}\tilde{\mathbf{s}}}}{\mathbf{Cor}_{\mathbf{s}\hat{\mathbf{s}}}} \ . \tag{25}$$

Substituting Eq. (6) into Eq. (23) and Eq. (22) into Eq. (24), we have, after simpli£cation, a simple analytical expression for the asymptotic estimation gain under the weak signal assumption

$$G_0 = \sqrt{\frac{2f_\eta^2(\gamma)}{1 - F_\eta(\gamma)}} \ , \tag{26}$$

where G_{est} tends to G_0 when the input $\mathrm{SNR_{in}} = \sigma_\mathrm{s}^2$ tends to zero. Therefore, when $G_0 > 1$, an improvement of the quantizer–estimator against the Wiener £lter estimator will be expected if the weak signal assumption is valid.

Let us consider the input–output SNR gain achieved by the 3–level quantizer de£ned as

$$G_{\mathrm{SNR}} = \frac{\mathrm{SNR_{out}}}{\mathrm{SNR_{in}}} \ , \tag{27}$$

with the ouput SNR de£ned as

$$\mathrm{SNR_{out}} = \frac{\left(\mathrm{E}[\mathbf{s}^\mathrm{T}\mathbf{y}]\right)^2 / \mathrm{E}[\mathbf{s}^\mathrm{T}\mathbf{s}]}{\sum_{\mathrm{i}=0}^{\mathrm{N}-1} \mathrm{var(y_i)}} \ . \tag{28}$$

It can be shown [5, 4], under weak signal assumption, that

$$G_{\mathrm{SNR}} = \frac{2f_\eta^2(\gamma)}{1 - F_\eta(\gamma)} \ . \tag{29}$$

As a result, maximizing the estimation gain G_0 of Eq. (26) is equivalent to maximizing the input–ouput signal to noise ratio gain G_{SNR} of the 3–level quantizer. A SNR gain greater than unity is interesting in the detection context where a higher SNR leads to a better detector performance. Here, we see that SNR gain exceeding unity will also improve the performance of an estimation task. The maximization, with respect to the threshold γ, of the SNR gain G_{SNR} of a 3–level quantizer has been developed and applied to generalized Gaussian and mixture of Gaussian noise pdf's by [5, 4]. As an illustration, Fig. 2 shows the evolution of the optimal estimation gain G_0 for the generalized Gaussian noise family and the mixture of Gaussian when the threshold γ is chosen in order to maximize G_{SNR}. It is shown by Fig. 2 that, if the noise is suf£ciently non-Gaussian and the quantizer thresholds are optimally chosen, then $G_0 > 1$, which means that the quantizer–estimator will theoretically exhibit better performance in the weak signal assumption than the Wiener £lter estimator.

4. SIMULATION RESULTS

Now we propose to con£rm the theoretical results of the previous section with numerical simulations. Monte Carlo

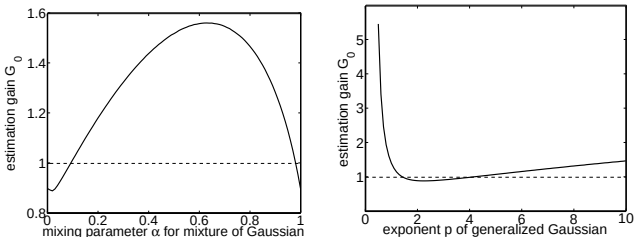

Fig. 2a Fig. 2b

Fig. 2. Optimal estimation gain G_0 under the weak signal assumption for the generalized Gaussian (panel (b)) plotted as a function of exponent p and the mixture of Gaussian (panel (a)) as a function of the mixing parameter α while the ratio of the standard deviations is £xed to $\beta = 4$. The region above the dashed line shows an improvement in the estimation of the quantizer–estimator over the Wiener £lter.

simulations have been done to compute the estimation gain G_{est} of Eq. (25) of the quantizer–estimator over the Wiener £lter in generalized Gaussian and mixture of Gaussian noise. The vector length taken for the samples is $N = 3000$ and the expectation operators in Eq. (25) are estimated with an averaging taken over 300 trials.

In Fig. 3, we show the evolution of the estimation gain G_{est} of Eq. (25) in given conditions for the noise and signal and for different input signal to noise ratio $\mathrm{SNR_{in}\ (dB)} = 10\log(\sigma_\mathrm{s}^2)$. In both Fig. 3a and Fig. 3b we £nd $G_{est} > 1$ for suf£ciently small $\mathrm{SNR_{in}}$ (approximately for $\mathrm{SNR_{in}\ (dB)}$ smaller than -3 dB in Fig. 3a and smaller than -5 dB in Fig. 3b). Figure 3a illustrates that the analytical estimation gain G_0 calculated in Eq. (26) is indeed an asymptotic theoretical result valid under the weak signal assumption. In Fig. 3b, the estimation gain G_{est} is well below the asymptotic value even for $\mathrm{SNR_{in}\ (dB)} = -20$ dB, although G_{est} is clearly greater than unity. This can be explained theoretically by including the third and higher order terms in the approximate expressions for $\mathrm{E}\left[s_i y_j\right]$ and $\mathrm{E}\left[y_i y_j\right]$ derived in Sec. 3. In order to complete the illustration provided by Fig. 3, we give in Tab. 1 and Tab. 2 the values of the correlations $\mathbf{Cor}_{\mathbf{s}\hat{\mathbf{s}}}$ and $\mathbf{Cor}_{\mathbf{s}\tilde{\mathbf{s}}}$ corresponding to some points of Fig. 3; from these tables, one can appreciate how the estimation performance of the Wiener £lter degrades when the $\mathrm{SNR_{in}\ (dB)}$ is decreasing and how the quantizer–estimator arrests this degradation. We have tested a large number of pdf among the generalized Gaussian and mixture of Gaussian noise. We have also studied the in¤uence of the length of the data set N and the signal correlation exponential decay parameter ζ on the estimation improvement. All our results con£rm the asymptotic analysis of the previous section. For weak signals in suf£ciently non-Gaussian noise the quantizer–estimator described in this paper outperforms the Wiener £lter.

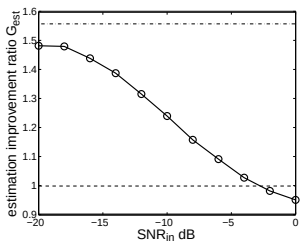

Fig. 3a

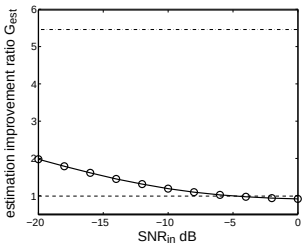

Fig.3b

Fig. 3. Estimation improvement ratio G_{est} as a function of the input signal to noise ratio $\mathrm{SNR_{in}}$ (dB). ($\circ$) stands for the numerical evaluation of G_{est}, solid line is only a guide for the eye, and the dash-dotted line at the top stands for the asymptotic estimation improvement ratio G_0 given in Eq. (26) under the weak signal assumption. In panel (a), the noise $\boldsymbol{\eta}$ is a mixture of Gaussian with $\alpha = 0.6$ and $\beta = 4$, the signal correlation decay parameter $\zeta = 0.5$. In panel (b), same conditions as in Fig. 3a but the noise has generalized Gaussian density with exponent $p = 0.5$.

SNRin (dB)	-20	-10	-4	0
Wiener £lter	0.14	0.40	0.62	0.73
Quantizer–estimator	0.21	0.50	0.64	0.69

Table 1. Values of the correlations $\mathbf{Cor}_{\mathbf{s}\hat{\mathbf{s}}}$ for the Wiener £lter and $\mathbf{Cor}_{\mathbf{s}\tilde{\mathbf{s}}}$ for the quantizer–estimator corresponding to some points in Fig. 3a.

5. CONCLUSION

In this paper, we have introduced a new nonlinear estimator capable of doing better than the conventional linear Wiener £lter for shape estimation of weak signals buried in additive non-Gaussian noise. We have assessed the performance of this nonlinear estimator both theoretically and numerically for non-Gaussian noise relevant for applications in underwater acoustic. In addition to providing an improved estimation, this nonlinear estimator composed of a 3–level symmetric quantizer followed by the Wiener £lter presents the advantage of being almost as simple as the Wiener £lter. A conceptually and practically interesting result of this study is that working with a parsimonious representation of the observable signal (here it was only a 3–level representation) can sometimes be more ef£cient for information processing than seeking a faithful representation of the original signal from the physical environment. Various perspectives and extensions of this work can be pursued, like considering other non-Gaussian noise distributions of practical interest, testing other types of simple nonlinear preprocessors (for example the array of quantizers studied in [6]) or even applying these nonlinear preprocessors to other signal processing tasks (for example enhancing the Kalman £lter for nonstationary signal estimation buried in non-Gaussian noise).

SNRin (dB)	-20	-10	-4	0
Wiener £lter	0.17	0.47	0.67	0.76
Quantizer–estimator	0.35	0.57	0.66	0.70

Table 2. Values of the correlations $\mathbf{Cor}_{\mathbf{s}\hat{\mathbf{s}}}$ and $\mathbf{Cor}_{\mathbf{s}\tilde{\mathbf{s}}}$ corresponding to some points in Fig. 3b.

6. REFERENCES

[1] S. Kay, "Fundamentals of Statistical Signal Processing, Vol. 1: Estimation Theory", *Prentice Hall*, Englewood Cliffs, 1993.

[2] F.W. Machell, C. S. Penrod, and G.E. Ellis, "Statistical Characteristics of Ocean Acoustic Noise Processes", *Topics in Non-Gaussian Signal Processing*, Springer, Wegman, E. J. and Schwartz, S. C. and Thomas, J. B., Berlin, 1989, pp. 29–57.

[3] F. Chapeau-Blondeau, "Periodic and Aperiodic Stochastic Resonance with Output Signal-to-noise Ratio Exceeding that at the Input", *International Journal of Bifurcation and Chaos*, 1999, Vol. 9, pp. 267–272.

[4] A. Saha, G. V. Anand, "Design of Detectors Based on Stochastic Resonance", *Signal Processing*, 2003, Vol. 83, pp. 1193–1212.

[5] V. G. Guha, "Detection of Weak Signals in Non-Gaussian Noise Using Stochastic Resonance", *M. Sc. (Engg.) Thesis*, Department of Electrical Communication Engineering, Indian Institute of Science, Bangalore, 2002.

[6] D. Rousseau, F. Chapeau-Blondeau, "Suprathreshold Stochastic Resonance and Signal-to-noise Ratio Improvement in Arrays of Comparators", *Physics Letters A*, 2004, Vol. 321, pp. 280–290.

F. CHAPEAU-BLONDEAU and D. ROUSSEAU. Raising the noise to improve performance in optimal processing. *Journal of Statistical Mechanics : Theory and Experiment*, P01003, 1–5, 2009.

Journal of Statistical Mechanics: Theory and Experiment
An IOP and SISSA journal

Raising the noise to improve performance in optimal processing

François Chapeau-Blondeau and David Rousseau

Laboratoire d'Ingénierie des Systèmes Automatisés (LISA), Université d'Angers, 62 avenue Notre Dame du Lac, F-49000 Angers, France
E-mail: chapeau@univ-angers.fr and david.rousseau@univ-angers.fr

Received 10 June 2008
Accepted 1 August 2008
Published 5 January 2009

Online at stacks.iop.org/JSTAT/2009/P01003
doi:10.1088/1742-5468/2009/01/P01003

Abstract. We formulate, in general terms, the classical theory of optimal detection and optimal estimation of signal in noise. In this framework, we exhibit specific examples of optimal detectors and optimal estimators endowed with a performance which can be improved by injecting more noise. From this proof of feasibility by examples, we suggest a general mechanism by which noise improvement of optimal processing, although seemingly paradoxical, may indeed occur. Beyond specific examples, this leads us to the formulation of open problems concerning the general characterization, including the conditions of formal feasibility and of practical realizability, of such situations of optimal processing improved by noise.

Keywords: analysis of algorithms

1742-5468/09/P01003+15$30.00

J. Stat. Mech. (2009) P01003

Contents

1. Introduction

Signal and information processing very often has to cope with noise. Noise commonly acts as a nuisance. However, specific phenomena such as those related to stochastic resonance, and currently under investigation, tend to show that noise can sometimes play a beneficial role [1]–[3]. Many situations of stochastic resonance or useful-noise effects have been reported for signal and information processing. This included demonstration of the possibilities of improvement by noise in standard signal processing operations like detection [4]–[13] or estimation [14]–[22] of signal in noise. However, most of these studies have focused on improvement by noise of suboptimal signal processors. By contrast, the present paper will focus on optimal processors. Examples of optimal processing improved by noise will be described, so as to exhibit some concrete proofs of feasibility. Next, a general mechanism will be uncovered which explains how improvement by noise of optimal processing can indeed occur, however paradoxical it may seem at first sight. Open questions will then be formulated concerning the general characterization of the optimal processing problems and their solutions, that can take advantage of improvement by noise.

This paper takes place within the classical frameworks of optimal detection and optimal estimation of signal in noise. For self-completeness of the paper, the classical theory of these frameworks will be briefly recalled. This will also serve to explicitly visualize the place of the classical derivations where the (unexpected) possibility of improvement by noise can make its way in. We will be considering a general optimal processing situation under the classical form as follows: an input signal $s(t)$ is coupled to a random noise $\xi(t)$ by some physical process, so as to produce an observable signal $x(t)$. At N distinct times t_k which are given, N observations are collected $x(t_k) = x_k$, for $k = 1$ to N. From the N observations $(x_1, \ldots, x_N) = \boldsymbol{x}$, one wants to perform, about the input signal $s(t)$, some inference that would be optimal in the sense of a meaningful criterion of performance.

doi:10.1088/1742-5468/2009/01/P01003

J. Stat. Mech. (2009) P01003

2. Optimal detection

2.1. Classical theory of optimal detection

As an embodiment of the general situation of section 1, we consider a standard two-hypotheses detection problem, where the input signal $s(t)$ can be any one of two known signals, i.e. $s(t) \equiv s_0(t)$ with known prior probability P_0 or $s(t) \equiv s_1(t)$ with prior probability $P_1 = 1 - P_0$. The input signal $s(t)$ is mixed in some way with the 'corrupting' noise $\xi(t)$ to yield the observable signal $x(t)$. From the observations $\boldsymbol{x} = (x_1, \ldots, x_N)$ one has then to detect whether $s(t) \equiv s_0(t)$ (hypothesis H_0) or $s(t) \equiv s_1(t)$ (hypothesis H_1) holds.

Following classical detection theory [23, 24], any detection procedure can be formalized by specifying that the detector will decide $s(t) \equiv s_0(t)$ whenever the data $\boldsymbol{x} = (x_1, \ldots, x_N)$ falls in the region $\mathcal{R}_0$ of $\mathbb{R}^N$, and it will decide $s(t) \equiv s_1(t)$ when $\boldsymbol{x}$ falls in the complementary region $\mathcal{R}_1$ of $\mathbb{R}^N$. In this context, a meaningful criterion of performance is (other criteria of Neyman–Pearson or minimax types are also possible) the probability of detection error $P_{\mathrm{er}} = \Pr\{s_1 \text{ decided}|\mathrm{H}_0 \text{ true}\}P_0 + \Pr\{s_0 \text{ decided}|\mathrm{H}_1 \text{ true}\}P_1$, also expressible as

$$P_{\mathrm{er}} = P_1 \int_{\mathcal{R}_0} p(\boldsymbol{x}|\mathrm{H}_1)\,\mathrm{d}\boldsymbol{x} + P_0 \int_{\mathcal{R}_1} p(\boldsymbol{x}|\mathrm{H}_0)\,\mathrm{d}\boldsymbol{x}, \tag{1}$$

where $p(\boldsymbol{x}|\mathrm{H}_j)$ is the probability density for observing $\boldsymbol{x}$ when hypothesis H_j holds, with $j \in \{0, 1\}$, and the notation $\int . \,\mathrm{d}\boldsymbol{x}$ stands for the N-dimensional integral $\int \cdots \int . \,\mathrm{d}x_1 \cdots \mathrm{d}x_N$.

Since $\mathcal{R}_0$ and $\mathcal{R}_1$ are complementary in $\mathbb{R}^N$, one has

$$\int_{\mathcal{R}_0} p(\boldsymbol{x}|\mathrm{H}_1)\,\mathrm{d}\boldsymbol{x} = 1 - \int_{\mathcal{R}_1} p(\boldsymbol{x}|\mathrm{H}_1)\,\mathrm{d}\boldsymbol{x}, \tag{2}$$

which, substituted in equation (1), yields

$$P_{\mathrm{er}} = P_1 + \int_{\mathcal{R}_1} [P_0 p(\boldsymbol{x}|\mathrm{H}_0) - P_1 p(\boldsymbol{x}|\mathrm{H}_1)]\,\mathrm{d}\boldsymbol{x}. \tag{3}$$

Following classical detection theory [23, 24], the detector that minimizes P_{er} can be obtained by making the integral over $\mathcal{R}_1$ on the right-hand side of equation (3) the more negative possible. This is realized by including in $\mathcal{R}_1$ all and only those points $\boldsymbol{x}$ for which the integrand $P_0 p(\boldsymbol{x}|\mathrm{H}_0) - P_1 p(\boldsymbol{x}|\mathrm{H}_1)$ is negative. This yields the optimal detector, which tests the likelihood ratio $L(\boldsymbol{x}) = p(\boldsymbol{x}|\mathrm{H}_1)/p(\boldsymbol{x}|\mathrm{H}_0)$ according to

$$L(\boldsymbol{x}) = \frac{p(\boldsymbol{x}|\mathrm{H}_1)}{p(\boldsymbol{x}|\mathrm{H}_0)} \underset{H_0}{\overset{H_1}{\gtrless}} \frac{P_0}{P_1}. \tag{4}$$

When the decision regions $\mathcal{R}_0$ and $\mathcal{R}_1$ are defined according to the optimal test of equation (4), then on the right-hand side of P_{er} in equation (1), the two quantities to be integrated over $\mathcal{R}_0$ or $\mathcal{R}_1$ can be uniformly expressed, simultaneously over $\mathcal{R}_0$ and $\mathcal{R}_1$, as $\min[P_0 p(\boldsymbol{x}|\mathrm{H}_0), P_1 p(\boldsymbol{x}|\mathrm{H}_1)]$. It results that the minimal P_{er} reached by the optimal detector of equation (4) is expressible as

$$P_{\mathrm{er}}^{\min} = \int_{\mathbb{R}^N} \min[P_0 p(\boldsymbol{x}|\mathrm{H}_0), P_1 p(\boldsymbol{x}|\mathrm{H}_1)]\,\mathrm{d}\boldsymbol{x}. \tag{5}$$

Since $\min(a,b) = (a+b-|a-b|)/2$, the minimal probability of error of equation (5) reduces to

$$P_{\rm er}^{\rm min} = \tfrac{1}{2} - \tfrac{1}{2}\int_{\mathbb{R}^N} |P_1 p(\boldsymbol{x}|\mathrm{H}_1) - P_0 p(\boldsymbol{x}|\mathrm{H}_0)|\,\mathrm{d}\boldsymbol{x}. \tag{6}$$

The classical theory of optimal detection, as reviewed in this section 2.1, thus specifies, through equation (4), the best exploitation of the data $\boldsymbol{x}$ in order to reach the minimal probability of detection error $P_{\rm er}^{\rm min}$ given by equation (6). This theory is general in the sense that it applies for the detection of any two arbitrary known signals $s(t) \equiv s_0(t)$ and $s(t) \equiv s_1(t)$, mixed in any way, to any definite noise $\xi(t)$. The specificity of each problem is essentially coded in the two conditional probability densities $p(\boldsymbol{x}|\mathrm{H}_j)$, for $j \in \{0,1\}$, which express the probabilization induced by the noise $\xi(t)$ once defined.

2.2. A classical detection example

For an application of the optimal detection procedure of section 2.1, we now consider that the signal–noise mixture $x(t)$ is the additive mixture

$$x(t) = s(t) + \xi(t), \tag{7}$$

with $\xi(t)$ a stationary white noise of cumulative distribution function $F_\xi(u)$ and probability density function $f_\xi(u) = \mathrm{d}F_\xi/\mathrm{d}u$. The level of the noise $\xi(t)$ is quantified by its root mean squared (rms) amplitude σ. The white noise assumption here means that, at any distinct observation times t_k, the noise samples $\xi(t_k)$, and consequently the observations $x_k = x(t_k)$, are statistically independent. It then follows that the conditional densities factorize as $p(\boldsymbol{x}|\mathrm{H}_j) = \prod_{k=1}^N p(x_k|\mathrm{H}_j)$, with

$$p(x_k|\mathrm{H}_j) = f_\xi[x_k - s_j(t_k)], \tag{8}$$

for $j \in \{0,1\}$. We further consider the simple situation where the signals to be detected are the constant signals $s_0(t) = s_0$ and $s_1(t) = s_1$, for all t, with two constants $s_0 < s_1$.

In the common case where the white noise $\xi(t)$ in equation (7) is zero-mean Gaussian, it is well known that the optimal detector of equation (4) reduces to

$$\frac{1}{N}\sum_{k=1}^N x_k \underset{H_0}{\overset{H_1}{\gtrless}} \frac{s_0+s_1}{2} + \frac{\sigma^2/N}{s_1-s_0}\ln\left(\frac{P_0}{P_1}\right) = x_T. \tag{9}$$

This optimal test of equation (9) achieves the probability of error of equation (6) which is also

$$P_{\rm er}^{\rm min} = \frac{1}{2}\left[1 + P_1\,\mathrm{erf}\left(\sqrt{N}\frac{x_T - s_1}{\sqrt{2}\sigma}\right) - P_0\,\mathrm{erf}\left(\sqrt{N}\frac{x_T - s_0}{\sqrt{2}\sigma}\right)\right]. \tag{10}$$

It is easy to verify that this minimal probability of detection error $P_{\rm er}^{\rm min}$ of equation (10) monotonically increases when the noise level σ increases. This is depicted in some illustrative conditions by figure 1.

Figure 1 illustrates a common behavior which can be intuitively expected: the performance $P_{\rm er}^{\rm min}$ of the optimal detector monotonically degrades as the noise level σ increases. Such an expectation matches the *a priori* intuition that noise usually has a detrimental effect on information processing. However, this may not be the rule in general, and we show next that improvement by noise can sometimes apply to optimal detectors.

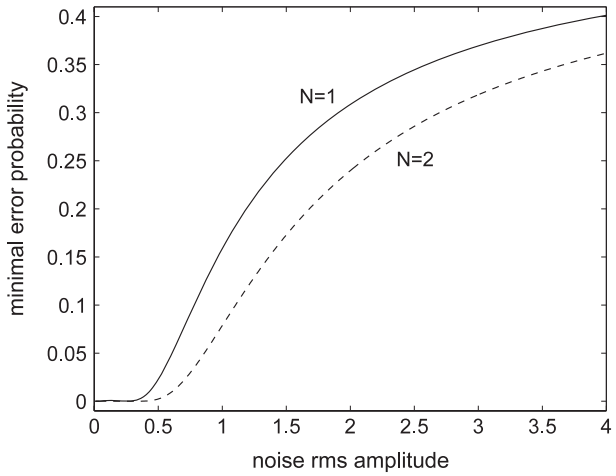

Figure 1. Minimal probability of error $P_{\rm er}^{\rm min}$ of equation (10) for the optimal detector of equation (9), as a function of the rms amplitude σ of the zero-mean Gaussian noise $\xi(t)$ with $N = 1$ and $N = 2$ data points. Also, $s_0(t) \equiv s_0 = -1$, $s_1(t) \equiv s_1 = 1$ and $P_0 = 1/2$.

2.3. Beneficial role of noise

We now turn for the additive white noise $\xi(t)$ in equation (7) to a non-Gaussian case by way of the family of zero-mean Gaussian mixture with standardized probability density (with $0 < m < 1$):

$$f_{\rm gm}(u) = \frac{1}{2\sqrt{2\pi}\sqrt{1-m^2}} \left\{ \exp\left[-\frac{(u+m)^2}{2(1-m^2)} \right] + \exp\left[-\frac{(u-m)^2}{2(1-m^2)} \right] \right\}, \quad (11)$$

and cumulative distribution function:

$$F_{\rm gm}(u) = \frac{1}{2} + \frac{1}{4} \left[{\rm erf}\left(\frac{u+m}{\sqrt{2}\,\sqrt{1-m^2}} \right) + {\rm erf}\left(\frac{u-m}{\sqrt{2}\,\sqrt{1-m^2}} \right) \right]. \quad (12)$$

As $m \to 0$, equation (11) approaches the zero-mean unit-variance Gaussian density; as $m \to 1$, equation (11) approaches the zero-mean unit-variance dichotomic density at ± 1, as in [25]. We consider for $\xi(t)$ the density $f_\xi(u) = f_{\rm gm}(u/\sigma)/\sigma$ which is a zero-mean Gaussian-mixture density with standard deviation σ. This density $f_\xi(u)$ is plugged into equation (8), and then via equation (6) it yields the performance $P_{\rm er}^{\rm min}$ of the optimal detection with Gaussian-mixture noise. Figure 2 represents different evolutions of the performance $P_{\rm er}^{\rm min}$ in equation (6) of the optimal detector as the noise rms amplitude σ increases.

Figure 2 exhibits the possibility, as also found in [26], of nonmonotonic evolutions of the performance $P_{\rm er}^{\rm min}$ of the optimal detector, as the level σ of the Gaussian-mixture noise is raised. When the noise level σ starts to rise above zero in figure 2, the probability of error $P_{\rm er}^{\rm min}$ starts to gradually degrade (to increase), manifesting here a detrimental action of the noise. However, this degradation of $P_{\rm er}^{\rm min}$ does not always proceed monotonically as σ is further increased. Conditions exist in figure 2, where the probability of error $P_{\rm er}^{\rm min}$ improves (decreases) when the noise level σ is further raised over some ranges. At even

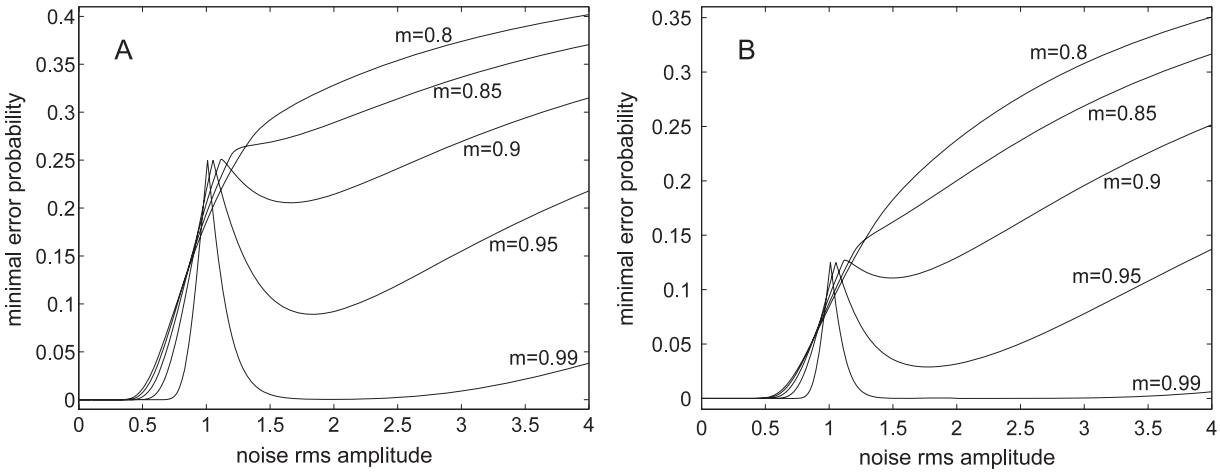

Figure 2. Minimal probability of error $P_{\rm er}^{\rm min}$ of equation (6) for the optimal detector of equation (4), as a function of the rms amplitude σ of the zero-mean Gaussian-mixture noise $\xi(t)$ from equation (11) at different m. Also, $s_0(t) \equiv s_0 = -1$, $s_1(t) \equiv s_1 = 1$ and $P_0 = 1/2$; $N = 1$ (panel A) or $N = 2$ (panel B).

larger levels of σ, the detrimental action of the noise resumes and $P_{\rm er}^{\rm min}$ degrades again by increasing towards the least favorable value of $\min(P_0, P_1)$ which is $1/2$ in figure 2.

The results of figure 2 demonstrate by example that the performance $P_{\rm er}^{\rm min}$ of an optimal detector does not necessarily degrade as the noise level increases. On the contrary, figure 2 shows conditions where, for an optimal detector initially operating at a noise level $\sigma \approx 1$, the optimal performance $P_{\rm er}^{\rm min}$ improves if the optimal detector is taken to operate at a higher noise level $\sigma \approx 1.5$. In the example of figure 2, the beneficial action of noise occurs when the noise $\xi(t)$ departs sufficiently from a Gaussian noise, i.e. when m in equation (11) is sufficiently close to 1. In contrast, values of m approaching zero in figure 2 lead to the Gaussian case of figure 1, where increase of the noise level σ monotonically degrades the performance $P_{\rm er}^{\rm min}$. Qualitatively, it can be realized that the non-Gaussian density $f_\xi(\cdot)$ at m close to 1 has two peaks which make the two noisy constants s_0 and s_1 more distinguishable as the noise level σ is raised over some range, as depicted in figure 3. Quantitatively, this translates into the improvement by noise of the performance $P_{\rm er}^{\rm min}$ in optimal detection, as visible in figure 2.

From a practical point of view, if one wants to take advantage of a beneficial increase in the noise level as it exists in figure 2, one cannot increase the noise level simply by adding an independent white noise $\eta(t)$ to the observation signal $x(t)$ of equation (7) so as to realize $x(t) + \eta(t) = s(t) + \xi(t) + \eta(t)$. In this way, the probability density of the augmented noise $\xi(t) + \eta(t)$ would no longer follow the initial non-Gaussian density $f_\xi(\cdot)$. The process would no longer adhere to the conditions of figure 2 which assume an invariant non-Gaussian density as the noise level is raised. The theoretical analysis of figure 2 should be extended to replace the initial density $f_\xi(\cdot)$ by the composite convolved density $f_\xi(\cdot) * f_\eta(\cdot)$ as the noise $\eta(t)$ with density $f_\eta(\cdot)$ is added. An alternative though, to raise the noise $\xi(t)$ while adhering to the conditions of figure 2, is to assume the possibility of a more internal physical parameter, like a temperature, which would allow to increase

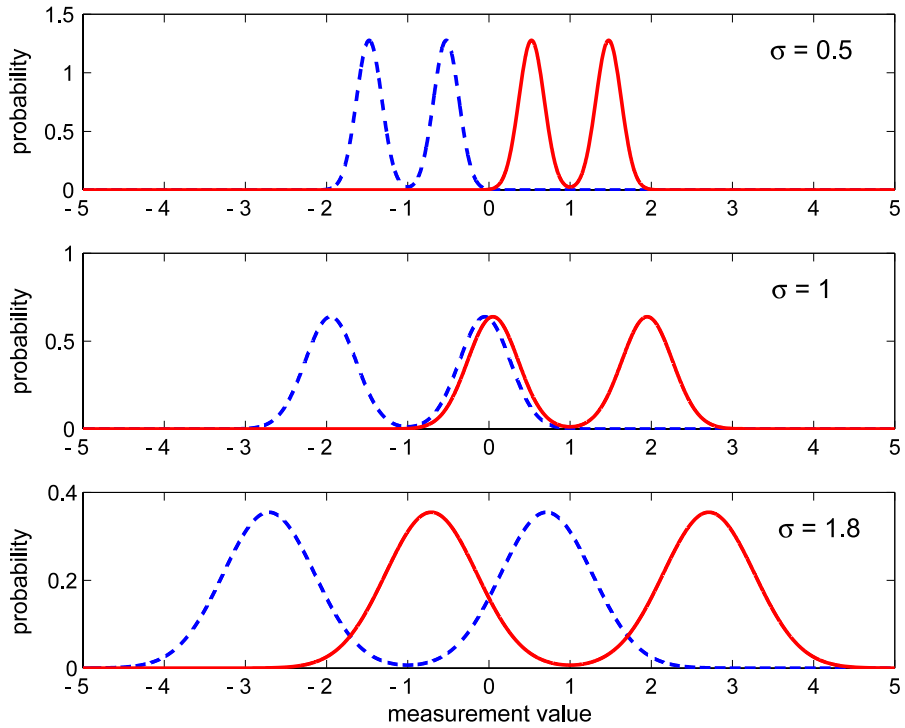

Figure 3. For a measurement x_k, probability densities from equation (8) under both hypotheses: $p(x_k|\mathrm{H}_0) = f_\xi(x_k - s_0)$ (blue dashed line) and $p(x_k|\mathrm{H}_1) = f_\xi(x_k - s_1)$ (red solid line). The noise probability density $f_\xi(u) = f_{\mathrm{gm}}(u/\sigma)/\sigma$ is the zero-mean Gaussian mixture from equation (11) at $m = 0.95$ with standard deviation σ. The signals to be detected are the constant $s_0(t) \equiv s_0 = -1$ and $s_1(t) \equiv s_1 = 1$; and $P_0 = 1/2$. At $\sigma = 1$ (middle panel), the densities $p(x_k|\mathrm{H}_0)$ and $p(x_k|\mathrm{H}_1)$ have a relatively strong overlap, and consequently, based on the measurement x_k, the signals $s_0 = -1$ and $s_1 = 1$ are more likely to be confused. Henceforth, this noise level $\sigma = 1$ is associated with a large probability of detection error $P_{\mathrm{er}}^{\mathrm{min}}$ in figure 2. By contrast, at $\sigma = 0.5$ (upper panel) and at $\sigma = 1.8$ (lower panel), the densities $p(x_k|\mathrm{H}_0)$ and $p(x_k|\mathrm{H}_1)$ have smaller overlap, and consequently, based on the measurement x_k, the signals $s_0 = -1$ and $s_1 = 1$ are less likely to be confused. This is associated with a smaller probability of detection error $P_{\mathrm{er}}^{\mathrm{min}}$ in figure 2 at these noise levels $\sigma = 0.5$ and 1.8. This illustrates the nonmonotonic action of an increase of the noise level σ on the performance $P_{\mathrm{er}}^{\mathrm{min}}$.

the noise level σ while maintaining the non-Gaussian density $f_\xi(\cdot)$ invariant in shape. The noise $\xi(t)$ at the level σ where it is, is certainly ruled by some definite physical process fixing σ, and a control is assumed in this process allowing us to raise σ. Also, to complement this practical perspective, noise bearing some similarity with the bimodal noise of this section 2.3 could be found in practice with a 'logical' noise formed as follows. A logical device or a random telegraphic signal would randomly switch between two fixed values coding the logical states 0 and 1; in addition, each of these two states would be corrupted by an additive Gaussian noise. The result then would be a bimodal noise with two Gaussian peaks, as could exist in the environment of logical or telegraphic devices.

Aside from these practical aspects and the specific mechanism depicted in figure 3, the main message we want to retain here from the results of figure 2 is in principle: the performance of an optimal detector can sometimes improve when the noise level increases. This property is demonstrated by an example in this section 2.3, which involves an additive signal–noise mixture with non-Gaussian noise. Other examples further demonstrate the same property for detection on non-additive signal–noise mixture [27, 28] with Gaussian noise [29]. Later in this paper, beyond demonstration by examples, we will address the open problem of a general characterization of such optimal detection tasks which can benefit from an increase in the noise. Before, we show next that improvement by noise of optimal processing can also be observed in optimal estimation.

3. Optimal estimation

3.1. Classical theory of optimal estimation

Another embodiment of the general situation of section 1 is a standard parameter estimation problem, where the input signal $s(t)$ is dependent upon an unknown parameter ν, i.e. $s(t) \equiv s_\nu(t)$. The input signal $s_\nu(t)$ is mixed to the noise $\xi(t)$ to yield the observable signal $x(t)$. From the observations $\boldsymbol{x} = (x_1, \ldots, x_N)$ one has then to estimate a value $\widehat{\nu}(\boldsymbol{x})$ for the unknown parameter. In this context [23, 30], a meaningful criterion of performance can be the rms estimation error

$$\mathcal{E} = \sqrt{\mathrm{E}\{[\widehat{\nu}(\boldsymbol{x}) - \nu]^2\}}. \tag{13}$$

When ν is a deterministic unknown parameter, the random noise $\xi(t)$ mixed to the input signal $s_\nu(t)$ induces a probability density $p(\boldsymbol{x}; \nu)$ for the data $\boldsymbol{x}$. The expectation $\mathrm{E}(\cdot)$, defining in equation (13) the rms estimation error $\mathcal{E}$ of estimator $\widehat{\nu}(\boldsymbol{x})$, then comes out as

$$\mathcal{E} = \sqrt{\int_{\mathbb{R}^N} [\widehat{\nu}(\boldsymbol{x}) - \nu]^2 \; p(\boldsymbol{x}; \nu) \, \mathrm{d}\boldsymbol{x}}. \tag{14}$$

An estimator with interesting properties is the maximum likelihood estimator defined as [23, 30]

$$\widehat{\nu}_{\mathrm{ML}}(\boldsymbol{x}) = \arg\max_{\nu} \; p(\boldsymbol{x}; \nu). \tag{15}$$

In the asymptotic regime $N \to \infty$ of a large data set, the maximum likelihood estimator $\widehat{\nu}_{\mathrm{ML}}(\boldsymbol{x})$ is the optimal estimator that minimizes the rms estimation error of equation (14), achieving a minimal rms error expressible as

$$\mathcal{E}_{\min} = \sqrt{\frac{1}{J(\boldsymbol{x})}}, \tag{16}$$

where $J(\boldsymbol{x})$ is the Fisher information contained in the data $\boldsymbol{x}$ about the unknown parameter ν and is defined as

$$J(\boldsymbol{x}) = \int_{\mathbb{R}^N} \frac{1}{p(\boldsymbol{x}; \nu)} \left[\frac{\partial}{\partial \nu} \, p(\boldsymbol{x}; \nu) \right]^2 \mathrm{d}\boldsymbol{x}. \tag{17}$$

The classical theory of optimal estimation, as reviewed in this section 3.1, applies for parameter estimation on any parametric signal $s_\nu(t)$, mixed in any way, to any definite noise $\xi(t)$. The specificity of each problem is essentially coded in the probability density $p(\boldsymbol{x}; \nu)$, which expresses the probabilization induced by the noise $\xi(t)$ once defined.

3.2. Estimation with phase noise

For an application of the optimal estimation procedure of section 3.1, we now consider our input signal $s_\nu(t)$ under the form of a periodic wave $s_\nu(t) = w(\nu t)$ of unknown frequency ν, where $w(t)$ is a known periodic 'mother' waveform of period unity. The noise $\xi(t)$ acts on the phase of the wave so as to form the observable signal

$$x(t) = w[\nu t + \xi(t)]. \tag{18}$$

Such a periodic signal corrupted by a phase noise will be seen, for instance, by a sensor receiving a periodic wave which traveled through a fluctuating or turbulent propagation medium producing the phase noise. Based on the data $\boldsymbol{x} = (x_1, \ldots, x_N)$ observed on the noisy signal $x(t)$, the frequency ν is to be estimated.

We assume a white noise $\xi(t)$, meaning that at distinct times t_k the noise samples $\xi(t_k)$, and therefore the data $x_k = x(t_k)$, are statistically independent, so that the probability density $p(\boldsymbol{x}; \nu)$ factorizes as $p(\boldsymbol{x}; \nu) = \prod_{k=1}^N p(x_k; \nu)$. Also, the samples $\xi(t_k)$ are identically distributed, with cumulative distribution function $F_\xi(u)$ and probability density function $f_\xi(u) = \mathrm{d}F_\xi/\mathrm{d}u$. We further consider the simple situation where $w(t)$ is a square wave of period 1 with $w(t) = 1$ when $t \in [0, 1/2)$ and $w(t) = -1$ when $t \in [1/2, 1)$. With $\delta(\cdot)$ the Dirac delta function, we have the density

$$p(x_k; \nu) = \Pr\{x_k = -1; \nu\}\delta(x_k + 1) + \Pr\{x_k = 1; \nu\}\delta(x_k - 1), \tag{19}$$

with the probability

$$\Pr\{x_k = 1; \nu\} = \Pr\{w[\nu t_k + \xi(t_k)] = 1\} \tag{20}$$

$$= \Pr\Big\{\nu t_k + \xi(t_k) \in \bigcup_\ell [\ell, \ell + 1/2)\Big\} \tag{21}$$

$$= \Pr\Big\{\xi(t_k) \in \bigcup_\ell [\ell - \nu t_k, \ell - \nu t_k + 1/2)\Big\} \tag{22}$$

$$= \sum_{\ell=-\infty}^{+\infty} \int_{\ell-\nu t_k}^{\ell-\nu t_k+1/2} f_\xi(u)\,\mathrm{d}u \tag{23}$$

$$= \sum_{\ell=-\infty}^{+\infty} [F_\xi(\ell - \nu t_k + 1/2) - F_\xi(\ell - \nu t_k)], \tag{24}$$

ℓ integer, and the probability

$$\Pr\{x_k = -1; \nu\} = 1 - \Pr\{x_k = 1; \nu\}. \tag{25}$$

Under the white noise assumption, Fisher information is additive and one has $J(\boldsymbol{x}) = \sum_{k=1}^N J(x_k)$, with

$$J(x_k) = \sum_{x_k=-1,1} \frac{1}{\Pr\{x_k; \nu\}} \left[\frac{\partial}{\partial \nu} \Pr\{x_k; \nu\}\right]^2 \tag{26}$$

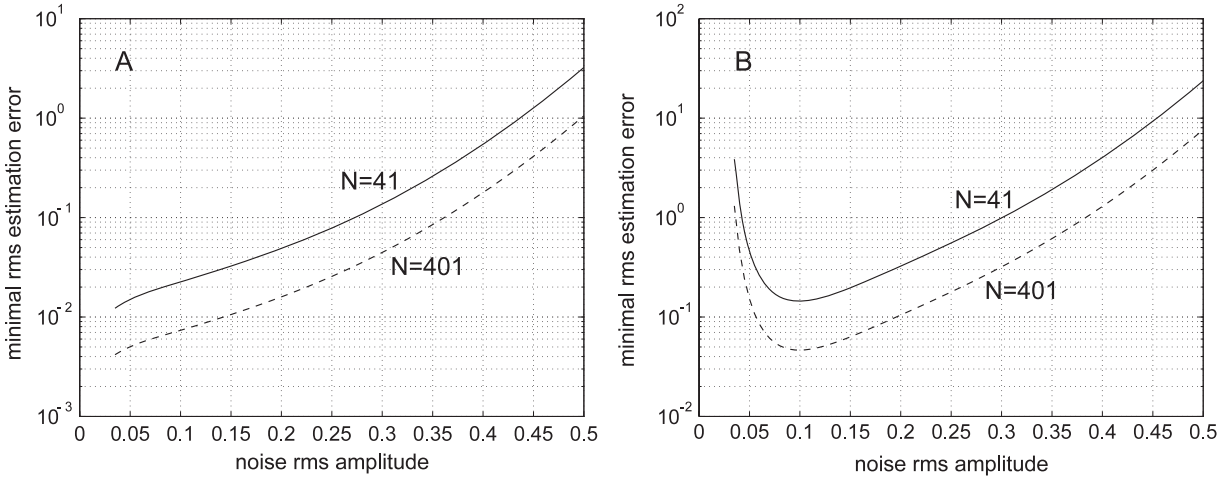

Figure 4. Minimal rms estimation error $\mathcal{E}_{\min}$ from equation (16) for the asymptotically optimal estimator formed by the maximum likelihood estimator of equation (15) at large N as a function of the rms amplitude σ of the zero-mean Gaussian noise $\xi(t)$. Estimation of the frequency $\nu = 1$ of a square wave is performed from N observations at times $\boldsymbol{t} = (t_1, t_2, \ldots, t_N)$ selected between t_1 and t_N with step Δt, which we denote $\boldsymbol{t} = [t_1 : \Delta t : t_N]$. Panel A: $\boldsymbol{t} = [0 : 5 \times 10^{-2} : 2]$ for $N = 41$ (solid line), $\boldsymbol{t} = [0 : 5 \times 10^{-3} : 2]$ for $N = 401$ (dashed line). Panel B: $\boldsymbol{t} = [0.25 : 2.5 \times 10^{-3} : 0.35]$ for $N = 41$ (solid line), $\boldsymbol{t} = [0.25 : 2.5 \times 10^{-4} : 0.35]$ for $N = 401$ (dashed line).

the Fisher information contained in the observation $x_k = x(t_k)$. In addition, from equation (24) one has the derivative

$$\frac{\partial}{\partial \nu} \Pr\{x_k = 1; \nu\} = -t_k \sum_{\ell=-\infty}^{+\infty} [f_\xi(\ell - \nu t_k + 1/2) - f_\xi(\ell - \nu t_k)]. \tag{27}$$

To complete the specification of the problem, we choose $\xi(t)$ as a zero-mean Gaussian noise with standard deviation σ. Figure 4 then represents the evolution of the performance $\mathcal{E}_{\min}$ from equation (16), at large N, in different conditions of estimation.

Figure 4(A) corresponds to a favorable configuration of the N given observation times $(t_1, t_2, \ldots, t_N) = \boldsymbol{t}$ that are well distributed in relation to the period $1/\nu$ of the wave. In this case, the phase noise $\xi(t)$ is felt as a nuisance and the optimal estimation error $\mathcal{E}_{\min}$ monotonically degrades (increases) as the noise level σ increases. By contrast, figure 4(B) corresponds to a less favorable configuration of the N observation times $\boldsymbol{t} = (t_1, t_2, \ldots, t_N)$ that concentrate over a duration less than one period $1/\nu$ of the wave. In this case, qualitatively, the phase noise $\xi(t)$ plays a constructive role as it allows more variability in the values accessible to the data $\boldsymbol{x} = (x_1, \ldots, x_N)$ observed from the noisy signal of equation (18). This is manifested quantitatively in figure 4(B) by an optimal estimation error $\mathcal{E}_{\min}$ experiencing a nonmonotonic evolution as the level σ of the phase noise grows, with ranges where the error $\mathcal{E}_{\min}$ decreases when the noise level σ increases.

The beneficial action in figure 4(B) is obtained with Gaussian noise. This means that the noise level σ can be increased by addition of an independent Gaussian noise $\eta(t)$ to a pre-existing initial Gaussian phase noise $\xi(t)$. This, from equation (18), realizes the

observable signal $x(t) = w[\nu t + \xi(t) + \eta(t)]$, with the augmented noise $\xi(t) + \eta(t)$ which remains Gaussian, as in figure 4, while its rms amplitude increases. In practice, for the periodic wave traveling through a fluctuating medium, as evoked just after equation (18), the initial phase noise $\xi(t)$ in equation (18) is due to random fluctuations in the propagating medium. Then, a receiving sensor subjected to random vibrations according to the additional noise $\eta(t)$ will produce the observable signal $x(t) = w[\nu t + \xi(t) + \eta(t)]$. In outline, optimal estimation on a periodic wave traveling through a fluctuating medium could be improved by randomly shaking the receiver in an appropriate way.

The results of this section 3.2 demonstrate, with an example, the possibility of improving the performance of an optimal estimator when the noise level increases. Section 3.2 addresses the estimation of a deterministic unknown parameter ν and it gives new results on noise-aided optimal estimation. A comparable property of improvement by noise in optimal estimation was demonstrated with another example in [31]. Reference [31] addresses estimation of a stochastic unknown parameter ν, with a classic Bayesian estimator minimizing the rms error of equation (13), when the expectation $\mathrm{E}(\cdot)$ in equation (13) is according to the probabilization established in conjunction by the noise $\xi(t)$ and the prior probability on ν.

4. The basic mechanism

Sections 2.3 and 3.2, as well as [27]–[29], [31], report examples of improvement by noise in optimal processing. We are dealing here with optimal processing (optimal detection and optimal estimation) in a classical sense, as defined by classical optimal detection and estimation theories [23, 24, 30]. The measures of performance which are analyzed are standard measures for detection and estimation, i.e. the probability of detection error P_{er} defined in equation (1) and the rms estimation error $\mathcal{E}$ of equation (13). These quantities are measures commonly used for performance evaluation in the classical theories of statistical detection and estimation, and they represent the performance that is reached in practice through ensemble average over a large number of realizations of the random signal $x(t)$ which is optimally processed. The results of figures 2 and 4 are ensemble averages in this sense, and they demonstrate in concrete examples the possibility of improvement by noise of the performance of optimal processors. In practice, as we briefly indicated, the example of figure 2 could be relevant, for instance, to the detection of signals in bimodal 'logical' noise, while the example of figure 4 could be relevant, for instance, to the estimation on periodic waves traveling through fluctuating media. However, our main purpose here is not to argue about the practical usefulness of these examples, but rather we want to focus on their meaning in principle. These examples stand as proofs of feasibility in principle that it is possible to improve the performance of optimal processors by increasing the noise. It may then seem paradoxical that optimal processors, in the classical sense, can be improved by raising the noise. If they are truly optimal, how can they be improved?

The point is that these processors are optimal in the sense that they represent the best possible deterministic processing that can be done on the data $\boldsymbol{x}$ to optimize a fixed given measure of performance Q (for instance, P_{er} of equation (1) or $\mathcal{E}$ of equation (13)). In the classical theory of these optimal processors, the performance Q is a functional of the probabilization established by the initial noise $\xi(t)$. This probabilization is expressed by

$p(\boldsymbol{x}|\mathrm{H}_j)$ in P_{er} of equation (1), and by $p(\boldsymbol{x};\nu)$ in $\mathcal{E}$ of equation (14). In the optimization of the performance Q, this probabilization is kept fixed: $p(\boldsymbol{x}|\mathrm{H}_j)$ and $p(\boldsymbol{x};\nu)$ are fixed given functions of the variable $\boldsymbol{x}$. Classical optimal theory then derives the best deterministic processing of the data $\boldsymbol{x}$ to optimize the performance Q at a level Q_1. This level Q_1 is therefore the best value of the performance that can be achieved by deterministic processing of the data $\boldsymbol{x}$ in the presence of a fixed probabilization of the problem and of the functional Q. What is realized by injection of more noise is a change of this probabilization of the problem. If the probabilization in the functional Q is changed, then the optimal processor, which is now optimal in the presence of the new probabilization of the functional Q, may achieve an improved performance Q_2 strictly better than Q_1. This is what happens in the examples of sections 2.3 and 3.2 (and in [27]–[29], [31]). It is even possible that a suboptimal processor in the sense of Q based on the new probabilization achieves a performance strictly better than the performance Q_1 optimal in the sense of the initial probabilization. An important point is that, even when the probabilization is changed by the injection of noise, it is the same detection or estimation problem which is addressed at the root: which signal $s(t)$ is hidden in the noise? And also, the measure of performance keeps the same physical signification and quantifies the same thing: the fraction of error in detection, or the mean squared difference between the estimate and the true value of the parameter. It is only the functional form of the measure of performance, as a function of the data, which is changed, not the signification of it.

5. Open problems of noise

We have described a general approach through which the possibility of improvement by noise of optimal processing can be analyzed. We have shown two specific examples concretely demonstrating situations of noise-improved optimal processing. We have argued that, at a general level, the basic mechanism possibly authorizing improvement by noise in optimal processing is a change of probabilization of the processing problem. To go further beyond the present proof by examples and the general mechanism we uncovered, an important step is now in making more explicit the favorable changes of probabilization that could possibly lead to improved optimal processing. The favorable changes of probabilization may be specific to any definite processing problems and need be explored separately. There are, however, several general open problems in this direction which can be formulated to serve as guidelines, and those we now discuss.

A favorable change of probabilization, to give way to what can be interpreted as a noise-improved performance, should be a change of probabilization that goes in the direction of raising the noise, something we can call an 'overprobabilization'. A formal change of probabilization that would only amount to reducing the level of the initial noise $\xi(t)$ would in general trivially lead to an improved performance of the optimal processor. This is apparent with $P_{\mathrm{er}}^{\mathrm{min}}$ of equation (10) which is the best performance achieved by the optimal deterministic detector of a constant signal in Gaussian white noise. This $P_{\mathrm{er}}^{\mathrm{min}}$ is a function of the noise rms amplitude σ assumed fixed in the optimization process (fixed probabilization) leading to the optimal detector of equation (9). In this $P_{\mathrm{er}}^{\mathrm{min}}$ of equation (10), if now σ is reduced (a change in the probabilization), the performance $P_{\mathrm{er}}^{\mathrm{min}}$ of the optimal detector is improved, as can be seen in figure 1. Yet, this is a trivial improvement through a change of probabilization amounting to reducing the initial noise.

The direction which is interesting to explore is the opposite: an improved performance by raising the noise. The possibility thereof is exemplified in sections 2.3 and 3.2.

Beyond these proofs of feasibility by examples in sections 2.3 and 3.2, we are thus led to the following open problem: is it possible to obtain a general characterization of the optimal processing problems and their solutions for which the optimal processors achieve a performance improvable by overprobabilization (a change of probabilization by increasing the noise)?

In this respect, noise-improved optimal processings were obtained in section 2.3 on an *additive* signal–noise mixture with *non-Gaussian* white noise (see figure 2) and in section 3.2 on a *non-additive* signal–noise mixture with *Gaussian* white noise (see figure 4(B)). One is thus led to ask whether general conditions exist concerning the additive/non-additive and Gaussian/non-Gaussian characteristics of the noise, in order to authorize improvement by noise in optimal processing.

Also, an important reference in detection and estimation is provided by the case of an *additive* signal–noise mixture with *Gaussian* white noise. Then another specific question is: is it possible to improve the optimal detection or optimal estimation of a signal in an *additive* signal–noise mixture with *Gaussian* white noise by injecting more noise ? Formally, this would amount to finding a change in the forms of functions $p(\boldsymbol{x}|\mathrm{H}_j)$ in P_{er} of equation (1), or $p(\boldsymbol{x};\nu)$ in $\mathcal{E}$ of equation (14), through an overprobabilization associated with an improvement of the functional measuring the performance. Alternatively, another question is: is there a proof of principle that this is not possible? To answer in one way or the other, a difficulty is that there exists *a priori* a large (infinite) number of possible overprobabilizations which can be considered to change, at least formally, the forms of functions $p(\boldsymbol{x}|\mathrm{H}_j)$ in equation (1) or $p(\boldsymbol{x};\nu)$ in equation (14).

Another issue is to characterize the beneficial overprobabilizations that are compatible with the underlying physics of the problem. Not all formally conceivable changes of probabilization are physically realizable in a given process. This issue of the physical realizability of a beneficial increase of the noise has already been discussed above for both examples of sections 2.3 and 3.2. Usually, inference about the information signal $s(t)$ is performed from the processing of an observation signal $x(t)$ resulting from an arbitrary mixture with the corrupting noise $\xi(t)$. This mixture expresses the underlying physics realizing the signal–noise coupling, and we shall here formally denote this mixture as $x(t) = \mathcal{M}_1[s(t), \xi(t)]$. Equations (7) and (18) are understood here as two examples of this initial mixture operation $\mathcal{M}_1(\cdot)$. Overprobabilization then can be performed by increasing the noise in several ways. A first possibility is as in figure 2, where the initial signal–noise mixture $x(t) = \mathcal{M}_1[s(t), \xi(t) \equiv \xi_1(t)]$ is changed to $x(t) = \mathcal{M}_1[s(t), \xi(t) \equiv \xi_2(t)]$ by increasing the initial noise $\xi(t) \equiv \xi_1(t)$ to a higher level $\xi(t) \equiv \xi_2(t)$. A second possibility for overprobabilization is as in figure 4(B), when another independent noise $\eta(t)$ can be injected into the process to realize a new mixture $\mathcal{M}_2(\cdot)$ of the three ingredients $s(t)$, $\xi(t)$ and $\eta(t)$, yielding the new observation signal $x(t) = \mathcal{M}_2[s(t), \xi(t), \eta(t)]$. The example of figure 4(B) is interpretable as the special case where $\mathcal{M}_2[s(t), \xi(t), \eta(t)] = \mathcal{M}_1[s(t), \xi(t) + \eta(t)]$. The above two possibilities of overprobabilization increase the noise by acting at the level of the underlying physical process that produces the observable signal $x(t)$. Their practical realizability is dependent upon the specific structure of the underlying physical process, and the external control available upon it, to authorize or not the implementation of the intended increase in the noise which has been formally

proved beneficial. A third possibility for overprobabilization does not assume action on the underlying physics but directly operates on the initial observation signal $\mathcal{M}_1[s(t), \xi(t)]$ to further mix it, by $\mathcal{M}_3(\cdot)$, to an independent noise $\eta(t)$ to realize the new observable mixture signal $\mathcal{M}_3\{\mathcal{M}_1[s(t), \xi(t)], \eta(t)\}$, with $\mathcal{M}_3(\cdot)$ a general mixing operation certainly not restricted to an additive mixing. Strictly speaking, we did not show any example of this third kind of improvement by noise in optimal processing. The question remains open of whether some exist or not.

When considering improvement of optimal processing by mixing with an external noise $\eta(t)$, it may be helpful to have gone through the following argument. In optimal processing, if a mixing with an external noise $\eta(t)$ is found beneficial, on average, to improve the performance, then there should exist one specific realization of $\eta(t)$ which is especially beneficial. This realization can then be taken as a deterministic set of values which could be mixed with the data to realize a deterministic processing which would improve the optimal performance. But this should not be possible, since no deterministic processing can do better than the initial optimal processor to maximize the performance. The point is that the measure of performance invoked by this argument is the initial measure of performance. Yet the measure of performance now has changed: introduction of the external noise $\eta(t)$ changes the functional form of the measure of performance. And, as explained in section 4, nothing prohibits *a priori* a processing according to this new measure of performance to improve over the optimal processing according to the initial measure of performance.

Returning to open questions, for a given optimal processing problem, ultimately one would like to be able to characterize, when it exists and among those physically realizable, the optimal overprobabilization, i.e. that yielding the best improvement by raising the noise.

For a given optimal processing problem, it appears that questions can be posed at two levels: (i) is it formally possible to find a beneficial overprobabilization of the problem associated with an improvement of the functional measuring the performance? and (ii) Is this overprobabilization formally proved beneficial, physically realizable in practice? These may seem two independent levels, the first one related to the abstract structure of the processing operations on the signals and the second related to the concrete structure of the physical processes generating the signals. A final question arises: are these two levels really independent, or are there connections between these informational and physical levels, limiting what can be ultimately achieved in optimal processing in the presence of noise?

References

[1] Gammaitoni L, Hänggi P, Jung P and Marchesoni F, *Stochastic resonance*, 1998 *Rev. Mod. Phys.* **70** 223

[2] Chapeau-Blondeau F and Rousseau D, *Noise improvements in stochastic resonance: from signal amplification to optimal detection*, 2002 *Fluct. Noise Lett.* **2** L221

[3] McDonnell M D, Stocks N G, Pearce C E M and Abbott D, 2008 *Stochastic Resonance: From Suprathreshold Stochastic Resonance to Stochastic Signal Quantization* (Cambridge: Cambridge University Press)

[4] Inchiosa M E and Bulsara A R, *Signal detection statistics of stochastic resonators*, 1996 *Phys. Rev.* E **53** R2021

[5] Galdi V, Pierro V and Pinto I M, *Evaluation of stochastic-resonance-based detectors of weak harmonic signals in additive white Gaussian noise*, 1998 *Phys. Rev.* E **57** 6470

[6] Tougaard J, *Signal detection theory, detectability and stochastic resonance effects*, 2002 *Biol. Cybernet.* **87** 79
[7] Zozor S and Amblard P O, *On the use of stochastic resonance in sine detection*, 2002 *Signal Process.* **82** 353
[8] Saha A A and Anand G V, *Design of detectors based on stochastic resonance*, 2003 *Signal Process.* **83** 1193
[9] Zozor S and Amblard P O, *Stochastic resonance in locally optimal detectors*, 2003 *IEEE Trans. Signal Process.* **51** 3177
[10] Rousseau D and Chapeau-Blondeau F, *Constructive role of noise in signal detection from parallel arrays of quantizers*, 2005 *Signal Process.* **85** 571
[11] Duan F and Abbott D, *Signal detection for frequency-shift keying via short-time stochastic resonance*, 2005 *Phys. Lett.* A **344** 401
[12] Rousseau D, Anand G V and Chapeau-Blondeau F, *Noise-enhanced nonlinear detector to improve signal detection in non-Gaussian noise*, 2006 *Signal Process.* **86** 3456
[13] Chen H, Varshney P K, Kay S M and Michels J H, *Theory of stochastic resonance effect in signal detection: part I—Fixed detectors*, 2007 *IEEE Trans. Signal Process.* **55** 3172
[14] Greenwood P E, Ward L M and Wefelmeyer W, *Statistical analysis of stochastic resonance in a simple setting*, 1999 *Phys. Rev.* E **60** 4687
[15] Chapeau-Blondeau F, *Noise-aided nonlinear Bayesian estimation*, 2002 *Phys. Rev.* E **66** 032101
[16] McDonnell M D, Abbott D and Pearce C E M, *An analysis of noise enhanced information transmission in an array of comparators*, 2002 *Microelectron. J.* **33** 1079
[17] Rousseau D, Duan F and Chapeau-Blondeau F, *Suprathreshold stochastic resonance and noise-enhanced Fisher information in arrays of threshold devices*, 2003 *Phys. Rev.* E **68** 031107
[18] Greenwood P E, Müller U U and Ward L M, *Soft threshold stochastic resonance*, 2004 *Phys. Rev.* E **70** 051110
[19] Wang Y and Wu L, *Stochastic resonance and noise-enhanced Fisher information*, 2005 *Fluct. Noise Lett.* **5** L435
[20] Chapeau-Blondeau F, Blanchard S and Rousseau D, *Noise-enhanced Fisher information in parallel arrays of sensors with saturation*, 2006 *Phys. Rev.* E **74** 031102
[21] Rousseau D and Chapeau-Blondeau F, *Noise-improved Bayesian estimation with arrays of one-bit quantizers*, 2007 *IEEE Trans. Instrum. Meas.* **56** 2658
[22] Chapeau-Blondeau F, Blanchard S and Rousseau D, *Fisher information and noise-aided power estimation from one-bit quantizers*, 2008 *Digital Signal Process.* **18** 434
[23] Van Trees H L, 2001 *Detection, Estimation, and Modulation Theory, Part 1* (New York: Wiley)
[24] Kay S M, 1998 *Fundamentals of Statistical Signal Processing: Detection Theory* (Englewood Cliffs, NJ: Prentice-Hall)
[25] Barik D, Ghosh P K and Ray D S, *Langevin dynamics with dichotomous noise; direct simulation and applications*, 2006 *J. Stat. Mech.* P03010
[26] Chapeau-Blondeau F and Rousseau D, *Constructive action of additive noise in optimal detection*, 2005 *Int. J. Bifur. Chaos* **15** 2985
[27] Chapeau-Blondeau F, *Stochastic resonance for an optimal detector with phase noise*, 2003 *Signal Process.* **83** 665
[28] Rousseau D and Chapeau-Blondeau F, *Stochastic resonance and improvement by noise in optimal detection strategies*, 2005 *Digital Signal Process.* **15** 19
[29] Chapeau-Blondeau F and Rousseau D, *Injecting noise to improve performance of optimal detector*, 2007 *Electron. Lett.* **43** 897
[30] Kay S M, 1993 *Fundamentals of Statistical Signal Processing: Estimation Theory* (Englewood Cliffs, NJ: Prentice-Hall)
[31] Chapeau-Blondeau F and Rousseau D, *Noise-enhanced performance for an optimal Bayesian estimator*, 2004 *IEEE Trans. Signal Process.* **52** 1327

S. BLANCHARD, D. ROUSSEAU, D. GINDRE, and F. CHAPEAU-BLONDEAU. Constructive action of the speckle noise in a coherent imaging system. *Optics Letters*, vol. 32:1983–1985, 2007.

Constructive action of the speckle noise in a coherent imaging system

Solenna Blanchard,[1] David Rousseau,[1,*] Denis Gindre,[2] and François Chapeau-Blondeau[1]

[1]*Laboratoire d'Ingénierie des Systèmes Automatisés (LISA), Université d'Angers, 62 Avenue Notre Dame du Lac, 49000 Angers, France*

[2]*Laboratoire des Propriétés Optiques des Matériaux et Applications (POMA), UMR 6136 CNRS, Université d'Angers, 2 Boulevard Lavoisier, 49000 Angers, France*

[*]*Corresponding author: david.rousseau@univ-angers.fr*

Received April 3, 2007; revised May 23, 2007; accepted May 24, 2006;
posted May 29, 2007 (Doc. ID 81793); published July 3, 2007

A coherent imaging system with speckle noise is devised and analyzed. This demonstrates the possibility of improving the nonlinear transmission of a coherent image by increasing the level of the multiplicative speckle noise. This noise-assisted image transmission is a novel instance of stochastic resonance phenomena by which nonlinear signal processing benefits from a constructive action of noise. © 2007 Optical Society of America

OCIS codes: 000.2690, 030.6140, 030.4280, 100.2000, 110.2970, 120.6150.

Coherent imaging is inherently associated with speckle noise. Speckle noise is a fluctuation of intensity over an image caused by very irregular spatial interference from the coherent phases. Speckle noise is often seen as a nuisance for many processing tasks in coherent imaging. Meanwhile, from other areas of information processing, it is progressively realized that noise can sometimes play a constructive role, such phenomena being known under the denomination of stochastic resonance [1,2]. *A priori* paradoxical in a linear context, stochastic resonance is a general nonlinear phenomenon that has been registered in various nonlinear physical processes, including electronic circuits, lasers (see for example [3]), magnetic superconducting devices, or neuronal systems. In all these processes, stochastic resonance was observed with a temporal (monodimensional) information signal. Up to now, only a few studies have reported stochastic resonance with spatial (bidimensional) signals or images. Stochastic resonance with images has been obtained in an optical Raman scattering experiment [4], in image perception by the visual system [5], in superresolution techniques for imaging sensors [6], and recently in image restoration [7]. Here, we demonstrate a new instance of stochastic resonance applied, to our knowledge for the first time, to coherent imaging, and taking the form of a noise-assisted image transmission by a nonlinear sensor in the presence of speckle noise. Also, as we recall here, speckle noise can be modeled as a multiplicative noise, and this feature is in itself challenging because most of the studies on stochastic resonance considered additive noise. The few that considered multiplicative noise dealt exclusively with temporal signals [8]. By contrast, we show a new form of stochastic resonance, for coherent images, with multiplicative speckle noise.

A grainylike pattern called speckle is observed when an object with roughness on a wavelength scale is illuminated by a coherent wave. On an imaging detector, the transmitted or backscattered wavefront perturbed by those irregularities produces intensity fluctuations superimposed on the macroscopic reflectivity or transparency contrast of the object. The effect on a coherent imaging system can be modeled [9] as a multiplicative noise in the following way. Let $S(u,v)$ be an input information-carrying image to be acquired, where the pixels are indexed by integer coordinates (u,v) and have intensity $S(u,v) \in [0,1]$. Let $N(u,v)$ be a multiplicative speckle noise, statistically independent of $S(u,v)$, which corrupts each pixel of image $S(u,v)$, to produce a nonlinear multiplicative mixture

$$X(u,v) = S(u,v) \times N(u,v), \tag{1}$$

where the noise values are independent from pixel to pixel, and are distributed according to the probability density $p_N(j)$ given by

$$p_N(j) = \frac{1}{\sigma_N} \exp\left(-\frac{j}{\sigma_N}\right), \quad j \geq 0, \tag{2}$$

with mean and standard deviation σ_N and root mean square (rms) amplitude $\sqrt{2}\sigma_N$. Equations (1) and (2) constitute a simple model of fully developed speckle noise that is valid if the detector pixel size is smaller than the speckle grain size [9]. The information-noise mixture $X(u,v)$ is then received by an image detector delivering the output image $Y(u,v)$ according to

$$Y(u,v) = g[X(u,v)], \tag{3}$$

the input–output characteristic $g(\cdot)$ of the imaging system being, at this stage, an arbitrary function. The coherent imaging system described in Eqs. (1)–(3) has been realized with the experimental setup of Fig. 1.

In order to assess the quality of the acquisition, we introduce an input–output measure of similarity between the information-carrying input image $S(u,v)$ [the object of the slide in Fig. 1] and output image $Y(u,v)$ [the image on the CCD matrix in Fig. 1]. We choose the input–output image rms error E_{SY}, a basic measure in the domain of image processing:

0146-9592/07/141983-3/$15.00

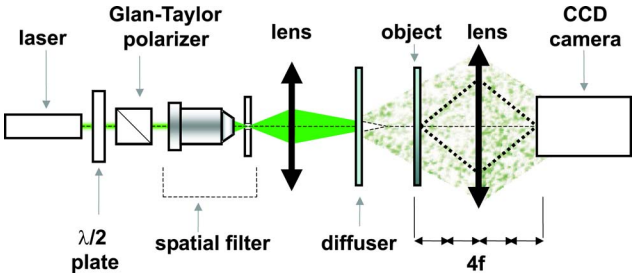

Fig. 1. (Color online) Experimental setup producing an optical version of the theoretical coherent imaging process of Eqs. (1)–(3). The λ/2 plate in association with the Glan-Taylor polarizer are used to control the intensity of the incident coherent wave coming from the second harmonic generation (532 nm, 10 mW) of a YAG:Nd compact laser. The spatial filter is used to obtain a uniform intensity on the static diffuser taken as a frosted glass. The first lens is adjusted with a micrometer-scale sensitivity linear stage to control the size of the speckle grain in the object plane. In Figs. 2 and 3 the speckle grain size has been adjusted to be much larger than the pixel size (the domain of validity of our model) and much smaller than the CCD matrix size (to diminish fluctuations from one acquisition to another). The object, a slide with calibrated transparency levels carrying the contrast of the input image $S(u,v)$, is illuminated by the speckled wave field. The second lens images the object plane on the CCD matrix of the camera. Variations of the speckle noise level in Figs. 2 and 3 are controlled by rotation of the λ/2 plate.

$$E_{SY} = \sqrt{\langle (S-Y)^2 \rangle} = \sqrt{\langle S^2 \rangle - 2\langle SY \rangle + \langle Y^2 \rangle}, \qquad (4)$$

where $\langle \cdots \rangle$ denotes an average over the images. We assume that image $S(u,v)$ and speckle noise $N(u,v)$ are large enough so that a statistical description of the distribution of intensities on the image is meaningful: image $S(u,v)$ and speckle noise $N(u,v)$ possess empirical histograms of intensities, the normalized version of which is defining probability density $p_S(j)$ and $p_N(j)$ for the intensity of image $S(u,v)$ and $N(u,v)$. In principle, when $p_S(j)$, $p_N(j)$, and $g(\cdot)$ are all given, it is possible to theoretically predict the input–output image rms error E_{SY}. For instance, for $g(\cdot)$, a memoryless function on real numbers, one can use

$$\langle SY \rangle = \int_s \mathrm{d}_s \, s \, p_S(s) \int_n \mathrm{d}_n \, g(s \times n) \, p_N(n), \qquad (5)$$

with similar expressions for $\langle S^2 \rangle$ and $\langle Y^2 \rangle$, and by such means one has, in principle, access to E_{SY}. We are going to show, with a specific memoryless function $g(\cdot)$, situations where an increase in the level of the speckle noise $N(u,v)$ can improve the quality of the output image $Y(u,v)$, measured by a decrease of the input-output image rms error of Eq. (4). In the following, we choose to consider, both for the experimental setup of Fig. 1 and for our theoretical coherent imaging model of Eqs. (1)–(3), a binary image, visible in Fig. 2, presenting gray level $S(u,v) \in \{R_0, R_1\}$ with $R_0 < R_1$ and 1024×1024 pixels, for which the probability of having a pixel with level R_1 is $\Pr\{S=R_1\}=p_1$ and $\Pr\{S=R_0\}=1-p_1$. For illustration, the image detector $g(\cdot)$ is taken as a memoryless hard limiter with threshold θ, i.e.,

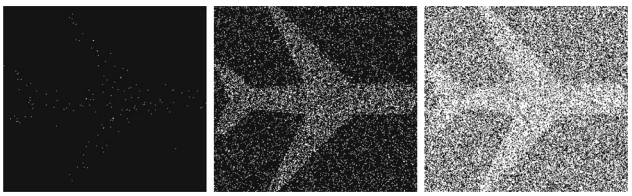

Fig. 2. Output image $Y(u,v)$ of the hard limiter of Eq. (6) for increasing rms amplitude $\sqrt{2}\sigma_N$ of the speckle noise $N(u,v)$. From left to right $\sqrt{2}\sigma_N = 0.28$, 0.84 (optimal value), 2.81; with threshold $\theta = 0.75$, $p_1 = 0.27$ and $\{R_0 = 1/2, R_1 = 1\}$.

$$g[X(u,v)] = \begin{cases} 0 & \text{for } X(u,v) \le \theta \\ 1 & \text{for } X(u,v) > \theta. \end{cases} \qquad (6)$$

This hard limiter constitutes a very basic model for imaging systems when they operate, in the low flux domain, close to their threshold. Alternatively, the hard limiter in Eq. (6) also can be viewed as a threshold in a high-level image processing task such as segmentation or detection. In addition, these simple choices for the input image and the image detector are going to allow a complete analytical treatment of our theoretical model.

We are now in a position to study the evolution of the input–output image rms error E_{SY} of Eq. (4) as a function of the level of the speckle noise $N(u,v)$. The input image $S(u,v)$ takes different values over the background (R_0) and over the object (R_1). As a consequence, the rms amplitude of the speckle noise takes different values over these two regions. As a common reference in the sequel, we define the speckle noise level as the rms amplitude $\sqrt{2}\sigma_N$, corresponding to the speckle noise rms amplitude before action of the multiplicative coupling by the object or background in Eq. (1). The quality of the images transmitted by the hard limiter of Eq. (6) is assessed here by the rms error between the output image $Y(u,v)$ and a binary reference $S'(u,v)$ similar to $S(u,v)$, but with $R_0 = 0$ (the background) and $R_1 = 1$ (the object). In this context, the input–output image rms error of Eq. (4) becomes

$$E_{S'Y} = \sqrt{p_1 + q_1 - 2p_1 p_{11}}, \qquad (7)$$

with conditional probabilities $p_{1k} = \Pr\{Y=1 | S=R_k\}$ and $q_1 = \Pr\{Y=1\} = p_1 p_{11} + (1-p_1) p_{10}$. The possibility of a useful role of the speckle noise in the image transmission process of Eqs. (1), (2), and (6) is visible in Fig. 3, where, for sufficiently large object-background contrast R_1/R_0 in input image $S(u,v)$, $E_{S'Y}$ follows a nonmonotonic evolution presenting a minimum for an optimal nonzero level $\sqrt{2}\sigma_{N\mathrm{opt}}$ of the speckle noise rms amplitude. This is the signature of a noise-assisted image transmission. Figure 3 also demonstrates a good agreement between experimental and theoretical results. In addition, it is possible to derive the theoretical expression $\sigma_{N\mathrm{opt}}$ minimizing the input–output image rms error $E_{S'Y}$ of Eq. (7) by solving $\partial E_{S'Y}/\partial \sigma_N = 0$, which leads to

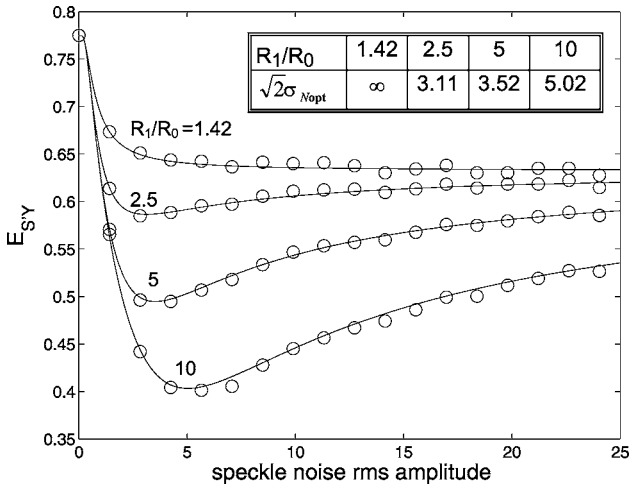

Fig. 3. Input–output image rms error $E_{S'Y}$ of Eq. (7) as a function of the rms amplitude $\sqrt{2}\sigma_N$ of the speckle noise $N(u,v)$ for various values of the input image contrast R_1/R_0. Solid lines stand for the theoretical expression of Eq. (7). The table gives the speckle noise optimal rms amplitude of Eq. (8). The discrete data sets (circles) are obtained by injecting in Eq. (1) real speckle images collected from the experimental setup of Fig. 1. The other parameters are $\theta=0.75$, $p_1=0.6$, $R_1=1$.

$$\sigma_{N\mathrm{opt}} = \frac{R_1 - R_0}{R_0 R_1} \frac{\theta}{\ln(K_a)}, \quad K_a = \frac{R_1}{R_0} \frac{1-p_1}{p_1}. \tag{8}$$

As seen in Eq. (8), there exist domains where the optimal speckle noise level $\sigma_{N\mathrm{opt}}$ is nonzero and positive when $\theta \neq 0$, $p_1 \neq 1$, $R_0 \neq R_1$ if $K_a > 1$. One can check in Fig. 3 that the positions of the optimal speckle noise level $\sqrt{2}\sigma_{N\mathrm{opt}}$ given by Eq. (8) show an exact agreement with the numerical calculations.

Finally, a visual appreciation of the cooperative effect of the speckle noise quantitatively illustrated in Fig. 3 is also presented in Fig. 2, where the multiplicative speckle noise injected in Eq. (1) comes from real speckle images collected from the experimental setup of Fig. 1.

We have demonstrated, theoretically and experimentally, the possibility of a constructive action of the multiplicative speckle noise in the transmission of an image in a coherent imaging system. For what we believe is a first report of this effect, the models for the input image, for the speckle noise, and for the imaging sensor have been purposely taken in their most simple forms. As a result, we obtained a theoretical prediction of the constructive role of the speckle noise, through an explicit theoretical analysis of the behavior of a relevant input–output similarity measure. The theoretical predictions displayed close agreement with experiment. A noticeable feature, in particular, is that our theoretical model authorizes an explicit derivation, without approximation, of an analytical expression (an outcome rarely accessible in studies of stochastic resonance in nonlinear systems) for the optimal level of the noise maximizing the performance in given conditions. The present demonstration of the feasibility of a constructive action of speckle noise in coherent imaging can be extended in various directions. More sophisticated images (with distributed gray levels, for example) could be considered, as well as other types of speckle noise, such as the one appearing in polarimetric imaging [10]. The simple threshold detector chosen here could be replaced by a multilevel quantizer or a linear sensor with saturation, closely matching attributes of digital cameras. It would then be interesting to confront, as done here, experiment and theoretical modeling, and examine how the phenomenon of improvement by noise evolves in these other conditions.

References

1. L. Gammaitoni, P. Hänggi, P. Jung, and F. Marchesoni, Rev. Mod. Phys. **70**, 223 (1998).
2. F. Chapeau-Blondeau and D. Rousseau, Fluct. Noise Lett. **2**, 221 (2002).
3. B. M. Jost and B. E. A. Saleh, Opt. Lett. **21**, 287 (1996).
4. F. Vaudelle, J. Gazengel, G. Rivoire, X. Godivier, and F. Chapeau-Blondeau, J. Opt. Soc. Am. B **13**, 2674 (1998).
5. F. Moss, L. M. Ward, and W. G. Sannita, Clin. Neurophysiol. **115**, 267 (2004).
6. R. Etchnique and J. Aliaga, Am. J. Phys. **72**, 159 (2004).
7. A. Histace and D. Rousseau, Electron. Lett. **42**, 393 (2006).
8. Y. Jia, S. N. Yu, and J.-R. Li, Phys. Rev. E **62**, 1869 (2000).
9. J. W. Goodman, *Statistical Optics* (Wiley, 1985).
10. F. Goudail and P. Réfrégier, Opt. Lett. **26**, 644 (2001).

F. CHAPEAU-BLONDEAU, D. ROUSSEAU, S. BLANCHARD, and D. GINDRE. Optimizing the speckle noise for maximum efficacy of data acquisition in coherent imaging. *Journal of the Optical Society of America A*, vol. 25:1287–1292, 2008.

Optimizing the speckle noise for maximum efficacy of data acquisition in coherent imaging

François Chapeau-Blondeau,[1] David Rousseau,[1,*] Solenna Blanchard,[1] and Denis Gindre[2]

[1]*Laboratoire d'Ingénierie des Systèmes Automatisés (LISA), Université d'Angers, 62 avenue Notre Dame du Lac, 49000 Angers, France*

[2]*Laboratoire des Propriétés Optiques des Matériaux et Applications (POMA), Université d'Angers, 2 boulevard Lavoisier, 49000 Angers, France*

[*]*Corresponding author: david.rousseau@univ-angers.fr*

Received December 14, 2007; revised April 2, 2008; accepted April 3, 2008; posted April 7, 2008 (Doc. ID 90824); published May 13, 2008

The impact of multiplicative speckle noise on data acquisition in coherent imaging is studied. This demonstrates the possibility to optimally adjust the level of the speckle noise in order to deliberately exploit, with maximum efficacy, the saturation naturally limiting linear image sensors such as CCD cameras, for instance. This constructive action of speckle noise cooperating with saturation can be interpreted as a novel instance of stochastic resonance or a useful-noise effect. © 2008 Optical Society of America

OCIS codes: 000.2690, 030.6140, 030.4280, 100.2000, 110.2970, 120.6150.

1. INTRODUCTION

In the domain of instrumentation and measurement, acquisition devices are generally linear for small inputs and saturate at large inputs. The linear part of their input–output characteristic usually sets the limit of the signal dynamic to be acquired with fidelity. In this paper, by contrast, we are going to show the possibility of a useful role of saturation: We report situations where the data acquisition is performed more efficiently when the information-carrying signal reaches the saturation level of the acquisition device than when it strictly remains located in its linear part. The beneficial role of saturation will be illustrated in the domain of optical coherent imaging. In this domain, because of very irregular spatial interference from the coherent phases, images have a grainy, noisy appearance called speckle. We will show how the level of the speckle noise can be optimally adjusted in order to maximize the benefit to be obtained from saturation of an image acquisition device. This constructive action of speckle noise cooperating with saturation will be interpreted as a new instance of the phenomenon of stochastic resonance. Stochastic resonance is a generic denomination that designates the possibility of improving the transmission or processing of an information-carrying signal by means of an increase in the level of the noise coupled to this signal. Since its introduction some twenty-five years ago in the context of climate dynamics, the phenomenon of stochastic resonance has experienced a large variety of extensions, developments, and observations in many areas of natural sciences (for overviews, see, for instance, [1,2]). In particular, occurrences of stochastic resonance have been reported in optics (for example, in [3–8]). Recently, stochastic resonance has been observed in coherent imaging with speckle noise in [8], where the possibility of a constructive action of speckle noise in the transmission of an image in a coherent imaging system is reported. For this first report in [8], the imaging sensor was purposely taken in the elementary form of a 1-bit quantizer. The present paper proposes to extend the result of [8] by considering a characteristic more realistic at the signal acquisition level and more similar to practical imaging sensors such as CCD cameras, involving both linear and saturation parts. Other nonlinear systems with saturation have been investigated for stochastic resonance, but this was with a temporal (monodimensional) information signal and additive noise [9,10]. By contrast, the possibility of stochastic resonance with speckle noise, which is multiplicative noise, in a (bidimensional) imaging system with saturation is demonstrated here, to the best of our knowledge, for the first time.

2. COHERENT IMAGING SYSTEM

The input image $S(u,v)$, with (u,v) spatial coordinates, is formed by a distribution of gray levels characterized by the probability density $p_S(s)$. The speckle noise $N(u,v)$, characterized by the probability density $p_N(n)$, acts through the multiplicative coupling

$$S(u,v) \times N(u,v) = X(u,v), \tag{1}$$

so as to form the intermediate image $X(u,v)$ corrupted by the speckle. The noisy image $X(u,v)$ is observed by means of an acquisition device, described by the input–output memoryless characteristic $g(\cdot)$, delivering the output image

$$Y(u,v) = g[X(u,v)]. \tag{2}$$

We introduce similarity measures between the information-carrying input image $S(u,v)$ and the output image $Y(u,v)$. One possibility is provided by the normalized cross covariance between images $S(u,v)$ and $Y(u,v)$, defined as

$$C_{SY} = \frac{\langle SY\rangle - \langle S\rangle\langle Y\rangle}{\sqrt{\langle S^2\rangle - \langle S\rangle^2}\sqrt{\langle Y^2\rangle - \langle Y\rangle^2}}, \tag{3}$$

where $\langle\cdot\rangle$ denotes an average over the images. The cross covariance C_{SY} is close to one when images $S(u,v)$ and $Y(u,v)$ carry strongly similar structures and is close to zero when the images are unrelated.

In addition, in the case where both input image $S(x,y)$ and output image $Y(x,y)$ take their values in the same range of gray levels, another input–output similarity measure is provided by the input–output rms error

$$Q_{SY} = \sqrt{\langle (S-Y)^2\rangle}. \tag{4}$$

We want to investigate the impact of speckle noise on the input–output similarity measures C_{SY} and Q_{SY} characterizing the transmission of the images. For the sequel, we consider for the acquisition device the characteristic

$$g(x) = \begin{cases} 0 & \text{for } x \leqslant 0 \\ x & \text{for } 0 < x < \theta \\ \theta & \text{for } x \geqslant \theta \end{cases}. \tag{5}$$

The characteristic $g(\cdot)$ of Eq. (5) is a standard model for many sensors or image acquisition devices, such as CCD cameras, for instance; $g(\cdot)$ of Eq. (5) is purely linear for small input levels above zero, and it saturates for large input levels above $\theta > 0$. For instance, $g(\cdot)$ of Eq. (5) offers a model for a CCD camera that will represent the input on, say, 256 levels between 0 and 255, and will saturate above 255.

Since in coherent imaging, following Eq. (1), the speckle noise $N(u,v)$ has a multiplicative action on the input image, the level of the speckle noise plays a key role in fixing the position of the dynamics of the image $X(u,v)$ applied onto the acquisition device $g(\cdot)$ in relation to its linear range $[0,\theta]$. For a given sensor with a fixed saturation level θ, too large a level of the multiplicative speckle noise $N(u,v)$ may strongly saturate the acquisition, while too low a level of $N(u,v)$ may result in a poor exploitation of the full dynamics $[0,\theta]$ of the sensor. We will use the similarity measures C_{SY} and Q_{SY} of Eqs. (3) and (4) to quantitatively characterize the existence of an optimal level of the speckle noise in given conditions of image acquisition. Interestingly, the optimal level of speckle noise will be found to deliberately exploit the saturation in the operation of the sensor. By taking advantage of the saturation in this way, the acquisition reaches a maximum performance that cannot be achieved when the sensor is operated solely in the linear part of its response.

3. EVALUATION OF THE INPUT–OUTPUT SIMILARITY MEASURES

With the sensor $g(\cdot)$ of Eq. (5), we now want to derive explicit expressions for the input–output similarity measures C_{SY} and Q_{SY} of Eqs. (3) and (4). For the computation of the output expectation $\langle Y\rangle$, it is to be noted that Y takes its values in $[0,\theta]$ as a consequence of Eqs. (2) and (5). We introduce the conditional probability $\Pr\{Y \in [y,y+dy[\,|S=s\}$. For the nonsaturated pixels in the output image $Y(u,v)$, with gray levels such that $0 < y < \theta$, one has

$$\begin{aligned}\Pr\{Y \in [y,y+dy[\,|S=s\} &= \Pr\{N \in [y/s, y/s+dy/s[\} \\ &= p_N(y/s)dy/s,\end{aligned} \tag{6}$$

and for the saturated pixels of the output image $Y(u,v)$, with a gray level such that $y=\theta$, one has

$$\Pr\{Y = \theta | S=s\} = \Pr\{sN \geqslant \theta\} = \Pr\{N \geqslant \theta/s\} = 1 - F_N(\theta/s), \tag{7}$$

with the cumulative distribution function $F_N(n) = \int_{-\infty}^{n} p_N(n')\mathrm{d}n'$ of the speckle noise. This is enough to deduce the expectation $\langle Y\rangle$ as

$$\langle Y\rangle = \int_s \int_{y=0}^{\theta} y p_N(y/s)\frac{dy}{s} p_S(s)ds + \int_s \theta[1 - F_N(\theta/s)]p_S(s)ds. \tag{8}$$

We introduce the auxiliary function $G_N(n) = \int_0^n n' p_N(n')\mathrm{d}n'$, and then Eq. (8) becomes

$$\langle Y\rangle = \theta + \int_s [sG_N(\theta/s) - \theta F_N(\theta/s)]p_S(s)\mathrm{d}s. \tag{9}$$

In a similar way, the expectation $\langle SY\rangle$ is

$$\langle SY\rangle = \int_s \int_{y=0}^{\theta} sy p_N(y/s)\frac{dy}{s} p_S(s)ds + \int_s s\theta[1 - F_N(\theta/s)]p_S(s)\mathrm{d}s, \tag{10}$$

amounting to

$$\langle SY\rangle = \theta\langle S\rangle + \int_s [s^2 G_N(\theta/s) - \theta s F_N(\theta/s)]p_S(s)\mathrm{d}s. \tag{11}$$

Evaluation of Eqs. (3) and (4) also requires the expectation $\langle Y^2\rangle$, which is

$$\langle Y^2\rangle = \int_s \int_{y=0}^{\theta} y^2 p_N(y/s)\frac{dy}{s} p_S(s)ds + \int_s \theta^2[1 - F_N(\theta/s)]p_S(s)\mathrm{d}s. \tag{12}$$

And with the auxiliary function $H_N(n) = \int_0^n n'^2 p_N(n')\mathrm{d}n'$, Eq. (12) becomes

$$\langle Y^2\rangle = \theta^2 + \int_s [s^2 H_N(\theta/s) - \theta^2 F_N(\theta/s)]p_S(s)\mathrm{d}s. \tag{13}$$

With $\langle S\rangle = \int_s s p_S(s)\mathrm{d}s$ and $\langle S^2\rangle = \int_s s^2 p_S(s)\mathrm{d}s$, Eqs. (9), (11), and (13) allow one to evaluate the input–output similarity measures C_{SY} and Q_{SY} of Eqs. (3) and (4) in given input conditions specified by $p_S(s)$ and $p_N(n)$.

4. EXPONENTIAL SPECKLE NOISE

A useful probability density $p_N(n)$ for the speckle noise $N(u,v)$ is provided [11] by the exponential density

$$p_N(n) = \frac{1}{\sigma}\exp\left(-\frac{n}{\sigma}\right), \quad n \geq 0, \tag{14}$$

the density being zero for the negative gray levels $n<0$. From Eq. (14), the parameter σ is both the standard deviation and the expectation $\langle N\rangle$ of the speckle noise. Also, it follows from Eq. (14) that

$$F_N(n) = 1 - \exp\left(-\frac{n}{\sigma}\right), \quad n \geq 0, \tag{15}$$

$$G_N(n) = \int_0^n n' p_N(n')\mathrm{d}n' = \sigma\left[1 - \left(\frac{n}{\sigma}+1\right)\exp\left(-\frac{n}{\sigma}\right)\right], \quad n \geq 0, \tag{16}$$

and

$$H_N(n) = \int_0^n n'^2 p_N(n')\mathrm{d}n' = \sigma^2\left\{2 - \left[\left(\frac{n}{\sigma}\right)^2 + 2\frac{n}{\sigma} + 2\right]\exp\left(-\frac{n}{\sigma}\right)\right\}, \quad n \geq 0. \tag{17}$$

Then it results from Eq. (9) that

$$\langle Y\rangle = \sigma\langle S\rangle - \sigma\int_s s\exp\left(-\frac{\theta}{s\sigma}\right)p_S(s)\mathrm{d}s, \tag{18}$$

from Eq. (11) that

$$\langle SY\rangle = \sigma\langle S^2\rangle - \sigma\int_s s^2\exp\left(-\frac{\theta}{s\sigma}\right)p_S(s)\mathrm{d}s, \tag{19}$$

and from Eq. (13) that

$$\langle Y^2\rangle = 2\sigma^2\langle S^2\rangle - 2\sigma\int_s (\sigma s^2 + \theta s)\exp\left(-\frac{\theta}{s\sigma}\right)p_S(s)\mathrm{d}s. \tag{20}$$

5. EXPONENTIAL SPECKLE NOISE WITH BINARY INPUT IMAGE

With the exponential speckle noise $N(u,v)$, we now choose to examine the situation of binary input images $S(u,v)$. This class of images represents, for instance, a basic model for images characterized by only two regions with very narrow probability density functions in each region. One can think of an object with an almost uniform gray level centered around $I_1 \geq 0$, standing over a background with an almost uniform gray level centered around $I_0 \geq 0$. Such a scene would be fairly approximated by its binary version containing only levels I_1 and I_0. In addition, the simple choice of a binary input image $S(u,v)$ with levels I_1 and I_0 will allow us to carry further the analytical treatment of our theoretical model. With Dirac delta functions, the probability density function associated with a binary image is

$$p_S(s) = p_1\delta(s - I_1) + (1-p_1)\delta(s - I_0), \tag{21}$$

where p_1 is the fraction of pixels at I_1 in image $S(u,v)$. It results from Eq. (21) that $\langle S\rangle = p_1 I_1 + (1-p_1)I_0$ and $\langle S^2\rangle = p_1 I_1^2 + (1-p_1)I_0^2$. One then obtains for Eq. (18)

$$\langle Y\rangle = \sigma\langle S\rangle - \sigma\left[p_1 I_1\exp\left(-\frac{\theta}{I_1\sigma}\right) + (1-p_1)I_0\exp\left(-\frac{\theta}{I_0\sigma}\right)\right], \tag{22}$$

for Eq. (19)

$$\langle SY\rangle = \sigma\langle S^2\rangle - \sigma\left[p_1 I_1^2\exp\left(-\frac{\theta}{I_1\sigma}\right) + (1-p_1)I_0^2\exp\left(-\frac{\theta}{I_0\sigma}\right)\right], \tag{23}$$

and for Eq. (20)

$$\langle Y^2\rangle = 2\sigma^2\langle S^2\rangle - 2\sigma\left[p_1(\sigma I_1^2 + \theta I_1)\exp\left(-\frac{\theta}{I_1\sigma}\right) + (1-p_1)(\sigma I_0^2 + \theta I_0)\exp\left(-\frac{\theta}{I_0\sigma}\right)\right]. \tag{24}$$

Equations (22)–(24) now make possible an explicit evaluation of the input–output similarity measures C_{SY} and Q_{SY} of Eqs. (3) and (4).

Figures 1(A) and 1(B) give an illustration, showing conditions of nonmonotonic evolutions of the performance measures C_{SY} and Q_{SY}, which can be improved when the level of the speckle noise increases. Figures 1(A) and 1(B) demonstrate that the performance measures C_{SY} and Q_{SY} are maximized when the level σ of the speckle noise is tuned at an optimal nonzero value, which can be computed with the present theory. In practice, the level σ of the speckle noise can be controlled by experimentally varying the intensity of the coherent source. This way of controlling σ makes possible a confrontation of the theoretical and experimental evolutions for the performance measures C_{SY} and Q_{SY}. This confrontation has been performed, and the results are also presented in Figs. 1(A) and 1(B). We briefly describe the experimental setup in the following section.

6. EXPERIMENTAL VALIDATION

An optical version of the theoretical coherent imaging system described in Section 2 has been realized in the following way. A laser beam of tunable intensity goes through a static diffuser to create a speckle field, which illuminates a slide with calibrated transparency levels carrying the contrast of the input image $S(u,v)$. A lens then images the slide plane on a camera CCD matrix to produce the output image $Y(u,v)$. This experimental setup was used in [8] with an image acquisition device reduced to a simple 1-bit quantizer. By contrast, here the input–output characteristic of the image acquisition device presents the more realistic characteristic given by Eq. (5). A digital representation of the binary input image $S(u,v)$ used to realize this experiment is shown in Fig. 2 (left), with the object representing an airplane surrounded by a dark

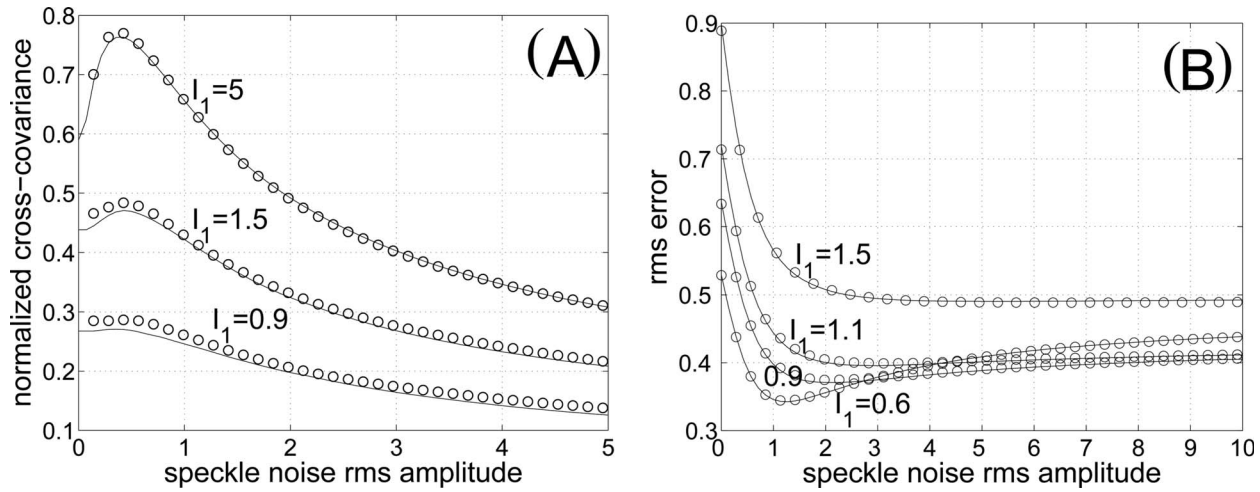

Fig. 1. Normalized cross covariance C_{SY} (A) and rms error Q_{SY} (B) as a function of the rms amplitude $\sqrt{2}\sigma$ of the exponential speckle noise when $\theta=1$, $p_1=0.27$, and $I_0=0.5$ at various I_1. The solid curve stands for the theoretical expressions of Eqs. (3) and (4). The discrete data sets (circles) are obtained by injecting into Eq. (1) real speckle images collected from the experimental setup of [8].

background. Some specific conditions arise to operate the experimental setup in the domain of validity of the speckle noise model of Eqs. (1) and (14). As is visible in Fig. 2, the experimental image appears with grains typical of speckle. The probability density of Eq. (14) describes the fluctuations of gray levels in the speckle at scales below the grain size, and it does not suffer from averages over several neighboring grains [11]. As such, the speckle noise model of Eqs. (1) and (14) is adequate to describe the situation where the detector pixel size is smaller than the speckle grain size [11]. At the same time, the statistical modeling based on the probability density of Eq. (14) is meaningful if the acquired image $Y(u,v)$ contains a large number of speckle grains for the statistics. Thus, the speckle grain size has to be controlled, like in Fig. 2 (right), in order to be much larger than the pixel size and much smaller than the CCD matrix. This control is obtained experimentally by adjusting the focus of the laser beam on the diffuser with a micrometer-scale sensitivity linear stage. Nevertheless, the speckle grain size is not a critical parameter, since it does not qualitatively affect the existence of the nonmonotonic evolution of the image acquisition performance with the speckle noise level. Quantitatively, too small a speckle grain size would change the speckle noise probability density function, since it would result from the integration over a pixel of multiple grains. Such probability density functions would be narrower than the exponential model considered here [11]. Too small a speckle grain size would therefore preserve and even enhance the nonmonotonic evolution of the image acquisition performance with the speckle noise level. Alternatively, too large a speckle grain size would not modify the speckle noise distribution but would impose a larger sensor CCD matrix in order to preserve similar efficacy in the estimation of the statistical averages, as in Fig. 1. Also, in the speckle noise model of Eq. (14), a single standard deviation σ is assumed for the speckle over the whole image $N(u,v)$. Therefore, special attention has to be devoted to control experimentally the uniformity of the laser beam. In our case, this is ensured by a spatial filter designed to obtain a clean laser beam quasiuniform around its center, covering the CCD matrix. Experimental results produced by the setup described above are also presented in Fig. 1 for comparison with the theoretical predictions. The results of Figs. 1(A) and 1(B) demonstrate, under the conditions indicated, a good agreement with the theoretical calculation of the performance measures C_{SY} and Q_{SY}.

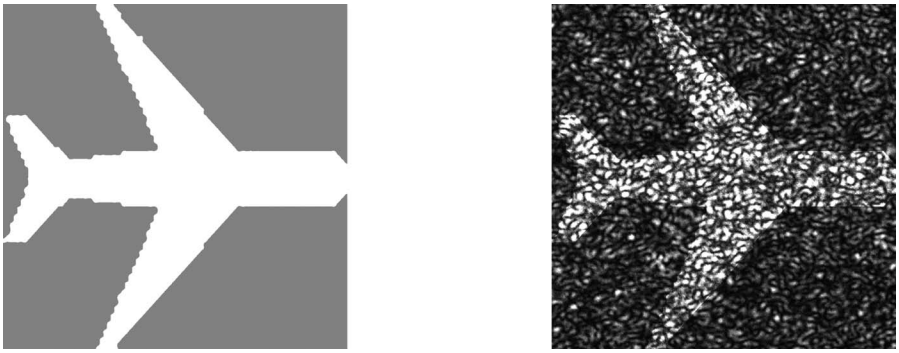

Fig. 2. (Left) Input image $S(u,v)$, with size 1024 ×1024 pixels, used for the experimental validation presented in Fig. 1, where the object is occupying $p_1=27\%$ of the image surface and parameters $I_0=0.5$, $I_1=1.5$. (Right) Corresponding intermediate image $X(u,v)$ obtained with a speckle noise rms amplitude $\sqrt{2}\sigma=0.42$.

7. INTERPRETATION

Figure 1 illustrates how an image can be acquired with maximum efficacy when a sufficient amount of speckle noise is injected in the present coherent imaging system. This feature can be interpreted as a form of stochastic resonance or a useful-noise effect. Stochastic resonance is an *a priori* counterintuitive phenomenon in a purely linear context, and it generally requires the presence of a nonlinear system in order to occur. The nonlinearity here is the saturating part in the response of the image acquisition device. As depicted in Fig. 3, at the optimal level of speckle noise, the saturation of the acquisition device affects almost only the pixels of one of the two regions (background and object) of the image. In Fig. 3, since $I_1 > I_0$, the pixels saturated in the acquired image $Y(u,v)$ almost all belong to the object region. Therefore, under the optimal speckle noise conditions of Fig. 3, the object region in the acquired image is somehow denoised by the saturation of the acquisition device. For too low a level of speckle noise, the acquired image is not saturated at all and cannot benefit from this denoising by saturation. For too high a level of the speckle noise, saturation progressively affects both regions of the acquired image, which loses its contrast and thus its similarity with the input binary image $S(u,v)$. This provides a qualitative interpretation for the nonmonotonic evolutions of the performance measures quantified in Fig. 1 when the level of the speckle noise is raised.

Based on the results of [9], it can be expected that the possibility of a beneficial exploitation of speckle noise in the presence of saturation will carry over to images with distributed gray levels. In essence, the effect is not critically dependent on the discrete binary nature of the information-carrying signal. In general terms, the starting point is an information-carrying signal at a given initial level of noise that places the sensor to operate essentially in the linear part of its input–output characteristic. Then, from this point, a sufficient increase in the level of noise at the input causes the sensor to operate in the saturation part of its response. As explained below, the saturation implements a clipping mechanism that has the ability to reduce the noise. With adequate control, this can lead to a situation at the output of the clipping device that is more favorable for the information-carrying signal than its initial situation with no clipping. The feasibility of such an effect was shown in [9] for continuously distributed 1D temporal signals with additive noise. Here we have demonstrated the feasibility of the effect on binary 2D spatial signals (images) with multiplicative speckle noise.

8. CONCLUSION

For coherent imaging, we have demonstrated that saturation of an acquisition device can be exploited to perform a signal transmission more efficient than that of a purely linear sensor. Optimal transmission is obtained by adjusting the speckle noise at a sufficient level, which deliberately operates the acquisition device in its saturating part. This constructive action of speckle noise cooperating with saturation is interpreted as a novel instance of stochastic resonance. The possibility of a constructive action of the multiplicative speckle noise has been illustrated with an exponential speckle probability density and binary images. Under these conditions, we have shown good agreement between theoretical and experimental results in relation to influence of speckle noise grain size. A qualitative explanation of the mechanism at the root of the improvement by the speckle noise has also been proposed. It appears in this way that, with binary images buried in speckle noise, clipping in the acquired images can be a useful operation that acts as a denoising stage, which can be, as demonstrated here, optimally controlled by tuning the speckle noise at a sufficient level. Because of the practical importance of saturating sensor characteristics, this result constitutes an interesting extension of [8], where

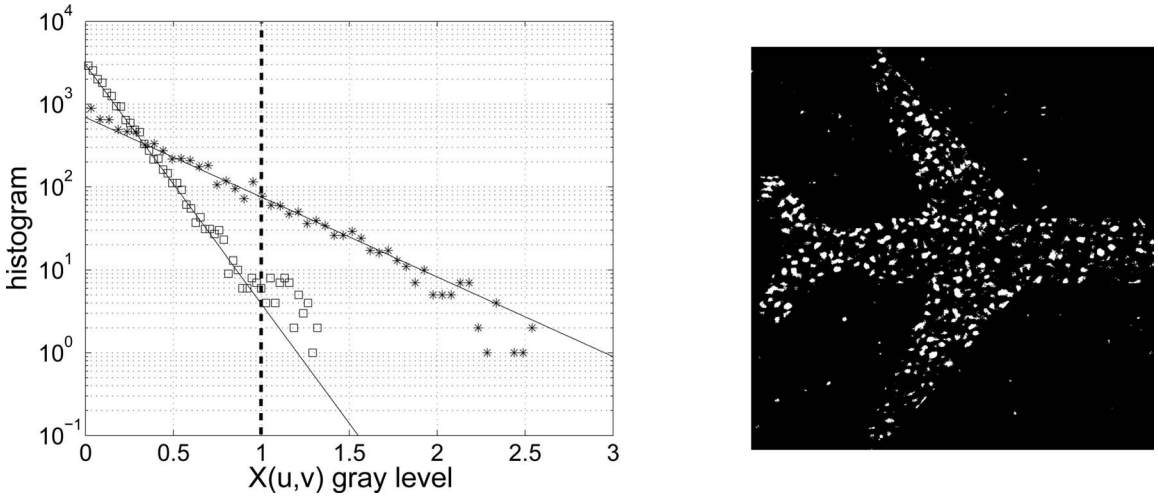

Fig. 3. (Left) Histogram of background (□) and object (∗) regions in intermediate image $X(u,v)$ of Eq. (1) on a logarithmic scale. Input image $S(u,v)$ is the same as in Fig. 2 (left). The solid curves are the theoretical histograms calculated from the exponential model of Eq. (14). The dashed curve stands for the saturating level $\theta=1$ of the acquisition image device. Speckle noise is obtained from the experimental setup of [8] with an rms amplitude $\sqrt{2}\sigma=0.42$, corresponding to the optimal value of normalized cross covariance C_{SY}. (Right) Binary image representing only the pixel saturated in the acquired image $Y(u,v)$ under the acquisition conditions of the left panel of this figure.

the possibility of nonmonotonic evolutions of image acquisition performance as a function of the speckle noise amplitude was shown with a simple 1-bit quantizer.

Acquisition, usually seen as the very first step in an information processing chain, is conventionally designed to reproduce a faithful representation of the physical signal with the highest linear fidelity. Here we have shown how the nonlinear saturating part of an acquisition device can also be used as a preprocessor capable of denoising properties usually undertaken at higher levels in the information processing chain. Comparable situations where the clipping effect of a saturating device can benefit from the processing of an information-carrying signal can also be found in other contexts. In signal detection [12], the effect can be used to reduce the detrimental impact on the performance of detectors of spikes due to non-Gaussian heavy-tailed additive noises. Some distinct nonlinear effects, bearing some similarity with the present clipping effect, have also been reported in other areas of coherent imaging [13–15]. Some benefits of clipping are shown in [13–15] for real-time image processing. Yet in these references, the clipping that is used is meant as hard clipping, which is, in fact, a 1-bit quantization of the image. This differs in essence from the type of clipping we consider here, arising from the linear response of a sensor that reaches saturation. Moreover, the processes addressed in [13–15] are postacquisition processes distinct from the acquisition task investigated here at the sensor level.

Results of this report could be extended in several directions. For example, more sophisticated images with distributed gray levels, instead of binary images, could be tested. The case of coherent images with distributed gray levels can be investigated by means of the general theoretical framework developed here, which is valid for any type of speckle noise and input image distribution. As discussed in Section 7, the stochastic resonance or useful-noise effect reported here is expected to carry over to images containing more than two gray levels. Therefore, it would be interesting to confront, as done here, theoretical and experimental results and to examine how the beneficial action of speckle noise in association with saturation evolves in these other conditions of coherent imaging. One could also consider image processing tasks other than the acquisition task treated here. Image processing techniques for coherent imaging that take into account the statistical properties of the noisy images are commonly implemented, for instance, for detection [16], segmentation [17], or parameter estimation [18] purposes. These techniques usually assume a perfectly linear model for the acquisition device, and the experimental images acquired for the validation of their theoretical performance are made at a low level of speckle noise to minimize the saturation that always exists in practice. Therefore, it would be interesting to investigate the performance of such detection, segmentation, or parameter estimation techniques as described in [16–18], with the presence of a saturating part in the response of the acquisition device, and in the light of the present results that predict an increased benefit that can be drawn from saturation.

REFERENCES

1. L. Gammaitoni, P. Hänggi, P. Jung, and F. Marchesoni, "Stochastic resonance," Rev. Mod. Phys. **70**, 223–287 (1998).
2. F. Chapeau-Blondeau and D. Rousseau, "Noise improvements in stochastic resonance: from signal amplification to optimal detection," Fluct. Noise Lett. **2**, 221–233 (2002).
3. B. M. Jost and B. E. A. Saleh, "Signal-to-noise ratio improvement by stochastic resonance in a unidirectional photorefractive ring resonator," Opt. Lett. **21**, 287–289 (1996).
4. F. Vaudelle, J. Gazengel, G. Rivoire, X. Godivier, and F. Chapeau-Blondeau, "Stochastic resonance and noise-enhanced transmission of spatial signals in optics: the case of scattering," J. Opt. Soc. Am. B **15**, 2674–2680 (1998).
5. K. P. Singh, G. Ropars, M. Brunel, and A. Le Floch, "Stochastic resonance in an optical two-order parameter vectorial system," Phys. Rev. Lett. **87**, 213901 (2001).
6. F. Marino, M. Giudici, S. Barland, and S. Balle, "Experimental evidence of stochastic resonance in an excitable optical system," Phys. Rev. Lett. **88**, 040601 (2002).
7. K. P. Singh, G. Ropars, M. Brunel, and A. Le Floch, "Lever-assisted two-noise stochastic resonance," Phys. Rev. Lett. **90**, 073901 (2003).
8. S. Blanchard, D. Rousseau, D. Gindre, and F. Chapeau-Blondeau, "Constructive action of the speckle noise in a coherent imaging system," Opt. Lett. **32**, 1983–1985 (2007).
9. D. Rousseau, J. Rojas Varela, and F. Chapeau-Blondeau, "Stochastic resonance for nonlinear sensors with saturation," Phys. Rev. E **67**, 021102 (2003).
10. F. Chapeau-Blondeau, S. Blanchard, and D. Rousseau, "Noise-enhanced Fisher information in parallel arrays of sensors with saturation," Phys. Rev. E **74**, 031102 (2006).
11. J. W. Goodman, *Speckle Phenomena in Optics* (Roberts & Company, 2007).
12. S. Kay, *Fundamentals of Statistical Signal Processing: Detection Theory* (Prentice Hall, 1998).
13. J. Ohtsubo and A. Ogiwara, "Effects of clippling threshold on clipped speckle intensity," Opt. Commun. **65**, 73–78 (1988).
14. A. Ogiwara, H. Sakai, and J. Ohtsubo, "Real-time optical joint transform correlator for velocity measurement using clipped speckle intensity," Opt. Commun. **78**, 322–326 (1990).
15. R. H. Sperry and K. J. Parker, "Segmentation of speckle images based on level-crossing statistics," J. Opt. Soc. Am. A **3**, 490–498 (1991).
16. F. Goudail, P. Réfrégier, and G. Delyon, "Bhattacharyya distance as a contrast parameter for statistical processing of noisy optical images," J. Opt. Soc. Am. A **21**, 1231–1240 (2004).
17. F. Goudail and P. Réfrégier, *Statistical Image Processing Techniques for Noisy Images* (Kluwer, 2004).
18. P. Réfrégier, J. Fade, and M. Roche, "Estimation precision of the degree of polarization from a single speckle intensity image," Opt. Lett. **32**, 739–741 (2007).

D. ROUSSEAU, A. DELAHAIES, F. CHAPEAU-BLONDEAU. Structural similarity measure to assess improvement by noise in nonlinear image transmission. *IEEE Signal Processing Letters*, vol. 17, 36–39, 2010.

Structural Similarity Measure to Assess Improvement by Noise in Nonlinear Image Transmission

David Rousseau, Agnès Delahaies, and François Chapeau-Blondeau

***Abstract*—We show that the structural similarity index is able to register stochastic resonance or improvement by noise in nonlinear image transmission, and sometimes when not registered by traditional measures of image similarity, and that in this task this index remains in good match with the visual appreciation of image quality.**

***Index Terms*—Image quality measure, improvement by noise, nonlinearity, stochastic resonance, structural similarity.**

I. Introduction

AUTOMATIC image quality assessment is an important task for many areas of image processing. Traditional metrics commonly used for image quality, such as mean squared error, peak signal-to-noise ratio and related indices, are simple to implement but are limited to providing a low-level-based assessment of images. Recently, the structural similarity (SSIM) index has been proposed as a novel measure of image quality [1], [2], with the potentiality for a more structural assessment based on evaluating image degradation as a combination of three different factors: loss of correlation, luminance and contrast distortions. The SSIM index has been shown to outperform simpler traditional metrics while avoiding the complexity of an explicit modeling of perception by the human visual system [1], [2]. This ability of SSIM to offer an efficient measure of image quality was established in [1], [2] in various image processing tasks such as compression, contrast stretching, mean shifting, noise contamination, blurring, and it was tested against visual appreciation of image quality. Yet, as a recently introduced index, SSIM may still benefit, as advocated in [1], from further experiments in order to fully appreciate its capabilities. In the present paper, we test SSIM as a relevant index to measure stochastic resonance or improvement by noise in nonlinear image transmission.

Stochastic resonance, in broad sense, designates situations where the noise can play a constructive role in signal processing [3]–[5]. Such possibility to occur usually demands the presence of a nonlinear process. Stochastic resonance or improvement by noise has been shown possible in different types of nonlinear image transmission or processing [6]–[11]. The most common indices that were used to manifest stochastic resonance for aperiodic signals or images were traditional similarity indices like correlation measures or mean squared error. Such an index measures the similarity between an input image and an output image resulting from nonlinear transmission in the presence of noise, and stochastic resonance is manifested by the input-output similarity index which culminates at a maximum occurring for a finite nonzero amount of noise. This identifies an improvement by noise of a nonlinear image transmission, yet with low-level-based indices of image quality. At the same time, stochastic resonance has been registered in psychovisual experiments when measuring the performance by visual perception of human subjects [6], [12]–[14]. Here, we complement the measures of stochastic resonance by testing the SSIM index of [1], [2] for the first time for this purpose.

Also, most reports on stochastic resonance with images have dealt with threshold or potential-barrier nonlinearities, where the noise essentially assists a small signal in overcoming a threshold or barrier. In this context of threshold nonlinearities, more specific techniques like dithering can be viewed as a special form of stochastic resonance [15]–[17]. Yet, stochastic resonance can occur in other types of nonlinearities, and we show it here with saturation as well as threshold nonlinearities. Saturation nonlinearities are common in imaging devices, and while testing the SSIM index here, we also illustrate the possibility of image saturation restored by noise.

II. Similarity Measures

For two images $\mathbf{x} = \{x_i | i = 1, 2, \dots N\}$ and $\mathbf{y} = \{y_i | i = 1, 2, \dots N\}$ with same size, we consider the SSIM index $S(\mathbf{x}, \mathbf{y})$ defined from [1] as

$$S(\mathbf{x}, \mathbf{y}) = \frac{4(\langle xy \rangle - \langle x \rangle \langle y \rangle)\langle x \rangle \langle y \rangle}{(\langle x^2 \rangle - \langle x \rangle^2 + \langle y^2 \rangle - \langle y \rangle^2)(\langle x \rangle^2 + \langle y \rangle^2)} \quad (1)$$

where $\langle \cdot \rangle$ stands for an average over the images, for instance $\langle xy \rangle = N^{-1} \sum_{i=1}^{N} x_i y_i$. The SSIM index $S(\mathbf{x}, \mathbf{y})$ of (1) varies in $[-1, 1]$; it achieves its best value of 1 when the two images $\mathbf{x}$ and $\mathbf{y}$ are equal; it is at zero when $\mathbf{x}$ and $\mathbf{y}$ are unrelated; it is at -1 when $\mathbf{x}$ and $\mathbf{y}$ are equal except for opposite signs of their fluctuations. References [1], [2], [18] motivate the definition of $S(\mathbf{x}, \mathbf{y})$ to quantify the structural departure between images $\mathbf{x}$ and $\mathbf{y}$ by combining loss of correlation, luminance and contrast distortions. In addition, we consider the two traditional measures given by the cross-correlation coefficient

$$C(\mathbf{x}, \mathbf{y}) = \frac{\langle xy \rangle - \langle x \rangle \langle y \rangle}{\sqrt{\langle x^2 \rangle - \langle x \rangle^2} \sqrt{\langle y^2 \rangle - \langle y \rangle^2}} \quad (2)$$

and root mean squared (rms) error

Manuscript received June 18, 2009; revised August 15, 2009. First published September 09, 2009; current version published October 14, 2009. The associate editor coordinating the review of this manuscript and approving it for publication was Dr. Alfred Mertins.

The authors are with the Laboratoire d'Ingénierie des Systèmes Automatisés (LISA), Université d'Angers, 49000 Angers, France (e-mail: chapeau@univ-angers.fr).

Digital Object Identifier 10.1109/LSP.2009.2031734

$$E(\mathbf{x},\mathbf{y}) = \sqrt{\langle (x-y)^2 \rangle}. \tag{3}$$

Additionally, $S(\mathbf{x},\mathbf{y})$ can be factored as $S = \mathrm{CMV}$ where $M(\mathbf{x},\mathbf{y}) = 2\langle x\rangle\langle y\rangle/(\langle x\rangle^2 + \langle y\rangle^2)$ measures the similarity in the means of $\mathbf{x}$ and $\mathbf{y}$, and $V(\mathbf{x},\mathbf{y}) = 2\sqrt{\langle x^2\rangle - \langle x\rangle^2}\sqrt{\langle y^2\rangle - \langle y\rangle^2}/(\langle x^2\rangle - \langle x\rangle^2 + \langle y^2\rangle - \langle y\rangle^2)$ measures the similarity in their contrasts [1].

We use and confront the three indices S, C and E of (1)–(3) to assess image transmission by nonlinear devices in the presence of noise. We specifically study the regime, related to a stochastic resonance effect, where the noise can play a constructive role in the nonlinear transmission. An input image $\mathbf{x}$ is corrupted by an additive noise $\mathbf{n}$ with the noise realizations assumed independent at each pixel. The noisy image $\mathbf{x}+\mathbf{n}$ is then acquired or transmitted by a nonlinear device modeled by the memoryless characteristic $g(\cdot)$ which delivers the output image $\mathbf{y}$ defined as

$$\mathbf{y} = g(\mathbf{x}+\mathbf{n}). \tag{4}$$

III. Hard-Limiter Transmission

As a first example, we consider $g(\cdot)$ a hard limiter with threshold θ,

$$g(u) = \begin{cases} 0, & \text{for } u \le \theta \\ 1, & \text{for } u > \theta \end{cases} \tag{5}$$

in charge of the transmission of binary images $\mathbf{x}$. We consider the case of a small-amplitude input image $\mathbf{x}$ with binary intensities at 0 or 1, which is everywhere below the threshold $\theta > 1$ of the transmission device of (5). In this condition, in absence of the noise $\mathbf{n}$ in (4), no transmission occurs and at the output $\mathbf{y}$ remains a blank image. Addition of the noise $\mathbf{n}$ in (4) enables a cooperative effect where the noise assists the subthreshold input image $\mathbf{x}$ in overcoming the threshold θ, so as to elicit an output image $\mathbf{y}$ carrying some similarity with the input image $\mathbf{x}$. This similarity is quantified in Fig. 1 with the three measures of (1)–(3), and as a function of the level of the noise $\mathbf{n}$.

In Fig. 1, each similarity index S, C or E experiences a nonmonotonic evolution as the noise level increases, passing through an extremum which identifies a nonzero optimal noise level where the similarity index is at its best. The optimal noise level is different for each index, expressing the notion that each index conveys some distinct aspect concerning the similarity. As yet another aspect, Fig. 2 provides a visual appreciation of the similarity at different levels of noise.

The sequence of images in Fig. 2 also makes clearly visible a nonmonotonic action of the noise $\mathbf{n}$, with a visually poor image transmission at low or high noise levels, and better quality of transmission in between. From Fig. 2, it can be argued that the SSIM index $S(\mathbf{x},\mathbf{y})$ and the cross-correlation $C(\mathbf{x},\mathbf{y})$ best match the visual assessment of the images, since images with good visual quality are obtained at the noise levels that maximize $S(\mathbf{x},\mathbf{y})$ and $C(\mathbf{x},\mathbf{y})$. By contrast, at the noise level minimizing the rms error $E(\mathbf{x},\mathbf{y})$, the visual quality appears poorer in Fig. 2, expressing that the rms error is not here in good match with the visual appreciation.

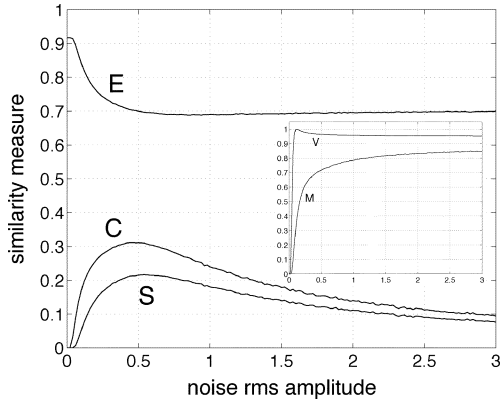

Fig. 1. For the transmission by (5) with threshold $\theta = 1.1$ of the binary image $\mathbf{x}$ of Fig. 2(a): as a function of the rms amplitude σ of the zero-mean Gaussian noise $\mathbf{n}$ in (4), the input-output similarity indices $S(\mathbf{x},\mathbf{y})$ of (1), $C(\mathbf{x},\mathbf{y})$ of (2) and $E(\mathbf{x},\mathbf{y})$ of (3). The inset shows the partial measures $M(\mathbf{x},\mathbf{y})$ and $V(\mathbf{x},\mathbf{y})$ versus σ.

IV. Transmission With Saturation

We now consider $g(\cdot)$ as a sensor which remains linear for small positive intensities but saturates when the intensities exceed some level θ, i.e.,

$$g(u) = \begin{cases} 0, & \text{for } u < 0 \\ u, & \text{for } 0 \le u \le \theta \\ \theta, & \text{for } u > \theta \end{cases} \tag{6}$$

in charge of the transmission of gray-level images $\mathbf{x}$. We consider the case of a high-amplitude input image $\mathbf{x}$ with intensities in $[0,1]$, and which strongly saturates the sensor of (6) having a saturation level $\theta < 1$. The resulting output image $\mathbf{y}$ is strongly affected by saturation. The impact of the added noise $\mathbf{n}$ in (4) is shown in Fig. 3 on the three input-output similarity indices of (1)–(3).

In Fig. 3 only the SSIM index $S(\mathbf{x},\mathbf{y})$ achieves its best value at a nonzero level of the noise $\mathbf{n}$. This expresses the possibility of a constructive action of the noise to improve image transmission in the presence of strong saturation of the sensor, as assessed by SSIM. On the contrary in Fig. 3, the cross-correlation $C(\mathbf{x},\mathbf{y})$ and the rms error $E(\mathbf{x},\mathbf{y})$ are at their best with no added noise $\mathbf{n}$, and in this respect do not manifest the possibility of a constructive action of noise in the nonlinear transmission. This again illustrates the notion that each index reflects some distinct aspect concerning the similarity.

Next, a visual appreciation regarding the impact of noise on the input-output similarity can be obtained from Fig. 4.

Again, in Fig. 4 the visual appreciation appears in good match with the behavior of the SSIM index $S(\mathbf{x},\mathbf{y})$, while the cross-correlation $C(\mathbf{x},\mathbf{y})$ and rms error $E(\mathbf{x},\mathbf{y})$ are comparatively less in tune with the visual appreciation. This is so because, with no added noise, $C(\mathbf{x},\mathbf{y})$ and $E(\mathbf{x},\mathbf{y})$ are at their best as shown in Fig. 4, yet from visual inspection in Fig. 4(b) significant features are missing in the output image $\mathbf{y}$ due to saturation. By contrast, missing features become perceivable in Fig. 4 as noise is added manifesting its ability to counteract the negative effect of the saturation. This restoration by noise visually appears specially efficient in Fig. 4(d) at the nonzero noise level maximizing the SSIM index $S(\mathbf{x},\mathbf{y})$ in Fig. 3.

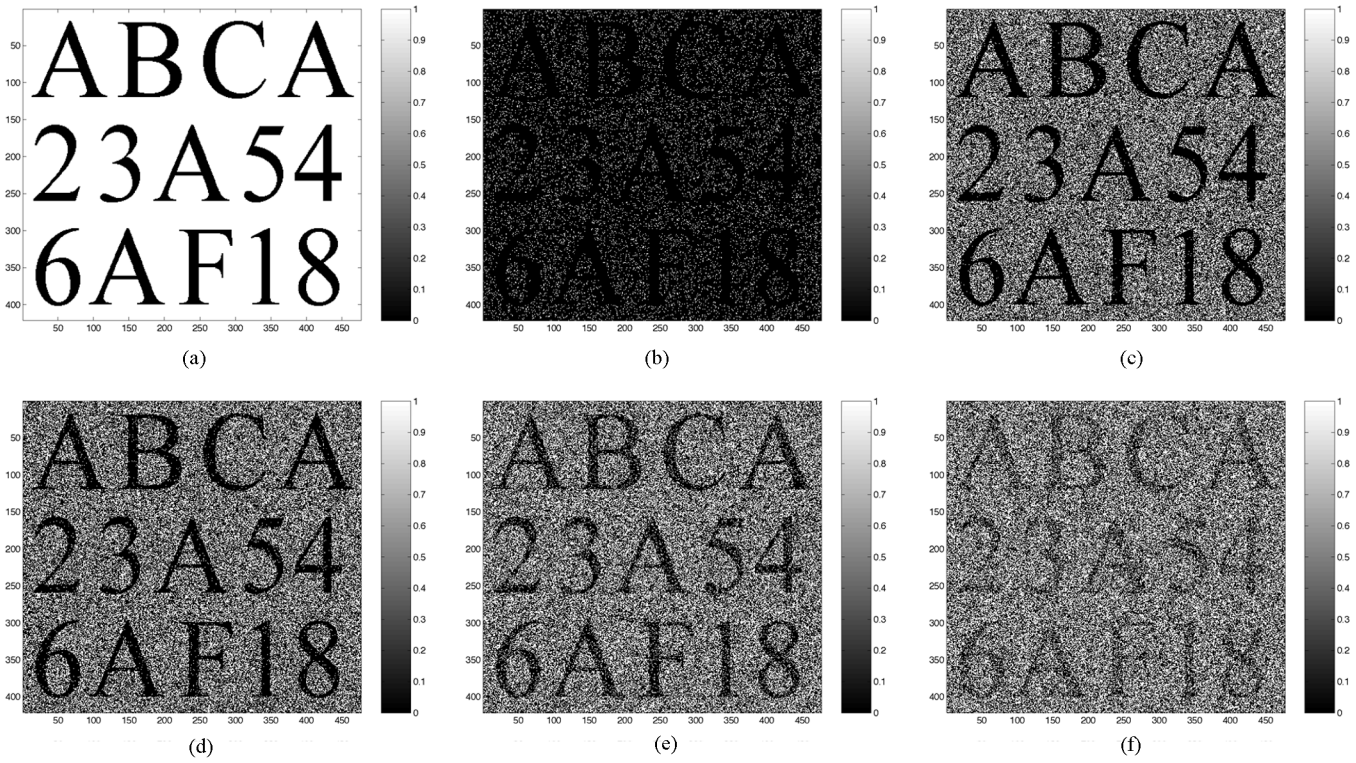

Fig. 2. (a) Binary input image $\mathbf{x}$. (b)–(f) binary image $\mathbf{y}$ at the output of the sensor of (5) with threshold $\theta = 1.1$, with the noise $\mathbf{n}$ zero-mean Gaussian of rms amplitude σ. (b) $\sigma = 0.07$. (c) $\sigma = 0.49$ maximizing the cross-correlation $C(\mathbf{x}, \mathbf{y})$ in Fig. 1. (d) $\sigma = 0.59$ maximizing the SSIM index $S(\mathbf{x}, \mathbf{y})$ in Fig. 1. (e) $\sigma = 0.99$ minimizing the rms error $E(\mathbf{x}, \mathbf{y})$ in Fig. 1. (f) $\sigma = 1.5$.

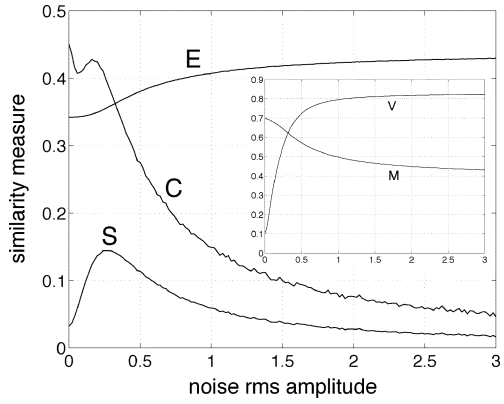

Fig. 3. For the transmission by (6) with saturation level $\theta = 0.2$ of the gray-level image $\mathbf{x}$ of Fig. 4(a): as a function of the rms amplitude σ of the zero-mean Gaussian noise $\mathbf{n}$ in (4), the input-output similarity indices $S(\mathbf{x}, \mathbf{y})$ of (1), $C(\mathbf{x}, \mathbf{y})$ of (2) and $E(\mathbf{x}, \mathbf{y})$ of (3). The inset shows the partial measures $M(\mathbf{x}, \mathbf{y})$ and $V(\mathbf{x}, \mathbf{y})$ versus σ.

Also, Figs. 1 and 3 show distinct influences of the partial measures M and V in contributing to the global index S, depending on the nonlinear operation. In particular, an approximation $S \approx CV$ inspired from [19] is not necessarily accurate at all noise levels σ when M significantly varies with σ.

V. Conclusion

The present study is the first demonstration of the capability of the SSIM index of [1], [2] to register an effect of stochastic resonance or improvement by noise in nonlinear image transmission. A possible extension now is to apply SSIM on blocks or patches or across scales [1], [2], [20], [19], in order to complement with a more local or regional evaluation at relevant subscales to be identified, the global assessment of the stochastic resonance obtained here on the images.

Although still in an early stage, the SSIM index, from the recent results [1], [20], [2], [21], [22], [18], [23], [24], [19], is gradually emerging as a specially useful metric for image quality, providing a specific intermediate approach exhibiting richer capabilities for structural assessment compared to simpler traditional low-level-based indices, while avoiding the complexity of modeling the human visual system. The present results, by testing its behavior in a new task of image processing, reinforces this position of SSIM as a valuable quality metric. Especially, the assessment of stochastic resonance by SSIM does not copy the assessments by traditional low-level-based indices, confirming its specific capabilities as a quality metric. At the same time, the assessment by SSIM appears to better match the visual appreciation of image quality in the stochastic resonance experiments. These two features of SSIM (specificity of behavior and good match with visual perception) were generally preserved when varying the images and types of noise in our stochastic resonance experiments. The present results thus contribute to establish SSIM as an index for image quality with many useful potentialities of application. Also, the results complement the possible approaches for the on-going analyses of stochastic resonance or improvement by noise in image transmission, with a new metric enabling structural assessment of images and with relevance toward visual perception.

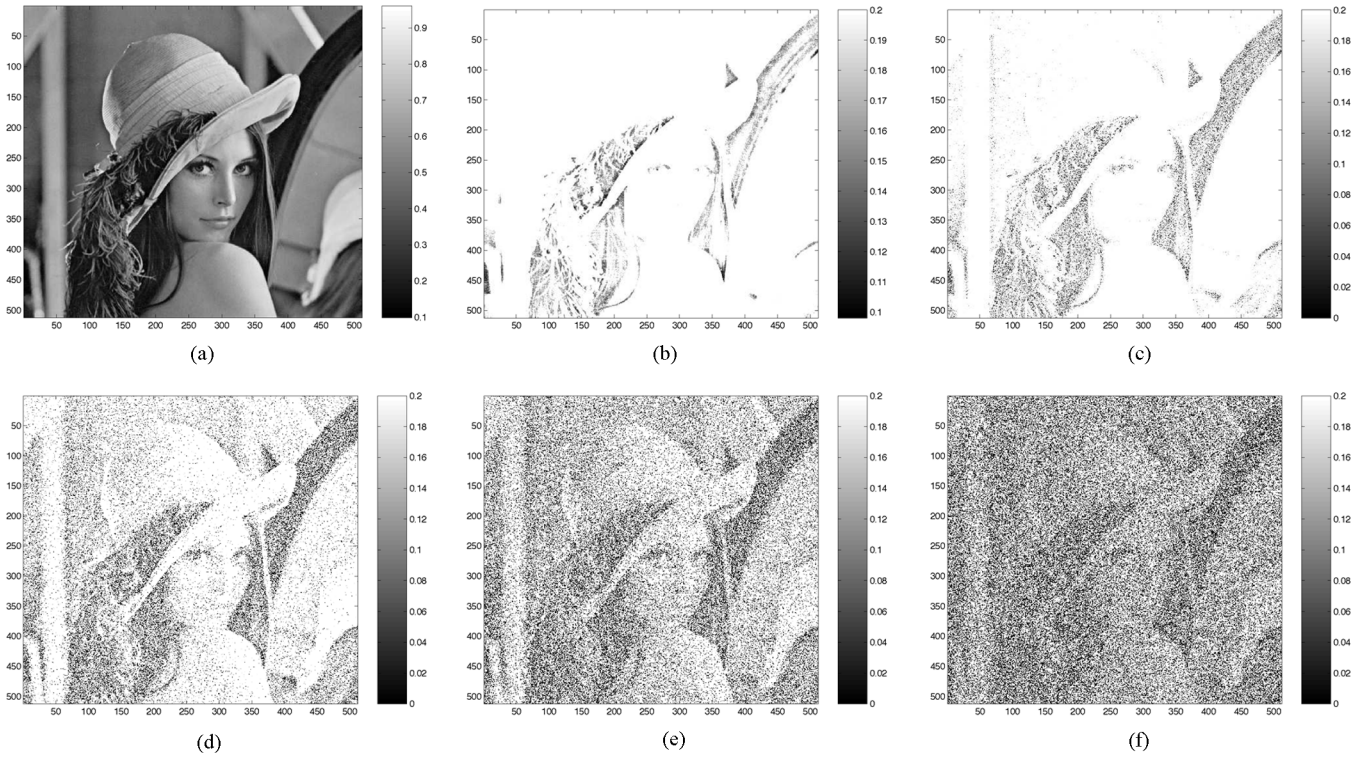

Fig. 4. (a) Gray-level input image $\mathbf{x}$. (b)–(f) gray-level image $\mathbf{y}$ at the output of the sensor of (6) with saturation level $\theta = 0.2$, with the noise $\mathbf{n}$ zero-mean Gaussian of rms amplitude σ. (b) $\sigma = 0$ maximizing the cross-correlation $C(\mathbf{x}, \mathbf{y})$ and minimizing the rms error $E(\mathbf{x}, \mathbf{y})$ in Fig. 3. (c) $\sigma = 0.1$. (d) $\sigma = 0.28$ maximizing the SSIM index $S(\mathbf{x}, \mathbf{y})$ in Fig. 3. (e) $\sigma = 0.5$. (f) $\sigma = 1$.

REFERENCES

[1] Z. Wang and A. C. Bovik, "A universal image quality index," *IEEE Signal Process. Lett.*, vol. 9, pp. 81–84, 2002.

[2] Z. Wang, A. C. Bovik, H. R. Sheikh, and E. P. Simoncelli, "Image quality assessment: From error visibility to structural similarity," *IEEE Trans. Image Process.*, vol. 13, pp. 600–612, 2004.

[3] B. Andò and S. Graziani, "Adding noise to improve measurement," *IEEE Instrumen. Meas. Mag.*, vol. 4, no. 1, pp. 24–30, Mar. 2001.

[4] G. P. Harmer, B. R. Davis, and D. Abbott, "A review of stochastic resonance: Circuits and measurement," *IEEE Trans. Instrum. Meas.*, vol. 51, pp. 299–309, 2002.

[5] F. Chapeau-Blondeau and D. Rousseau, "Noise improvements in stochastic resonance: From signal amplification to optimal detection," *Fluct. Noise Lett.*, vol. 2, pp. L221–L233, 2002.

[6] E. Simonotto, M. Riani, C. Seife, M. Roberts, J. Twitty, and F. Moss, "Visual perception of stochastic resonance," *Phys. Rev. Lett.*, vol. 78, pp. 1186–1189, 1997.

[7] F. Vaudelle, J. Gazengel, G. Rivoire, X. Godivier, and F. Chapeau-Blondeau, "Stochastic resonance and noise-enhanced transmission of spatial signals in optics: The case of scattering," *J. Opt. Soc. Amer. B*, vol. 15, pp. 2674–2680, 1998.

[8] M. O. Hongler, Y. L. de Meneses, A. Beyeler, and J. Jacot, "The resonant retina: Exploiting vibration noise to optimally detect edges in an image," *IEEE Trans. Pattern Anal. Machine Intell.*, vol. 25, pp. 1051–1062, 2003.

[9] A. Histace and D. Rousseau, "Constructive action of noise for impulsive noise removal in scalar images," *Electron. Lett.*, vol. 42, pp. 393–395, 2006.

[10] S. Blanchard, D. Rousseau, D. Gindre, and F. Chapeau-Blondeau, "Constructive action of the speckle noise in a coherent imaging system," *Opt. Lett.*, vol. 32, pp. 1983–1985, 2007.

[11] Y. Yang, Z. Jiang, B. Xu, and D. W. Repperger, "An investigation of two-dimensional parameter-induced stochastic resonance and applications in nonlinear image processing," *J. Phys. A*, vol. 42, pp. 145207,1–145207,9, 2009.

[12] T. Yang, "Adaptively optimizing stochastic resonance in visual system," *Phys. Lett. A*, vol. 245, pp. 79–86, 1998.

[13] M. Piana, M. Canfora, and M. Riani, "Role of noise in image processing by the human perceptive system," *Phys. Rev. E*, vol. 62, pp. 1104–1109, 2000.

[14] H. Sasaki, M. Todorokihara, T. Ishida, J. Miyachi, T. Kitamura, and R. Aoki, "Effect of noise on the contrast detection threshold in visual perception," *Neurosci. Lett.*, vol. 408, pp. 94–97, 2006.

[15] L. Gammaitoni, "Stochastic resonance and the dithering effect in threshold physical systems," *Phys. Rev. E*, vol. 52, pp. 4691–4698, 1995.

[16] F. Chapeau-Blondeau and X. Godivier, "Theory of stochastic resonance in signal transmission by static nonlinear systems," *Phys. Rev. E*, vol. 55, pp. 1478–1495, 1997.

[17] R. A. Wannamaker, S. P. Lipshitz, and J. Vanderkooy, "Stochastic resonance as dithering," *Phys. Rev. E*, vol. 61, pp. 233–236, 2000.

[18] Z. Wang, A. C. Bovik, and H. R. Sheikh, "Structural similarity based image quality assessment," in *Digital Video Image Quality and Perceptual Coding*, H. R. Wu and K. R. Rao, Eds. Boca Raton, FL: Taylor & Francis, 2006, pp. 225–236, ch. 7.

[19] D. M. Rouse and S. S. Hemami, "Understanding and simplifying the structural similarity metric," in *Proc. 15th IEEE Int. Conf. Image Processing*, San Diego, CA, Oct. 12–15, 2008, pp. 1188–1191.

[20] Z. Wang, E. P. Simoncelli, and A. C. Bovik, "Multiscale structural similarity for image quality assessment," in *Proc. 37th IEEE Asilomar Conf. Signals, Systems and Computers*, Pacific Grove, CA, Nov. 9–12, 2003, vol. 2, pp. 1398–1402.

[21] Z. Wang, L. Lu, and A. C. Bovik, "Video quality assessment based on structural distortion measurement," *Signal Process.: Image Commun.*, vol. 19, pp. 121–132, 2004.

[22] D. Kalenova, D. Dochev, V. Bochko, P. Toivanen, and A. Kaarna, "A novel technique of spectral image quality assessment based on structural similarity measure," in *Proc. 3rd Eur. Conf. Color in Graphics, Imaging and Vision*, Leeds, UK, June 19–22, 2006, pp. 499–503.

[23] A. C. Brooks and T. N. Pappas, "Using structural similarity quality metrics to evaluate image compression techniques," in *Proc. 32nd IEEE Int. Conf. Acoustics, Speech, and Signal Processing (ICASSP)*, Honolulu, HI, Apr. 15–20, 2007, vol. 1, pp. 873–876.

[24] J. H. Lee and T. Horiuchi, "Image quality assessment for color halftone images based on color structural similarity," *IEICE Trans. Fund. Electron., Commun. Comput. Sci.*, vol. E91-A, pp. 1392–1399, 2008.

A. HISTACE and D. ROUSSEAU. Constructive action of noise for impulsive noise removal in scalar images. *Electronics Letters*, vol. 42:393–395, 2006.

Constructive action of noise for impulsive noise removal in scalar images

A. Histace and D. Rousseau

A nonlinear variational approach to remove impulsive noise in scalar images is proposed. Taking benefit from recent studies on the use of stochastic resonance and the constructive role of noise in nonlinear processes, the process is based on the classical restoration process of Perona-Malik in which a Gaussian noise is purposely injected. It is shown that this new process can outperform the original restoration process of Perona-Malik.

Aim and motivation: Removing impulsive noises from scalar images is a problem of great interest since these short duration and high energy noises can degrade the quality of digital images in a large variety of practical situations [1]. In this context of non-Gaussian noise, nonlinear processes are often invoked. Among these nonlinear processes median filtering is a classical tool leading to good results [2]. Nevertheless, these median filtering techniques involve strong statistics calculation and can turn out to be highly time consuming to compute. Another nonlinear process classically used for restoration tasks is the diffusion process of Perona-Malik [3]. This process, based on a variational approach, presents short implementation time and has the ability to remove noise while keeping edges stable on many scales. The Perona-Malik process also has its own limitations. Among these limitations, the smoothing property of the diffusion process does not preserve the information present in areas with texture or small but significative gradients [4]. As paradoxical as it may seem, to limit the effect of this drawback, we propose a new variant of the Perona-Malik process in which a controlled amount of noise is injected into the nonlinear process. The possibility of constructive action of noise in nonlinear processes is now a well established paradigm known under the name of stochastic resonance (see [5] for a recent overview). To date, this paradigm has essentially been illustrated with mono-dimensional signals. This work is a new feature of noise enhanced information processing presented here for the first time in the context of image restoration.

Method: Let ψ_{ori} denote an original image and ψ_0 denote the same image corrupted by an input impulsive noise ξ imposed by the external environment:

$$\psi_0(x,y) = \psi_{ori}(x,y) + \xi(x,y) \tag{1}$$

The restoration of ψ_0 aims at the removal of ξ from ψ_0 to obtain an image as similar as possible to ψ_{ori} of (1).

The Perona-Malik restoration approach of ψ_0 is equivalent to an iterative minimisation problem [6], solved by the resolution of the partial differential equation (PDE) given by:

$$\frac{\partial\psi(x,y,t)}{\partial t} = div(g(|\nabla\psi(x,y,t)|)\nabla\psi(x,y,t)), \quad \psi(x,y,t=0) = \psi_0 \tag{2}$$

where $g(.)$ is a nonlinear decreasing function of the gradient (∇) of ψ the restored image at a scale t (which can be interpreted as a time evolution parameter) and *div* is the divergence operator. For practical numerical implementation, the process of (2) is discretised with a time step τ. The images $\psi(t_n)$ are calculated, with (2), at discrete instant $t_n = n\tau$ with n the number of iterations in the process. We now compare the standard Perona-Malik process of (2) with the following diffusion process

$$\frac{\partial\psi(x,y,t)}{\partial t} = div(g_\eta(|\nabla\psi(x,y,t)|)\nabla\psi(x,y,t)) \tag{3}$$

in which the nonlinear function $g(.)$ in (2) has been replaced by $g_\eta(.)$ with

$$g_\eta(u(x,y)) = \frac{1}{M}\sum_{i=1}^{M} g(u(x,y) + \eta_i(x,y)) \tag{4}$$

where η_i functions are M independent noises assumed independent and identically distributed with probability density function (PDF) f_η and RMS amplitude σ_η. The noises η_i which are purposely added noises applied to influence the operation of the $g(.)$ have to be clearly distinguished from the input noise ξ of (1), which is considered as a noise imposed by the external environment that we wish to remove. The choice of g_η in (4) is inspired by recent studies on the constructive action of noise in parallel arrays of nonlinear electronic devices [7] and transposed here in the domain of image processing. The quality of the restored image $\psi(t_n)$ at a given instant t_n is assessed by the normalised cross-covariance $C_{\psi ori\psi(t_n)}$ given by:

$$C_{\psi ori\psi(t_n)} = \frac{\langle(\psi_{ori} - \langle\psi_{ori}\rangle)(\psi(t_n) - \langle\psi(t_n)\rangle)\rangle}{\sqrt{\langle(\psi_{ori} - \langle\psi_{ori}\rangle)^2\rangle\langle(\psi(t_n) - \langle\psi(t_n)\rangle)^2\rangle}} \tag{5}$$

where $\langle..\rangle$ denotes the spatial average.

Results: For illustration of the processes of (2) and (3), the image 'cameraman' (see image *a* in Fig. 2), which presents strong and small gradients, textured and non-textured regions of interest, has been taken as the reference image in this study.

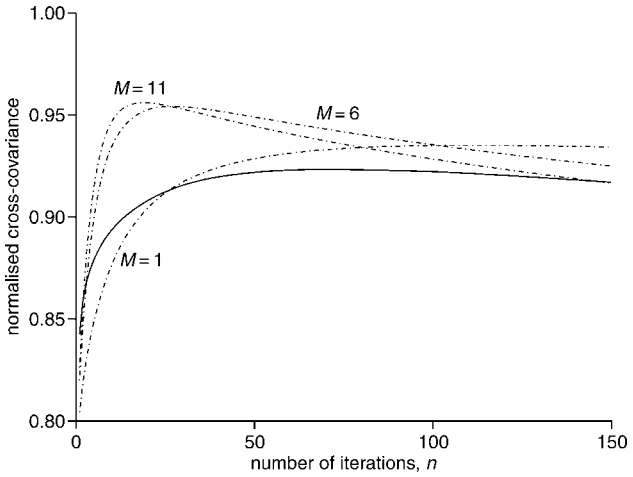

Fig. 1 *Normalised cross-covariance of (5) against iteration number n of restoration process*

– · – · – our modified version of Perona-Malik process of (3) and (4) for various number M of independent noises η_i

——— classical Perona-Malik process of (2)

RMS amplitude σ_η of M noises η_i fixed to $\sigma_\eta = 0.7$. Parameter k in nonlinear function $g(.)$ and step time τ, characterising convergence speed of the diffusion process, fixed to $k = 0.2$ and $\tau = 0.25$ in both (2) and (3)

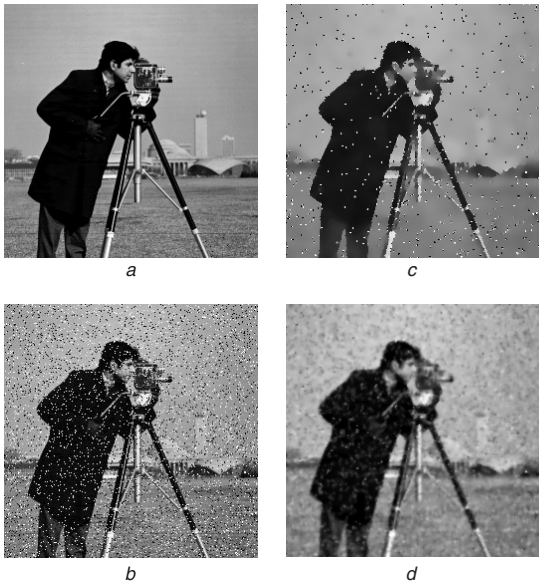

Fig. 2 *Visual comparison of performance of restoration processes by (2) and (3)*

a: original 'cameraman' image ψ_{ori} of (1). *b*: noisy version ψ_0 of ψ_{ori} corrupted by additive salt and pepper noise ξ (1) of standard deviation 0.1. *c* and *d* obtained with (2) and (3), respectively, for optimal number of iterations n corresponding to highest value of normalised cross-covariance in Fig. 1 ($M = 11$ in the case of *d*)

The original nonlinear function $g(.)$ proposed by Perona-Malik in [3], with $g(u(x,y)) = e^{-u(x,y)/k^2}$, is chosen in this study. The PDF f_η of the M

noises η_i in (3) are chosen Gaussian. Other measures of similarity (like the peak-signal-to-noise ratio), images and PDF for η_i have been tested. Results were quantitatively and qualitatively similar to the ones presented below. In Fig. 1, the similarity between the restored and original image, assessed by the normalised cross-covariance of (5), surpasses the classical Perona-Malik process for all values tested for M. This demonstrates the possibility of improving the performance of the Perona-Malik process by injecting a nonzero amount of the M noises η_i in (4). Moreover, in Fig. 1, one can also notice that the convergence speed of the diffusion process is increased with the presence of the M noises η_i. This acceleration of the convergence is another benefit shown in Fig. 1, which is also perceptible within the images themselves (Fig. 2). The addition of noise leads to a better contrast and a better preservation of the structure, which are characterised by small gradient (e.g. the buildings in the background are more visible and the texture of the grass is preserved by comparison with the classical Perona-Malik process). In Fig. 3, the number of iterations n of the diffusion processes of (3) and (4) is fixed. The normalised cross-covariance of (5) culminates at a maximum for an optimal nonzero noise level of the M noises injected in (4). This clearly demonstrates the possibility of a constructive role of noise in the diffusion process of (3) and (4) for an image restoration task.

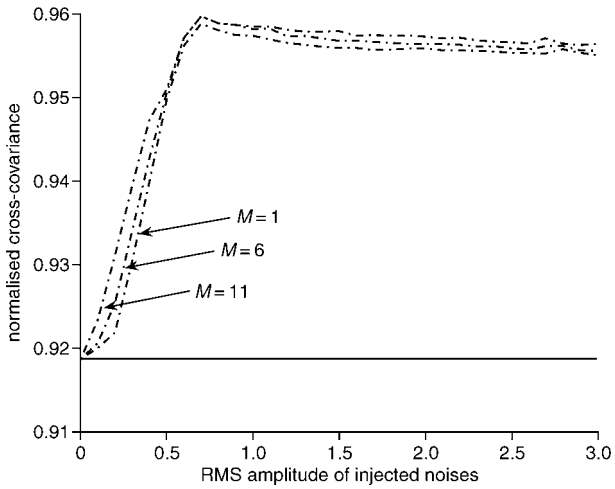

Fig. 3 *Normalised cross-covariance of (5) against RMS amplitude σ_η of noise purposely injected in (4)*

– · – · – our modified version of Perona-Malik process of (3) and (4) for various number M of independent noises η_i

——— classical Perona-Malik process of (2)

Number of iterations n fixed for all lines to $n = 75$

27 January 2006
Electronics Letters online no: 20060180
doi: 10.1049/el:20060180

A. Histace and D. Rousseau (*Laboratoire d'Ingénierie des Systèmes Automatisées (LISA CNRS FRE 2656), 62 avenue Notre Dame du Lac, 49000 Angers, France*)

E-mail: aymeric.histace@univ-angers.fr

References

1 Boncelet, C.G.: 'Image noise models' *in* 'Bovik, A. (Ed.): 'Handbook of image and video processing' (Academic Press, New York, 2000)
2 Maheshwari, O., and Ebenezer, D.: 'Simultaneous removal of positive and negative impulses in images by using adaptive length recursive weighted median filter', *WSEAS Trans. Commun.*, 2005, **4**, (12), pp. 1350–1355
3 Perona, P., and Malik, J.: 'Scale-space and edge detection using anistropic diffusion', *IEEE Trans. Pattern Anal. Mach. Intell.*, 1990, **12**, (7), pp. 629–639
4 Catte, F., Coll, T., Lions, P., and Morel, J.: 'Image selective smoothing and edge detection by nonlinear diffusion', *SIAM J. Appl. Math.*, 1992, **29**, (1), pp. 182–193
5 Harmer, G.P., Davis, B.R., and Abbott, D.: 'A review of stochastic resonance: circuits and measurement', *IEEE Trans. Instrum. Meas.*, 2002, **51**, pp. 299–309
6 Komprobst, P., Deriche, R., and Aubert, G.: 'Image sequence analysis via partial differential equations', *J. Math. Imaging Vis.*, 1999, **11**, (1), pp. 5–26
7 Chapeau-Blondeau, F., and Rousseau, D.: 'Enhancement by noise in parallel arrays of sensors with power-law characteristics', *Phys. Rev. E*, 2004, **70**, pp. 060 101(R), 1–4

F. CHAPEAU-BLONDEAU, D. ROUSSEAU, The minimum description length principle for probability density estimation by regular histograms, *Physica A*, vol. 388, 3969–3984, 2009.

Physica A 388 (2009) 3969–3984

Contents lists available at ScienceDirect

Physica A

journal homepage: www.elsevier.com/locate/physa

The minimum description length principle for probability density estimation by regular histograms

François Chapeau-Blondeau *, David Rousseau

Laboratoire d'Ingénierie des Systèmes Automatisés (LISA), Université d'Angers, 62 avenue Notre Dame du Lac, 49000 Angers, France

ARTICLE INFO

Article history:
Received 17 December 2008
Received in revised form 15 May 2009
Available online 16 June 2009

PACS:
05.45.Tp
05.40.-a

Keywords:
Statistical information processing
Data analysis
Random signal analysis
Probability density estimation
Minimum description length
Statistical information theory

ABSTRACT

The minimum description length principle is a general methodology for statistical modeling and inference that selects the best explanation for observed data as the one allowing the shortest description of them. Application of this principle to the important task of probability density estimation by histograms was previously proposed. We review this approach and provide additional illustrative examples and an application to real-world data, with a presentation emphasizing intuition and concrete arguments. We also consider alternative ways of measuring the description lengths, that can be found to be more suited in this context. We explicitly exhibit, analyze and compare, the complete forms of the description lengths with formulas involving the information entropy and redundancy of the data, and not given elsewhere. Histogram estimation as performed here naturally extends to multidimensional data, and offers for them flexible and optimal subquantization schemes. The framework can be very useful for modeling and reduction of complexity of observed data, based on a general principle from statistical information theory, and placed within a unifying informational perspective.

1. Introduction

In statistical information processing, probability density estimation is a ubiquitous and very useful process. For probability density estimation from observed data, a much common approach proceeds through the construction of an empirical histogram with regular (equal width) bins. When a fixed number of bins is imposed, the construction of a histogram is a rather straightforward operation. However, the number of bins in itself has a major impact on the quality of the estimation realized by the histogram for the underlying probability density. For a given number N of observed data points, if the number of bins is too small, the resolution of the histogram is poor and leads to a very raw estimate of the probability density. On the contrary, if the number of bins is too large, the counts of data points in the bins fluctuate strongly to yield a very jerky histogram as a poor estimate for the probability density. This points to an optimal number of bins between these two extremes that will lead to an optimal histogram for estimating the probability density. Any approach aiming at determining an optimal number of bins needs necessarily to rely on a definite criterion to measure optimality in this context with histograms. A specially interesting approach of this type is based on the principle of minimum description length.

The minimum description length (MDL) principle provides a general approach for statistical modeling and inference from observed data [1–3]. Briefly stated, this principle amounts to choosing for data, among a class of possible models, the model that allows the shortest description of the data. The MDL approach is rooted in the Kolmogorov theory of complexity [4]. Since its formal introduction some thirty years ago [5], the MDL principle has developed along both theoretical and practical directions. The theoretical foundations of the MDL principle have been investigated to great depth in statistics, and new theoretical aspects are still being explored [1,3,6]. At the same time, the MDL principle has been considered to provide solutions to a large variety of problems, including nonlinear time series modeling [7,8], Markov-

* Corresponding author.
E-mail address: chapeau@univ-angers.fr (F. Chapeau-Blondeau).

0378-4371/$ – see front matter © 2009 Elsevier B.V. All rights reserved.
doi:10.1016/j.physa.2009.05.044

process order estimation [9,10], data clustering [11,12], signal denoising [13,14], image segmentation [15,16], curve fitting [17,18], analysis of chaotic systems [19,20], genomic sequencing [21,22], neural networks [23,24]. Novel applications also are still emerging [6]. We believe that the MDL approach still holds many potentialities relevant to scientific investigation. A specifically interesting aspect is that the MDL principle offers a unifying thread for approaching many distinct tasks of signal and data processing that otherwise would stand as separate problems. Furthermore, the unified view which is provided is formulated as a information-theoretic framework, and this may be specially relevant to advance an information point of view in science [25–27].

Application of the MDL principle to probability density estimation by histograms was introduced in Ref. [28]. Part of the present paper consists in reviewing this approach of Ref. [28], and also in providing additional illustrative examples, through a presentation emphasizing intuitive and concrete arguments. Implementation of the MDL principle critically relies on definite specifications for measuring the description lengths. As another part of the present paper, we also consider alternative ways of measuring the description lengths, which differ from the choice made in Ref. [28], and which arguably can be found more suited in this context of probability density estimation by histograms. We also explicitly exhibit here the complete forms of the description lengths that arise from the various choices, through formulas involving the information entropy and redundancy of the data, and which are not given in other studies. And we analyze and compare these formulas for the description lengths. We also provide an application to measured data, in the line of a presentation emphasizing concrete and physical appreciation of the MDL approach. In this way, for a part the present paper has a pedagogical and illustrative intent as it proposes a detailed and illustrated review emphasizing concrete interpretations and intuition, on the MDL principle for probability density estimation by histograms. For another part, the paper provides additional results and insight with comparison of alternative choices and complementary analyses.

Minimum description length is often associated with another comparable approach identified as minimum stochastic complexity. These are two distinct, although related, approaches. In particular, stochastic complexity is usually based on the introduction, for the parameters of the model, of a specific prior probability distribution, upon which the subsequent results depend. A uniform prior can be used as in Ref. [28], or the so-called Jeffreys prior as in Ref. [3]. Both description length and stochastic complexity are examined in Ref. [28] for probability density estimation by histograms. Ref. [29] concentrates on stochastic complexity with uniform prior for probability density estimation by histograms. These two notions of description length and stochastic complexity can be defined as distinct notions, as it emerges from Refs. [28,29,3]. However, some other studies imply the terminologies "description length" and "stochastic complexity" as synonyms to designate a same underlying notion. Ref. [30] uses the terminologies "description length" and "stochastic complexity" essentially as synonymous, although there is a single underlying notion which is description length as we understand it here, and not stochastic complexity as in Refs. [28,29,3]. Ref. [30] provides detailed mathematical proofs concerning asymptotic properties and a general theoretical bound, through the introduction of an index of resolvability, for the statistical accuracy and efficacy of probability density estimation by any type of estimators, not necessarily histograms. Further refinements and improvements on these theoretical properties are given in Ref. [31]. Two asymptotic theorems are also proved in Ref. [28], and two theorems concerning upper bounds are established in Ref. [29]. Ref. [32] confronts, for histogram estimation, several forms of penalized maximum-likelihood methods that include the MDL and stochastic complexity based approaches of Ref. [28]. Refs. [33,34] present another form of MDL for histogram density estimation, as they define stochastic complexity by means of the notion of normalized maximum likelihood to avoid a specific prior and in order to obtain a minimax optimality, and then complement this stochastic complexity by a measure of the description length of the parameters to form the criterion to be minimized. In our present paper, for probability density estimation by histograms, we concentrate on the minimum description length, as in Ref. [28] and Ref. [30], and not on the minimum stochastic complexity as considered in Refs. [28,29] with uniform prior, or in Ref. [3] with Jeffreys' prior, or in Refs. [33,34] via normalized maximum likelihood. We see this minimum description length endowed with the advantage of a simple and concrete informational interpretation which is not shared by the minimum stochastic complexity. We review, illustrate and complement the MDL approach here. So far, MDL for probability density estimation by histograms has mainly been discussed in the literature connected to information theory and statistics. Formal proofs have been established for important mathematical properties of the approach. As a complement, we propose here to discuss the MDL methodology in a more physically-oriented presentation, leaning on concrete intuition and illustrative examples. Such a relation between information theory and statistical physics seems interesting to us to promote for the potentialities of mutual enrichment, as for instance illustrated by the recent studies of Refs. [35–38].

2. A histogram model for probability density

One disposes of N observed data points x_n forming the data set

$$\mathbf{x} = \{x_n, n = 1, \ldots N\}. \tag{1}$$

These N data points x_n are assumed to be N independent realizations of a random variable X distributed according to the probability density function $f(x)$. The probability $P(\mathbf{x})$ of observing a given data set $\mathbf{x}$ is therefore expressible as

$$P(\mathbf{x}) = \mathrm{d}x^N \prod_{n=1}^{N} f(x_n), \tag{2}$$

where dx measures the infinitesimal domain of reference around x_n.

One seeks to estimate the probability density $f(x)$ from the N data points x_n of Eq. (1). For this purpose, a histogram model is introduced for the unknown density $f(x)$ under the common form of an approximation by a piecewise constant function. This histogram model is denoted $\mathcal{M}$ and is defined as follows. The density $f(x)$ is modeled by K constant plateaus of value f_k, for $k = 1$ to K, each of these plateaus being defined in the abscissa between $x_{\min}$ and $x_{\max}$ over a regular bin of width

$$\delta x = \frac{x_{\max} - x_{\min}}{K} = \frac{\Delta x}{K}, \tag{3}$$

with $x_{\min}$ and $x_{\max}$ respectively the minimum and maximum values of the x_n's over the data set $\mathbf{x}$ of Eq. (1). Especially, consistency of the probability density model imposes

$$\sum_{k=1}^{K} f_k \delta x = 1. \tag{4}$$

The probability $P(\mathbf{x})$ of Eq. (2), based on the histogram model $\mathcal{M}$ for the density $f(x)$, is expressible as

$$P(\mathbf{x}) = \mathrm{d}x^N \prod_{k=1}^{K} f_k^{N_k}, \tag{5}$$

where N_k is the number of data points x_n of the data set $\mathbf{x}$ that fall within bin number k, verifying $\sum_{k=1}^{K} N_k = N$.

3. Maximum-likelihood histogram estimation

When the number of bins K is fixed, the density model $\mathcal{M}$ is specified by the K parameters f_k for $k = 1$ to K. To determine these parameters from the data, a standard approach is the maximum-likelihood method [39] which consists in selecting those values of the parameters f_k that maximize the probability $P(\mathbf{x})$ in Eq. (5) of the observed data set $\mathbf{x}$. Maximizing $P(\mathbf{x})$ of Eq. (5) under the constraint of Eq. (4) is achieved by the well-known maximum-likelihood solution

$$\widehat{f}_k = \frac{N_k}{N\delta x}, \quad k = 1, \ldots K. \tag{6}$$

The maximum-likelihood solution of Eq. (6) completely specifies, for the probability density $f(x)$, the histogram model with a fixed number K of regular bins.

4. Minimum description length

Another point of view can be adopted to arrive at the solution of Eq. (6). Information theory stipulates that to code data x_n appearing with probability $P(x_n)$, the optimal code assigns a codeword with length $-\log P(x_n)$. To code the whole data set $\mathbf{x}$ of Eq. (1), the optimal code assigns a length $-\log P(\mathbf{x})$, which by the probability model of Eq. (5) is

$$L_{\text{data}} = -\log P(\mathbf{x}) = -\log(\mathrm{d}x^N) - \sum_{k=1}^{K} N_k \log(f_k). \tag{7}$$

The maximum-likelihood solution of Eq. (6) maximizes the likelihood $P(\mathbf{x})$ of Eq. (5) and equivalently the loglikelihood $\log P(\mathbf{x})$. Therefore, the solution of Eq. (6) also minimizes the code length $L_{\text{data}} = -\log P(\mathbf{x})$ of Eq. (7). The solution of Eq. (6) selects from the data, the K parameters f_k of the probability density model $\mathcal{M}$, so that the optimal code designed for the data from this density model, achieves the minimal code length. This is the rationale of the MDL principle: to select the parameters of the model that allow the shortest coding of the complete data. This guarantees that the selected model is the best (within its class) at capturing the structures and regularities in the data.

We can add here, that the minimum of the description length (7) achieved by the solution of Eq. (6) can be expressed as

$$L_{\min} = NH(\{\widehat{p}_k\}) - N\log(K) + N\log\left(\frac{\Delta x}{\mathrm{d}x}\right), \tag{8}$$

where we have introduced the entropy

$$H(\{\widehat{p}_k\}) = -\sum_{k=1}^{K} \widehat{p}_k \log(\widehat{p}_k) \tag{9}$$

of the empirical probabilities $\widehat{p}_k = \widehat{f}_k \delta x = N_k/N$ deduced from Eq. (6).

Here, when the number of bins K of the histogram model is fixed in an a priori way, the MDL solution coincides with the maximum-likelihood solution of Eq. (6). However, the MDL principle can be extended to also optimally select the number of bins K of the model from the data, along with the K parameter values f_k for $k = 1$ to K. This extension proceeds in the

following way. The complete coding of the data should here include two parts. The first part is the coding of the data based on a definite probability density model to assign the code lengths. For a given data set $\mathbf{x}$, the description length needed by this first part is L_{data} of Eq. (7), that we can also write $L_{\text{data}} \triangleq L(\mathbf{x}|\mathcal{M})$, the description length of the data given a definite model $\mathcal{M}$ of probability density. The second part needed for a complete coding of the data is the description of the parameters that completely specify the underlying probability density model $\mathcal{M}$. These parameters include the number of bins K along with the K values f_k for $k = 1$ to K. The description length needed by this second part in charge of coding the parameters of the model $\mathcal{M}$ is denoted $L_{\text{model}} \triangleq L(\mathcal{M})$; and we shall soon see how to explicitly quantify this description length $L(\mathcal{M})$. Now the complete coding of the data set $\mathbf{x}$ has a total description length L_{total} which sums up the two parts as

$$L_{\text{total}} \triangleq L(\mathbf{x}|\mathcal{M}) + L(\mathcal{M}), \tag{10}$$

signifying that the total description length of the data is the description length of the data given the model plus the description length of the model.

For a given data set $\mathbf{x}$, the MDL principle then dictates to select the model parameters $\{K; f_k, k = 1, \ldots K\}$ so as to minimize the total description length L_{total} of Eq. (10), i.e.

$$\{\widehat{K}; \widehat{f}_k, k = 1, \ldots \widehat{K}\} = \arg\min_{\{K;f_k\}} L_{\text{total}} = \arg\min_{\{K;f_k\}} [L(\mathbf{x}|\mathcal{M}) + L(\mathcal{M})]\,. \tag{11}$$

This is an optimization principle based on optimal coding and information theory. In a prescribed class of models (histograms with regular bins here), the best model for the data is the model that, when known, enables the most efficient (shortest) coding of these data.

5. Description length for the data

As already stated, the description length $L(\mathbf{x}|\mathcal{M})$ for the data given the model is supplied by Eq. (7). The term $-\log(\mathrm{d}x^N)$ in Eq. (7) is a constant common to all models. For the purpose of discriminating among models, it is often chosen to omit this constant $-\log(\mathrm{d}x^N)$ in the description length, with no impact on the final result concerning the model choice. However here, we prefer to maintain this term, in order to keep track of the complete value of the description length, and convey some additional insight into the modeling process beyond the choice of the model itself. So equivalently, the description length of Eq. (7) for the data given the model is written as

$$L(\mathbf{x}|\mathcal{M}) = -\sum_{k=1}^{K} N_k \log(f_k \mathrm{d}x). \tag{12}$$

Next, we have to address the quantification of the description length $L(\mathcal{M})$ for the model.

6. Description length for the model parameters as independent real variables

To quantify the description length $L(\mathcal{M})$ of the model, a possibility is to use a procedure derived from Ref. [28]. The approach from Ref. [28] to quantify the description length $L(\mathcal{M})$ of the model, considers the K model parameters f_k as K independent real (continuously-valued) variables, which need to be quantized to finite precision in order to allow their coding. The histogram model for the density of the data assigns a probability $p_k = f_k\delta x$ to bin k with width δx. Under this model also, the number N_k of data points falling in bin k has expected value $\mathrm{E}(N_k) = Np_k = Nf_k\delta x$ and standard deviation $\sigma(N_k) = [Nf_k\delta x(1-f_k\delta x)]^{1/2}$, according to the properties of the binomial distribution [40]. Therefore, since $f_k = \mathrm{E}(N_k)/(N\delta x)$, for all k, estimating f_k is equivalent to estimating the mean $\mathrm{E}(N_k)$ of random variable N_k with standard deviation $\sigma(N_k)$. The value $\sigma(f_k) = \sigma(N_k)/(N\delta x) = [f_k(1-f_k\delta x)/(N\delta x)]^{1/2}$ fixes a natural precision with which f_k can be estimated and need to be coded. This determines $\sigma(f_k)$ as the quantization step relevant for coding the model parameters f_k. One has the probability $p_k \in [0, 1]$ and the density $f_k = p_k\delta x^{-1} \in [0, \delta x^{-1}]$. The parameter f_k therefore can take its values in the interval $[0, \delta x^{-1}]$ and is estimated and quantized with the precision $\sigma(f_k)$. Accordingly, a total number $\delta x^{-1}/\sigma(f_k)$ of different values for f_k can be distinguished and need to be coded separately, at a code length $\log[\delta x^{-1}/\sigma(f_k)]$. For the K parameters f_k the code length results as

$$L(\{f_k\}) = \sum_{k=1}^{K} \log\left[\frac{\delta x^{-1}}{\sigma(f_k)}\right] = \frac{K}{2}\log(N) - \frac{1}{2}\sum_{k=1}^{K} \log[f_k\delta x(1 - f_k\delta x)]. \tag{13}$$

An alternative, comparable, approach to quantify the cost of coding continuously-valued parameters is described in Ref. [1], based on a slightly more involved mathematical formulation. It turns out that quantifying the coding cost of continuously-valued model parameters is an important and recurrent step when applying the MDL principle. We review this alternative approach from Ref. [1] in the Appendix, for better appreciation of different existing variants for applying the MDL principle. With the present approach derived from Ref. [28] and proceeding through Eq. (13), the description length

for the model is $L(\mathcal{M}) = L(\{f_k\})$, which is then added to the description of the data given the model $L(\mathbf{x}|\mathcal{M})$ of Eq. (12). The total description length $L_{\text{total}} = L(\mathbf{x}|\mathcal{M}) + L(\mathcal{M})$ of Eq. (10) then results as

$$L_{\text{total}} = -\sum_{k=1}^{K}\left(N_k \log(f_k \mathrm{d}x) + \frac{1}{2}\log[f_k\delta x(1-f_k\delta x)]\right) + \frac{K}{2}\log(N). \tag{14}$$

The model parameters $\{K; f_k\}$ are then determined by minimizing the total length L_{total} of Eq. (14), under the constraint of Eq. (4). To simplify this minimization, it is possible to use an approximation as in Ref. [28]. In Eq. (14), the quantity $f_k\delta x$ is the probability p_k of bin k under the histogram model of the probability density. The number of bins K can often be expected to be sufficiently large to assume this probability $f_k\delta x \ll 1$, authorizing the approximation

$$\log(1-f_k\delta x) \approx -f_k\delta x. \tag{15}$$

Under this approximation, the code length of Eq. (13) for the model parameters reduces to (in nats)

$$L(\{f_k\}) = \frac{K}{2}\log(N) + \frac{1}{2} - \frac{1}{2}\sum_{k=1}^{K}\log(f_k\delta x), \tag{16}$$

and the minimization of L_{total} of Eq. (14) can be performed in two steps. First, at given K, the solution for the f_k's realizing, under the constraint of Eq. (4), the minimum of L_{total}, is accessible in closed form as

$$\widehat{f}_k = \frac{N_k + 1/2}{N + K/2}\frac{1}{\delta x}, \quad k = 1, \ldots K. \tag{17}$$

Then, when the $\widehat{f}_k$'s of Eq. (17) are plugged back into L_{total} of Eq. (14), one obtains

$$\begin{aligned} L_{\text{total}} = &-\sum_{k=1}^{K}\left[\left(N_k+\frac{1}{2}\right)\log\left(N_k+\frac{1}{2}\right) + \frac{1}{2}\log\left(1-\frac{N_k+1/2}{N+K/2}\right)\right] \\ &+\left(N+\frac{K}{2}\right)\log\left(N+\frac{K}{2}\right) + \frac{K}{2}\log(N) - N\log(K) + N\log\left(\frac{\Delta x}{\mathrm{d}x}\right). \end{aligned} \tag{18}$$

A useful equivalent expression of Eq. (18) is

$$L_{\text{total}} = \left(N+\frac{K}{2}\right)H(\{\widehat{p}_k\}) - \frac{1}{2}\sum_{k=1}^{K}\log\left(1-\frac{N_k+1/2}{N+K/2}\right) + \frac{K}{2}\log(N) - N\log(K) + N\log\left(\frac{\Delta x}{\mathrm{d}x}\right), \tag{19}$$

where the entropy $H(\cdot)$ as in Eq. (9) is with the empirical probabilities $\widehat{p}_k = \widehat{f}_k\delta x = (N_k + 1/2)/(N + K/2)$ deduced from Eq. (17). Moreover, in the conditions of the approximation of Eq. (15), the sum over k in Eq. (19) evaluates to -1 nat, so as to yield for Eq. (19),

$$L_{\text{total}} = \left(N+\frac{K}{2}\right)H(\{\widehat{p}_k\}) + \frac{1}{2} + \frac{K}{2}\log(N) - N\log(K) + N\log\left(\frac{\Delta x}{\mathrm{d}x}\right). \tag{20}$$

Eq. (18), or Eq. (19) or (20), defines a function $L_{\text{total}} = L_{\text{total}}(K)$ of the sole (unknown) variable K, whose minimum can be numerically found to determine the minimizer $\widehat{K}$. Together this $\widehat{K}$ and the $\widehat{f}_k$'s of Eq. (17) form the minimum description length solution to the density estimation problem according to the approach proposed in Ref. [28]. It is to be noted that Ref. [28] rather chooses to estimate the bin probabilities p_k rather than the density values f_k as we do in this Section 6, and so the specific formulas may differ between both places; but the philosophy is the same, as far as we understand it in Ref. [28].

An important aspect should be emphasized concerning the approach of this Section 6 to quantify the description length $L(\mathcal{M})$ of the model. The approach codes the model parameters f_k, for $k = 1$ to K, as if they were independent and real (continuously-valued) parameters. Because of the constraint of Eq. (4), the parameters f_k are not independent. Furthermore, any effective estimation of the f_k's will be performed from the integers N_k, which form a minimal sufficient statistic here. Since the K nonnegative integers N_k sum to N, there are only a finite number of feasible configurations for the N_k's, and accordingly only a finite number of possible values for the f_k's (instead of a continuum of values as would suggest their being considered as real variables). By taking these two features (dependency and discreteness) into account, a more efficient coding could be envisaged. Also, the coding of the model parameters in this Section 6 takes the form of a lossy coding, in connection with Eq. (13), based on the quantization at a finite precision $\sigma(f_k)$ of the f_k's treated as continuously-valued parameters. Instead, a lossless coding could be envisaged. This we address now, by considering another way of quantifying the description length $L(\mathcal{M})$ of the model.

7. Description length for the model with joint parameters

As in the previous Section 6, the aim is to code the parameter values f_k, for $k = 1$ to K, that instantiate the histogram model for the probability density of an observed data set $\mathbf{x}$ of Eq. (1). These f_k's to be coded are matched to the data set $\mathbf{x}$ and in actuality are estimated from this data set $\mathbf{x}$. Any effective estimation of the f_k's from $\mathbf{x}$ must be based on the counts N_k of data points per bin, which form a minimal sufficient statistic here. Therefore, coding the model parameters f_k amounts to coding the integers N_k, for $k = 1$ to K. Each integer N_k can assume $N + 1$ distinct values, between 0 and N. As a simple proposal then, lossless coding of an N_k can be realized with a code length of $\log(N + 1)$. There are K of these integers N_k, however they always sum to N, so only $K - 1$ of them need be coded explicitly, the last one being recoverable since N is assumed known by the decoder (at a coding cost common to all models and not included in the description length $L(\mathbf{x})$). So the code length $L(\{f_k\})$ to code the K parameters f_k can be taken as

$$L(\{f_k\}) = (K - 1)\log(N + 1). \tag{21}$$

If one forms the description length of the model as $L(\mathcal{M}) = L(\{f_k\})$ and then adds it to the description $L(\mathbf{x}|\mathcal{M})$ of the data given the model in Eq. (12), the total description length $L_{\text{total}} = L(\mathbf{x}|\mathcal{M}) + L(\mathcal{M})$ of Eq. (10) follows as

$$L_{\text{total}} = -\sum_{k=1}^{K} N_k \log(f_k \mathrm{d}x) + (K - 1)\log(N + 1). \tag{22}$$

The minimization of Eq. (22) according to Eq. (11) can be solved (analytically) first for the f_k's, with the solution again given by Eq. (6), which is also

$$\widehat{f}_k = \frac{N_k K}{N \Delta x}, \quad k = 1, \ldots K. \tag{23}$$

When these $\widehat{f}_k$'s of Eq. (23) are plugged back into Eq. (22), one obtains the description length

$$L_{\text{total}} = NH(\{\widehat{p}_k\}) + (K - 1)\log(N + 1) - N\log(K) + N\log\left(\frac{\Delta x}{\mathrm{d}x}\right), \tag{24}$$

with the probabilities $\widehat{p}_k = N_k/N$ deduced from Eq. (23) used in the entropy $H(\cdot)$ of Eq. (9). Eq. (24) is seen as a function $L_{\text{total}}(K)$ of K alone, to be minimized (numerically) to obtain the minimizer $\widehat{K}$. This $\widehat{K}$ together with the $\widehat{f}_k$'s of Eq. (23) provide a complete solution to the problem of optimal probability density estimation by a histogram with regular bins.

It is possible to suggest an improvement for the code length $L(\{f_k\})$ of Eq. (21) for the K parameters f_k. Eq. (21) is based on a separate coding of $K - 1$ values of N_k, but it does not fully exploit the dependence between the N_k's. The fact that the N_k's sum to N, for instance restrains configurations with several N_k's simultaneously close to N. Because of the dependence of the N_k's a global coding of the K values N_k can be achieved, which is more efficient than a separate coding. For K integers N_k ranging between 0 and N and verifying $\sum_{k=1}^{K} N_k = N$, there is a number $A_{N,K}$ of distinct possible configurations given by Ref. [40, p. 38] as

$$A_{N,K} = \frac{(N + K - 1)!}{N!(K - 1)!}. \tag{25}$$

Then, a lossless coding of the K values N_k is feasible by coding one among the $A_{N,K}$ distinct possible configurations. This is achievable with a code length of $\log(A_{N,K})$, leading to the replacement of Eq. (21) by

$$L(\{f_k\}) = \log(A_{N,K}) = \log\left[\frac{(N + K - 1)!}{N!(K - 1)!}\right], \tag{26}$$

which can be verified to be indeed a more efficient (shorter) code length than Eq. (21).

With this description length $L(\{f_k\}) = L(\mathcal{M})$ for the model, added to the description length $L(\mathbf{x}|\mathcal{M})$ of the data given the model in Eq. (12), one obtains the total description length $L_{\text{total}} = L(\mathbf{x}|\mathcal{M}) + L(\mathcal{M})$ of Eq. (10) as

$$L_{\text{total}} = -\sum_{k=1}^{K} N_k \log(f_k\, \mathrm{d}x) + \log(A_{N,K}). \tag{27}$$

At fixed K, the description length L_{total} of Eq. (27) is again minimized by the f_k's given in Eq. (23). When these values are plugged back into L_{total} of Eq. (27), one obtains a total length expressible as

$$L_{\text{total}} = NH(\{\widehat{p}_k\}) + \log(A_{N,K}) - N\log(K) + N\log\left(\frac{\Delta x}{\mathrm{d}x}\right), \tag{28}$$

with again the probabilities $\widehat{p}_k = N_k/N$ deduced from Eq. (23) used in the entropy $H(\cdot)$ of Eq. (9). Eq. (28) is seen as a function $L_{\text{total}}(K)$ of K alone, to be minimized to obtain the minimizer $\widehat{K}$, this providing, in conjunction with the $\widehat{f}_k$'s of Eq. (23), a complete solution to the problem of optimal probability density estimation by a histogram with regular bins.

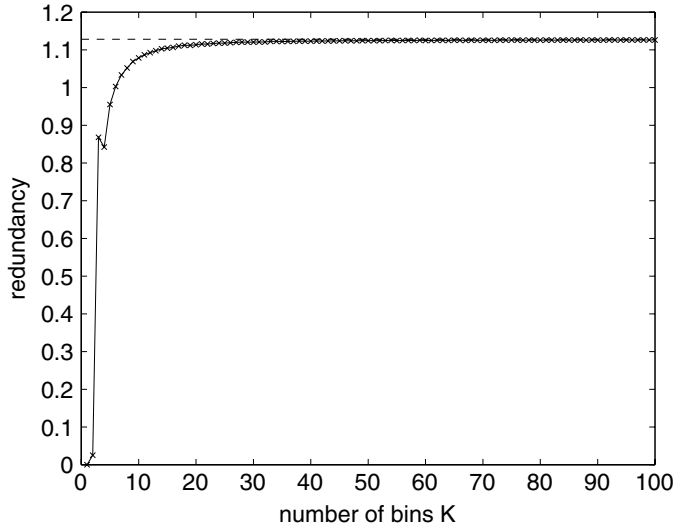

Fig. 1. Redundancy $H_{\max}(K) - H(\{\widehat{p}_k\})$ in bits of the data represented over K bins, as a function of the number of bins K. The data set is formed by $N = 10^5$ points x_n drawn from a Gaussian probability density $f(\cdot)$ with standard deviation $\sigma = \Delta x/9$. The dashed line is the saturation level $\log(\Delta x) - H_{\text{diff}}[f]$ which for the Gaussian density here is $\log[(2\pi\,\mathrm{e})^{-1/2}\,\Delta x/\sigma]$.

8. Analysis of the total description lengths

It is now interesting to analyze and compare the various total description lengths L_{total} obtained with the different possible coding strategies, and which are provided by Eqs. (8), (20), (24) and (28). These total lengths show in common a term $N\log(\Delta x/\mathrm{d}x)$. In this term, $\mathrm{d}x$ is the precision or resolution with which the data points x_n are measured or defined, while Δx is the total range over which the data points x_n take their values. For instance, a typical situation could be data represented with 16 binary digits, for which $\Delta x/\mathrm{d}x = 2^{16}$. This amounts to $N\log(\Delta x/\mathrm{d}x) = 16N$ bits which represents the description length associated with direct fixed-length coding of the N data points, with no attempt of optimizing the coding based on a probability model for the data. This common term can thus be understood as the initial description length L_{initial} prior to any optimized coding:

$$L_{\text{initial}} = N\log\left(\frac{\Delta x}{\mathrm{d}x}\right). \tag{29}$$

In the total description lengths, another common term is $N\log(K)$. With K bins to distribute the data points, $\log(K)$ can be interpreted as the maximum entropy $H_{\max}(K) = \log(K)$ achieved with uniform probability over the K bins. In these conditions, the total description length of Eq. (8) takes the form

$$L_{\text{total}} \equiv L_1 = L_{\text{initial}} - N[H_{\max}(K) - H(\{\widehat{p}_k\})]. \tag{30}$$

We recall that this total length L_1 of Eq. (30), is the optimal coding length $L(\mathbf{x}|\mathcal{M}) = -\log P(\mathbf{x}|\mathcal{M})$ for the data set $\mathbf{x}$ based on the histogram model $\mathcal{M}$ of probability density, but when we omit to include any coding cost $L(\mathcal{M})$ for the model itself. In Eq. (30), $H(\{\widehat{p}_k\})$ is the entropy of the empirical probability distribution $\{\widehat{p}_k\}$ estimated from the data over the K bins. It cannot be above the maximum entropy $H_{\max}(K)$, so that in Eq. (30) the difference $H_{\max}(K) - H(\{\widehat{p}_k\})$ is nonnegative, and it measures the information redundancy of the data represented over K bins. The nonnegative redundancy usually expresses in Eq. (30), a reduction of the initial coding length L_{initial} which is afforded by nonuniform (variable-length) coding based on a probability model for the data. This reduction is possible except when the data are distributed with uniform probability, in which case the empirical entropy $H(\{\widehat{p}_k\})$ matches the maximum entropy $H_{\max}(K)$, the redundancy vanishes and no gain on L_{initial} is achieved in Eq. (30) because the uniform (fixed-length) coding in L_{initial} already corresponds to the optimal coding. On the contrary, if the departure of the data from uniform probability is strong, then $H(\{\widehat{p}_k\})$ is much less than $H_{\max}(K)$, the nonnegative redundancy $H_{\max}(K) - H(\{\widehat{p}_k\})$ is large, and a large reduction on L_{initial} is accessible in Eq. (30).

Also in Eq. (30), when the number of bins K is increased, entropy $H_{\max}(K) = \log(K)$ increases as well; in addition, provided K grows while adhering to $K \ll N$, the empirical entropy $H(\{\widehat{p}_k\})$ usually increases as a consequence of this increased resolution K. Moreover, the redundancy $H_{\max}(K) - H(\{\widehat{p}_k\})$ usually also increases with K. This redundancy grows from 0 at $K = 1$ to $\log(\Delta x) - H_{\text{diff}}[f]$ at large K, where $H_{\text{diff}}[f] = -\int f\log f$ is the differential entropy associated with the probability density $f(\cdot)$ of the data. A typical evolution with K of the redundancy $H_{\max}(K) - H(\{\widehat{p}_k\})$ is shown in Fig. 1 when $f(\cdot)$ is a Gaussian density. With $H_{\max}(K) - H(\{\widehat{p}_k\})$ an increasing function of K, the coding length L_1 in Eq. (30) decreases with K, since L_{initial} is invariant with K. Larger K implies higher accuracy in modeling the probabilities of the data, which in turn implies more efficiency in the nonuniform coding based on these probabilities; whence the decreasing coding length L_1 in Eq. (30) as K grows.

However, complete coding of the data, as understood by the MDL principle, implies to count also the coding cost $L(\mathcal{M})$ of the model. This is achieved by the total lengths in Eqs. (20), (24) and (28), yet with different ways of quantifying $L(\mathcal{M})$. Eq. (24) results from a simple yet exact (lossless) coding of the model parameters $\{f_k\}$ according to Eq. (21). The resulting total description length of Eq. (24) can be expressed as

$$L_{\text{total}} \equiv L_3 = L_{\text{initial}} + L_{\text{model}} - N[H_{\max}(K) - H(\{\widehat{p}_k\})], \tag{31}$$

with $L_{\text{model}} = L(\mathcal{M})$ the coding length for the model, which here, from Eq. (21), is

$$L_{\text{model}} = (K-1)\log(N+1). \tag{32}$$

Eq. (28) results from a more efficient lossless coding of the model parameters $\{f_k\}$ according to Eq. (26). The resulting total description length of Eq. (28) can be expressed in a similar form

$$L_{\text{total}} \equiv L_4 = L_{\text{initial}} + L_{\text{model}} - N[H_{\max}(K) - H(\{\widehat{p}_k\})], \tag{33}$$

with now for the model, from Eq. (26),

$$L_{\text{model}} = \log(A_{N,K}). \tag{34}$$

Eq. (20) results from an approximate (lossy) coding of the model parameters $\{f_k\}$ treated as independent real variables quantized to a finite precision. The resulting total description length of Eq. (20) can also be expressed in a rather similar form as

$$L_{\text{total}} \equiv L_2 = L_{\text{initial}} + L_{\text{model}} - \left[NH_{\max}(K) - \left(N + \frac{K}{2}\right) H(\{\widehat{p}_k\})\right], \tag{35}$$

with now for the model, from Eq. (20),

$$L_{\text{model}} = \frac{1}{2} + \frac{K}{2}\log(N). \tag{36}$$

The total description lengths L_{total} of Eqs. (31), (33) and (35) are similar in form with Eq. (30) yet with the visible difference that they explicitly include the coding cost L_{model} of the model, measured in one form or another according to Eqs. (32), (34) and (36). In each case, the final step to the histogram estimation problem rests in solving

$$\widehat{K} = \arg\min_K L_{\text{total}}(K). \tag{37}$$

The total description lengths L_{total} of Eqs. (31), (33) and (35) have in common to include the initial data length L_{initial} which is independent of K, plus the model length L_{model} which usually increases with the number K of model parameters, minus the redundancy which usually is an increasing function of K (see Fig. 1). $L_{\text{total}}(K)$ is then usually formed by an increasing function of K (i.e. $L_{\text{initial}} + L_{\text{model}}$) plus a decreasing function of K (minus the redundancy). One expects then to have a unique minimum and minimizer $\widehat{K}$ for $L_{\text{total}}(K)$ in Eq. (37). This is at least the expected, overall behavior, for a typical data set. In practice, local fluctuations of the estimated empirical entropy $H(\{\widehat{p}_k\})$ can induce small local increase of minus the redundancy with K, as visible in the figures of Section 9. But this does not affect the methodology for solving the problem of histogram estimation.

Before explicitly solving the problem of Eq. (37) in several illustrative examples, it is interesting to compare the coding length L_{model} assigned to the model by the various coding strategies of Eqs. (32), (34) and (36). These three coding lengths are presented in Fig. 2 as a function of the model size K.

Fig. 2 illustrates the behavior that generally holds in the ranges of interest for N and K. In general, the coding length L_{model} from Eq. (36) is the shortest, as it is associated with a lossy coding of the K model parameters. The coding length L_{model} from Eq. (32) is the longest, as it is associated with a lossless coding of the K model parameters yet without taking full advantage of the dependence among these parameters. The coding length L_{model} from Eq. (34) is intermediate, as it is associated with a lossless coding of the K model parameters taking full advantage of the dependence among these parameters. Further insight can be obtained in the condition $1 \leq K \ll N$ which may frequently hold in practice; then the coding length of Eq. (36) becomes $L_{\text{model}} \approx (K/2)\log(N)$, while that of Eq. (32) becomes $L_{\text{model}} \approx (K-1)\log(N)$, and that of Eq. (34) becomes $L_{\text{model}} \approx (K-1)\log(N) - \log[(K-1)!]$. If in addition one considers the condition $1 \ll K \ll N$, Eq. (34) further gives $L_{\text{model}} \approx (K-1)[\log_b(N) - \log_b(K-1) + 1/\ln(b)]$, where b is the logarithm base. These approximate expressions for L_{model} are also shown in Fig. 2, while we keep in mind that it is the dependence in K of L_{model} at given N which is relevant to solve the problem of Eq. (37).

The model description length L_{model} is thus shorter with the lossy coding associated with the total length $L_{\text{total}} = L_2$ of Eq. (35), and by comparison the model description length L_{model} is longer with the lossless coding associated with the total length $L_{\text{total}} = L_4$ of Eq. (33) (and still even longer with $L_{\text{total}} = L_3$ of Eq. (31)).

The other term in the total description length L_{total} formed by minus the redundancy behaves in the opposite way. The entropy $H(\{\widehat{p}_k\})$ in Eqs. (31) and (33) is based on the empirical probabilities $\widehat{p}_k = N_k/N$, while in Eq. (35) entropy $H(\{\widehat{p}_k\})$ is based on the probabilities $\widehat{p}_k = (N_k + 0.5)/(N + K/2)$. In general, for a given set of counts $\{N_k\}$, the probability distribution $\{(N_k + 0.5)/(N + K/2)\}$ in Eq. (35) is closer to uniformity than the distribution $\{N_k/N\}$ in Eqs. (31) and (33). As a result, the entropy $H(\{\widehat{p}_k\})$ is closer to the maximum $H_{\max}(K)$ in Eq. (35) than in Eq. (33). The redundancy $NH_{\max}(K) - (N+K/2)H(\{\widehat{p}_k\})$

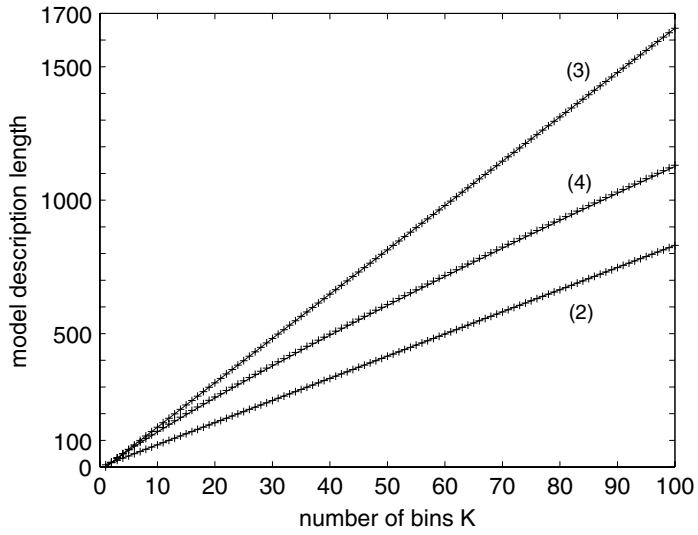

Fig. 2. Description length L_{model} in bits for coding the model, as a function of the number of bins K, for a data set with $N = 10^5$ points. Solid lines: (2) lossy coding of Eq. (36), (3) lossless coding of Eq. (32), (4) lossless coding of Eq. (34). Crosses (+): approximate expressions $L_{\text{model}} \approx (K/2)\log(N)$ for (2), $L_{\text{model}} \approx (K-1)\log(N)$ for (3), $L_{\text{model}} \approx (K-1)[\log_b(N) - \log_b(K-1) + 1/\ln(b)]$ for (4).

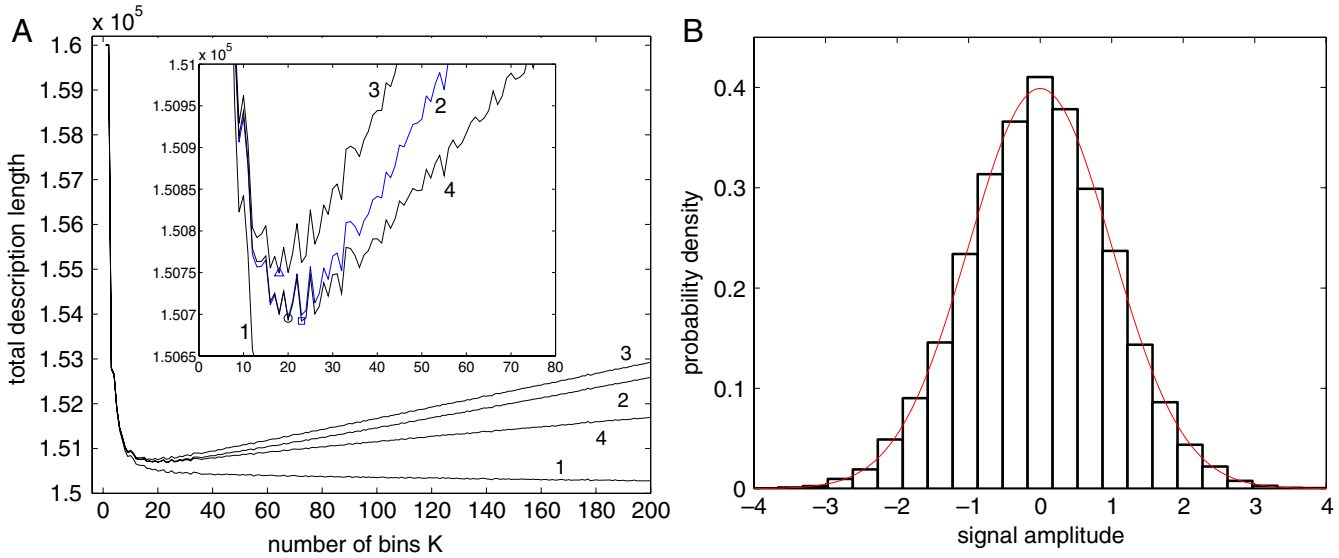

Fig. 3. Panel A: Total description length L_{total} in bits, as a function of the number of bins K, for a data set with $N = 10^4$ points, and $L_{\text{initial}} = 16N = 160\,000$ bits, drawn from probability density $f(\cdot)$ which is the Gaussian $\mathcal{N}(0, \sigma = 1)$ with zero mean and standard deviation $\sigma = 1$: (1) L_1 from Eq. (30) with no model coding, (2) L_2 from Eq. (35) with lossy coding of the model, (3) L_3 from Eq. (31) with lossless coding of the model, (4) L_4 from Eq. (33) with more efficient lossless coding of the model. The inset magnifies the region where the minimum of L_{total} is shown by marker (○): $(\widehat{K} = 20, L_2(\widehat{K}) = 150\,695$ bits), (△): $(\widehat{K} = 18, L_3(\widehat{K}) = 150\,749$ bits), (□): $(\widehat{K} = 23, L_4(\widehat{K}) = 150\,692$ bits). Panel B: Histogram model at the optimum number of bins $\widehat{K} = 23$ minimizing L_4 of Eq. (33), superimposed to the true Gaussian probability density $f(\cdot)$.

in Eq. (35) is therefore smaller than the redundancy $NH_{\max}(K) - NH(\{\widehat{p}_k\})$ in Eq. (33); the effect in this direction is even accentuated by the prefactor $(N + K/2)$ which is stronger in Eq. (35) than the prefactor N in Eq. (33), contributing to the smaller redundancy in Eq. (35).

To summarize, both the model length L_{model} and the redundancy increase with K and are smaller for the lossy coding of Eq. (35) than for the lossless codings of Eqs. (31) and (33). The difference of these two functions of K controls the total description length L_{total}, and one can expect well-defined minimum and minimizer $\widehat{K}$ for $L_{\text{total}}(K)$ in Eq. (37). We now explicitly solve the minimization of Eq. (37) in several illustrative examples.

9. Examples

As a first example, $N = 10^4$ data points x_n were drawn from the probability density $f(\cdot)$ taken as the Gaussian density $\mathcal{N}(0, \sigma = 1)$ with zero mean and standard deviation $\sigma = 1$. The total description length L_{total} has been computed according to the four strategies compared in Section 8, and is shown in Fig. 3A as a function of the number of bins K.

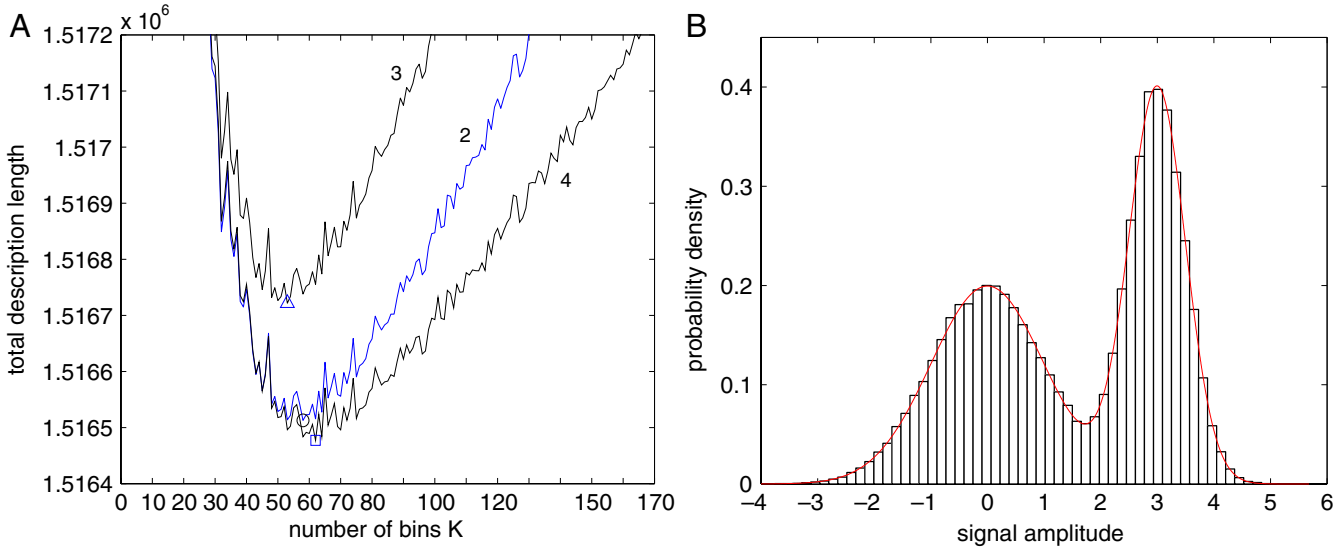

Fig. 4. Panel A: Total description length L_{total} in bits, as a function of the number of bins K, for a data set with $N = 10^5$ points, and $L_{\text{initial}} = 16N = 1\,600\,000$ bits, drawn from probability density $f(\cdot)$ which is the bi-Gaussian mixture $0.5\mathcal{N}(0, 1) + 0.5\mathcal{N}(3, 0.5)$: (2) L_2 from Eq. (35) with lossy coding of the model, (3) L_3 from Eq. (31) with lossless coding of the model, (4) L_4 from Eq. (33) with more efficient lossless coding of the model. The minimum of L_{total} is shown by marker (○): ($\widehat{K} = 58$, $L_2(\widehat{K}) = 1\,516\,513$ bits), (△): ($\widehat{K} = 53$, $L_3(\widehat{K}) = 1\,516\,722$ bits), (□): ($\widehat{K} = 62$, $L_4(\widehat{K}) = 1\,516\,477$ bits). Panel B: Histogram model at the optimum number of bins $\widehat{K} = 62$ minimizing L_4 of Eq. (33), superimposed to the true bi-Gaussian probability density $f(\cdot)$.

In Fig. 3A, the total description length L_1 from Eq. (30), steadily decreases with K, as announced, because L_1 does not incorporate the model description length. On the contrary in Fig. 3A, the total description lengths L_2, L_3 and L_4, which incorporate the model description length, exhibit a minimum for an optimal value of K. In Fig. 3A, the length L_3, which comes from a relatively poor coding strategy for the parameters, is, as a rule, always larger than the lengths L_2 and L_4. In the region of the minimum in Fig. 3A, the lengths L_2 and L_4, although they are based on distinct coding strategies, assume very close values. L_2 from Eq. (35) is based on a lossy approximate coding of the parameters: this provides a shorter code length for the parameters associated with a less accurate (longer) coding for the data. On the contrary, L_4 from Eq. (33) is based on an exact lossless coding of the parameters: this costs a longer code length for the parameters associated with a more accurate (shorter) coding for the data. These two complementary situations of L_2 and L_4 tend to compensate in the region of the minimum in Fig. 3A, to lead to close values of the total description length. However, there is a slight superiority of L_4 over L_2 in Fig. 3A, in the sense that L_4, at the optimal setting ($\widehat{K} = 23$, $L_4(\widehat{K}) = 150\,692$ bits), achieves a slightly shorter minimal total length $L_4(\widehat{K}) = 150\,692$ bits and at the same time a higher resolution in the histogram definition with an optimal number of bins $\widehat{K} = 23$. Fig. 3B shows the optimal histogram model estimated for the probability density $f(\cdot)$ of the data set, at $\widehat{K} = 23$.

A second example is presented in Fig. 4, for data points drawn from a Gaussian mixture density. A similar overall behavior is observed in Fig. 4 for the total description lengths L_2, L_3 and L_4 as in Fig. 3. The length L_3 is always larger, while L_2 and L_4 take close values in the region of the minimum. Also in Fig. 4, the shortest description length and at the same time the highest histogram resolution $\widehat{K}$, are achieved by L_4 at the optimal setting ($\widehat{K} = 62$, $L_4(\widehat{K}) = 1\,516\,477$ bits). This is a double benefit associated with L_4: shortest minimal code length and at the same time highest optimal resolution $\widehat{K}$. Although the length L_2 is close to L_4 in the region of the minimum, and both L_2 and L_4 fluctuate in these regions from one data set to another with same size N, this double benefit observed with L_4 in Fig. 4, was never exchanged between L_4 and L_2. This was the rule for all the configurations we tested, for all the densities in this Section 9.

We also tested probability densities that accept a very small number of regular bins for accurate estimation. For uniform densities for which a single bin is adequate, the estimation based on the total lengths L_2, L_3 and L_4, all generally yield the optimal number of bins $\widehat{K} = 1$, with in general the shortest code length afforded by $L_4(\widehat{K})$. Comparable conditions are presented in Fig. 5 with a density which is constant over two separate intervals of equal width, separated by an interval with zero probability.

As visible in Fig. 5, the total lengths L_2, L_3 and L_4, all yield the appropriate number of bins $\widehat{K} = 3$, while the shortest code length is afforded by $L_4(\widehat{K}) = 15\,434$ bits.

Fig. 6 presents the example of a density which is constant over two separate intervals of unequal widths, separated by an interval with zero probability. The total lengths L_2, L_3 and L_4, all yield the appropriate number of regular bins $\widehat{K} = 4$, while the shortest code length is afforded by $L_4(\widehat{K}) = 15\,531$ bits.

10. Application to measured data

This section presents an application of histogram estimation by MDL on measured data. The data x_n are formed by the intensities of gray-level images with size $N = 512 \times 512$ pixels. These intensities are initially measured over 256 levels,

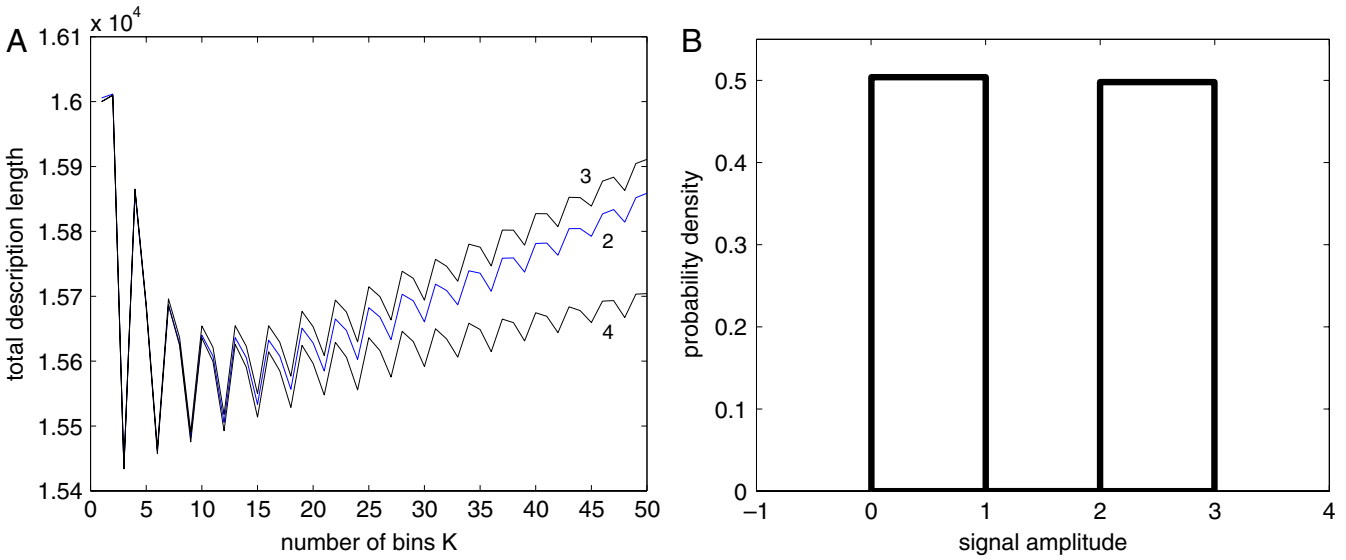

Fig. 5. Panel A: Total description length L_{total} in bits, as a function of the number of bins K, for a data set with $N = 10^3$ points, and $L_{\text{initial}} = 16N = 16\,000$ bits, drawn from probability density $f(\cdot) \sim 0.5\mathcal{U}([0, 1]) + 0.5\mathcal{U}([2, 3])$ which is the mixture of two uniform densities over $[0, 1]$ and $[2, 3]$: (2) L_2 from Eq. (35) with lossy coding of the model, (3) L_3 from Eq. (31) with lossless coding of the model, (4) L_4 from Eq. (33) with more efficient lossless coding of the model. The minimum of L_{total} is, for (2): ($\widehat{K} = 3$, $L_2(\widehat{K}) = 15\,438$ bits), for (3): ($\widehat{K} = 3$, $L_3(\widehat{K}) = 15\,435$ bits), for (4): ($\widehat{K} = 3$, $L_4(\widehat{K}) = 15\,434$ bits). Panel B: Histogram model at the optimum number of bins $\widehat{K} = 3$.

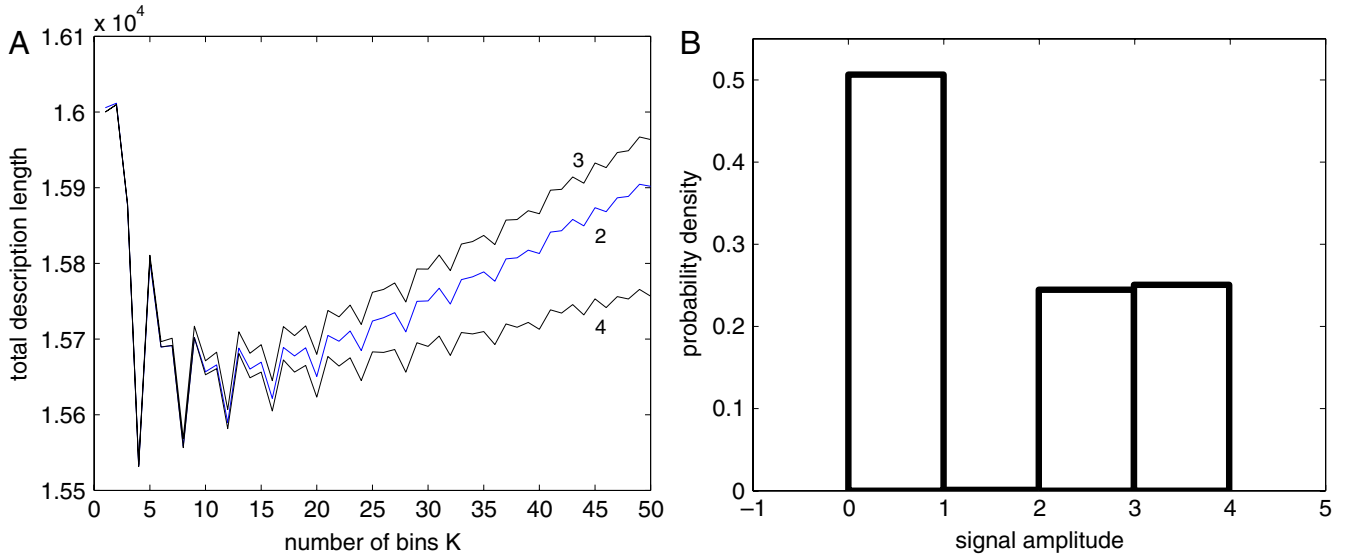

Fig. 6. Panel A: Total description length L_{total} in bits, as a function of the number of bins K, for a data set with $N = 10^3$ points, and $L_{\text{initial}} = 16N = 16\,000$ bits, drawn from probability density $f(\cdot) \sim 0.5\mathcal{U}([0, 1]) + 0.5\mathcal{U}([2, 4])$ which is the mixture of two uniform densities over $[0, 1]$ and $[2, 4]$: (2) L_2 from Eq. (35) with lossy coding of the model, (3) L_3 from Eq. (31) with lossless coding of the model, (4) L_4 from Eq. (33) with more efficient lossless coding of the model. The minimum of L_{total} is, for (2): ($\widehat{K} = 4$, $L_2(\widehat{K}) = 15\,532$ bits), for (3): ($\widehat{K} = 4$, $L_3(\widehat{K}) = 15\,534$ bits), for (4): ($\widehat{K} = 4$, $L_4(\widehat{K}) = 15\,531$ bits). Panel B: Histogram model at the optimum number of bins $\widehat{K} = 4$.

across a range from $x_{\min} = 0$ to $x_{\max} = 1$, with measurement resolution $dx = 1/256$. For two standard images, minimization of the description length $L_{\text{total}}(K)$ from Eq. (28) leads to the optimal MDL histograms shown in Fig. 7.

The results of Fig. 7 show that the optimal trade-off between accuracy and parsimony according to the MDL principle, is achieved by histograms that employ a number of bins $\widehat{K}$ which is less than the initial 256 levels over which the intensities are initially measured. These optimal values of $\widehat{K}$ derived from an information-theoretic principle, are also consistent with the qualitative appreciation resulting from visual inspection: Image "Lena" displays comparatively less variability and richness of details across the gray levels, and consistently can be adequately represented over a relatively small number $\widehat{K} = 83$ of levels. Meanwhile, image "Boats" displays more variability and richness of details across the gray levels, and consistently requires a larger number $\widehat{K} = 160$ of levels for adequate representation.

In addition, the optimal MDL histograms of Fig. 7 realize what can be viewed as an automatic subquantization of the intensities of the initial images. This subquantization is optimal in an information-theoretic sense expressed by MDL. At the same time, by visual inspection of the images at the optimal subquantization in Fig. 7, no essential features and details concerning the informational content of the images appear to be lost. We have here two properties simultaneously registered

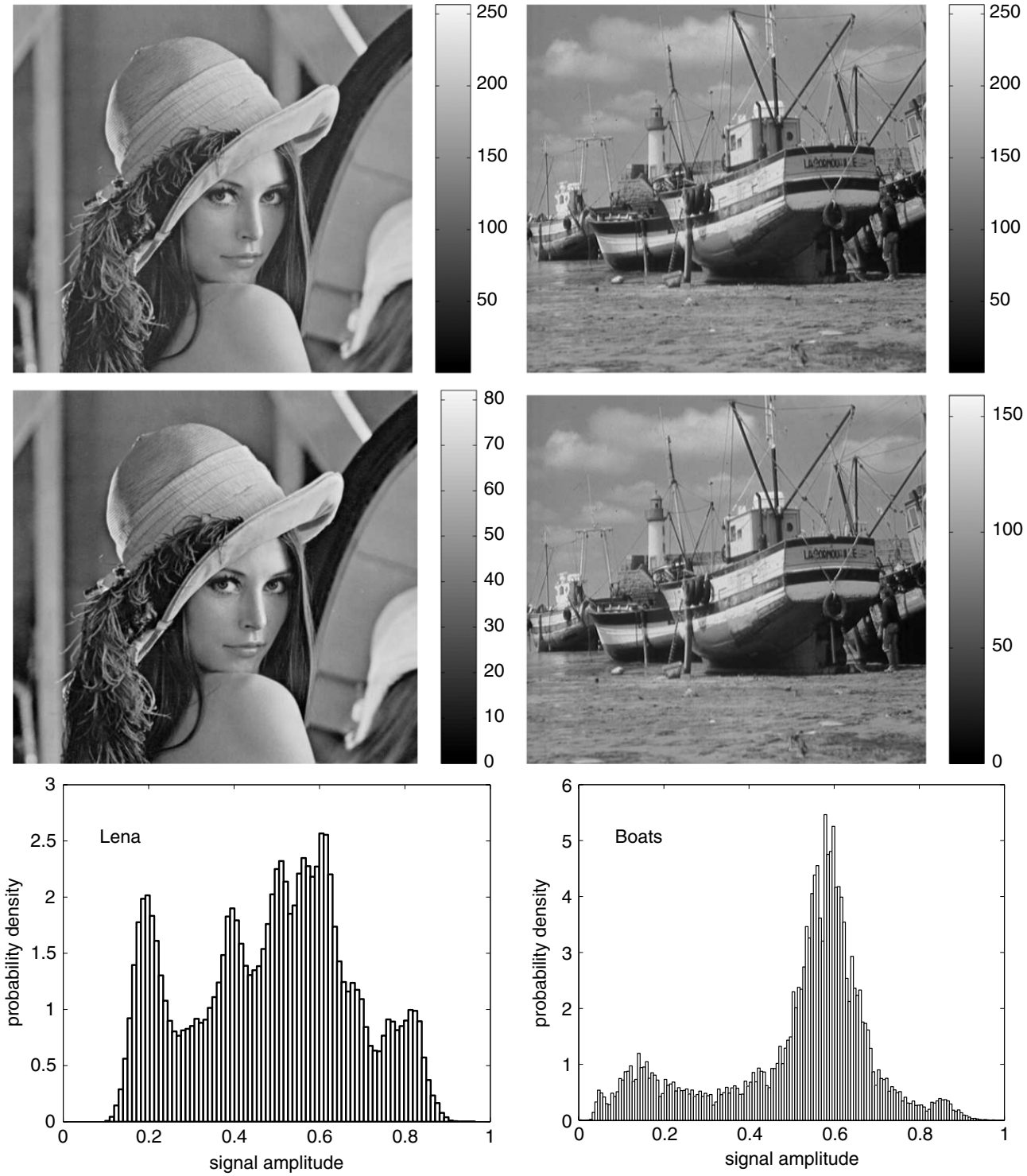

Fig. 7. Top row: Two gray-level images with size $N = 512 \times 512$ pixels initially measured over 256 levels of intensity. Middle row: Images subquantized over the optimal number of bins $\widehat{K}$ minimizing the description length $L_{\text{total}}(K)$ of Eq. (28): $\widehat{K} = 83$ (Lena), $\widehat{K} = 160$ (Boats). Bottom row: Optimal MDL histograms over the $\widehat{K}$ bins.

at two distinct levels (optimal MDL subquantization and visual perception). No connection is explicitly introduced by the MDL procedure between these two properties. However, their simultaneous occurrence could be a mark of some deeper connection originating in the fact that both properties have in common to relate to the informational content of the images.

11. Discussion

As we already mentioned, the approach of Section 6 is based on Ref. [28], and it treats the K model parameters as continuously-valued independent variables, which are approximated to a finite precision and coded separately through a

lossy coding. By contrast, the approach of Section 7 treats the K model parameters as discrete dependent variables, which are jointly coded through an exact lossless coding. These two distinct approaches are best represented by the total description lengths L_2 from Eq. (35) and L_4 from Eq. (33). It is remarkable to observe, based on the examples of Section 9, that these two distinct approaches lead nevertheless to results which are close for the optimal histogram models. This may be interpreted as a mark of robustness of the optimal solutions resulting from the MDL principle, which are not strongly affected by the specific ways used to describe or code the data, provided reasonable and efficient coding methods are confronted. This contributes to confirm that an essential significance of this principle is at a general informational level, and for a part it transcends the quantitative details of the descriptions. From the results of Section 9, a slight superiority though can be granted to the approach via L_4 of Eq. (33) when, for a shorter minimum description length, it affords at the same time a larger resolution of the histogram. There is however another important aspect relevant for a differentiated assessment of the two approaches.

A specificity of the approach from Ref. [28] and Section 6 is that it uses for the model parameters $\{f_k\}$, a code which is not decodable by the receiver. The reason is that this approach is based on a coding procedure, as described in Section 6, which arranges for each parameter f_k a code length which is dependent upon the value of this parameter, instantiated at $\widehat{f}_k$ from the data. This is expressed by the parameter code length of Eq. (13), or under Eq. (15), the approximation of Eq. (16), both bearing explicit dependence on the parameters $\{f_k\}$. The coder, as it knows the data, knows the parameter values $\widehat{f}_k$ estimated from the data, and can therefore arrange the code for these parameters, which is a variable-length code as implied by Eq. (13) or Eq. (16). The receiver receives first the coded parameters, and it needs to decode these parameters to be in a position then to decode the data coded with the variable-length coding based on the probability model specified by the decoded parameters. Therefore, when the coder uses for the parameters a code which depends on the values of these parameters as established by the data, the receiver is unable to decode the parameters since it does not know the data yet. Such a nondecodable coding procedure, however, can still be employed as a benchmark for probability density estimation: It provides a definite coding strategy for which the best achievable coding parsimony (minimum description length) serves to determine an optimal model for the probability density. The approach can thus be felt adequate, because the problem which is tackled at the root is the estimation of a probability density not the actual transmission of data to a putative receiver.

Yet, if the code for the complete data is decodable only by a receiver which already knows the data, one can feel that an adequate model for the data has not been obtained through the coding process. The alternative approach of Section 7 is not limited in this way. It provides a code for the complete data which is perfectly decodable by a receiver which knows nothing about the data. This is obtained based on a coding of the model parameters $\{f_k\}$, which is independent of the actual values of the parameters being coded, as expressed by the parameter code length of Eq. (26) or Eq. (21). In this respect, the approach based on L_4 of Eq. (33) can be preferred as a more appropriate way of applying the MDL principle to probability density estimation by regular histograms.

We add that in principle, the optimal value of $\widehat{K}$ selected by the MDL process should also be coded. This would incur a small additional cost to the total description length L_{total}. An estimate for the code length of $\widehat{K}$ is of order $\log(\widehat{K})$. This, as soon as the number N of data points is not too small, becomes negligible when compared to the parameters code length $L(\{f_k\})$ or the data code length $L(\mathbf{x}|\mathcal{M})$. As a consequence, this additional cost is not included here, with no sensible impact. Finally, for a thorough coding of the complete data set, a few additional informations may also need to be coded, like the number N of data points or the two limits $x_{\min}$ and $x_{\max}$ of the histogram. This would incur another small extra cost to the total description, but this cost is fixed and common to all models so it plays no role in the model selection and is therefore omitted in the MDL process.

The MDL principle for probability density estimation by histograms, can be extended in several directions. A possible direction can consider a wider model class of parametric histograms, consisting of nonregular histograms with a variable number K of bins of unequal widths δx_k, for $k = 1$ to K. At a general level the MDL principle still applies, with all the different widths δx_k which need to be coded at a cost to be included in the description length $L(\mathcal{M})$ of the model. The resulting total description length L_{total} then has to be minimized also as a function of the adjustable variables δx_k. In practice, this leads to a much more computationally demanding multivariate minimization process, in comparison to the approach with equal-width bins which ultimately requires only a minimization according to the single variable K according to Eq. (37). Nonregular histograms are considered in this way in Refs. [29,33,34].

In another direction, the MDL principle for histogram estimation, especially under the form of Section 7 and Eqs. (26)–(28), can be easily extended to histograms in higher dimensionality. For instance in three dimensions, a single data point x_n in Eq. (1) is replaced by a triplet coordinate (x_n, y_n, z_n) representing a joint realization of the random variables (X, Y, Z) distributed according to the three-dimensional probability density $f(x, y, z)$ that one seeks to estimate by a three-dimensional histogram. Each coordinate axis can be divided into, respectively, K_x, K_y and K_z bins with three distinct widths δx, δy and δz. The total number of bins (cells) in three dimensions is $K = K_x K_y K_z$. With this K, the code length for the K model parameters (the K constant values for the density over the K cells) is as before $L(\mathcal{M}) = \log(A_{N,K})$ as in Eq. (26). The total description length L_{total} is given by an expression similar to Eq. (28), controlled by an entropy $H(\{\widehat{p}_k\})$ which is now the entropy in three dimensions estimated from the empirical probabilities $\widehat{p}_k = N_k/N$ over the K three-dimensional cells. One then scans the bin numbers (K_x, K_y, K_z) and associated empirical entropy, searching for the minimum of L_{total} as in Eq. (28). The same process can be performed in arbitrary dimension D. Of course, the search process for the minimization of L_{total} will get more computationally demanding as the dimensionality D of the data space increases, but the principle of the method remains the same. Alternatively, all D coordinate axes can be divided into a unique similar number K_0 of bins, the same for

each axis, leading to a total number $K = K_0^D$ of cells in D dimensions. The search for the minimization of L_{total} is then now reduced to a one-dimensional search in K_0. A much simpler minimization process results, at the price of reduced resolution in the D-dimensional histograms. Other strategies can be envisaged to organize the division of the coordinate axes associated with the MDL criterion. In this same direction of multidimensional histograms with MDL, a recent study [41] introduces a new family of multidimensional histograms in the context of data mining for query answering. A local parametric model is employed to describe each multidimensional bin of the histogram, and local application of MDL is performed to optimize the parameterization. This approach of Ref. [41] is reminiscent of kernel methods, which form a different methodology for probability density estimation based on a definite choice of parametric kernel functions, and which although quite distinct from histograms, can also be handled with MDL for optimal parameterization. Beyond histogram estimation, such extensions of the MDL principle naturally offer, as suggested by the examples of Fig. 7, flexible and optimal subquantizations of multidimensional data based on an informational principle. This can be very useful for reduction of the complexity of multidimensional data sets, which are more and more pervasive in many areas of observational sciences, and with a control of the procedure obtained in an informational framework.

Appendix. Quantization of continuously-valued parameters

In this Appendix, we describe an alternative but comparable approach to Section 6, for quantifying the cost of coding continuously-valued model parameters, based on Ref. [1, p. 55]. The K model parameters f_k take their values in $[0, \delta x^{-1}]$. When considered as continuously-valued, each parameter f_k has to be quantized to a finite precision to make its coding possible. A quantization step or precision h_k is assumed for the quantization of parameter f_k, for $k = 1$ to K. It results in a total number $\delta x^{-1}/h_k$ of different values for f_k which can be distinguished and need to be coded separately, at a code length $\log(\delta x^{-1}/h_k)$. For the K parameters f_k the code length results as

$$L(\{f_k\}) = \sum_{k=1}^{K} \log\left(\frac{\delta x^{-1}}{h_k}\right) = K \log(\delta x^{-1}) - \sum_{k=1}^{K} \log(h_k). \tag{A.1}$$

Given the model parameters $\{f_k\}$, the data $\mathbf{x}$ are coded as in Eq. (7) at the cost $-\log P(\mathbf{x}|\{f_k\})$, which is added to the model cost of Eq. (A.1) to yield the total description length

$$L_{\text{total}}(\{f_k\}) = -\log P(\mathbf{x}|\{f_k\}) + L(\{f_k\}). \tag{A.2}$$

In Eq. (A.2), the f_k's that minimize $L_{\text{total}}(\{f_k\})$ also minimize $-\log P(\mathbf{x}|\{f_k\})$ and are given by the $\widehat{f_k}$'s of Eq. (6). This is so because in Eq. (A.2), the model code length $L(\{f_k\})$ does not (cannot) depend on the f_k's, since these are not known to the decoder. However, it is not the exact $\widehat{f_k}$'s of Eq. (6) which are used to code the data $\mathbf{x}$ at the minimum cost $-\log P(\mathbf{x}|\{\widehat{f_k}\})$. Instead, it is a set $\{f_k\}$, which is close to $\{\widehat{f_k}\}$, and which results from quantization of the $\widehat{f_k}$'s at the finite precisions h_k. This induces a total description length $L_{\text{total}}(\{f_k\})$ slightly longer than the minimum $L_{\text{total}}(\{\widehat{f_k}\})$. Since h_k measures the maximum deviation of f_k from $\widehat{f_k}$, the maximum of the overcost $L_{\text{total}}(\{f_k\})$ above $L_{\text{total}}(\{\widehat{f_k}\})$ can be obtained through the Taylor expansion

$$L_{\text{total}}(\{f_k\}) = -\log P(\mathbf{x}|\{\widehat{f_k}\}) + \frac{1}{2}\sum_{i=1}^{K}\sum_{j=1}^{K} J_{ij}(\{\widehat{f_k}\})h_i h_j + L(\{f_k\}), \tag{A.3}$$

with

$$J_{ij}(\{f_k\}) = \frac{\partial^2}{\partial f_i \partial f_j} - \log P(\mathbf{x}|\{f_k\}), \tag{A.4}$$

and no contribution of the first derivatives since $L_{\text{total}}(\{f_k\})$ and $-\log P(\mathbf{x}|\{f_k\})$ are at a minimum in $\{f_k\} = \{\widehat{f_k}\}$. It is then useful to express the total length of Eq. (A.3) as $L_{\text{total}}(\{f_k\}) = -\log P(\mathbf{x}|\{\widehat{f_k}\}) + \Phi(\{h_k\})$. This new function $\Phi(\{h_k\})$, defined from Eq. (A.3), captures the dependence of $L_{\text{total}}(\{f_k\})$ with the precisions $\{h_k\}$ for coding the K parameters f_k. It is then natural to select the precisions $\{h_k\}$ in order to minimize the cost expressed by $\Phi(\{h_k\})$. If the quantization steps $\{h_k\}$ are small, long code lengths are entailed for the parameters $\{f_k\}$, but also high precision is obtained in describing the probabilities of the data, allowing to come close to the minimum code length $-\log P(\mathbf{x}|\{\widehat{f_k}\})$. On the contrary, larger quantization steps $\{h_k\}$ entail shorter code lengths for the parameters $\{f_k\}$, but also less accuracy in describing the probabilities of the data with a coding performance further away from the minimum $-\log P(\mathbf{x}|\{\widehat{f_k}\})$. One can thus expect an optimal configuration for the precisions $\{h_k\}$ that will minimize the total description length of Eq. (A.3), and that will come by nullifying the derivatives

$$\frac{\partial \Phi}{\partial h_k} = \frac{\partial}{\partial h_k}\left[\frac{1}{2}\sum_{i=1}^{K}\sum_{j=1}^{K} J_{ij}(\{\widehat{f_k}\})h_i h_j - \sum_{k=1}^{K}\log(h_k)\right]. \tag{A.5}$$

Due to the symmetry $J_{ij} = J_{ji}$, it follows from Eq. (A.5),

$$\sum_{i=1}^{K} J_{ik}(\{\widehat{f_k}\})h_i - \frac{1}{h_k} = 0, \tag{A.6}$$

for all $k = 1$ to K.

To make the J_{ij}'s explicit, one has from Eq. (5), $\partial[-\log P(\mathbf{x}|\{f_k\})]/\partial f_i = -N_i/f_i$, and then $J_{ij}(\{f_k\}) = N_i/f_i^2$ if $i = j$, and $J_{ij}(\{f_k\}) = 0$ if $i \neq j$. The optimal precisions $\{h_k\}$ then follow from Eq. (A.6) as

$$h_k = \frac{\widehat{f}_k}{\sqrt{N_k}} = \frac{\sqrt{N_k}}{N}\delta x^{-1}, \tag{A.7}$$

for all $k = 1$ to K. The optimal precisions $\{h_k\}$ of Eq. (A.7) are dependent upon the optimal parameter values $\{\widehat{f}_k\}$. For consistency of their derivation, the optimal coding precisions h_k's of Eq. (A.7) are determined by the $\widehat{f}_k$'s but would not vary for coding other f_k's that would deviate from the $\widehat{f}_k$'s.

At the optimal $\{h_k\}$ of Eq. (A.7) one finds $\sum_i \sum_j J_{ij}(\{\widehat{f}_k\})h_i h_j = K$ and a minimum for $\Phi(\{h_k\})$ which is $K/2 + K\log(N) - \sum_{k=1}^{K}\log(\sqrt{N_k})$, leading to a parameter code length in Eq. (A.1) as

$$L(\{\widehat{f}_k\}) = \frac{K}{2}\log(N) - \frac{1}{2}\sum_{k=1}^{K}\log\left(\frac{N_k}{N}\right). \tag{A.8}$$

Also, in Eq. (A.3), the data code length $-\log P(\mathbf{x}|\{\widehat{f}_k\})$ is provided by Eq. (8). This leads, at the optimal $\{h_k\}$ of Eq. (A.7), for the total description length of Eq. (A.2), to the minimum

$$L_{\text{total}}(\{\widehat{f}_k\}) = -\sum_{k=1}^{K}\left(N_k + \frac{1}{2}\right)\log(N_k) + \frac{K}{2} + \left(N + \frac{K}{2}\right)\log(N) + \frac{K}{2}\log(N) - N\log(K) + N\log\left(\frac{\Delta x}{\mathrm{d}x}\right), \tag{A.9}$$

or equivalently

$$L_{\text{total}}(\{\widehat{f}_k\}) = \left(N + \frac{K}{2}\right)H(\{\widehat{p}_k\}) + \frac{K}{2} + \frac{K}{2}\log(N) - N\log(K) + N\log\left(\frac{\Delta x}{\mathrm{d}x}\right), \tag{A.10}$$

with this time the entropy estimator

$$H(\{\widehat{p}_k\}) = -\sum_{k=1}^{K}\frac{N_k + 1/2}{N + K/2}\log\left(\frac{N_k}{N}\right). \tag{A.11}$$

Eqs. (A.8), (A.9) and (A.10) are close, respectively, to Eqs. (16), (18) and (20) from Section 6. However, this approach based on Eqs. (A.8)–(A.10) suffers from the same limitation as the approach of Section 6, as explained in Section 11: the code it uses for the model parameters $\{\widehat{f}_k\}$ is not decodable by the receiver. This is so because Eq. (A.8) arranges for the parameters $\{\widehat{f}_k\}$ a code length which depends on the data through the N_k's. Since these counts N_k are not known to the receiver when it starts its decoding task, this first step of decoding the parameters cannot take place. To circumvent this limitation, a simpler approach [1] would quantify the code length for K real independent parameters as $K\log(N)/2$, specially at large N, to replace Eq. (A.8) or Eq. (16). But for the present histogram parameters, as we mentioned, K independent real (continuously-valued) independent parameters is not a natural assumption, and this is not needed by the alternative approach of Section 7.

References

[1] J. Rissanen, Stochastic Complexity in Statistical Inquiry, World Scientific, Singapore, 1989.
[2] A.R. Baron, J. Rissanen, B. Yu, The minimum description length principle in coding and modeling, IEEE Transactions on Information Theory 44 (1998) 2743–2760.
[3] P.D. Grünwald, The Minimum Description Length Principle, MIT Press, Cambridge, MA, 2007.
[4] M. Li, P. Vitányi, An Introduction to Kolmogorov Complexity and its Applications, Springer, Berlin, 1997.
[5] J. Rissanen, Modeling by shortest data description, Automatica 14 (1978) 465–471.
[6] P. Grünwald, I.J. Myung, M. Pitt, Advances in Minimum Description Length: Theory and Applications, MIT Press, Cambridge, MA, 2005.
[7] K. Judd, A. Mees, On selecting models for nonlinear time series, Physica D 82 (1995) 426–444.
[8] L. Diambra, Maximum entropy approach to nonlinear modeling, Physica A 278 (2000) 140–149.
[9] E.J. Hannan, B.G. Quinn, The determination of the order of an autoregression, Journal of the Royal Statistical Society B 41 (1979) 190–195.
[10] O. Alata, C. Olivier, Choice of a 2-D causal autoregressive texture model using information criteria, Pattern Recognition Letters 24 (2003) 1191–1201.
[11] P. Kontkanen, P. Myllymäki, W. Buntine, J. Rissanen, H. Tirri, An MDL framework for data clustering, in: P. Grünwald, I.J. Myung, M. Pitt (Eds.), Advances in Minimum Description Length: Theory and Applications, MIT Press, Cambridge, MA, 2005, pp. 323–353.
[12] D.J. Navarro, M.D. Lee, An application of minimum description length clustering to partitioning learning curves, in: Proceedings IEEE International Symposium on Information Theory, Adelaide, Australia, 4–9 Sept. 2005, pp. 587–591.
[13] T. Hediger, A. Passamante, M.E. Farrell, Characterizing attractors using local intrinsic dimensions calculated by singular-value decomposition and information-theoretic criteria, Physical Review A 41 (1990) 5325–5332.
[14] J. Rissanen, MDL denoising, IEEE Transactions on Information Theory 46 (2000) 2537–2543.
[15] S.C. Zhu, A. Yuille, Region competition: Unifying snakes, region growing, and Bayes/MDL for multiband image segmentation, IEEE Transactions on Pattern Analysis and Machine Intelligence 18 (1998) 884–900.
[16] F. Galland, N. Bertaux, P. Réfrégier, Minimum description length synthetic aperture radar image segmentation, IEEE Transactions on Image Processing 12 (2003) 995–1006.
[17] T.C.M. Lee, Regression spline smoothing using the minimum description length principle, Statistics and Probability Letters 48 (2000) 71–81.
[18] F. Chapeau-Blondeau, Le principe de longueur de description minimale pour la modélisation des données, ou la théorie statistique de l'information pour bien exploiter les mesures, Le Bup - Bulletin de l'Union des Professeurs de Physique et de Chimie 100 (889 (2)) (2006) 145–155.
[19] R. Brown, N.F. Rulkov, E.R. Tracy, Modeling and synchronizing chaotic systems from experimental data, Physics Letters A 194 (1994) 71–76.

[20] S.S. Chen, L.F. Chen, Y.T. Wu, Y.Z. Wu, P.L. Lee, T.C. Yeh, J.C. Hsieh, Detection of synchronization between chaotic signals: An adaptive similarity-based approach, Physical Review E 76 (2007) pp. 066208, 1–11.
[21] W. Szpankowski, W. Ren, L. Szpankowski, An optimal DNA segmentation based on the MDL principle, International Journal of Bioinformatics Research and Applications 1 (2005) 3–17.
[22] J.S. Conery, Aligning sequences by minimum description length, EURASIP Journal on Bioinformatics and Systems Biology 72936 (2007) 1–14.
[23] R. Meir, J.F. Fontanari, Data compression and prediction in neural networks, Physica A 200 (1993) 644–654.
[24] M. Small, C.K. Tse, Minimum description length neural networks for time series prediction, Physical Review E 66 (2002) pp. 066701, 1–12.
[25] D.G. Luenberger, Information Science, Princeton University Press, Princeton, 2006.
[26] F.A. Bais, J.D. Farmer, The physics of information, in: P. Adriaans, J. van Benthem (Eds.), Philosophy of Information, in: Handbook of the Philosophy of Science, North Holland, Amsterdam, 2008 (Chapter 5b). Also arXiv:0708.2837v2.
[27] M. Mézard, A. Montanari, Information, Physics, and Computation, Oxford University Press, Oxford, 2009.
[28] P. Hall, E.J. Hannan, On stochastic complexity and nonparametric density estimation, Biometrika 75 (1988) 705–714.
[29] J. Rissanen, Density estimation by stochastic complexity, IEEE Transactions on Information Theory 38 (1992) 315–323.
[30] A.R. Baron, T.M. Cover, Minimum complexity density estimation, IEEE Transactions on Information Theory 37 (1991) 1034–1054.
[31] T. Zhang, From ϵ-entropy to KL-entropy: Analysis of minimum information complexity density estimation, The Annals of Statistics 34 (2006) 2180–2210.
[32] L. Birgé, Y. Rozenholc, How many bins should be put in a regular histogram, European Series in Applied and Industrial Mathematics: Probability and Statistics 10 (2006) 24–45.
[33] P. Kontkanen, P. Myllymäki, Information-theoretically optimal histogram density estimation, Technical Report 2006-2 Helsinki Institute for Information Technology, Finland, 17 March 2006.
[34] P. Kontkanen, P. Myllymäki, MDL histogram density estimation, in: Proceedings 11th International Conference on Artificial Intelligence and Statistics, San Juan, Puerto Rico, 21–24 March 2007.
[35] J.W. Lee, J.B. Park, H.H. Jo, J.S. Yang, H.T. Moon, Minimum entropy density method for the time series analysis, Physica A 388 (2009) 137–144.
[36] G. Nicolis, Equality governing nonequilibrium fluctuations and its information theory and thermodynamic interpretations, Physical Review E 79 (2009) pp. 011106, 1–8.
[37] A. Carbone, H.E. Stanley, Scaling properties and entropy of long-range correlated time series, Physica A 384 (2007) 21–24.
[38] S. Martinez, A. Plastino, B.H. Soffer, Information and thermodynamics first law, Physica A 356 (2005) 167–171.
[39] A. Papoulis, Probability, Random Variables, and Stochastic Processes, McGraw-Hill, New York, 1991.
[40] W. Feller, An Introduction to Probability Theory and Its Applications, vol. I, Wiley, New York, 1968.
[41] H. Wang, K.C. Sevcik, Histograms based on the minimum description length principle, The VLDB (Very Large Data Base) Journal 17 (2008) 419–442.

J. CHAUVEAU and D. ROUSSEAU and F. CHAPEAU-BLONDEAU, Fractal capacity dimension of three-dimensional histogram from color images. *Multidimensional Systems and Signal Processing*, in press, DOI 10.1007/S11045-009-0097-0, 2009.

Multidimensional Systems and Signal Processing manuscript No.
(will be inserted by the editor)

Fractal capacity dimension of three-dimensional histogram from color images

Julien Chauveau · David Rousseau · François Chapeau-Blondeau

Received: date / Accepted: date

Abstract To contribute to the important task of characterizing the complex multidimensional structure of natural images, a fractal characterization is proposed for the colorimetric organization of natural color images. This is realized from their three-dimensional RGB color histogram, by applying a box-counting procedure to assess the dimensionality of its support. Non-integer values for the resulting capacity dimension of the histograms emerge for natural color images. This manifests a fractal colorimetric organization with a self-similar structure of the color palette typically composing natural images. Such a fractal characterization complements other previously known fractal properties of natural images, some reported recently in their colorimetric organization, and others reported more classically in their spatial organization. Such fractal multiscale features uncovered in natural images provide helpful clues relevant to image modeling, processing and visual perception.

Keywords Color images · Three-dimensional histogram · Fractal dimension · Multicomponent images

1 Introduction

Natural images are complex multidimensional information-carrying signals. Their understanding and modeling are essential to many tasks in image processing and vision, and advances are still needed in this direction. Among specific properties that have been found constitutive of the complex structure of natural images are fractal properties. Principally, fractal or self-similarity or scaling properties have been observed in the spatial organization of natural images [23, 22, 14]. Such spatial fractal properties can be related to the many features and details which usually exist across many spatial scales, in a self-similar way, in natural scenes. Such fractal self-similar structures have also been found to extend to the temporal organization of time-varying sequences of natural images, as perceived by the visual system [6]. These findings of such spatial or temporal fractal scaling properties are helpful to construct more realistic models

Laboratoire d'Ingénierie des Systèmes Automatisés (LISA),
Université d'Angers, 62 avenue Notre Dame du Lac, 49000 Angers, France.

for natural images, and carry relevance for image coding and processing [21,26,4] and vision systems [16,20].

In the present paper, we will address another, complementary, aspect of the fractal properties of natural images. Beyond the spatial and temporal organizations of natural images, we address here their colorimetric organization. Some evidence has recently been reported that a fractal or self-similar organization also exists in the colorimetric domain for natural images [3,2]. The pixels of natural color images would tend to distribute, over the colorimetric space, in a self-similar fractal arrangement. This has been shown in [3,2] by means of the evaluation of the correlation dimension of the distribution of pixels in the colorimetric space, as represented by the three-dimensional color histogram of the images. Two distinct estimators in [3] and in [2] have been tested for the correlation dimension, which confirm the presence of non-integer correlation dimension manifesting a fractal distribution of the pixels in the colorimetric space. We complement these investigations here by considering another approach to further characterize a fractal colorimetric organization. We evaluate the capacity dimension of the three-dimensional histogram of color images. Such a capacity dimension characterizes the structure of the support of the three-dimensional histogram, which expresses, in the colorimetric space, which colors are present in an image and which are not. In other words, the capacity dimension characterizes the structure of the color palette employed by Nature to compose a given natural image. We show here that such a color palette tends to display a fractal organization, identified by a non-integer capacity dimension. By contrast, the correlation dimension of [3,2] offers a more composite view, as it simultaneously characterizes the color palette and the populations of pixels distributing among these existing colors. These are two complementary approaches on the fractal colorimetric organization of images, which are made possible by the evaluation of the capacity dimension we perform here.

2 Three-dimensional color histogram

We consider RGB color images [25], with each component R red, G green and B blue varying among Q possible integer values in $[0, Q-1]$ at each pixel of spatial coordinate (x_1, x_2). The histogram of such color images is a three-dimensional structure comprising Q^3 colorimetric cells, each of which containing the pixels with this color in the image. For the very common choice $Q = 2^8 = 256$, the histogram with its $Q^3 = 2^{24} \approx 16.8 \times 10^6$ cells is a large data structure which can display complex organization. Instead of the full three-dimensional histogram, three marginal one-dimensional histograms, separately for each R, G or B component, are often considered to lead to simpler data handling. In addition, the full three-dimensional histogram can be highly nonuniform. For a typical RGB color image with size 512×512 and $Q = 256$, a total of $512^2 = 2^{18}$ pixels distibute among the $Q^3 = 2^{24}$ colorimetric cells. This means that in the three-dimensional color histogram, most of the cells are likely to be empty, while cells corresponding to dominant colors in the image may be highly populated. A typical three-dimensional color histogram is thus a large data structure, highly nonuniform, with possibly large voids, some high local concentrations of pixels, an overall diffuse character, and not so often considered (in place of the three marginal histograms). Such features can be perceived on the two examples of three-dimensional color histograms from natural images shown in Fig. 7. We will implement here a characterization of the three-dimensional color histogram, manifesting the prevalence of a fractal organization.

3 Fractal characterization

RGB color images have been tested for their fractal organization by applying a box-counting procedure as follows. The colorimetric cube $[0, Q-1]^3$ is successively covered with boxes of side a and volume a^3, with varying a. For each box size a, one computes the number $N(a)$ of boxes which are needed to cover the support of the three-dimensional histogram, i.e. to cover all the cells of the colorimetric cube which are occupied by pixels of the image.

For calibration purpose, we apply first this measuring process on reference RGB images with known properties for their three-dimensional histogram. We consider a random image $\boldsymbol{I_3}(x_1, x_2)$ for which each color component R, G or B is uniformly drawn at random in $[0, 255]$ independently at each pixel (x_1, x_2). Such a color image $\boldsymbol{I_3}(x_1, x_2)$ is endowed with a three-dimensional histogram where the pixels uniformly distribute over the colorimetric cube $[0, Q-1=255]^3$, as shown in Fig. 1.

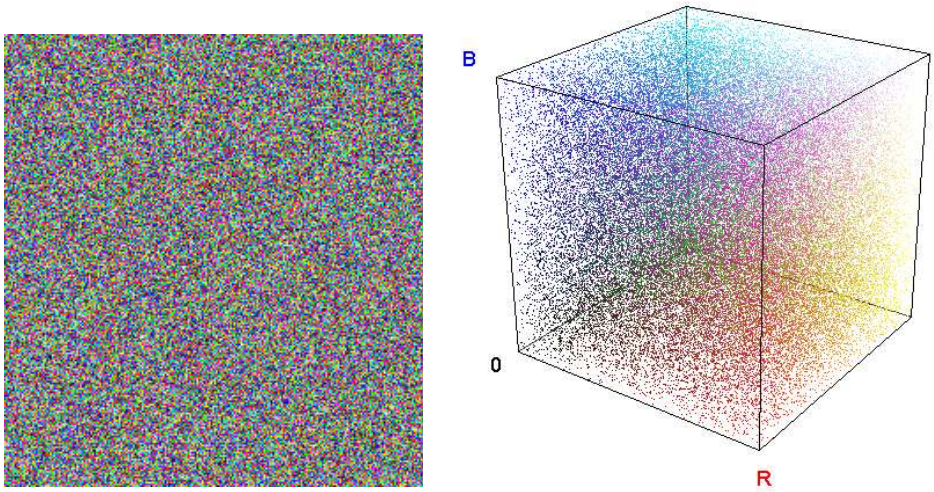

Fig. 1 Random RGB color image $\boldsymbol{I_3}(x_1, x_2)$ of size 512×512 pixels (left) and its three-dimensional histogram in the colorimetric cube $[0, Q-1=255]^3$ as a three-dimensional manifold (right).

In a similar way, we also consider a random image $\boldsymbol{I_2}(x_1, x_2)$ for which the two components R and G are uniformly drawn at random in $[0, 255]$ independently at each pixel (x_1, x_2). In addition, the B component is fixed everywhere to the constant value 128. Such a color image $\boldsymbol{I_2}(x_1, x_2)$ is endowed with a three-dimensional histogram which reduces to a two-dimensional manifold: the pixels uniformly distribute over the plane with equation $B = 128$ in the colorimetric cube $[0, Q-1=255]^3$, as shown in Fig. 2.

Finally we introduce a random image $\boldsymbol{I_1}(x_1, x_2)$ for which the component R is uniformly drawn at random in $[0, 255]$ independently at each pixel (x_1, x_2). In addition, the remaining G and B components are determined according to the value of the R component as $G = R$ and $B = 255 - R$ at each pixel (x_1, x_2). Such a color image $\boldsymbol{I_1}(x_1, x_2)$ is endowed with a three-dimensional histogram which reduces to a one-

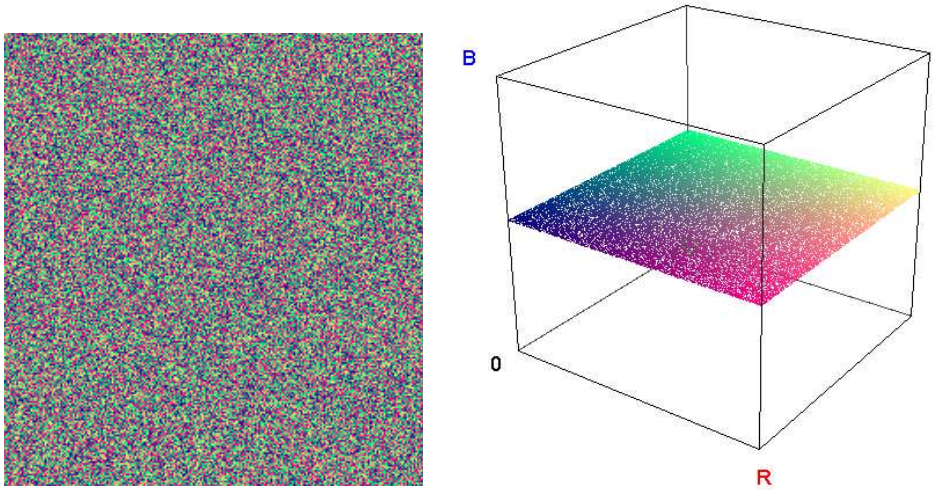

Fig. 2 Random RGB color image $\boldsymbol{I_2}(x_1, x_2)$ of size 512×512 pixels (left) and its three-dimensional histogram in the colorimetric cube $[0, Q-1 = 255]^3$ as a two-dimensional manifold (right).

dimensional manifold: the pixels uniformly distribute over the diagonal with equation $(G = R, B = 255 - R)$ in the colorimetric cube $[0, Q - 1 = 255]^3$, as shown in Fig. 3.

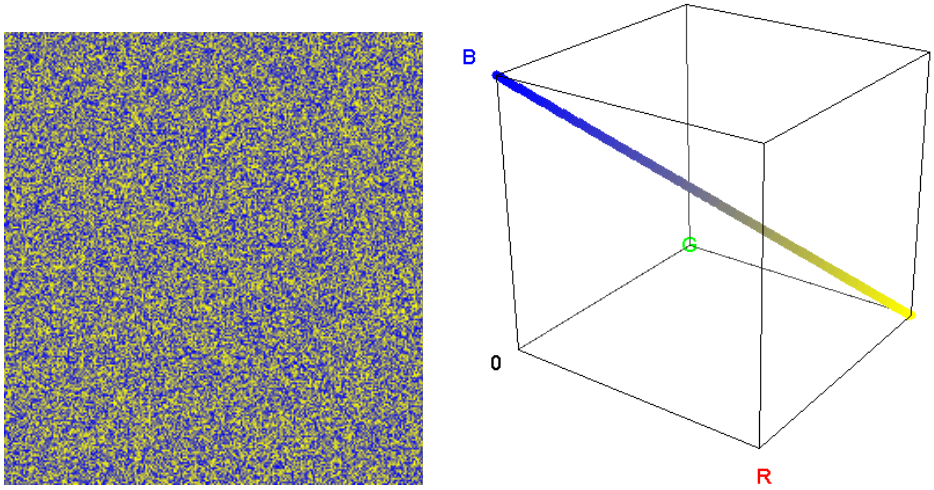

Fig. 3 Random RGB color image $\boldsymbol{I_1}(x_1, x_2)$ of size 512×512 pixels (left) and its three-dimensional histogram in the colorimetric cube $[0, Q-1 = 255]^3$ as a one-dimensional manifold (right).

For each three-dimensional histogram of reference shown in Figs. 1–3, we count the number $N(a)$ of covering boxes at scale[1] a. For the histogram which is a one-

[1] In the plots like Fig. 4, non-integer values of the box size a correspond to the cubic root of the volume of boxes of the form $b \times b \times b/2$ or $b \times b/2 \times b/2$ with b a power of 2. The

dimensional manifold in Fig. 3, the count $N(a)$ is expected to follow a simple power law $N(a) \propto a^{-D}$ with an exponent $D = 1$. This is verified in Fig. 4. For the histogram which is a two-dimensional manifold in Fig. 2, the count $N(a)$ is expected to follow a power law $N(a) \propto a^{-D}$ with $D = 2$. This is also verified in Fig. 4.

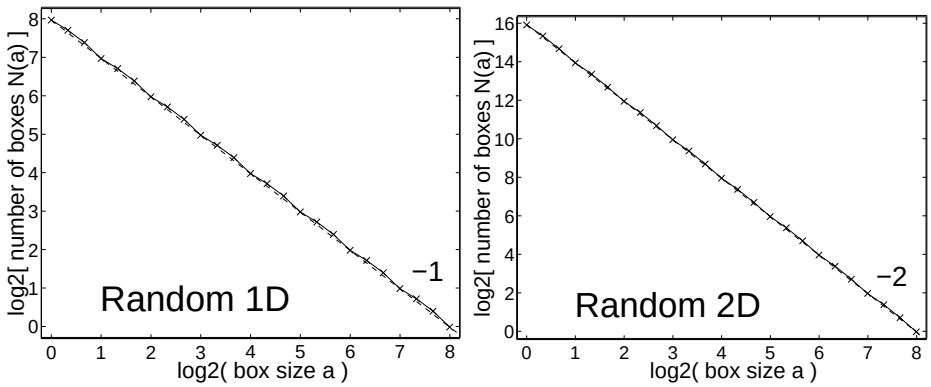

Fig. 4 Number $N(a)$ of covering boxes with size a to cover the three-dimensional histogram of image $\boldsymbol{I_1}(x_1, x_2)$ from Fig. 3 (left), and image $\boldsymbol{I_2}(x_1, x_2)$ from Fig. 2 (right). Dotted lines show the slopes -1 (left) and -2 (right).

For the histogram in Fig. 1 where the pixels uniformly distribute over the whole colorimetric cube $[0, Q-1 = 255]^3$, the count $N(a)$ is expected to follow a power law $N(a) \propto a^{-D}$ with $D = 3$. This is verified in Fig. 5 only at large scales a. At the smallest scale $a = 1$, the straight line with slope -3 in log-log figuring the power law $N(a) \propto a^{-3}$ in Fig. 5, points to a count $N(a = 1) = 2^{24}$ which precisely matches the total number of colorimetric cells in the colorimetric cube $[0, Q-1 = 255]^3$. However, the original image $\boldsymbol{I_3}(x_1, x_2)$ of Fig. 1 contains only a total of $N_{\text{pix}} = 512 \times 512 = 2^{18}$ pixels. Therefore at scale $a = 1$, a total number of 2^{18} boxes of size a is sufficient to cover all the occupied cells of the three-dimensional histogram in Fig. 1. Clearly, if only $N_{\text{pix}} = 2^{18}$ pixels uniformly distribute among 2^{24} colorimetric cells, there will be no more than 2^{18} occupied cells, as seen in Fig. 5. In this way, as the box size a is reduced, if the power law $\propto a^{-D}$ predicts a number of occupied boxes larger than the total number N_{pix} of pixels in the image, the experimental count $N(a)$ of occupied boxes will deviate from the power law to saturate as it cannot exceed N_{pix}. It is important to realize this possibility of saturation of the number of covering boxes $N(a)$ at small scales a, which will saturate in practice according to the total number of pixels N_{pix} in the image, and may therefore deviate from an underlying power law $N(a) \propto a^{-D}$ at small scales a due to the limited number of observed pixels. This possibility will be relevant to interpret the observations on natural images to come next.

A final random test image $\boldsymbol{I_g}(x_1, x_2)$ was generated with, at each pixel (x_1, x_2), the value of each component R, G and B selected independently from a Gaussian probability density with mean 128 and standard deviation 256/6, and then clipped

corresponding count $N(a)$ results from an average over the three possible configurations of such boxes relative to the three coordinate axes (R, G, B).

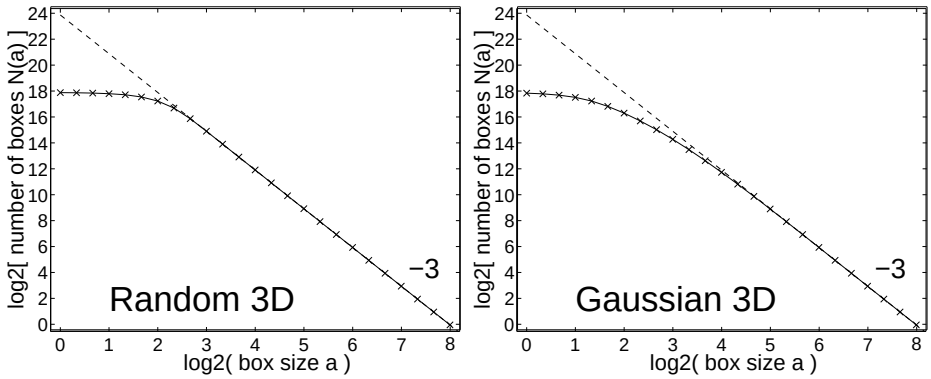

Fig. 5 Number $N(a)$ of covering boxes with size a to cover the three-dimensional histogram of uniform random image $\boldsymbol{I_3}(x_1, x_2)$ from Fig. 1 (left), and a Gaussian random image $\boldsymbol{I_g}(x_1, x_2)$ (right). Dotted lines show the slope -3.

into $[0, 255]$. This Gaussian random image $\boldsymbol{I_g}(x_1, x_2)$ is also characterized by a compact distribution of the colors in the colorimetric cube $[0, 255]^3$. This is associated in Fig. 5 for $\boldsymbol{I_g}(x_1, x_2)$, with a number of covering boxes $N(a) \propto a^{-D}$ with $D = 3$, as shown by the log-log plot matching a straight line with slope -3, at least at large scales a, and with a similar saturation as for $\boldsymbol{I_3}(x_1, x_2)$, at small scales a, due to the limited number of pixels.

4 Natural color images

We now apply the box-counting procedure of Section 3 to characterize the three-dimensional histogram of natural color images. We have considered various common RGB color images, with size $N = 512 \times 512$ pixels and $Q = 256$ levels. Examples of such images are shown in Fig. 6, with two typical three-dimensional color histograms depicted in Fig. 7.

For the images of Fig. 6, log-log plots of the number $N(a)$ of covering boxes are presented in Fig. 8.

The remarkable observation in Fig. 8 is that the plots of $\log[N(a)]$ versus $\log(a)$ are well approximated by straight lines with slope $-D$, over a significant range of scales a. This is equivalent to a number $N(a)$ of covering boxes following a power law $N(a) \propto a^{-D}$, and with the exponent D from Fig. 8 which tends to assume non-integer values significantly below 3. At small scales a, there is usually a departure from the power law $N(a) \propto a^{-D}$ which can be related to the finite number of pixels present in the images, which limits the total count of boxes $N(a)$, as explained at the end of Section 3. This saturation of $N(a)$ is image-dependent since at the smallest scale $a = 1$, the number of covering boxes $N(a = 1)$ saturates exactly at the number of distinct colors present in the image.

The results of Fig. 8 manifesting a power law $N(a) \propto a^{-D}$ are typical of the behavior that was observed while testing many natural color images, with an exponent D that was found to vary between 2.1 and 2.5 typically for natural images. This type of behavior, with non-integer exponent D, identifies what can be viewed as a fractal organization of the colors present in natural images. The box covering procedure as

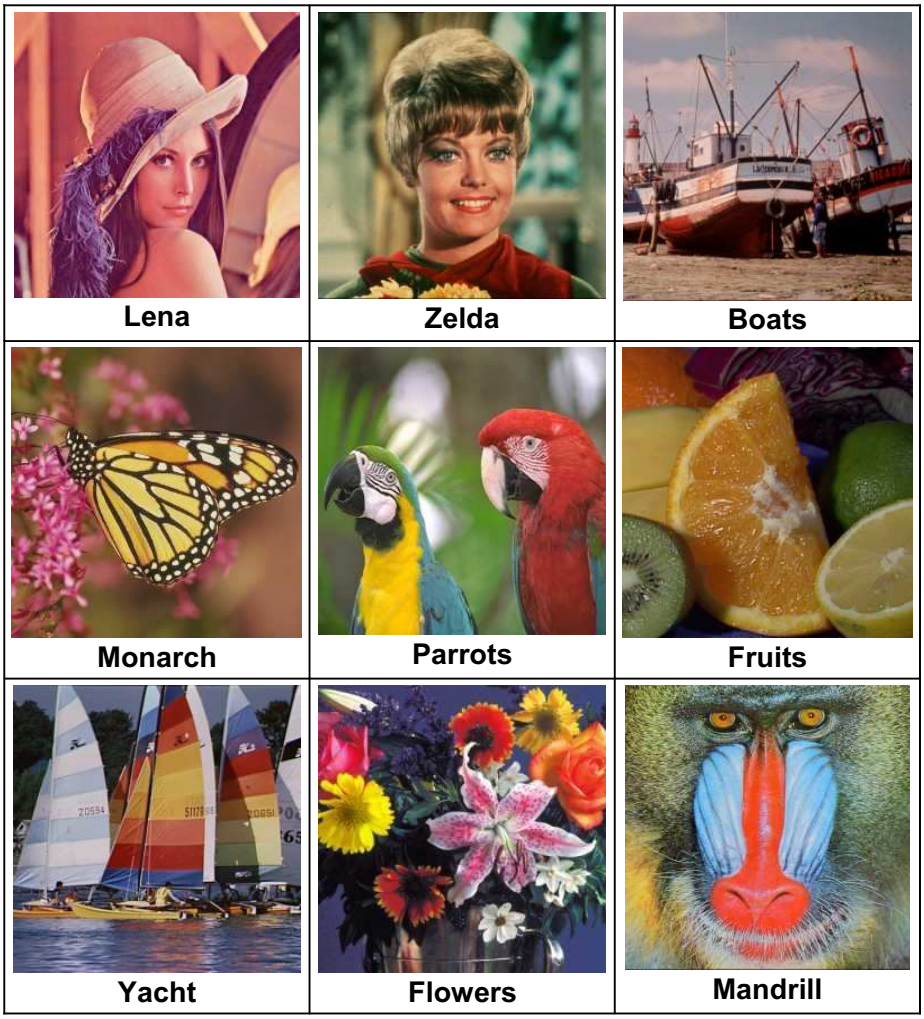

Fig. 6 Nine RGB color images with size 512×512 pixels, and $Q = 256$ levels.

used here, characterizes the structure of the support of the three-dimensional histogram of color images. It shows how the color that are present in the images distribute across the colorimetric cube, according to the colorimetric scale, for close neighboring colors or far apart distant colors. Alternatively, the measure of Fig. 8 characterizes the regions of the colorimetric cube that contribute in providing colors that are employed in the images. A fractal organization, as identified by straight lines with non-integer slopes in Fig. 8, represents images containing clusters of close neighboring colors as well as colors that are far apart. At the same time, a fractal structure with exponent D less than 3, indicates voids of all sizes with no colors for the three-dimensional histograms in the colorimetric cube. Natural images tend to involve colors that are selected in a non-trivial self-similar fractal fashion over the colorimetric cube, with color selected uniformly across many scales. Small scales are related to the many different shades and

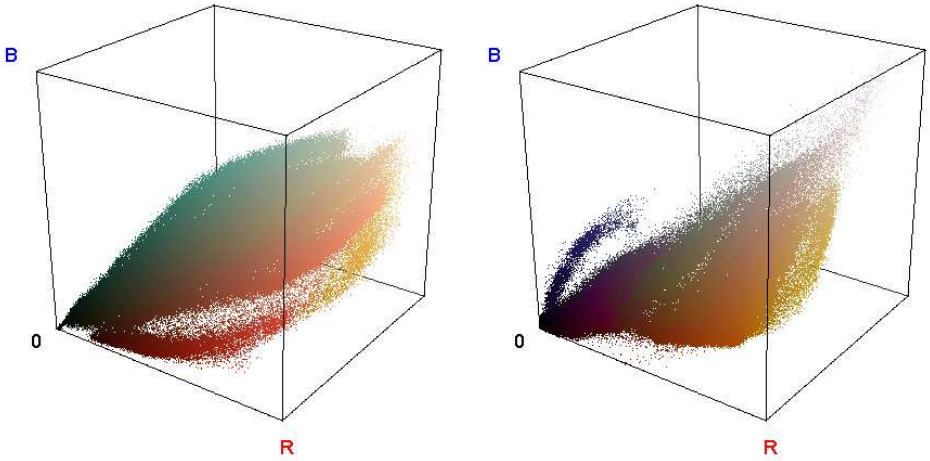

Fig. 7 Color histogram in the RGB colorimetric cube $[0, 255]^3$ for image "Zelda" (left) and image "Fruits" (right) from Fig. 6.

variations of some generic reference colors, large scales are related to the several largely distinct colors that frequently compose natural images. And these different colors are usually recruited in a self-similar way across scales, as manifested by Fig. 8.

The fractal property of the colorimetric organization of natural images, as manifested by Fig. 8, complements other fractal properties of the colors recently reported in [3,2]. The results of Fig. 8 with the box-counting method, characterize, as we already mentioned, the support of the three-dimensional histogram. Equivalently, this measures which colors are used and which are not used in the image. This support, according to Fig. 8, tends to display a fractal structure, with clusters and voids spanning many scales. This is identified, from the slopes in Fig. 8, by a fractal dimension D which is known as the box-counting or capacity dimension, or dimension of the support of the distribution [19,24]. By contrast, references [3,2] measure the correlation dimension of the three-dimensional histograms, with two different estimators in [3] and in [2]. This is a distinct dimension compared to the capacity dimension measured here. The capacity dimension and the correlation dimension are two important instances in the infinite series of fractal dimensions which can be defined for fractal structures [13,24]. In general, the capacity dimension is $\geq$ to the correlation dimension, and this is indeed verified for color histograms here and in [3,2]. The fractal characterization of [3,2], via the correlation dimension, characterizes simultaneously, in a joint manner, both the support of the histogram and the populations in the histogram. Equivalently, this measures simultaneously which colors are used in the histograms, and which populations of pixels distribute among these occupied colors. A fractal organization is found in [3,2], for the way the pixels populate the occupied colorimetric cells of the histogram. The results of Fig. 8 here, reveal that the occupied colorimetric cells alone, irrespective of their populations, display a fractal organization. These are two distinct fractal properties, which are both useful to characterize the complex colorimetric organization of natural images.

A consistent behavior of the capacity dimension can be observed when the box-counting procedure is applied to natural gray images coded as RGB colors images with three identical color components $R = G = B$. In this case, as shown in Fig. 9, the num-

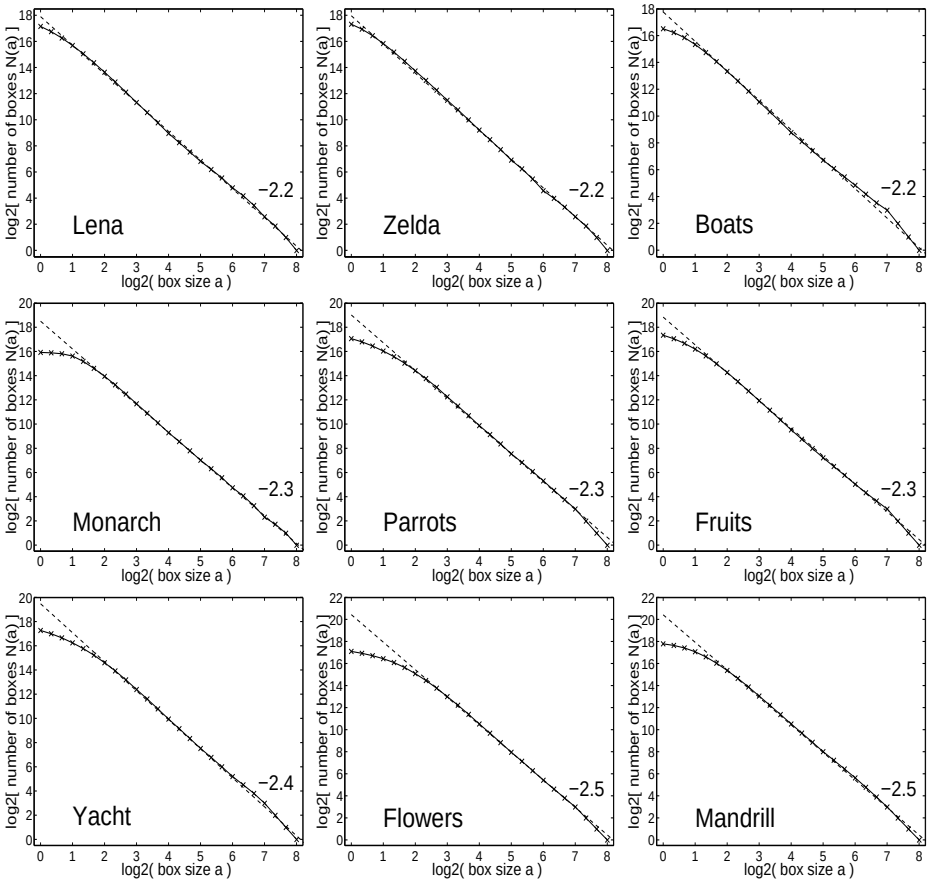

Fig. 8 Number $N(a)$ of covering boxes with size a to cover the three-dimensional histogram, for the nine RGB color images of Fig. 6. For each image, the dotted line shows the slope $-D$.

ber of covering boxes is $N(a) \propto a^{-D}$ with $D = 1$, because the three-dimensional RGB histogram of the gray images is supported by the principal diagonal of the colorimetric cube, which is a one-dimensional manifold, much like in Fig. 3.

5 Discussion

The characterization by the box-counting method performed in Section 4 indicates that the three-dimensional histograms from natural color images tend to display a support with a fractal structure. This complements the other recent characterization of [3,2] showing a fractal organization also for the populations of pixels over the populated colors of the histograms. These results represent a first stage of exploration in this direction for characterizing the complex structure of images in the colorimetric domain. They should be confirmed by examination of extended series of natural images, possibly with control on their typologies. For natural images, such characterizations of fractal properties in their colorimetric organization complement other fractal properties previously

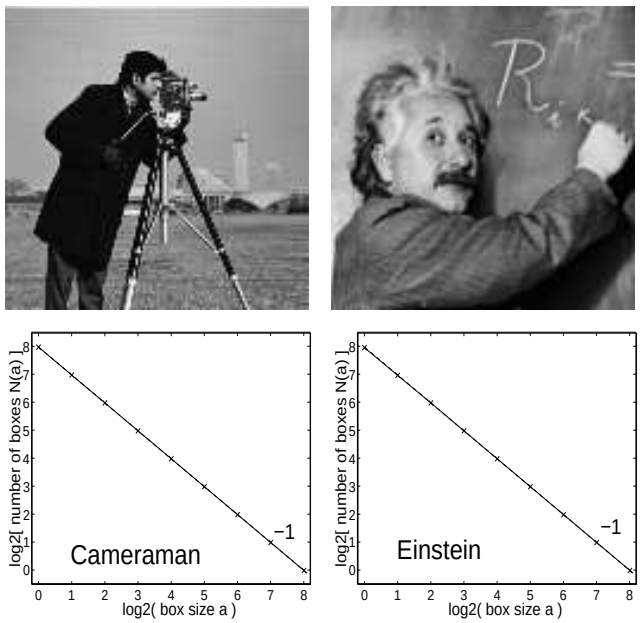

Fig. 9 Two gray-level images with size 512×512 pixels and $Q = 256$ levels, coded as RGB color images with three identical color components $R = G = B$; and corresponding number $N(a)$ of covering boxes with size a to cover their three-dimensional histogram.

reported in their spatial organization [23, 22, 14]. In this respect, current application of fractal concepts to image compression is more related to the spatial organization of images [15, 10, 7], while here fractality in the colorimetric organization constitutes a novel direction for exploration. Also, similar fractal approaches as addressed here for the three-dimensional histogram of color images, could be extended to multispectral images, to characterize the complex structure of their multidimensional histograms, contribute to assess their intrinsic dimensionality, and suggest efficient representations in reduced coordinate systems [17].

For color images as considered here, the fractal dimensions resulting from such analyses of their three-dimensional histograms, could be taken as simple characteristic parameters, which can be helpful to various purposes such as image classification or indexing, or contribute to metrics for realistic synthesis of images [11, 1, 5, 18, 25]. Also, a fractal organization indicates clusters of occupied colorimetric cells exhibiting many sizes, over many scales, in the three-dimensional histograms. This is to be contrasted with simpler structures composed of a few clusters, with a few definite sizes, for the occupied colorimetric cells of the histograms. This may bear relevance to segmentation of color images based on pixel clustering from the color histogram. The presence of a fractal organization suggests that there is no such thing as a small number of well defined clusters that would emerge in the three-dimensional histograms, but on the contrary, many clusters and sub-clusters co-existing over many scales in a self-similar way.

Uncovering fractal structures also provides clues useful to developing models for natural images [26, 12]. This is an important task for many areas of image processing and computer vision. The fractal organization observable in the three-dimensional color

histograms of natural images can have its origin in the spatial structures present in natural scenes, typically containing features and details spanning many scales. In this direction, the fractal colorimetric organization reported here for natural images, would share some common origin with the distinct fractal spatial organization previously reported for natural images [23,22,14]. Also, trichromacy for color representation is a coding modality inherent to the visual system. Fractal organization in the colorimetric structure of natural images could reveal some coding principles implemented by the visual system itself [8,9,20]. Fractal self-similar organization of the colors perceived in natural images, could represent some optimal way of distributing the contrast discrimination capabilities of the visual system across the colorimetric domain. In this way, the visual system would be equally capable of distinguishing small colorimetric contrasts of close colors as well as large contrasts of very different colors. All these aspects connected to fractal properties in images, and possibly relevant to many areas of image processing and artificial or natural vision, offer promising directions for further investigation.

Acknowledgements Julien CHAUVEAU acknowledges support from *La Communauté d'Agglomération du Choletais*, France.

References

1. Batlle, J., Casalsb, A., Freixeneta, J., Martía, J.: A review on strategies for recognizing natural objects in colour images of outdoor scenes. *Image and Vision Computing, 18*, 515–530 (2000)
2. Chapeau-Blondeau, F., Chauveau, J., Rousseau, D., Richard, P.: Fractal structure in the color distribution of natural images. *Chaos, Solitons & Fractals*, doi:10.1016/j.chaos.2009.01.008, (in press) (2009)
3. Chauveau, J., Rousseau, D., Chapeau-Blondeau, F.: Pair correlation integral for fractal characterization of three-dimensional histograms from color images. In: *Lecture Notes in Computer Science*, vol. LNCS 5099, pp. 200–208. Springer, Berlin (2008)
4. Chen, Y.C., Ji, Z., Hua, C.: Spatial adaptive Bayesian wavelet threshold exploiting scale and space consistency. *Multidimensional Systems and Signal Processing, 19*, 157–170 (2008)
5. Distasi, R., Nappi, M., Tucci, M.: FIRE: Fractal indexing with robust extensions for image databases. *IEEE Transactions on Image Processing, 12*, 373–384 (2003)
6. Dong, D.W., Atick, J.J.: Statistics of natural time-varying images. *Network: Computation in Neural Systems, 6*, 345–358 (1995)
7. Faraoun, K.M., Boukelif, A.: Speeding up fractal image compression by genetic algorithms. *Multidimensional Systems and Signal Processing, 16*, 217–236 (2005)
8. Field, D.J.: Relations between the statistics of natural images and the response properties of cortical cells. *Journal of the Optical Society of America A, 4*, 2379–2394 (1987)
9. Field, D.J.: What is the goal of sensory coding? *Neural Computation, 6*, 559–601 (1994)
10. Fisher, Y.: *Fractal Image Compression: Theory and Applications*. Springer, Berlin (1995)
11. Gevers, T., Smeulders, A.W.M.: Color-based object recognition. *Pattern Recognition, 32*, 453–464 (1999)
12. Gousseau, Y., Roueff, F.: Modeling occlusion and scaling in natural images. *SIAM Journal of Multiscale Modeling and Simulation, 6*, 105–134 (2007)
13. Hentschel, H.G.E., Procaccia, I.: The infinite number of generalized dimensions of fractals and strange attractors. *Physica D, 8*, 435–444 (1983)
14. Hsiao, W.H., Millane, R.P.: Effects of occlusion, edges, and scaling on the power spectra of natural images. *Journal of the Optical Society of America A, 22*, 1789–1797 (2005)
15. Jacquin, A.E.: Image coding based on a fractal theory of iterated contractive image transformation. *IEEE Transactions on Image Processing, 1*, 18–30 (1992)
16. Knill, D.C., Field, D., Kersten, D.: Human discrimination of fractal images. *Journal of the Optical Society of America A, 7*, 1113–1123 (1990)

17. Landgrebe, D.: Hyperspectral image data analysis. *IEEE Signal Processing Magazine, 19(1)*, 17–28 (Jan. 2002)
18. Lian, S.: Image authentication based on fractal features. *Fractals, 16*, 287–297 (2008)
19. Maggi, F., Winterwerp, J.C.: Method for computing the three-dimensional capacity dimension from two-dimensional projections of fractal aggregates. *Physical Review E, 69*, 011,405,1–8 (2004)
20. Olshausen, B.A., Field, D.J.: Vision and the coding of natural images. *American Scientist, 88*, 238–245 (2000)
21. Pesquet-Popescu, B., Lévy Véhel, J.: Stochastic fractal models for image processing. *IEEE Signal Processing Magazine, 19(5)*, 48–62 (Sep. 2002)
22. Ruderman, D.L.: Origins of scaling in natural images. *Vision Research, 37*, 3385–3398 (1997)
23. Ruderman, D.L., Bialek, W.: Statistics of natural images: Scaling in the woods. *Physical Review Letters, 73*, 814–817 (1994)
24. Schroeder, M.: *Fractals, Chaos, Power Laws*. Freeman, New York (1999)
25. Sharma Ed., G.: *Digital Color Imaging Handbook*. CRC Press, Boca Raton (2003)
26. Srivastava, A., Lee, A.B., Simoncelli, E.P., Zhu, S.C.: On advances in statistical modeling of natural images. *Journal of Mathematical Imaging and Vision, 18*, 17–33 (2003)

A. HUMEAU, F. CHAPEAU-BLONDEAU, D. ROUSSEAU, and P. ABRAHAM. Numerical simulation of laser Doppler flowmetry signals based on a model of nonlinear coupled oscillators. Comparison with real data in the frequency domain. In *29th Annual International Conference of the IEEE Engineering in Medicine and Biology (SFGBM)*, pages 4068–4071, Lyon, France, Août 2007.

29th Annual International Conference of the IEEE Engineering in Medicine and Biology Society, p. 4068-4071;
Lyon, France, 23-26 Aug. 2007.

Numerical simulation of laser Doppler flowmetry signals based on a model of nonlinear coupled oscillators. Comparison with real data in the frequency domain

Anne Humeau, François Chapeau-Blondeau, David Rousseau, and Pierre Abraham

Abstract—**Laser Doppler flowmetry (LDF) technique is widely used in clinical investigations to monitor microvascular blood flow. It can be a very interesting tool to diagnose impairment in the microcirculation caused by pathologies. However, this can be done in an efficient way only if the processed signals are well understood. Therefore, in order to gain a better insight into LDF signals, this work presents numerically simulated data generated by a model based on nonlinear coupled oscillators. Linear and parametric couplings, as well as fluctuations are analyzed. Each simulated signal is processed to obtain its power spectrum in the frequency domain and a comparison with real data is proposed. The results show that the power spectra of the simulated signals reflect the presence of the cardiac, respiration, myogenic, neurogenic and endothelial related metabolic activities. However, their amplitude in the frequency domain are more pronounced than they are on real LDF signals. Moreover, the modeling of fluctuations is essential to reproduce the noise present on real data. Finally, linear couplings seem more adequate than parametric couplings to describe power spectra at frequencies higher than 1 Hz. This work will now serve as a basis to elaborate more powerful models of LDF data**.

I. Introduction

LASER Doppler flowmetry (LDF) is a noninvasive method to monitor microvascular blood flow [1]-[4]. LDF measurements from the skin reflect perfusion in capillaries, arterioles, venules, and dermal vascular plexa [5]-[7]. Some studies have shown that LDF signals have complex dynamics, with fractal structures and chaos [8].

The LDF technique is now widely used in clinical and physiological investigations of blood microcirculation. Nevertheless, some efforts are still needed to model and numerically generate the signals. Such simulations could help in the diagnosis or prevention of pathologies. The knowledge of the processes giving rise to LDF signals is of course very important to build such simulations. Recent studies conducted on LDF oscillations have shown the existence of five characteristic frequencies, that reflect the heart beats, the respiration, the myogenic, neurogenic and endothelial related metabolic activities (frequencies respectively near to 1.1 Hz, 0.36 Hz, 0.1 Hz, 0.04 Hz, and 0.01 Hz for healthy humans) [5], [6], [9]-[11].

Based on these results, the goal of our work is to go further into the simulation of LDF signals. For that purpose, we use a model of the cardiovascular system relying on nonlinear coupled oscillators [12]-[14]. We simulate the five above-mentioned activities, and we numerically generate LDF signals. To our knowledge, it is the first time that LDF signals are computed with five nonlinear coupled oscillators. This work also determines the power spectra of simulated and real LDF signals. A comparison between the two kinds of spectra is then proposed. Moreover, the influence of the couplings chosen in the model, and the presence of fluctuations, are analyzed in the frequency domain. To our knowledge, this work is also the first one to propose a comparison, in the frequency domain, of numerically simulated LDF data with real recordings.

II. Modeling of LDF Signals

A. Introduction

It has recently been shown that, on the time scale of one average circulation period, the cardiovascular system behaves in many ways as a set of five coupled, autonomous, nonlinear oscillators of different frequencies [10], [13]-[16]. Indeed, on a time scale of around one minute there are five almost periodic oscillatory subsystems contributing to the regulation of blood flow. Each oscillation observed in the cardiovascular signals is therefore hypothesized to originate from a subsystem that can oscillate autonomously [14]. The subsystem can be described as an oscillator and the interactions between the subsystems as couplings between the oscillators [12]. Based on physiological understanding and analysis of measured time series, an oscillator that possesses a structural stability and robustness was proposed for the basic unit to model the cardiovascular system [13].

A. Humeau is with Groupe ISAIP-ESAIP, 18 rue du 8 mai 1945, BP 80022, 49180 Saint Barthélémy d'Anjou cedex, France (phone: +33 (0)2 41 95 65 10; fax: +33 (0)2 41 95 65 11; e-mail: ahumeau@isaip.uco.fr) and with Laboratoire d'Ingénierie des Systèmes Automatisés (LISA), Université d'Angers, 62 avenue Notre Dame du Lac, 49000 Angers, France.

F. Chapeau-Blondeau and D. Rousseau are with Laboratoire d'Ingénierie des Systèmes Automatisés (LISA), Université d'Angers, 62 avenue Notre Dame du Lac, 49000 Angers, France.

P. Abraham is with Laboratoire de Physiologie et d'Explorations Vasculaires, UMR CNRS 6214-INSERM 771, Centre Hospitalier Universitaire d'Angers, 49033 Angers cedex 01, France.

Our study relies on this modeling; the two state variables x_i and y_i correspond to the blood flow and the velocity of the flow, respectively, where $i = 1$ is generated by the heart, $i = 2$ by respiration, $i = 3$ by the myogenic oscillator, $i = 4$ by the neurogenic oscillator, and $i = 5$ by the metabolic oscillator. Each of the five oscillators generates or regulates the flow, the pressure or the resistance.

The preliminary simulations of the model were restricted to the cardio-respiratory interactions, with only two oscillators $i = 1, 2$ taken into account [12], [17]. In our work we go further by taking into account the whole cardiovascular system. The five above-mentioned activities are thus numerically generated with five nonlinear coupled oscillators. Based on these simulations, we then propose to compute LDF data. Moreover, the first simulations of the cardio-respiratory interactions suggested that there is a mixture of linear and parametric couplings, but that the linear couplings seem to dominate [12]. However, it is essential to take into account the influence of stochastic effects resulting from the (unmodeled) rest of the system [12], [17]. In what follows, linear and parametric couplings are studied, and the influence of the rest of the system is modeled by introducing slight time variations for the characteristic frequencies.

B. Linear couplings

For this case, the modeling is chosen as [12]:

$$\dot{x}_1 = -x_1 q_1 - y_1 \omega_1 + \eta_2 x_2 - \eta_3 x_3 - \eta_4 x_4 + \eta_5 x_5 \quad (1)$$

$$\dot{y}_1 = -y_1 q_1 + x_1 \omega_1 + \eta_2 y_2 - \eta_3 x_3 - \eta_4 x_4 + \eta_5 x_5 \quad (2)$$

$$\dot{x}_2 = -x_2 q_2 - y_2 \omega_2 + \theta_4 x_4 + \theta_5 x_5 \quad (3)$$

$$\dot{y}_2 = -y_2 q_2 + x_2 \omega_2 + \theta_4 x_4 + \theta_5 x_5 \quad (4)$$

$$\dot{x}_3 = -x_3 q_3 - y_3 \omega_3 + \gamma_4 x_4 - \gamma_5 x_5 \quad (5)$$

$$\dot{y}_3 = -y_3 q_3 + x_3 \omega_3 + \gamma_4 y_4 - \gamma_5 y_5 \quad (6)$$

$$\dot{x}_4 = -x_4 q_4 - y_4 \omega_4 - \rho_2 x_2 + \rho_3 x_3 - \rho_5 x_5 \quad (7)$$

$$\dot{y}_4 = -y_4 q_4 + x_4 \omega_4 - \rho_2 y_2 + \rho_3 y_3 - \rho_5 y_5 \quad (8)$$

$$\dot{x}_5 = -x_5 q_5 - y_5 \omega_5 + \sigma_2 x_2 - \sigma_3 x_3 - \sigma_4 x_4 \quad (9)$$

$$\dot{y}_5 = -y_5 q_5 + x_5 \omega_5 + \sigma_2 y_2 - \sigma_3 y_3 - \sigma_4 y_4 \quad (10)$$

where η_i, θ_i, γ_i, ρ_i, and σ_i are coupling terms ($1 \le i \le 5$).

$$q_i = \alpha_i \left(\sqrt{x_i^2 + y_i^2} \right) - a_i \quad (11)$$

where α_i, a_i are constants, $\omega_i = 2\pi \left(f_{i\_s} + C \times f_{i\_s} \times \zeta_i(t) \right)$ with f_{i_s} the characteristic frequencies, C a constant, and $\zeta_i(t)$ a white Gaussian noise with mean 0 and variance 1.

C. Parametric couplings

For this other case, the modeling is chosen as [12]:

$$\dot{x}_1 = -x_1 q_1 - y_1 \left(\omega_1 + \eta_2 x_2 - \eta_3 x_3 - \eta_4 x_4 + \eta_5 x_5 \right) \quad (12)$$

$$\dot{y}_1 = -y_1 q_1 + x_1 \left(\omega_1 + \eta_2 y_2 - \eta_3 x_3 - \eta_4 x_4 + \eta_5 x_5 \right) \quad (13)$$

$$\dot{x}_2 = -x_2 q_2 - y_2 \left(\omega_2 + \theta_4 x_4 + \theta_5 x_5 \right) \quad (14)$$

$$\dot{y}_2 = -y_2 q_2 + x_2 \left(\omega_2 + \theta_4 x_4 + \theta_5 x_5 \right) \quad (15)$$

$$\dot{x}_3 = -x_3 q_3 - y_3 \left(\omega_3 + \gamma_4 x_4 - \gamma_5 x_5 \right) \quad (16)$$

$$\dot{y}_3 = -y_3 q_3 + x_3 \left(\omega_3 + \gamma_4 y_4 - \gamma_5 y_5 \right) \quad (17)$$

$$\dot{x}_4 = -x_4 q_4 - y_4 \left(\omega_4 - \rho_2 x_2 + \rho_3 x_3 - \rho_5 x_5 \right) \quad (18)$$

$$\dot{y}_4 = -y_4 q_4 + x_4 \left(\omega_4 - \rho_2 y_2 + \rho_3 y_3 - \rho_5 y_5 \right) \quad (19)$$

$$\dot{x}_5 = -x_5 q_5 - y_5 \left(\omega_5 + \sigma_2 x_2 - \sigma_3 x_3 - \sigma_4 x_4 \right) \quad (20)$$

$$\dot{y}_5 = -y_5 q_5 + x_5 \left(\omega_5 + \sigma_2 y_2 - \sigma_3 y_3 - \sigma_4 y_4 \right) \quad (21)$$

where η_i, θ_i, γ_i, ρ_i, et σ_i are coupling terms ($1 \le i \le 5$).

$$q_i = \alpha_i \left(\sqrt{x_i^2 + y_i^2} \right) - a_i \quad (22)$$

where α_i, a_i are constants, $\omega_i = 2\pi \left(f_{i\_s} + C \times f_{i\_s} \times \zeta_i(t) \right)$ with f_{i_s} the characteristic frequencies, C a constant, and $\zeta_i(t)$ a white Gaussian noise with mean 0 and variance 1.

D. Couplings values and LDF signal computation

For the linear and parametric couplings, the following values are chosen [12]:
$\eta_3 = -0.5$, $\rho_3 = 0.1$, $\sigma_3 = 0.1$, $\eta_2 = -\eta_4 = \eta_5 = 0.5$, $\theta_4 = \theta_5 = 0.1$, $\gamma_4 = \gamma_5 = 0.1$, $\rho_2 = \rho_5 = 0.1$, and $\sigma_2 = \sigma_4 = 0.1$. $\alpha_i = 1$ for $i = 1$ to 5, and finally $a_1 = a_5 = 0.5$; $a_2 = a_3 = a_4 = 1$.

In order to simulate LDF signals recorded on humans, the values of the characteristic frequencies are set as follows: $f_1 = 1.1$ Hz, $f_2 = 0.36$ Hz, $f_3 = 0.1$ Hz, $f_4 = 0.04$ Hz, and $f_5 = 0.01$ Hz. The influence of the rest of the system is studied by modifying the value of C. The latter is chosen equal to 0, 0.1, 0.2, 0.3, or 0.4. Moreover, a sampling frequency of 20 Hz is proposed for the computations.

No simulation of LDF data has ever relied on the five nonlinear coupled oscillators. In our work we propose to compute the blood flow as:

$$BloodFlow = \sum_{i=1}^{5} x_i \,, \quad (23)$$

and 21324 points of signals are simulated. Once the blood flow numerically computed, the data are processed in order to obtain their power spectra.

III. Results and Discussion

The power spectrum of a simulated signal is shown in Fig. 1. For each kind of coupling, and for each value of C, five peaks appear on the power spectra of the simulated data. For the linear couplings, and for $C = 0$, the peaks appear at the following frequencies: 1.1002 Hz, 0.3606 Hz, 0.0910 Hz, 0.0385 Hz, and 0.0150 Hz. A comparison with the characteristic frequencies chosen in the model allows to conclude that these peaks correspond to the cardiac, respiratory, myogenic, neurogenic, and endothelial related metabolic activities, respectively. The simulated data thus reflect the underlying processes of the microcirculation (this is true for each coupling and for each value of C). These

results are meaningful to better appreciate the amount and impact of the couplings between the nonlinear oscillators. Strong couplings and nonlinearities would be expected to lead to broadband spectra. Meanwhile, both the simulated and experimental data reveal that the harmonic frequencies (peaks) of the underlying individual oscillators are relatively preserved in the spectra, suggesting a moderate impact of the couplings between the nonlinear oscillators. The computation of the power spectrum for a real LDF signal reveals that one broad peak is predominant for real data (see Fig. 2). It appears at 0.9131 Hz, and thus may reflect the cardiac activity. The other peaks seem to be hidden by "noise": respiration, myogenic, neurogenic, and endothelial related metabolic activities are difficult to distinguish from the power spectra of real data.

Moreover, whatever the couplings chosen for the simulated data, we note that the higher the value of C, the more noisy the power spectra are (see Figs. 1 and 3). For the linear couplings and for $C = 0.4$, the peaks appear at 1.0810 Hz, 0.3616 Hz, 0.0915 Hz, 0.0385 Hz, and 0.0155 Hz. A comparison with the values mentioned above for $C = 0$ shows that the peak frequencies on the power spectra are only very slightly modified by the noise. As mentioned previously, noise is also present on power spectra of real LDF signals (see Fig. 2). Therefore, in order to simulate data behaving close to real LDF signals, we will choose $C \neq 0$ in what follows.

An analysis of the power spectra obtained by each kind of coupling can also be made. For a given value of C ($C \neq 0$), the power spectra of data obtained with linear couplings are more noisy at frequencies higher than 1 Hz than the spectra of data obtained with parametric couplings (see Fig. 4). We also note that the power spectrum of a real signal is very noisy at high frequencies (see Fig. 2). The linear couplings seem therefore more adequate than the parametric couplings to reflect power spectra of LDF signals at frequencies higher than 1 Hz. Moreover, the power spectra of real data are much more noisy in the lowest frequency band than the power spectra of simulated data. For the latter, at low frequencies, we can see that the five peaks generated by the five activities are present at the nearly same frequencies for the two kinds of coupling (see Fig. 4).

Our study relies on a mathematical model based on nonlinear coupled oscillators. Linear and parametric couplings have been tested. In reality, each oscillator of the model represents a whole set of oscillators which are spatially distributed. Moreover, couplings change with the state of the system. It has been shown that better-trained subjects have stronger couplings, whereas weak couplings lead to some pathological stages (subjects in coma for example, have almost no couplings) [18]. Understanding the physical and physiological nature of these couplings is therefore essential to gain a better insight into the functioning of the whole system. Furthermore, several observations demonstrated clearly that different states of the organism may correspond to different regimes of synchronization (see [12], and references therein). This can be of clinical significance.

Previous studies using a similar mathematical model to simulate the the cardio-respiratory interactions suggested that there is a mixture of linear and parametric couplings, but that the linear couplings seem to dominate [12]. The results of our work are in accordance with the authors conclusion. Indeed, we have shown that the linear couplings are more adequate than the parametric couplings to reflect power spectra of LDF signals at frequencies higher than 1 Hz. Moreover, the same authors have shown that, in order to explain the variability of cardiac and respiratory frequencies, it is essential to take into account the rest of the system, i.e. to consider the effect of noise [12]. Physiological data recordings contain noise that can come from the instrument, from the quantization of analog signals or from physiological phenomena (interactions with the rest of the system). This implies a complex modulation of the natural frequency in the subsystem under study. In the case of weak noise, the generalized phase

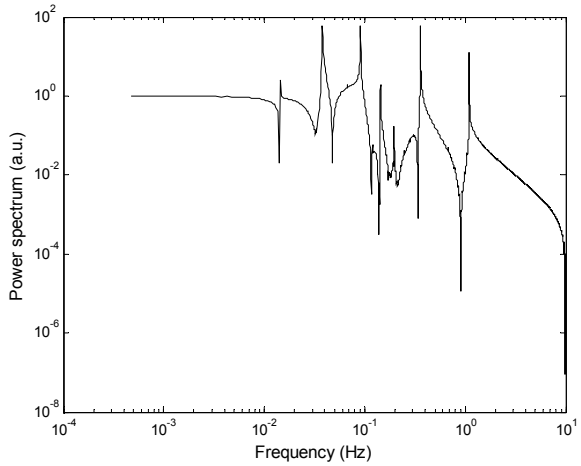

Fig. 1. Power spectrum of a simulated LDF signal obtained with five nonlinear coupled oscillators. Linear coupling is used and $C = 0$.

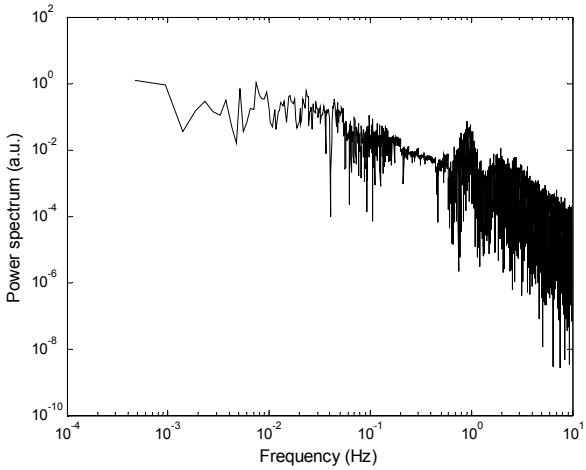

Fig. 2. Power spectrum of a LDF signal recorded on a healthy subject at rest.

difference (relative phase), corresponding to the synchronization, fluctuates in a random way around a constant value. For strong noise, phase slips may occur. Our study on power spectra of simulated data leads to the same conclusion: in order to simulate data behaving close to real LDF signals, the constant C have to be set to a value different from 0.

An improvement in the understanding of the couplings is now necessary for the construction of more complex mathematical models of LDF signals that will provide relevant physiological information. For that purpose, we could add a part of parametric couplings to the linear couplings, or find other more appropriate couplings. Once the knowledge on these couplings adequate, it will become possible to reverse the process, i.e. to diagnose the state of the system from a single measurement of the peripheral blood flow.

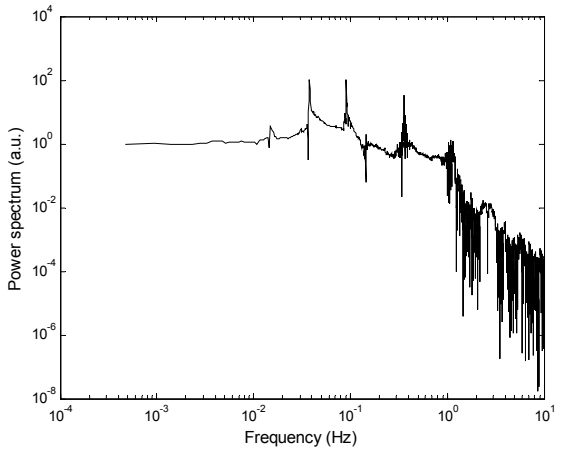

Fig. 3. Power spectrum of a simulated LDF signal obtained with five nonlinear coupled oscillators. Linear coupling is used and $C = 0.4$.

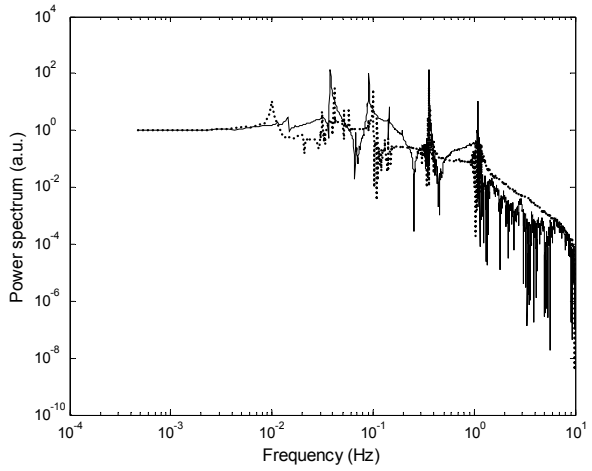

Fig. 4. Power spectra of simulated LDF signals, when linear couplings are chosen (full line), and when parametric couplings are chosen (dotted line). $C = 0.1$ for both couplings.

ACKNOWLEDGMENT

The authors would like to thank A. Stefanovska and P. V. E. McClintock for their helpful comments on the model used.

REFERENCES

[1] A. Humeau, W. Steenbergen, H. Nilsson, and T. Strömberg, "Laser Doppler perfusion monitoring and imaging: novel approaches," *Med. Biol. Eng. Comput.*. DOI: 10.1007/s11517-007-0170-5, 2007.

[2] G. E. Nilsson, T. Tenland, and P. Å. Öberg, "A new instrument for continuous measurement of tissue blood flow by light beating spectroscopy," *IEEE Trans. Biomed. Eng.*, vol. BME-27, pp. 12-19, 1980.

[3] G. E. Nilsson, T. Tenland, and P. Å. Öberg, "Evaluation of a laser Doppler flowmeter for measurement of tissue blood flow," *IEEE Trans. Biomed. Eng.*, vol. BME-27, pp. 597-604, 1980.

[4] D. W. Watkins and G. A. Holloway, "An instrument to measure cutaneous blood flow using the Doppler shift of laser light," *IEEE Trans. Biomed. Eng.*, vol. BME-25, pp. 28-33, 1978.

[5] H. D. Kvernmo, A. Stefanovska., K. A. Kirkerboen, and K. Kvernebo, "Oscillations in the human cutaneous blood perfusion signal modified by endothelium-dependent and endothelium-independent vasodilators," *Microvasc. Res.*, vol. 57, pp. 298-309, 1999.

[6] H. D. Kvernmo, A. Stefanovska, M. Bracic, K. A. Kirkerboen, and K. Kvernebo, "Spectral analysis of the laser Doppler perfusion signal in human skin before and after exercise," *Microvasc. Res.*, vol. 56, pp. 173-182, 1998.

[7] A. Bollinger, A. Yanar, U. Hoffmann, and U. K. Franzeck, "Is high-frequency flux motion due to respiration or to vasomotion activity?," in Vasomotion and flow motion. Progress in Applied Microcirculation, C. Allegra, M. Intaglietta, K. Messmer, Basel, Karger, vol. 20, 1993, pp. 52-58.

[8] D. Popivanov, A. Mineva, and J. Dushanova, "Dynamic characteristics of laser-Doppler flux data," *Technology and Health Care*, vol. 7, pp. 205-218, 1999.

[9] T. Söderström, A. Stefanovska, M. Veber, and H. Svensson, "Involvement of sympathetic nerve activity in skin blood flow oscillations in humans," *Am. J. Physiol. Heart Circ. Physiol.*, vol. 284, pp. H1638-H1646, 2003.

[10] A. Stefanovska, M. Bracic, and H. D. Kvernmo, "Wavelet analysis of oscillations in the peripheral blood circulation measured by laser Doppler technique," *IEEE Trans. Biomed. Eng.*, vol. 46, pp. 1230-1239, 1999.

[11] A. Humeau, A. Koïtka, P. Abraham, J. L. Saumet, and J. P. L'Huillier, "Spectral components of laser Doppler flowmetry signals recorded on healthy and type 1 diabetic subjects at rest and during a local and progressive cutaneous pressure application: scalogram analyses," *Phys. Med. Biol.*, vol. 49, pp. 3957-3970, 2004.

[12] A. Stefanovska, D. G. Luchinsky, and P. V. E. McClintock, "Modelling couplings among the oscillators of the cardiovascular system," *Physiol. Meas.*, vol. 22, pp. 551-564, 2001.

[13] A. Stefanovska, M. Bracic Lotric, S. Strle, and H. Haken, "The cardiovascular system as coupled oscillators?," *Physiol. Meas.*, vol. 22, pp. 535-550, 2001.

[14] A. Stefanovska, S. Strle, M. Bracic, and H. Haken, "Model synthesis of the coupled oscillators which regulate human blood flow dynamics," *Nonlinear Phenomena in Complex Systems*, vol. 2, pp. 72-87, 1999.

[15] A. Stefanovska and M. Bracic, "Physics of the human cardiovascular system," *Contemporary Physics*, vol. 40, pp. 31-55, 1999.

[16] M. Bracic Lotric, A Stefanovska, D. Stajer, and V. Urbancic-Rovan, "Spectral components of heart rate variability determined by wavelet analysis," *Physiol. Meas.*, vol. 21, pp. 441-457, 2001.

[17] P. V. E. McClintock and A. Stefanovska, "Noise and determinism in cardiovascular dynamics," *Physica A*, vol. 314, pp. 69-76, 2002.

[18] M. Bracic and A. Stefanovska, "Reconstructing cardiovascular dynamics," *Control Eng. Pract.*, vol. 7, pp. 161-172, 1999.

A. HUMEAU, B. BUARD, F. CHAPEAU-BLONDEAU, D. ROUSSEAU G. MAHE, P. ABRAHAM. Multifractal analysis of central (electrocardiography) and peripheral (laser Doppler flowmetry) cardiovascular time series from healthy human subjects. *Physiological Measurement*, vol. 30, 617–629, 2009.

IOP PUBLISHING PHYSIOLOGICAL MEASUREMENT

Physiol. Meas. **30** (2009) 617–629 doi:10.1088/0967-3334/30/7/007

Multifractal analysis of central (electrocardiography) and peripheral (laser Doppler flowmetry) cardiovascular time series from healthy human subjects

Anne Humeau[1,2,4], Benjamin Buard[1,2], François Chapeau-Blondeau[2], David Rousseau[2], Guillaume Mahe[3] and Pierre Abraham[3]

[1] Groupe Esaip, 18 Rue du 8 Mai 1945, BP 80022, 49180 Saint Barthélémy d'Anjou cedex, France
[2] Laboratoire d'Ingénierie des Systèmes Automatisés (LISA), Université d'Angers, 62 Avenue Notre Dame du Lac, 49000 Angers, France
[3] Laboratoire de Physiologie et d'Explorations Vasculaires, UMR CNRS 6214-INSERM 771, Centre Hospitalier Universitaire d'Angers, 49033 Angers Cedex 01, France

E-mail: ahumeau@esaip.org

Received 17 January 2009, accepted for publication 18 May 2009
Published 5 June 2009
Online at stacks.iop.org/PM/30/617

Abstract

Analysis of the cardiovascular system (CVS) activity is important for several purposes, including better understanding of heart physiology, diagnosis and forecast of cardiac events. The *central* CVS, through the study of heart rate variability (HRV), has been shown to exhibit multifractal properties, possibly evolving with physiologic or pathologic states of the organism. An additional viewpoint on the CVS is provided at the *peripheral* level by laser Doppler flowmetry (LDF), which enables local blood perfusion monitoring. We report here for the first time a multifractal analysis of LDF signals through the computation of their multifractal spectra. The method for estimation of the multifractal spectra, based on the box method, is first described and tested on *a priori* known synthetic multifractal signals, before application to LDF data. Moreover, simultaneous recordings of both central HRV and peripheral LDF signals, and corresponding multifractal analyses, are performed to confront their properties. With the scales chosen on the partition functions to compute Renyi exponents, LDF signals appear to have broader multifractal spectra compared to HRV. Various conditions for LDF acquisitions are tested showing larger multifractal spectra for signals recorded on fingers than on forearms. The results uncover complex interactions at central and peripheral CVS levels.

Keywords: laser Doppler flowmetry, heart rate variability, electrocardiogram, multifractal analysis

[4] Author to whom any correspondence should be addressed.

1. Introduction

The processing of cardiovascular data is of interest for research and clinical purposes. The processing of the electrocardiogram (ECG), and R–R intervals of ECG signals—the heart rate variability (HRV)—provides a better understanding of heart physiology, can help in some diagnosis and forecast cardiac events. These signals represent a *central* viewpoint of the cardiovascular system. An analysis from a *peripheral* point of view is also useful under many conditions. The peripheral cardiovascular system can be studied non-invasively with laser Doppler flowmetry (LDF) which is a technique enabling the monitoring of (skin) microvascular blood flow (see for example Humeau *et al* (2007b), Nilsson (1984), Nilsson *et al* (1980a, 1980b), Rajan *et al* (2009) and Stern (1975)). LDF research and clinical applications are related to diabetes microangiopathy, peripheral vascular diseases, Raynaud's phenomenon, thermal injury, plastic surgery, flap surveillance, skin diseases, pharmacological applications, etc (see for example Belcaro *et al* (1994), Chao *et al* (2006), Gomes *et al* (2008), Humeau *et al* (2004), Kienle (2001), Kim *et al* (2008), Li *et al* (2006), Liu *et al* (2006), Öberg (1990) and Shepherd and Öberg (1990)). The LDF technique relies on the Doppler effect generated by the interactions between photons from a laser light and moving blood cells of the microcirculation. It gives a signal corresponding to the product of the concentration of moving blood cells in the measuring volume by the mean velocity of these cells.

A few years ago, by processing HRV signals with nonlinear analyses, some authors had shown that HRV data are multifractal for healthy human subjects (see for example Ching and Tsang (2007), Havlin *et al* (1999) and Ivanov *et al* (1999, 2001)). These findings revealed that HRV dynamics has a high complexity for healthy human subjects. Since these studies, many other multifractal HRV works have been published revealing that this multifractal property may evolve with physiologic and pathologic states of the organism, thus leading to physiological knowledge or diagnoses possibilities. By contrast, very few multifractal studies have been conducted on LDF signals (Humeau *et al* 2007a, 2008) and the corresponding works only focused on the time evolution of the signals' Hölder exponents. Moreover, to the best of our knowledge, no analysis has been conducted on the confrontation of multifractal properties for cardiovascular data recorded *simultaneously* from *central* and *peripheral* levels.

Therefore, in order to have a better knowledge of LDF possible multifractal properties and to compare them to the ones observed on central cardiovascular signals, we propose herein (1) to compute *multifractal spectra* of LDF signals and (2) to compare these multifractal spectra of LDF data (peripheral cardiovascular system) to the ones of HRV signals (central cardiovascular system) recorded *simultaneously* in human subjects without known disease.

2. Multifractal analysis and calibration

For a positive measure represented by a signal $X(t)$, the Hölder exponent α at $t = t_0$ characterizes the strength of the singularity at t_0 (Struzik 2000). When a 'broad' range of Hölder exponents is found for a signal, it is considered as multifractal. A 'narrow' range implies monofractality. Multifractality in a process is a mark of a higher complexity compared to monofractal processes. The multifractal spectrum $f(\alpha)$ is defined as the fractal dimension of the subset of points with the Hölder exponent α. In what follows, we compute the multifractal spectra of LDF and HRV data with the so-called box method (Halsey *et al* 1986). In the latter method, the set S of each processed signal X is subdivided into cells of the same linear size ε. Let $\mu_i(\varepsilon)$

denote the measure on the intersection of S with the ith cell of size ε. The partition function $Z(q, \varepsilon)$ is then defined as (Halsey *et al* 1986)

$$Z(q, \varepsilon) = \sum_{i=1}^{N_{\text{boxes}}(\varepsilon)} \mu_i^q(\varepsilon), \tag{1}$$

where $N_{\text{boxes}}(\varepsilon)$ indicates the number of boxes of size ε needed to cover the signal. The exponent q represents a selective parameter: high values of q enhances boxes with relatively high values for $\mu_i(\varepsilon)$, while low values of q favor boxes with relatively low values of $\mu_i(\varepsilon)$. Moreover, the box size ε can be considered as a filter (big values of the size are equivalent to applying a large scale filter). When changing the size ε, the signal is explored at different scales. As a result, the partition function $Z(q, \varepsilon)$ gives information at different scales and moments. The Renyi exponents $\tau(q)$ are estimated from the partition function as

$$\tau(q) = \lim_{\varepsilon \to 0} \frac{\log(Z(q, \varepsilon))}{\log \varepsilon}. \tag{2}$$

The multifractal spectrum $f(\alpha)$ is then obtained by Legendre transformation as (Halsey *et al* 1986)

$$\alpha(q) = \frac{\mathrm{d}\tau(q)}{\mathrm{d}q} \tag{3}$$

and

$$f(\alpha) = \alpha(q)q - \tau(q). \tag{4}$$

In our work, the multifractal spectra of the LDF and HRV data are thus determined by computing the discrete partition functions of the signals with non-overlapping boxes of increasing size, then by determining their Renyi exponents and finally by computing their Legendre transform.

In order to validate our methodology for estimating the multifractal spectra, we first test its application on synthetic signals with known multifractal properties. We turn to binomial measures, also called Bernoulli measures, that we synthesize through multiplicative cascades (Mandelbrot 1999). This approach is considered as it allows us to synthesize signals with completely controllable multifractal spectra.

A binomial measure is recursively generated with a multiplicative cascade, as detailed by Evertsz and Mandelbrot (1992). This cascade starts ($k = 0$) with a uniformly distributed unit of mass on the unit interval $I = I_0 = [0, 1]$. The next stage ($k = 1$) fragments this mass by distributing a fraction m_0 uniformly on the left half $I_{0.0} = [0, 1/2]$ of the unit interval, and the remaining fraction $m_1 = 1 - m_0$ uniformly on the right half $I_{0.1} = [1/2, 1]$. At the next stage ($k = 2$) of the cascade, the subintervals $I_{0.0}$ and $I_{0.1}$ receive the same treatment as the original unit interval. At the kth stage of the cascade, the mass is fragmented over the dyadic intervals $[i2^{-k}, (i + 1)2^{-k}]$ where $i = 0, \ldots, 2^k - 1$ (Evertsz and Mandelbrot 1992). Binomial measures computed with $k = 12$ and different values for m_0 and m_1 are presented in figure 1. The parameters m_0 and m_1 of the binomial measure are tuned in order to synthesize multifractal spectra in the range of the ones found for our cardiovascular signals (see below).

For binomial measures, the Hölder exponents are defined as (Evertsz and Mandelbrot 1992)

$$\alpha = \frac{n_0}{k} v_0 + \frac{k - n_0}{k} v_1, \tag{5}$$

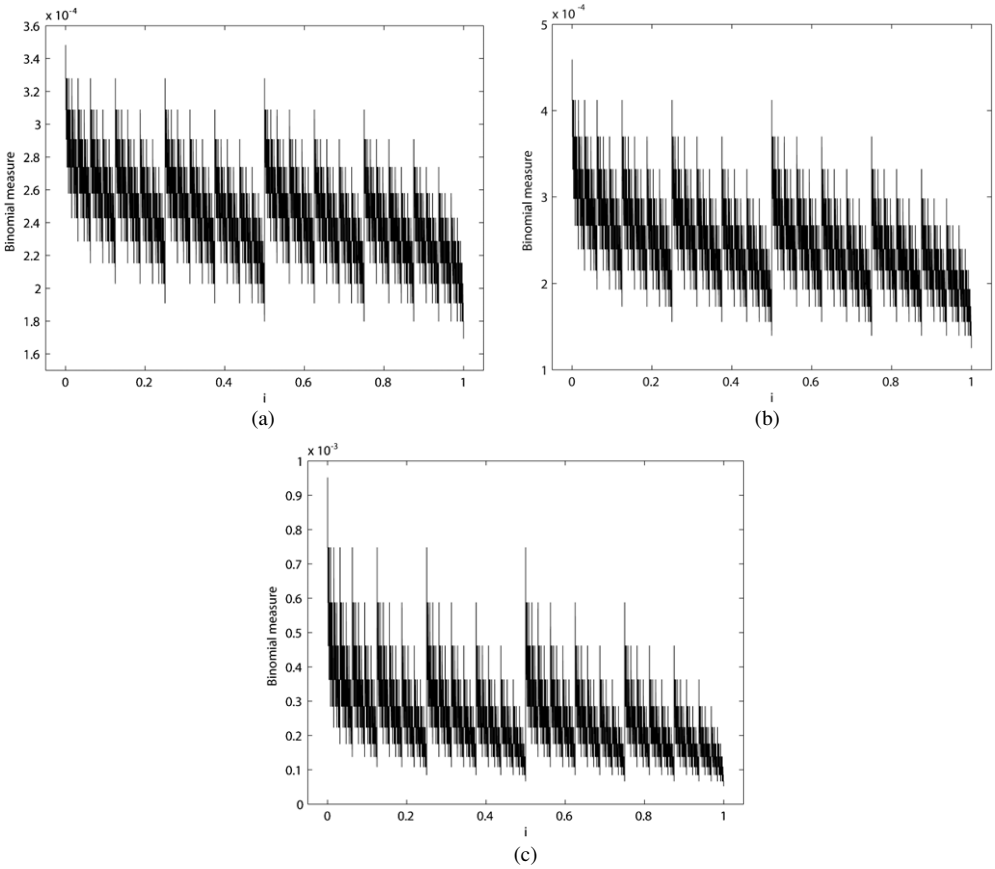

Figure 1. Binomial measures computed with (a) $k = 12$, $m_0 = 0.515$ and $m_1 = 0.485$; (b) $k = 12$, $m_0 = 0.527$ and $m_1 = 0.473$; (c) $k = 12$, $m_0 = 0.560$ and $m_1 = 0.440$.

where n_0 is the number of digits 0 in the interval where the local exponent is computed, $v_0 = -\log_2(m_0)$ and $v_1 = -\log_2(m_1)$. Moreover, the multifractal spectrum is given by (Evertsz and Mandelbrot 1992)

$$f(\alpha) = -\frac{\alpha_{\max} - \alpha}{\alpha_{\max} - \alpha_{\min}} \log_2 \left(\frac{\alpha_{\max} - \alpha}{\alpha_{\max} - \alpha_{\min}} \right) - \frac{\alpha - \alpha_{\min}}{\alpha_{\max} - \alpha_{\min}} \log_2 \left(\frac{\alpha - \alpha_{\min}}{\alpha_{\max} - \alpha_{\min}} \right), \quad (6)$$

where $\alpha_{\min} = v_0$ and $\alpha_{\max} = v_1$.

In order to compare the *theoretical* multifractal spectrum of a binomial measure with the one *numerically estimated* with our methodology, we compute the numerical multifractal spectra of the three binomial measures presented in figure 1. The results of the estimated partition functions and corresponding multifractal spectra are shown in figure 2. From this figure, we can observe that the theoretical and numerically estimated multifractal spectra coincide. Thus, the widths of the multifractal spectra when $f(\alpha) = 0.5$ (called later on as mid-width) are 0.07, 0.12 and 0.27 for the theoretical multifractal spectra (corresponding to figures 1(a), (b) and (c)), and also for the numerically estimated multifractal spectra. The calibration shown in figure 2 operates over a range of Hölder exponents similar to the range that will be met later on during the investigation of experimental LDF and HRV signals. This

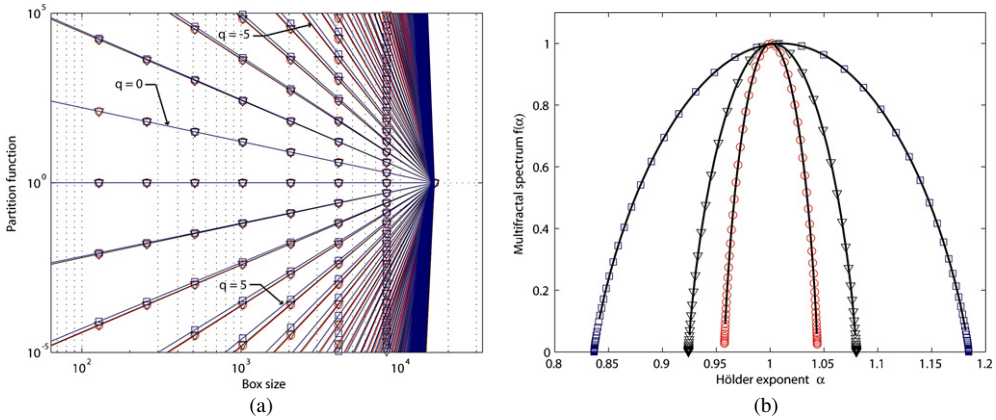

Figure 2. (a) Partition functions (circles, triangles, squares) for the three binomial measures shown in figure 1 ((a), (b), (c) respectively), computed with the box method. (b) Solid line: *theoretical* multifractal spectra for the three binomial measures shown in figure 1. Circles, triangles, squares: *numerically estimated* multifractal spectra for the binomial measures shown in figures 1(a), (b) and (c), respectively. To estimate the slope of the scaling region on the partition functions, we used boxes of size between 64 and 16 384 samples.

therefore validates the ability of our method to estimate multifractal spectra in the characteristic domain relevant to our experimental data. We thus propose thereafter to use this processing approach on LDF and HRV signals.

3. Multifractal analysis of LDF and HRV signals

3.1. Signal acquisition

By definition, HRV signals are derived from ECG recordings: they are obtained from the time intervals between consecutive heartbeats. In what follows, the multifractal spectra of HRV and LDF signals from human subjects are computed. The ECG and LDF signals processed in our work were recorded simultaneously in 14 subjects (mean age 28.8 ± 11.2 years; 9 men, 5 women) without known disease, who gave their written informed consent to participate. Subjects were placed *supine* in a quiet room with the ambient temperature set at 23 ± 1 °C, and left at rest for 15 min before each measurement, for temperature and cardiovascular adaptations. For the ECG acquisition, a Lifescope (Nihon Kohden Corporation) was used, and the signals were recorded with a sampling frequency of 1000 Hz and then sub-sampled to 250 Hz. To record the LDF signals, a laser Doppler probe (PF408, Perimed, Stockholm, Sweden) connected to a laser Doppler flowmeter (Periflux PF4001, Perimed, Stockholm, Sweden) was positioned on the *forearm* ventral face of the subjects. Skin blood flow was assessed in arbitrary units (au) and recorded on a computer via an analog-to-digital converter (Biopac System) with a sampling frequency of 250 Hz. A sub-sampling to 25 Hz was then performed. ECG and LDF signals were recorded *simultaneously* for at least 25 min.

For 7 of the 14 above-mentioned subjects, another laser Doppler flowmeter probe was positioned on the distal phalanx of the second *finger* (palmar surface of the index). For these seven subjects, two LDF signals were thus recorded simultaneously (in addition to ECG data): one on the forearm and another one on the finger. Moreover, for five of these seven subjects

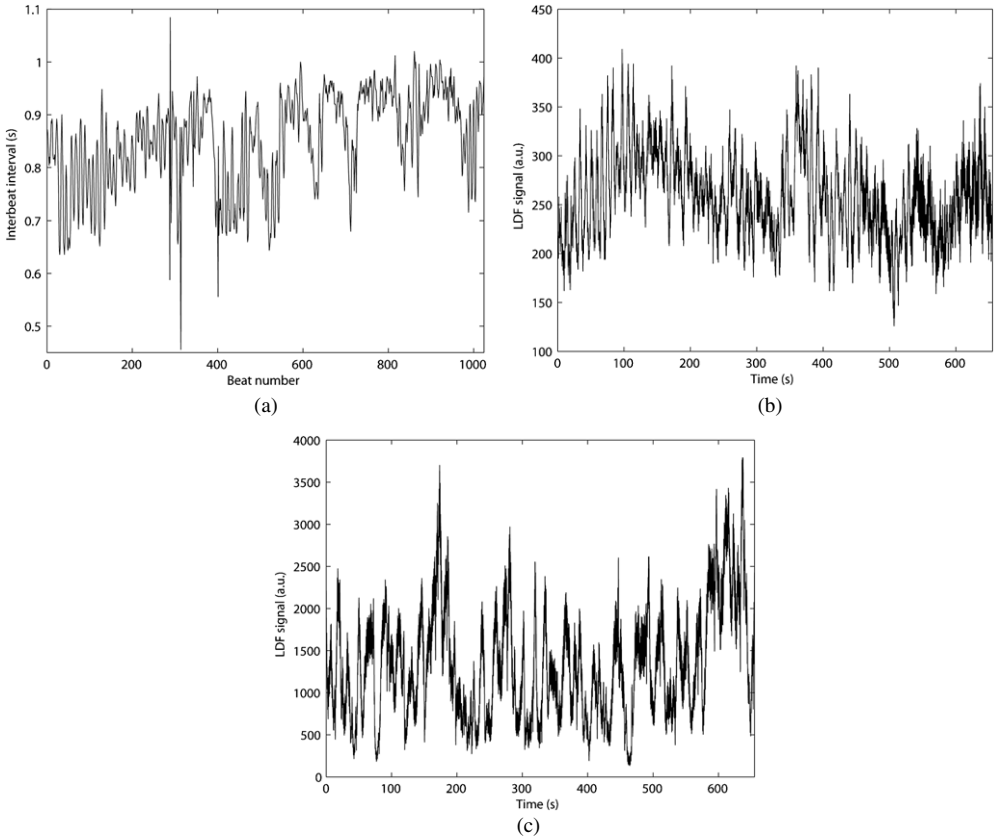

Figure 3. (a) HRV signal from a healthy subject at rest, in the supine position. (b) Skin LDF signal recorded in a healthy subject at rest in the supine position. The LDF probe is positioned on the ventral face of the forearm. (c) Skin LDF signal recorded in a healthy subject at rest in the supine position. The LDF probe is positioned on the distal phalanx of the second finger (palmar side of the index).

who had two LDF probes, the recordings made in the *supine* position were preceded by 8 min of recordings (ECG + two LDF signals) in the *upright* position.

After acquisition, ECG signals were processed to obtain the HRV data: a computer program was developed by our group (written in Matlab, The MathWorks, Inc.) to automatically detect the *R* peaks of the ECG time series; the results given by the automatic detection were then visually checked and corrected if needed, and the R–R intervals were computed. HRV and LDF data are shown in figure 3. In what follows, the previously described methodology estimating the multifractal spectra is applied on LDF and HRV signals.

3.2. Multifractal spectra obtained in the supine position

For the *supine* position, 16 384 samples of LDF signals (∼11 min of data) and 1024 samples of HRV data (this corresponds to a mean of 14.19 min of ECG signals for the 14 subjects studied in this position) were processed. Partition functions of LDF and HRV data for one subject are shown in figures 4(a) and (b), respectively. The average multifractal spectra of

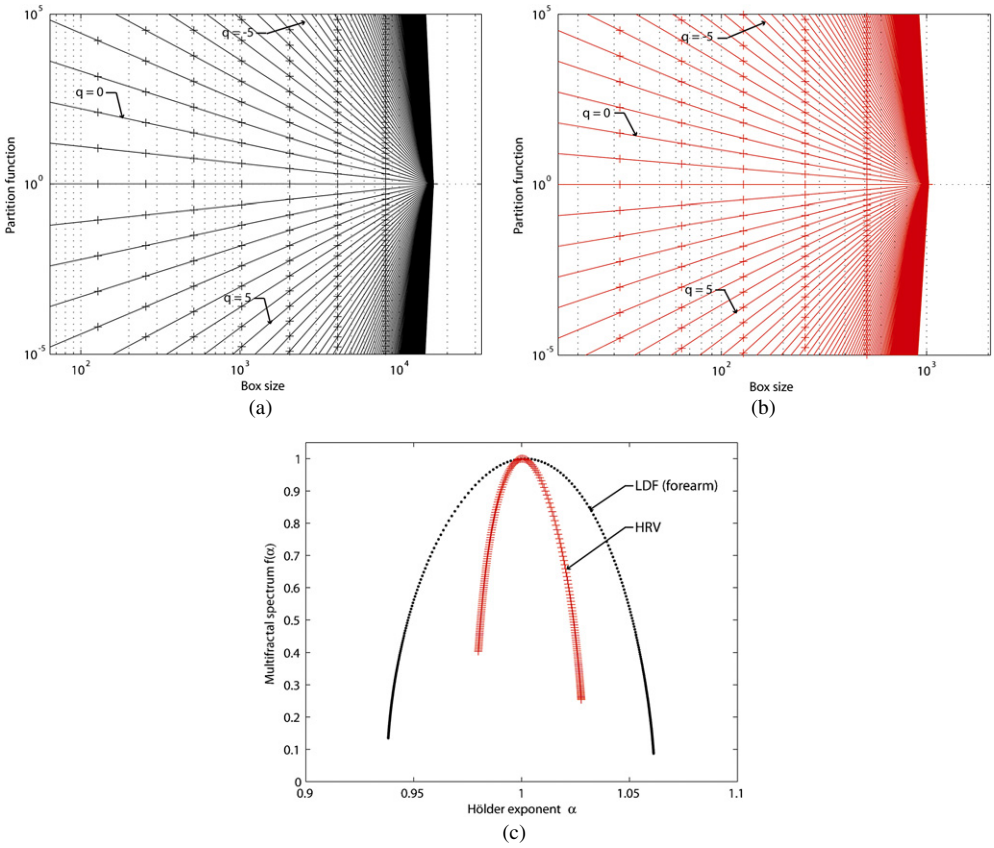

Figure 4. (a) Partition function of a LDF signal from a healthy subject at rest in the supine position. The LDF probe is positioned on the ventral face of the forearm. (b) Partition function of a HRV signal from a healthy subject at rest in the supine position. (c) Average multifractal spectra of HRV and LDF signals for 14 healthy subjects in the supine position. The LDF probe is positioned on the forearm (see the text). To estimate the slope of the scaling region on the partition functions, we used boxes of size between 16 and 512 samples for HRV, and between 64 and 16 384 samples for LDF signals.

LDF and HRV signals for the 14 subjects, when the LDF probe is on the forearm, are shown in figure 4(c). From the latter figure, we observe that the average multifractal spectrum of LDF signals recorded on the forearm is larger than the one of HRV data. This is true on average, but also for all the 14 subjects studied. Thus, the mid-width is 0.10 for LDF signals recorded on the forearm, whereas it is 0.04 for the average multifractal spectrum of HRV data.

Moreover, the average multifractal spectra of LDF and HRV signals, for the two LDF probe positions, when the subjects are supine are shown in figure 5. The average multifractal spectrum of LDF signals recorded on the finger is larger than the one of HRV data. Thus, the mid-width is 0.17 for the average multifractal spectrum of LDF signals recorded on the finger, whereas it is 0.04 for the one of HRV data. Furthermore, the average multifractal spectrum of LDF signals recorded on the finger is larger than the one of LDF signals recorded on the forearm. We also note that the average multifractal spectrum of LDF signals recorded on the finger is more asymmetric than the one of LDF signals recorded on the forearm.

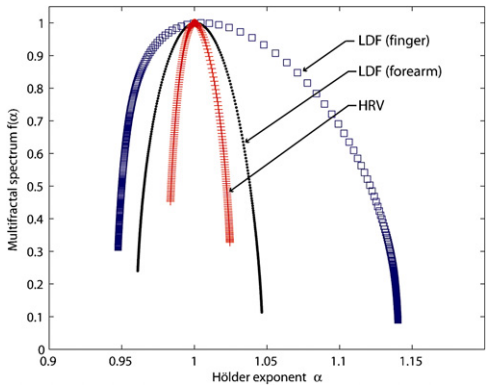

Figure 5. Average multifractal spectra of HRV and LDF signals for seven healthy subjects in the supine position. Forearm: the LDF probe is positioned on the ventral face of the forearm; finger: the LDF probe is positioned on the distal phalanx of the second finger (palmar side of the index) (see the text). To estimate the slope of the scaling region on the partition functions, we used boxes of size between 16 and 512 samples for HRV, and between 64 and 16 384 samples for LDF signals.

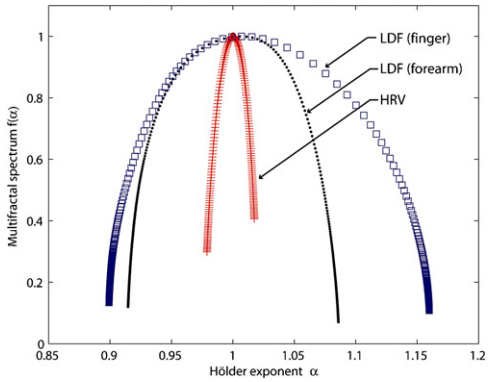

Figure 6. Average multifractal spectra of HRV and LDF signals for five healthy subjects in the upright position. Forearm: the LDF probe is positioned on the ventral face of the forearm; finger: the LDF probe is positioned on the distal phalanx of the second finger (palmar side of the index) (see the text). To estimate the slope of the scaling region on the partition functions, we used boxes of size between 16 and 256 samples for HRV, and between 256 and 8192 samples for LDF signals.

3.3. Multifractal spectra obtained in the upright position

For the *upright* position, 8192 samples of LDF signals (5.46 min of data) and 512 samples of HRV signals (this corresponds to a mean of 5.03 min of ECG data for the five subjects studied in this position) are processed. Figure 6 shows the average multifractal spectra of HRV data and LDF signals (recorded on the forearm and on the finger). From this figure we can observe that, as in the supine position, the average multifractal spectrum of LDF signals recorded on the forearm is larger than the one of HRV data. This is true on average, but also for all the five subjects studied. The mid-width is 0.15 for the average multifractal spectrum of LDF signals recorded on the forearm, whereas it is 0.03 for the one of HRV data. Furthermore, the average multifractal spectrum of LDF signals recorded on the finger is larger than the one of HRV data

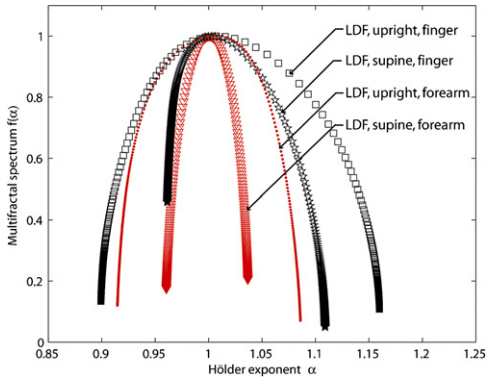

Figure 7. Average multifractal spectra of LDF signals for five healthy subjects. Forearm: the LDF probe is positioned on the ventral face of the forearm; finger: the LDF probe is positioned on the distal phalanx of the second finger (palmar side of the index) (see the text). For LDF signals, the estimation of the slope for the scaling region on the partition functions was done using boxes of size between 256 and 8192 samples.

(see figure 6). The average multifractal spectrum of LDF signals recorded on the finger is also larger than the average multifractal spectrum of LDF signals recorded on the forearm (as found for the supine position). The mid-width is 0.23 for the average multifractal spectrum of LDF signals recorded on the finger, whereas it is 0.15 for the one of LDF signals recorded on the forearm. Moreover, as in the supine position, the average multifractal spectrum of LDF signals recorded on the finger is more asymmetric than the one of LDF signals recorded on the forearm.

We also observe (see figure 7) that the average multifractal spectra of LDF signals have different patterns between upright and supine positions (for figure 7, 8192 samples of LDF signals (5.46 min of data) and 512 samples of HRV signals are considered for both upright and supine positions).

4. Discussion

From figures 4(a) and (b) we observe that the partition functions exhibit a power-law behavior, or a linear behavior in log–log coordinates, over a significant range of scales and of exponents. This type of scaling behavior, or regular evolution across scales, is an important property to identify fractal data. From these observations, we can infer that LDF and HRV signals present multifractal properties.

Moreover, our results show that the average numerically estimated multifractal spectrum of HRV data has a mid-width of 0.04 for the supine position (average value computed with 14 subjects). The recent nonlinear studies dealing with HRV mostly analyzed data from long series of R–R intervals based on ambulatory 24 h ECG recordings. Our study was designed to analyze and compare the multifractal spectra of short series (series of a few minutes; long periods of LDF recordings are not possible due to the high sensibility of the LDF technique to movements). However, we note that the average multifractal spectra we obtain with HRV short series are close to the ones presented by Munoz-Diosdado *et al* (2005a, 2005b) and by Guzman-Vargas *et al* (2005) who analyzed longer periods of data (2 h of ECG for Munoz-Diosdado *et al* 2005a, 2005b, and around 8 h of ECG for Guzman-Vargas *et al* 2005).

Therefore, the multifractal spectra of HRV data may not vary much between short (laboratory conditions) and longer recordings (Holter ECG).

From our results we also observe that, whatever the LDF probe position (finger or forearm), and whatever the subject position (supine or upright), the average multifractal spectra of LDF time series are larger than the ones of HRV data. The width of a multifractal spectrum measures the length for the range of fractal exponents in the signal. Therefore, the wider the range, the 'richer' the signal in structure. From our results, we may deduce that LDF signals are 'richer' in structure than HRV data. When LDF signals are reduced to samples acquired during the R peaks of the ECG data, the results are the same: we find larger multifractal spectra for these reduced data than for HRV.

Our results also show that the width for the average multifractal spectrum of LDF signals is larger when the data are recorded on the palmar side of the finger than when they are recorded on the ventral face of the forearm; the average multifractal spectrum is also more asymmetric in the finger than in the forearm. Moreover, from our results we observe that LDF signals recorded in the upright position do not have the same multifractal spectra as the ones recorded in the supine position (see figure 7). Several hypotheses can be proposed to explain all these differences.

(1) The differences observed between HRV and LDF multifractal spectra may come from the nature and origins of the signals: ECG signals (from which HRV data are extracted) come from the recording of the potential changes at the skin surface resulting from depolarization and repolarization of heart muscle. The ECG signal, being a straightforward recording of the electrical activity of the heart, is simpler (it has been produced by a simpler system) than that recorded by LDF. LDF signals come from light beating spectroscopy. In the LDF technique, a heterodyne detection process is used: shifted and non-shifted laser light is mixed together forming a dynamic self-beating speckle pattern at the detector. The coherence of the laser light and the Doppler effect lead to temporal intensity variations of the speckle areas (for the influence of the coherence laser light in the speckle variations, see for example Federico and Kaufmann (2006) and Funamizu and Uozumi (2007)). Therefore, many signal-processing steps are present between the recording of the backscattered photons and the LDF visualization device. This may lead to LDF signals becoming more noisy than HRV data. In order to analyze the possible role played by the instrumentation noise in the width of the multifractal spectra, we computed the multifractal spectrum of a noisy HRV signal (see figure 8). The latter figure shows that a very large amount of noise (3.5 times the standard deviation of the original HRV signal) has to be added to a HRV signal to cause its multifractal spectrum to become similar to that of a LDF signal. The study of the noise influence in the width of the multifractal spectra could be continued; a multifractal analysis of LDF speckles could also be conducted.

(2) The larger multifractal spectra of LDF signals compared to the ones of HRV data may also come from the microcirculation flow. LDF measurements from the skin reflect perfusion in capillaries, arterioles, venules and dermal vascular plexa. The diameters of some vessels probed may therefore be in the same range as the ones of the red blood cells. The complexity of the flow in such conditions could contribute to the width of the multifractal spectra for LDF signals. This hypothesis could be analyzed by computing and processing models describing microvascular flow.

(3) The differences observed between multifractal spectra of LDF signals recorded on the ventral face of the forearm and on the palmar side of the finger could be due to physiological aspects: on the palmar side of the finger, the sympathetic activity is higher than on the forearm (see for example Azman-Juvan *et al* (2008)). Moreover, the index microvasculature includes venoarteriolar anastomoses that largely influences the blood

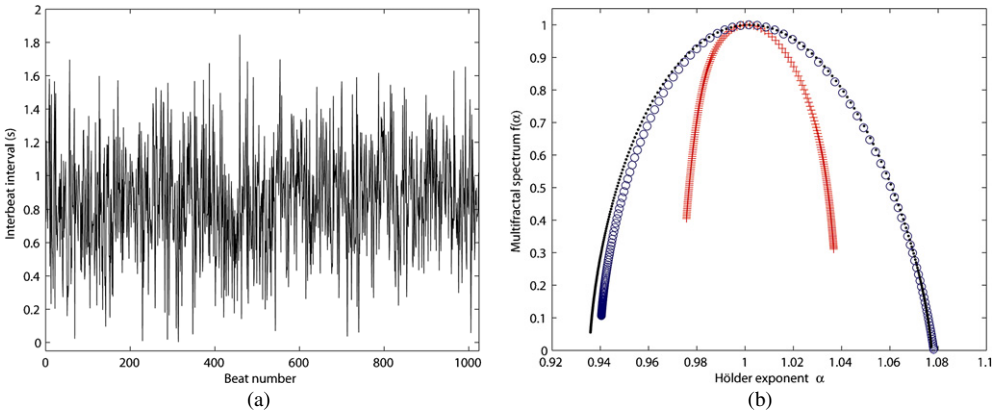

Figure 8. (a) Noisy version of the HRV signal presented in figure 3(a). The Gaussian noise added has a standard deviation equal to 3.5 times the standard deviation of the original HRV signal. (b) Multifractal spectra of the original (+ curve) and noisy version (circle curve) of a HRV signal, and of a LDF signal (dotted curve) recorded in the same subject. The original HRV signal is presented in figure 3(a); the noisy version is presented in figure 8(a); the LDF signal is presented in figure 3(b). To estimate the slope of the scaling region on the partition functions for the computation of the multifractal spectra, we used boxes of size between 16 and 512 samples for HRV, and between 64 and 16 384 samples for LDF signals.

flow recorded at this level contrary to the one recorded in the forearm. Furthermore, palmar surface of the index corresponds to glabrous skin whereas forearm skin is non-glabrous skin.

(4) The differences observed between upright and supine positions may come from physiological aspects: in the upright position, the sympathetic and parasympathetic activities differ from the ones in the supine position, modulating heart period (see for example Cooke *et al* (1999), Lurie and Benditt (1996) and Malliani (1999)). Moreover, the renin–angiotensin–aldosterone system also probably comes into account. To analyze hypotheses (3) and (4), other physiological experiments could be conducted.

5. Summary and conclusion

Many biomedical signals were recently processed to report on their mono or multifractality. Most of them were recorded from the central cardiovascular system. In the present paper, we analyzed data recorded *simultaneously* from *peripheral* and *central* levels in human subjects without known disease. To our knowledge, this study is the first one to report on the multifractal spectra of LDF signals, and to compare these multifractal spectra to those of HRV data. To conduct our work we used a method based on the computation of the partition function of the signals, on the estimation of their Renyi exponents and on the computation of their Legendre transform. This method was first tested on *a priori* known synthetic multifractal processes which led to the computation of numerically estimated multifractal spectra that coincide with theoretical multifractal spectra.

With the box sizes chosen in the estimation of the slope for the scaling region on the partition functions, the results of our multifractal analysis show the following:

- Whatever the LDF probe position (ventral face of the forearm or palmar side of the distal phalanx of the second finger), and whatever the subject position (supine or upright), the

peripheral cardiovascular system (studied through the LDF signals) has on average larger multifractal spectra than the central cardiovascular system corresponding to HRV data.

- The peripheral cardiovascular system (studied through the LDF signals recorded in the ventral face of the forearm or in the palmar side of the distal phalanx of the second finger) has different multifractal spectra in the supine position compared to the upright position.
- Whatever the subject position (supine or upright), the peripheral cardiovascular system (studied through the LDF signals) has on average larger multifractal spectra when the signals are recorded on the distal phalanx of the second finger (palmar side) than when the signals are recorded on the ventral face of the forearm.
- Whatever the subject position (supine or upright), the average multifractal spectrum of LDF signals recorded in the palmar side of the distal phalanx of the second finger is more asymmetric than the average multifractal spectrum of LDF signals recorded in the ventral face of the forearm.

Further work is now needed in order to compare the present results with multifractal spectra for which the Renyi exponents would have been determined with boxes of different sizes. Moreover, other studies have to be conducted in order to determine the origin of the large multifractal spectra for LDF signals, and to explain the differences observed between multifractal spectra of LDF and HRV data.

Acknowledgment

Benjamin BUARD thanks the 'Région des Pays de la Loire (France)' for its financial support.

References

Azman-Juvan K, Bernjak A, Urbancic-Rovan V, Stefanovska A and Stajer D 2008 Skin blood flow and its oscillatory components in patients with acute myocardial infarction *J. Vasc. Res.* **45** 164–72

Belcaro G V, Hoffman U, Bollinger A and Nicolaides A N 1994 *Laser Doppler* (London: Med-Orion Publishing)

Chao P T, Jan M Y, Hsiu H, Hsu T L, Wang W K and Lin Wang Y Y 2006 Evaluating microcirculation by pulsatile laser Doppler signal *Phys. Med. Biol.* **51** 845–54

Ching E S C and Tsang Y K 2007 Multifractality and scale invariance in human heartbeat dynamics *Phys. Rev.* E **76** 041910

Cooke W H, Hoag J B, Crossman A A, Kuusela T A, Tahvanainen K U O and Eckberg D L 1999 Human responses to upright tilt: a window on central autonomic integration *J. Physiol.* **517** 617–28

Evertsz C J and Mandelbrot B B 1992 Multifractal measures *Chaos and Fractals* ed H O Peitgen, H Jürgens and D Saupe (New York: Springer) pp 921–54

Federico A and Kaufmann G H 2006 Multifractals and dynamic speckle *Proc. SPIE* **6341** 63412J

Funamizu H and Uozumi J 2007 Multifractal analysis of speckle intensities produced by power-law illumination of diffusers *J. Mod. Opt.* **54** 1511–28

Gomes M B, Matheus A S and Tibirica E 2008 Evaluation of microvascular endothelial function in patients with type 1 diabetes using laser-Doppler perfusion monitoring: which method to choose? *Microvasc. Res.* **76** 132–3

Guzman-Vargas L, Munoz-Diosdado A and Angulo-Brown F 2005 Influence of the loss of time-constants repertoire in pathologic heartbeat dynamics *Physica* A **348** 304–16

Halsey T C, Jensen M H, Kadanoff L P, Procaccia I and Shraiman B I 1986 Fractal measures and their singularities—the characterization of strange sets *Phys. Rev.* A **33** 1141–51

Havlin S, Amaral L A N, Ashkenazy Y, Goldberger A L, Ivanov P Ch, Peng C K and Stanley H E 1999 Application of statistical physics to heartbeat diagnosis *Physica* A **274** 99–110

Humeau A, Chapeau-Blondeau F, Rousseau D, Rousseau P, Trzepizur W and Abraham P 2008 Multifractality, sample entropy, and wavelet analyses for age-related changes in the peripheral cardiovascular system: preliminary results *Med. Phys.* **35** 717–23

Humeau A, Chapeau-Blondeau F, Rousseau D, Tartas M, Fromy B and Abraham P 2007a Multifractality in the peripheral cardiovascular system from pointwise Hölder exponents of laser Doppler flowmetry signals *Biophys. J.* **93** L59–61

Humeau A, Koïtka A, Abraham P, Saumet J L and L'Huillier J P 2004 Spectral components of laser Doppler flowmetry signals recorded in healthy and type 1 diabetic subjects at rest and during a local and progressive cutaneous pressure application: scalogram analyses *Phys. Med. Biol.* **49** 3957–70

Humeau A, Steenbergen W, Nilsson H and Strömberg T 2007b Laser Doppler perfusion monitoring and imaging: novel approaches *Med. Biol. Eng. Comput.* **45** 421–35

Ivanov P C, Amaral L A N, Goldberger A L, Havlin S, Rosenblum M G, Stanley H E and Struzik Z R 2001 From 1/f noise to multifractal cascades in heartbeat dynamics *Chaos* **11** 641–52

Ivanov P C, Amaral L A N, Goldberger A L, Havlin S, Rosenblum M G, Struzik Z R and Stanley H E 1999 Multifractality in human heartbeat dynamics *Nature* **399** 461–5

Kienle A 2001 Non-invasive determination of muscle blood flow in the extremities from laser Doppler spectra *Phys. Med. Biol.* **46** 1231–44

Kim S W, Kim S C, Nam K C, Kang E S, Im J J and Kim D W 2008 A new method of screening for diabetic neuropathy using laser Doppler and photoplethysmography *Med. Biol. Eng. Comput.* **46** 61–7

Li Z, Tam E W, Kwan M P, Mak A F, Lo S C and Leung M C 2006 Effects of prolonged surface pressure on the skin blood flowmotions in anaesthetized rats-an assessment by spectral analysis of laser Doppler flowmetry signals *Phys. Med. Biol.* **51** 2681–94

Liu X, Zeng B, Fan C, Jiang P and Hu X 2006 Spectral analysis of blood perfusion in the free latissimus dorsi myocutaneous flap and in normal skin *Phys. Med. Biol.* **51** 173–83

Lurie K G and Benditt D 1996 Syncope and the autonomic nervous system *J. Cardiovasc. Electrophysiol.* **7** 760–76

Malliani A 1999 The pattern of sympathovagal balance explored in the frequency domain *News Physiol. Sci.* **14** 111–7

Mandelbrot B B 1999 *Multifractals and 1/F Noise—Wild Self-Affinity in Physics (1963–1976)* (New York: Springer)

Munoz-Diosdado A, Angulo Brown F and De Rio-Correa J L 2005a Changes in multifractality with aging and heart failure in heartbeat interval time series *Conf. Proc. IEEE Eng Med. Biol. Soc.* vol 7 pp 6981–4

Munoz-Diosdado A, Guzman-Vargas L, Ramirez-Rojas A, De Rio-Correa J L and Angulo Brown F 2005b Some cases of crossover behaviour in heart interbeat and electroseismic time series *Fractals* **13** 253–63

Nilsson G E 1984 Signal processor for laser Doppler tissue flowmeters *Med. Biol. Eng. Comput.* **22** 343–8

Nilsson G E, Tenland T and Öberg P Å 1980a A new instrument for continuous measurement of tissue blood flow by light beating spectroscopy *IEEE Trans. Biomed. Eng.* **27** 12–9

Nilsson G E, Tenland T and Öberg P Å 1980b Evaluation of a laser Doppler flowmeter for measurement of tissue blood flow *IEEE Trans. Biomed. Eng.* **27** 597–604

Öberg P Å 1990 Laser-Doppler flowmetry *Crit. Rev. Biomed. Eng.* **18** 125–63

Rajan V, Varghese B, van Leeuwen T G and Steenbergen W 2009 Review of methodological developments in laser Doppler flowmetry *Lasers Med. Sci.* **24** 269–83

Shepherd A P and Öberg P Å 1990 *Laser-Doppler Blood Flowmeter* (Dordrecht: Kluwer)

Stern M D 1975 In vivo evaluation of microcirculation by coherent light scattering *Nature* **254** 56–8

Struzik Z R 2000 Determining local singularity strengths and their spectra with the wavelet transform *Fractals* **8** 163–79